SPECTROSCOPIC AND MICROSCOPIC STUDIES OF AGGREGATED MOLECULES COATED ONTO NANOMATERIALS

by

FLEUMINGUE JEAN-MARY

A dissertation submitted to the Graduate Faculty in Chemistry in partial fulfillment of the requirements for degree of Doctor of Philosophy, The City University of New York

2006

UMI Number: 3231995

ProQuest Information and Learning Company
300 North Zeeb Road
P.O. Box 1346
Ann Arbor, MI 48106-1346

This manuscript has been read and accepted for the Graduate Faculty in Chemistry in satisfaction of the dissertation requirement for the degree of Doctor of Philosophy.

Date	**Dr. Daniel L. Akins** Chair of Examining Committee
Date	**Dr. Gerald W. Koeppl** Executive Officer
	Dr. Luis E. Brus
	Dr. Lynn Francesconi
	Dr. Maria C. Tamargo

Supervisory Committee

The City University of New York

ABSTRACT

SPECTROSCOPIC AND MORPHOLOGICAL STUDIES OF AGGREGATED MOLECULES COATED ONTO NANOMATERIALS

by

Fleumingue Jean-Mary

Advisor: Professor Daniel L. Akins

Small self-assembled groupings of molecules (in particular, the so-called J-type molecular aggregates) can possess remarkable linear and nonlinear optical responses to radiation. Such inherent responses coupled with the enhanced efficiencies of some optical processes when noble metal nanostructures are present may engender composite systems with useful functionalities. This dissertation, hence, focuses on three principal missions. The first centered on the synthesis of stable, reproducible, monodisperse nanometric noble-metal spheres and nanoshells, the second on the fabrication of well-organized molecular assemblies on the nanoparticles surface, and the third on developing or implementing nanofabrication strategies to orient and pattern these nanostructures onto two-dimensional substrates.

Nanosize, spherical silver and gold particles and gold nanoshells are formed by chemical reduction, occasionally, in the presence of protective agents. The synthesized nanoparticles have one or more peaks in the absorption spectrum in the visible range, depending on the particles' sizes and shapes. The resulting metal nanoparticles having sizes between 5-100 nm and spherical morphology have their structures evaluated qualitatively evaluated from their surface plasmon band and quantitatively measured using dynamic light scattering (DLS), atomic force microscopy (AFM) and transmission

electron microscopy (TEM).

The present dissertation reports, among other things, on the adsorption and aggregate formation of four related cyanine dyes on nanoparticle surfaces in solution and cast films. By using a combination of UV-Visible absorption, fluorescence and Raman spectroscopy, AFM, near-field scanning optical microscopy (NSOM), and quantum chemical calculations, insight has been gained in the relationship between chemical structure, aggregate structure and optical properties. The observations confirm aggregation by the characteristic narrow J-absorption and J-emission bands. J-aggregation was found to depend strongly on the nanoenvironement, with the presence of nanoparticles greatly improving the stability of the J-aggregates.

Tailoring the optical properties of metal nanoparticles by organizing chromophores of specific properties on them can yield photoresponsive nanohybrid materials with exciting opportunities for the design of novel, photon-based devices for sensing and optical switching. Applications of nanoparticle-based materials, in which collective nanoparticle optical properties are exploited, are currently emerging for surface-enhanced Raman (SERS), metal-enhanced fluorescence (MEF), surface plasmon resonance (SPR) and colorimetric assays.

PREFACE

Nanotechnology is a broad, interdisciplinary area of research and industrial activity that has been rapidly growing world wide for the past decade. Activities in the nanotechnology arena often involve multidisciplinary grouping of partners, as well as a range of techniques, all connected because of the dimensions involved. Nanoparticles can be formed through a wide variety of physical, chemical and biological processes, some of which are quite novel, while others are quite commonplace.

Nanotechnology involves the creation and/or manipulation of materials at the nanometer (nm) scale either by scaling up from single groups of atoms (bottom-up approach) or by refining or reducing bulk materials (top-down approach). A nanometer is a billionth of a meter (i.e, 1×10^{-9} m). To give a sense of this scale, a human hair is of the order of 10,000 to 50,000 nm, a single red blood cell has a diameter of around 5000 nm, viruses typically have a maximum dimension of 10 to 100 nm and a DNA molecule has a diameter of 2 – 12 nm (www.nano.gov). The use of the term "nanotechnology" can be misleading since it is not a single technology or scientific discipline. Rather, it is a multidisciplinary grouping of physical, chemical, biological, engineering, and electronic, processes, materials, applications and concepts in which the defining characteristic is one of size. Also, nanotechnology is a rapidly evolving and expanding discipline and has aroused growing media and public interest. Articles appear frequently in the scientific and popular press and on a host of websites dedicated to the field.

The production and characterization of nanoparticles, molecular aggregates, also known as another nanoscale material, and their composites have attracted intense research interest owing to the nanomaterials unique chemical and physical properties, and

vast potential for use in electronic, magnetic and optoelectronic, biomedical, pharmaceutical, cosmetic, energy, catalytic and materials applications. A simple search of ACS Scifinder Scholar, in May 2006, showed 67679 references containing the concept of nanoparticles and 345 containing nanoshells; 2664 references were found containing the J-aggregate concept. There were 57 references with both J-aggregate and nanoparticles as concepts and none containing both J-aggregates and nanoshells.

The research described in this dissertation has focused on three principal missions: one being on the synthesis of stable, reproducible, monodisperse nanometric noble-metal spheres and nanoshells, a second, on the fabrication of well-organized molecular assemblies on the nanoparticles surface, and a third on developing or implementing nanofabrication strategies to orient and pattern these nanostructures onto two-dimensional substrates. On the whole, the research efforts in this dissertation contribute to the body of knowledge concerning nanoparticles and molecular aggregates coated nanoparticles.

The dissertation consists of seven chapters which present fundamental and experimental exploration of metal nanoparticles and dye-coated nanoparticles in solution and deposited on glass substrates. Some experimental results are supported by theoretical calculations. The organization of the dissertation is as follows: Chapter 1 presents an introductory overview, defining molecular aggregates and specifying different types of aggregates. In addition, cyanine dyes and their tendency to aggregate are presented together with the molecular exciton model used to explain different structural arrangements of molecular aggregates, in particular, H- and J-type aggregates. A discussion of metal nanoparticles, their history, properties, applications and means of

preparation is provided. Also, a theoretical background is presented to help explain their optical properties. Chapter 2 deals with the variety of experimental techniques and instrumentations used in this dissertation to characterize the prepared nanostructured materials. Chapters 3 to 6 are devoted to the preparation and characterization of the various nanoparticles and dye-coated nanoparticle systems. Chapter 7 summarizes the achievements of the research efforts and suggests future directions for study and applications for heterostructured "hybrid" materials that utilize inorganic templates functionalized with organic constituents.

ACKNOWLEDGEMENTS

Forces far beyond those that I might summon have aided me as I have pursued the Ph.D. degree. Indeed, all the support, help, encouragement, prayer, and love from friends, colleagues, advisors, and family, throughout my scholastic journey, have aided and guided me. I would like to give my thanks to all who have played a role in helping me in furthering my education.

I take this opportunity to sincerely thank my adviser, Professor Daniel L. Akins, Distinguished Service Professor of Chemistry and Director of CUNY-Center for Analysis of Structures and Interfaces (CASI), for giving me the chance to reach this milestone in my life. I am very grateful to him for all the advice, encouragement, patience and continual support he has afforded me throughout my studies. I am deeply appreciative for the many opportunities he has provided me, and last but not least the granted freedom to raise a family while continuing my research.

I would also like to express my sincere gratitude to my committee members, Professors James D. Batteas, Associate Professor of Chemistry, Texas A & M University, Louis E. Brus, S. L. Mitchell Professor, Columbia University, and Maria C. Tamargo, Professor of Chemistry and Dean of Science, The City College of CUNY for taking the time and interest in sharing their insights, knowledge and experience with me, both in informal conversations and on committee report forms. Their valuable suggestions, discussions have aided me in understanding and solving many research issues and consequently have greatly facilitated my transformation into an able scientist. I am enormously grateful to Professor Lynn Francesconi, Professor of Chemistry, Hunter College of CUNY, for agreeing to serve on the committee towards the end of my

graduate studies.

I owe a special thanks to Professor Vernon G. S. Box, Professor of Chemistry, The City College of CUNY, for allowing me the chance to conduct research in my senior undergraduate year under his supervision. Professor Box helped me understand computational chemistry very early on with great enthusiasm. I also thank him for my first publication.

I am grateful to Dr. David Adebimpe for encouraging me to pursue the doctorate degree and for all his advice, discussion and encouragement along the course of my studies. Also, I thank Professors Glen Kowach and John Lombardi for engaging me in discussions that are project related and other generally technique or concept related. I have benefited a lot from these hallway conversations and from your precious comments.

I would like to acknowledge Dr. Amy Michaels and Dr. Jiang Jiang in Professor Brus's laboratory at Columbia University for their help in conducting some of the early AFM studies and also thank Professor Brus for access to the AFM scanner and the resonance Rayleigh scattering acquisition instrumentation. I thank Professor Charles Michael Drain of the Hunter College of CUNY for use of the dynamic light scattering instrumentation. Special thanks are owed to Dr. Noemi Perez-Paz for fruitful discussions derived from applying the AFM instrument in our laboratory to her research problems.

My gratitude is also express to my colleagues in the Center for Analysis of Structures and Interfaces (CASI) who have contributed their time, helpful discussion and a friendly atmosphere that contributed much to the successful completion of my dissertation. These colleagues include Dr. Metin Aydin, Philippe Mercier, Dionne Miller, Dr. Nathan Stevens, Dr. Haiquan Guo, Dr. Hui Yang, and Shiunchin C. Wang.

A large portion of my work would not have been possible if it were not for the undergraduate researchers that I worked with, namely Leoni Hayles and Kaliq Williams. In particular, I thank Kaliq for conducting the initial nanoshells work. I thank both of them for their help in carrying out work to ensure the reproducibility of the systems studied.

Sincere thanks also to Mrs. Sandra Smith and Mrs. Diane Adebowale for their unceasing assistance and to my friends Mrs. Deserine Baker, Dr. Ducce Paul, Robert Romain and Richard Livingston for all their words of encouragement.

I owe my deepest thanks to my family for their unconditional love and support. To my mom and dad, thank you for making it clear, from the start, that school was the only thing that I was responsible for. You have taught me what is important and what to pursue in life; to my brother Wilkens and his family for encouraging me always and my sister-in-law Mrs. Sherley Warden for all your support and love. Finally, to my loving wife Enency, thank you for your patience, support and love and of course my angels. You gave me the precious feeling that you have always been and will be here for me: For these and for tens other reasons. Thank you!

Last but most important, I would like to thank God for giving me the opportunity to pursue the doctorate degree and helping me to accomplish it.

With the strength of will, people change themselves.
With the strength of love, people change others.
With the strength of thinking, people change the world.

--Confucius Chinese philosopher & reformer (551 BC - 479 BC)

To my

Parents*- Helene & Depestre for their love, care and encouragement*

Wife*- Enency for her undying support and love*

Kids*- Jayvyn and Nyere for bringing purpose into my life*

TABLE OF CONTENTS

LIST OF TABLES

LIST OF FIGURES

1 Introduction

1.1 Molecular Aggregates

Ordered molecular aggregates, specially referred to as supramolecular materials, are complex systems formed through self-assembly[1] driven by noncovalent intermolecular forces. The term self-assembly generally denotes spontaneous assembly of several molecules into a single, highly structured supramolecular aggregate. The self-organizing nature of such molecular aggregates would be based on the spontaneous stacking or alignment of nanostructures dictated by their geometrical (shape, size) requirements and contact energies.[2] In addition, molecular aggregates are macroscopic clusters of molecules with intermediate sizes between isolated molecules and crystals. The size of these complex systems may vary from a few nanometers (e.g., folding polymers, micelles) to several micrometers and longer (e.g., thin films and wires, membranes).[2] A point of interest is learning how the properties evolve as aggregates of molecules grow from the smallest size, i.e., dimers, through successively larger ones, toward bulk matter.[3] Molecular aggregates can serve as a medium to bridge between an understanding of the changing properties of matter with size and at the same time providing a means of investigating the onset of new optical and electronic properties that evolve from the interactions of an assembly of molecules. More important, molecular aggregates offer the prospect of the development of new materials. Understanding such molecular assemblies is important because they serve as potential candidates for biomimetic systems, optoelectronic molecular devices, liquid crystal displays, solar photovoltaic cells and organic light emitting diodes (OLEDs).[4,5]

Examples of molecular aggregates include organized self-assemblies such as

micelles (made up of surfactants in water), reverse micelles (made of up surfactants in a non-polar solvent) and liposomes (vesicles, made up of lipid molecules in water), etc.[6,2]

1.1.1 J- and H-Aggregates

Aggregation of organic dye molecules, another type of molecular aggregates, is a common phenomenon. Most organic molecular aggregates are basically crystal like structures with three dimensional molecular lattice arrangements.[2] Aggregation of molecules that form a low-dimensional solid is rare.[2] However, cyanine dyes were discovered to be theoretically describable as one-dimensional aggregates in the mid-nineteen thirties.[7,8] Scheibe[7] and, independently, Jelley[8] discovered that upon increasing the concentration of the dye pseudo-isocyanine (PIC) in water, a narrow absorption band is created, which is red-shifted relative to that of the monomer band. The narrow absorption band, the so-called J-band, was ascribed to the optical excitation of the aggregates formed. In contrast to the ideal crystal, molecular aggregates have finite dimensions. Their optical properties differ strongly from those of single molecules and pure crystals, properties that make them interesting systems to be investigated. It has been established that the change in spectroscopic properties upon aggregation originates from intermolecular interactions in the aggregates that couple the optical transitions of individual molecules.

Cyanine dyes aggregates, that are usually referred to as J-aggregates or, occasionally, Sheibe aggregates,[9] are used as efficient photosensitizers in photographic emulsions, optical probes in biological systems[10] and, because of their enhanced nonlinear optical susceptibilities,[11] as materials for use in nonlinear optical devices.[12] J-aggregates represent a particular case of molecular assemblies and are bright examples of

self-organization of matter. Certain water-soluble ionic porphyrins were discovered in 1971[13] to form similar aggregates.

The H-aggregate is also depicted as a one dimensional array of molecules but differ from the J-aggregate in many aspects. For example, corresponding to the geometric arrangement for the adjacent stacking monomers, the J-aggregate is a one-dimensional head-to-tail arrangement of molecules in which the individual transition moments are parallel to each other and parallel to the line joining them.[14] In contrast to the head-to-tail arrangement of molecules in J-aggregates, a head-to-head, one-dimensional arrangement leads to formation of so-called H-aggregates.[14] These two different kinds of aggregates are also distinguished by a blue-shifted absorption band for the H-aggregate, relative to the monomer. Moreover, the aggregates are differentiable by a characteristic angle θ between the molecular transition dipole moments and the long aggregate axis.

This dissertation, among other things, describes in detail the experimental study of the formation and characterization of the J-aggregate of four cyanine dyes in a variety of environments, particularly, adsorbed on metal nanoparticles.

1.2 Cyanine Dyes

Organic cyanine dyes are intensely colored compounds. They were added as a new class of dyes to the supply of commercial dyestuffs with the synthesis of the first polymethine dye; viz., pseudo-isocyanine by C. Williams in 1856.[15] Cyanine dyes did not become commercial dyes for coloration purposes immediately after their discovery, because they are prone to decolorization by light and acid. Cyanine dyes delineate a class of conjugated organic molecules that were initially studied because of their commercial application as effective spectral sensitizers for silver halide micro-crystals in

photographic films, given that their absorption spectra are easily shifted by chemical substitution and by aggregation.[16] A typical structure, to be discussed below, consists of two heteroaromatic fragments linked by a polymethine chain. The photophysical properties of cyanine dyes are readily tuned by varying the heterocyclic moieties and polymethine bridge length. In the course of exploiting their spectral sensitizing property, it was determined early that these molecules self-assembled to form noncovalent aggregates in the ground state, which, upon optical excitation, resulted in the formation of excitonic states. These later states were found to be dramatically different in their spectral and dynamical properties than those of the related monomers.[17] Cyanines are well known to form J-aggregates at a relatively high concentration (~mM region) and perhaps are the most extensively studied class of molecules that form molecular aggregates.[18] The dissertation describes in detail the experimental study of the formation and characterization of heterostructured "hybrid" materials that utilized inorganic templates functionalized with molecular aggregates of several cyanine dyes. A molecular aggregate on a supporting template, which potentially gives shape and directionality for the growth of the aggregate, will be an interesting class of advanced materials.

1.2.1 Structure and Classification

The generic cyanine dye structure typically consists of two basic (electron donating) nitrogen containing heterocyclic ring systems, which terminate a chain of conjugated double bonds. One of the nitrogen atoms' can be viewed as positively charged and is linked by the chain consisting of an odd number of carbon atoms to the other nitrogen. The absorption of visible light by a cyanine dye is mainly determined by the sequence of methine groups (- CH =), which are normally in the E or trans configuration,

using the cis (Z)-trans (E) designation for geometrical isomerism of polyenes. The carbon atoms of the methine chain can be substituted by hetero atoms (e.g., S in thiacyanines), and they can carry other groups than hydrogen; they can also be parts of carbocyclic or heterocyclic ring systems.[15]

Extensive conjugation of the methine chain leads to the long wavelength absorption maxima and large molar absorptivities typical for cyanine dyes. Bond lengths, which can be determined by x-ray analysis, indicate that the positive charge on the nitrogen atom is significantly delocalized along the chain extending to the opposite heterocycle, which can result in the case of symmetrically substituted cyanine dyes in a structure in which the two end groups carry the same amount of (a half) positive charge.[19] Though the preferred geometry of these dyes is planar, solid–state structures[20] and analysis of solution spectra of cyanine dyes[21] reveal that steric interactions can induce twist deformations along the polymethine chain. Examination of variable temperature ^{1}H NMR spectra[22] and absorption spectra[23] indicate that this twist can persist in solution.

In discussing the electronic structure of polymethine dyes, it is of benefit to consider the two terminating groups as an electron acceptor A and an electron donor D as shown in Figure 1.1.[15]

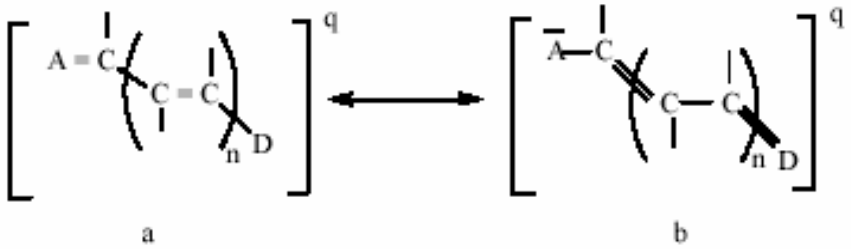

n = 0, 1, 2, 3... q = -1, 0, +1

Figure 1.1: Schematic representation of polymethine dyes.

The systematic nomenclature of the polymethine dyes is somewhat confusing due to the number of different classification schemes in use. Usually they are classified by the number of methine groups, as mono-, tri-, penta- … methine n = 1, 3, 5… (Figure 1.1). The terms simple cyanine, carbocyanine, dicarbocyanine, and so on, have also been used to designate the specific dyes derived from heterocycles with 1, 3, 5, and so on, methine carbon atoms.[24] In this scheme, only the methine groups (or their equivalents, such as –N= groups) in the chain are counted. Methine groups belonging to the terminal heterocyclic ring of the electron donor or acceptor group are not counted.

The polymethine chain can be further subdivided with respect to the electron acceptor and donor groups, *i.e.*, A and D in Figure 1.1. With A and D containing nitrogen, the polymethine dye is cationic (q = +1 in Figure 1.1). According to whether or not both or one of the nitrogens are components of the heterocyclic rings, these dyes are called cyanines, hemicyanines, or streptocyanines as shown in Table 1.1.

Table 1.1: Classification of polymethine dyes.[15]

Group name	General formula	Example
Cyanine		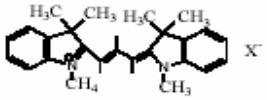 Astraphloxine FF
Hemicyanine	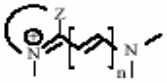	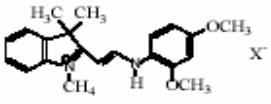 Maxilon Yellow 5G
Streptocyanine	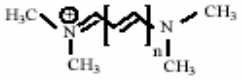	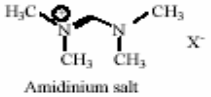 Amidinium salt
Oxonol	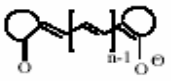	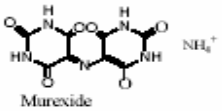 Murexide

Hemicyanine-like polymethine dyes, in which A and D are heterocycles containing oxygen, sulfur, or phosphorus in place of nitrogen, have also been described. The oxonols, in Table 1.1, are anionic polymethine dyes (q = -1 in Figure 1.1), which are of some commercial importance.

1.2.2 Molecular Aggregation of Cyanine Dyes

Cyanine dyes (cyanines, carbocyanines, hemicyanines and merocyanines) have a natural tendency to aggregate spontaneously in homogeneous aqueous solution when their concentration is increased or the temperature is lowered. Additionally, studies on the formation of aggregates, specifically, J-aggregates have been conducted for various systems, e.g., dispersed solutions,[25,26] polymer,[27] and sol-gel matrixes,[28,29] layer-by-layer assemblies,[30] vapor deposition films[31] and crystalline states.[32] Aggregation may be facilitated by concentrating and orienting a dye at the oppositely charged sites of dissolved polyelectrolytes, such as polyphosphates, which influence or even control the formation of dye aggregates, generally by non-bonding reversible interactions. Aggregation is also promoted by adsorption of the dye at solid-liquid interfaces such as aqueous dispersion of zinc oxide or silver halide[33] and other noble-metal nanoparticles.[34] Similarly, the air-liquid interface can also serves the same purpose, as demonstrated using the Langmuir-Blodgett technique, to spread a cyanine dye as a film on a water surface that resulted in aggregation formation.[35]

Various mechanisms have been suggested to explain the forces holding dye molecules together; these include intermolecular van der Waals-like attractive forces between the molecules,[36] hydrogen bonding with the solvent,[37] or coordination with metal ions.[36,37] The aggregation behavior of cyanine dyes has been extensively

investigated by studying the photophysical and photochemical properties of these aggregates, which result from the dispersion forces between the nearest-neighbor molecules (often referred to as π-π interactions) created by small local dipole moments and high polarizability of π-electrons in the polymethine backbone of cyanine dyes.

The most spectacular indication for the formation of aggregates is the dramatic change of the absorption spectrum. Upon J-aggregation, in addition to a broad monomeric band, one observes the rise of a new absorption band, which is significantly red-shifted and strongly narrowed compared to the monomer absorption band. Besides the aggregate species absorption spectra being markedly different compared to the monomeric species, the Lambert-Beer law is also no longer obeyed.

There are several factors affecting the tendency of a dye to aggregate, namely the structure of the dye; but also environment parameters, such as the polarity of solvent, the pH, the presence of electrolytes (ionic strength), concentration, and the temperature.

1.2.3 The Molecular Exciton Model

From the spectral shifts caused by aggregation, various aggregation types of dyes have been proposed. H-type and J-type aggregates are the two common types of aggregates formed. The relationship between the relative orientation of chromophores and the spectral shifts and widths of a dye aggregate has been explained in terms of the molecular exciton theory. [38]

With regards to the J-band, there are possibly two published theories describing its nature. First, Frank and Teller[39] proposed that the extremely strong and narrow J-band is due to the formation of an excitonic state through the electronic coupling of the tightly packed dye molecules in the aggregates. This theory received further development in

numerous publications and is currently generally accepted.[40] A second, recently suggested by Egorov,[41] gives the J-band a different origin. According to this latter theory, the J-band originates from an electron transfer between neighbor molecules in the aggregates and an unusual resonance between electronic motion and environmental nuclear motion. Both theories assume that the formation of the J-band is caused by the aggregation of dye molecules.

Below, some aspects of the conventional exciton band theory for one-dimensional molecular excitons are presented. This theoretical description of the linear response is relatively straightforward because it involves only the ground state of the aggregate (in which all molecules are in their ground states) and states in which the molecules share one excitation: the conventional Frenkel exciton or one-exciton. It will be shown that this theory can explain the essential features of the absorption spectrum of the aggregates.

The molecular exciton model provides a framework for treating the resonance interaction of excited states of weakly coupled molecules. In weakly coupled molecules, it is assumed that there is negligible intermolecular electron overlap and electron exchange. The transition moment of the electronic transition associated with individual component molecules is assumed to be localized, and the molecular unit, that is the chromophores, preserves their individual characteristics in the aggregates. The electronic states of the aggregate are expressed in terms of the electronic states of the component light absorbing unit.

The spectral properties of molecular aggregates are related to the spectral properties of the individual molecules by theoretical expressions involving observable experimental parameters: specifically, intermolecular distance, mutual intermolecular

orientation and geometry, and intensity (oscillator strength) of light absorption by the component molecules. Although the spectral effects of aggregation are small enough to satisfy the use of quantum chemical perturbation method, their effects are on the basis of the quantum mechanical resonance of excited states. Accordingly, blue and red-shifts or spectral splitting may be observed, depending on the geometry of the aggregate.

The starting point in the molecular exciton model treatment is the singlet electronic energy states and their corresponding electronic state wavefunctions for molecular monomers incorporated in a weekly bound aggregate. It is assumed that the electronic singlet energies E_0, E_1, E_2,$\cdots E_n$ and wave functions ψ_0, ψ_1, ψ_2,$\cdots \psi_n$ are known, satisfying the individual molecule Schrödinger equations:

$$H_i\psi_i = E_i\psi_i \tag{1.1}$$

Generally, each problem involves a two-level system, a ground and an excited singlet state energy with wavefunctions ψ_i and ψ_i^*, respectively, for molecule *i*. All molecules of an aggregate are considered to be identical. The zeroth order wave functions for molecular aggregates are used to derive the first order energies for the electronic states of the aggregate.

The structure, spectral properties and energy levels for simple aggregate systems, specifically, for a dimer, are treated here.

1.2.3.1 Molecular Dimers

The ground-state wavefunction for a molecular dimer consisting of two identical molecules is:

$$\psi_{gs} = \psi_a\,\psi_b \tag{1.2}$$

and is totally symmetric with respect to all symmetry operations. The first excited state of the dimer can be described equally well by two possible wavefunctions given by:

$$\Phi_1 = \psi_a \psi_b^* \text{ and } \Phi_2 = \psi_a^* \psi_b \tag{1.3}$$

These wavefunctions relate to degenerate states and do not describe stationary states of the system. The correct zeroth order wavefunctions are:

$$\begin{aligned} \Psi_I &= \frac{1}{\sqrt{2}}(\Phi_1 + \Phi_2) = \frac{1}{\sqrt{2}}(\psi_a \psi_b^* + \psi_a^* \psi_b) \\ \Psi_{II} &= \frac{1}{\sqrt{2}}(\Phi_1 - \Phi_2) = \frac{1}{\sqrt{2}}(\psi_a \psi_b^* - \psi_a^* \psi_b) \end{aligned} \tag{1.4}$$

In both of the stationary exciton wavefunctions, Ψ_I and Ψ_{II}, the excitation is on both molecules, *a* and *b*, i.e., the exciton is collective or delocalized. The node corresponding to the minus sign in the exciton wavefunction is an excitation node, not an electron orbital node. At an excitation node, the phase relation between transition moments on the respective molecular centers changes sign. Parallel treatments can be carried out for larger molecular aggregate systems, for example, tetramers, and infinite array of molecules etc.

1.2.3.2 Hamiltonian for Aggregates

Briefly, the Hamiltonian for an aggregate is the sum of the individual molecules Hamiltonian H_n in the aggregate and the potential energy terms V_{mn} that specify the intermolecular interactions between molecules m and n; the Hamiltonian can be expressed as:

$$H = \sum_n H_n + \sum_{n,m>n} V_{mn} \tag{1.5}$$

Here, electron-phonon coupling is neglected. The use of an exact coulombic potential

would involve $1/r_{mn}$ as an operator, where r_{mn} is the intermolecular distance between molecule m and molecule n. Hence, a point-multiple expansion is used:

$$V_{coul} = V_{mono-mono} + V_{mono-di} + V_{di-di} + V_{quad-quad} + V_{di-quad} + \ldots \quad (1.6)$$

For neutral charge distribution the monopole interactions are zero. For allowed electric-dipole transitions, the dipole-dipole term becomes the leading term and the higher multipoles are neglected. Consequently, the allowed electric dipole transitions can be written as:

$$V_{coul} \cong V_{dipole-dipole} = -\frac{e^2}{r_{kl}^3}\sum_{i,j}(2z_k^i z_l^j - x_k^i x_l^j - y_k^i y_l^j) \quad (1.7)$$

where, as in the classical dipole-dipole potential, r_{kl} is the distance between the point dipoles in molecules k and l, and x_k^i is the x coordinate of the i^{th} electron on molecule k, x_l^j the x coordinate of the j^{th} electron on molecule l, and so forth; the coordinate system being chosen with the z axis parallel to the line of molecular centers and the summation over all electrons in each molecule.

1.2.4 Spectral and Structural Properties

Spectral and structural properties of dimers, for example, co-facial parallel, head-to-tail, oblique, coplanar inclined and linear chain aggregates can be evaluated using the Hamiltonians and wavefunctions discussed above for certain structural models. The energy of interaction will be given by the expectation value of the interaction potential with respect to the degenerate excited states of the dimer as:

$$\varepsilon = \iint \psi_a \psi_b^* V_{ab} \psi_a^* \psi_b \, d\tau_a d\tau_b \quad (1.8)$$

Inserting in eq. (1.8) the form of V_{ab} appropriate to an x-polarized electric-dipole transition in molecule a and b yields eq. (1.9):

$$\varepsilon = \iint \psi_a \psi_b^* \left(\sum_{i,j} x_k^i x_l^j \right) \psi_a^* \psi_b \, d\tau_a d\tau_b$$

$$\varepsilon = \frac{1}{r_{kl}^3} \left[\int \psi_a \left(\sum_i ex_a^i \right) \psi_a^* d\tau_a \right] \cdot \left[\int \psi_b^* \left(\sum_j ex_b^j \right) \psi_b d\tau_b \right] \tag{1.9}$$

Each integral in eq. (1.9) is precisely the transition moment integral for the excitation of the individual (monomer) molecules a and b, and can be written as:

$$M_a = \int \psi_a \left(\sum ex_a^i \right) \psi_a^* d\tau_a \tag{1.10}$$

Now, an arbitrary feature regarding the phase factor of the transition moment should be considered. A phase relationship exists such that the exciton stationary state wave-function Ψ_I lies the lowest. Thus, in order to make the exciton wave stationary wave-function Ψ_I correspond to a lowering of energy ε, the phase factor should be chosen as:

$$M_a = -M_b \tag{1.11}$$

This phase factor is completely arbitrary. Thus, if we defined $M_a = +M_b$, then the stationary state exciton wavefunction Ψ_{II} would lie lowest. The expression for the interaction energy for the parallel dimer is found to be:

$$\varepsilon = -\frac{M_a^2}{r_{ab}^3} \tag{1.12}$$

The resulting exciton bandwidth will be twice this value, i.e., 2ε.[42]

The energy lowering for the simple dimer is given by the monomer transition moment squared, i.e., it is proportional to the probability or intensity of the electric dipole allowed transition in the monomer, divided by the intermolecular distance cubed. Consequently, the stronger the absorption band, the greater the exciton band splitting will be. Also, one observes that the r-dependence demonstrate a comparatively long-range

interaction.

1.2.4.1 A Sample Calculation of Exciton Splitting

This calculation can be made using the definition of oscillator strength:

$$f = 4.704 \times 10^{29} \bar{\nu} M^2 \tag{1.13}$$

where $\bar{\nu}$ is the frequency in cm^{-1} and M is the transition moment in e.s.u.; the expression obtained combining eq. (1.12) and (1.13) can be written as:

$$\varepsilon = -\frac{f}{4.704 \times 10^{29} \bar{\nu} r_{ab}^3} \tag{1.14}$$

where r_{ab} defines the nearest neighbor dipole-dipole distance. The order of magnitude can be assessed by using selected data. For example, using $f = 1$ for a strongly allowed band, $\bar{\nu}$ = 20,000 cm^{-1} for absorption at 500 nm, a transition moment of $M \cong 10^{-17}\, e.s.u.$, and with r_{ab} having the values 1 nm and 0.5 nm, respectively, the resulting values of ε are -870 cm^{-1} and -6960 cm^{-1}.

1.2.4.2 Selection Rules

Let us now examine the spectral selection rules by evaluating the matrix elements of the electric dipole operator between the ground state and the ground stationary exciton states of the dimer. The transition moment vector of the dimer is given by:

$$\begin{aligned} M^{I} &= \iint \Psi_{gs} \left(m_a + m_b\right) \Psi_{I}\, d\tau_a d\tau_b \\ M^{II} &= \iint \Psi_{gs} \left(m_a + m_b\right) \Psi_{II}\, d\tau_a d\tau_b \end{aligned} \tag{1.15}$$

where m_a and m_b are the electric dipole operators corresponding to the molecular electronic coordinates of molecules a and b. Substituting eq. (1.14) into (1.15), the two transition moments can be expressed as:

$$M^{I,II} = \frac{1}{\sqrt{2}} \iint \psi_a \psi_b (m_a + m_b)(\psi_a \psi_b^* \pm \psi_a^* \psi_b)\, d\tau_a\, d\tau_b \tag{1.16}$$

Due to orthogonality and normalization properties of the intramolecular wavefunctions, eq. (1.16) can be represented as:

$$\begin{aligned} M^I &= \frac{1}{\sqrt{2}} \int \psi_a m_a \psi_a^* d\tau_a + \frac{1}{\sqrt{2}} \int \psi_b m_b \psi_b^* d\tau_b = \frac{1}{\sqrt{2}} (M_a + M_b) \\ M^{II} &= \frac{1}{\sqrt{2}} \int \psi_a m_a \psi_a^* d\tau_a - \frac{1}{\sqrt{2}} \int \psi_b m_b \psi_b^* d\tau_b = \frac{1}{\sqrt{2}} (M_a - M_b) \end{aligned} \tag{1.17}$$

Using eq. (1.11) for the parallel dimer that we had defined as the required phase relations for the wavefunctions Ψ_I and Ψ_{II}, the transition moments in eq (1.17) corresponding to the stationary exciton states, therefore become:

$$\begin{aligned} M^I &= \frac{1}{\sqrt{2}} (M_a + M_b) = 0 \\ M^{II} &= \frac{1}{\sqrt{2}} (M_a - M_b) = \frac{2M_a}{\sqrt{2}} \end{aligned} \tag{1.18}$$

As a result, the transition moments for the dimer are given as a superposition of the transition moments for the monomers. Moreover, the oscillator strengths for the electric dipole transitions between the dimer ground state and the stationary exciton states are given by:

$$\begin{aligned} f &\propto \left(M^I\right)^2 = 0 \\ f &\propto \left(M^{II}\right)^2 = 2M_a^2 \text{ or } f_{II,\,\mathrm{dim}er} = 2 f_{monomer} \end{aligned} \tag{1.19}$$

Figure 1.2 (a) shows the typical one-dimensional arrangement of the individual molecules in an ordered molecular aggregate. As stated above, dye molecules can aggregate either in a head-to-head (H-aggregation) or in a head-to-tail (J-aggregation)

fashion. The angle θ (often called the angle of slippage) between the ″line-of-centers″ and the transition dipole moments of individual molecules determines whether the aggregate is J-type, or H-type for which θ is equal to 0º or 90º, respectively. The interactions between the monomers in the aggregate are explained by the molecular exciton theory.

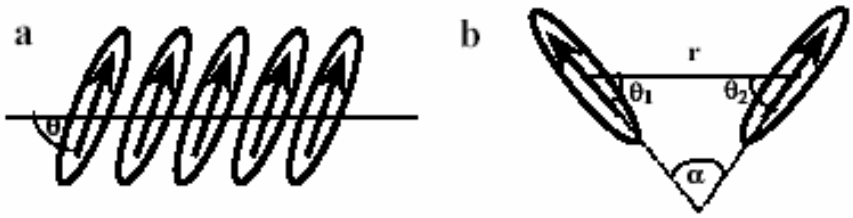

Figure 1.2: a) Typical ordered arrangement of monomers in a molecular aggregate. J-aggregate (θ = 0º) and H-aggregate (θ = 90º), with arrows indicating the transition dipole moments of individual molecules. b) Oblique arrangement of two transition dipole moments. Reprinted with permission from reference 2.

For the case of an oblique dimer as shown in Figure 1.2 b, the exciton coupling energy ($\Delta\varepsilon$)[43] can be written as shown in equation 1.20 below:

$$\frac{\Delta\varepsilon = 2\left|M\right|^2\left(\cos\alpha + 3\cos\theta_1\cos\theta_2\right)}{r^3} \qquad (1.20)$$

where M is the transition dipole moment of the monomer and the angles α, θ_1, θ_2 and distance r are indicated in Figure 1.2 (b). The resultant expressions for the exciton coupling energies of typical H- and J- dimers are tabulated below.

Table 1.2: Exciton coupling energies ($\Delta\varepsilon$) of J and H-dimers.[2]

Type	α	θ_1	θ_2	ΔE
H-dimer	0º	90º	90º	$\frac{2\left\|M\right\|^2}{r^3}$
J-dimer	0º	180º	0º	$-\frac{4\left\|M\right\|^2}{r^3}$

In addition to the oblique dimer, a co-planar inclined dimer is also possible. The molecular exciton model permits the discussion of such dimer as well. Moreover, the model can also be applied to long chain linear aggregates.

Organic dyes that form H- and J-aggregates, apart from cyanines and porphyrins, include the xanthines,[44] squaraines,[45] and polycyclic aromatic hydrocarbons.[46] These dyes also form H- and J-dimers.[47]

Arrangements proposed for dimer, and H- and J-aggregates of cyanine dyes are shown in Figure 1.3.[28] The arrangement of H-aggregates of cyanine dyes is that of a ladder, and that of J-aggregates of cyanine dyes is a staircase. The different arrangements of the cyanine dyes give different oscillations of the interacting molecules according to the molecular exciton model.

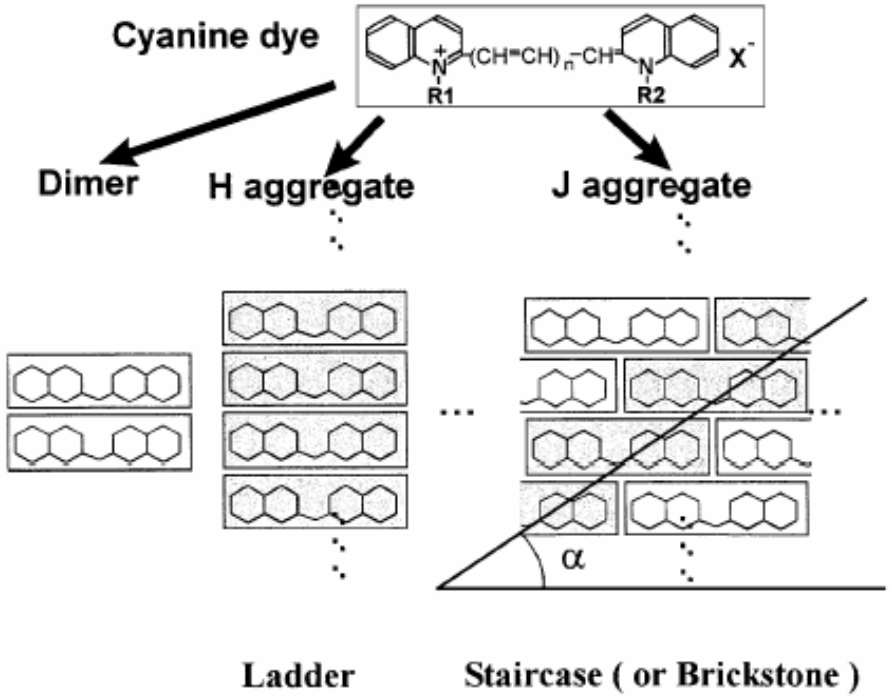

Figure 1.3: The arrangements proposed for dimer and H- and J-aggregates of cyanine dyes.

Extensive studies on J- and H-aggregates lead to the proposal that these aggregates can be represented, effectively, as a one–dimensional assembly in solution that can be viewed as having the ladder-, or staircase-type of arrangement[48]; but, recently, studies using near-field scanning optical microscopy (NSOM) has proposed a herringbone-like structural model[49] for thin films of J-aggregates of a cyanine dye.

1.3 Metal Nanoparticles

Metal nanoparticles have novel material properties that are greatly different from their bulk properties. As a result, they have attracted a great deal of interest in recent years. They are the focus of intense research activity not only because of their unusual behavior compared to the bulk metal but because they also have wide spread applications in the practical world. This dissertation, in addition to dealing with silver and gold nanoparticles, deals with nanoshells, which consist of a core surrounded by a thin metallic shell of nanometer dimensions. Metal nanoshells, specifically gold nanoshell, as in this dissertation, is another type of nanoparticles with special structures and many distinct properties different from the general solid-metal nanoparticles.

1.3.1 History

Silver and gold have been among the most ancient naturally occurring materials that captured the attention of researchers. A recent resurgence in interest has lead to an exponentially increasing number of publications, especially in the context of the emerging nanoscience and nanotechnology fields. Silver and gold nanoparticles in solution, which were referred to as “finely dispersed metals” by Faraday,[50] are also called silver and gold colloids, sols as well as colloidal solutions.

Both Ag and Au have a long history. Succinctly, the extraction of gold started in

the 5th millennium B.C.; it reached to a level of 10 tons per year in Egypt around 1200-1300 B.C. when the statue of Tutankhamun was constructed.[51] It is also probable that soluble gold appeared around the 5th and 4th century B.C. in Egypt and China.[51] From that time, the first book on colloidal gold was published by Francisci Antonii in 1618,[51] in which there existed considerable information on the formation of colloidal gold sols and their medical uses. In 1857, Faraday reported the formation of deep red solutions of colloidal gold by reducing an aqueous solution of chloroaurate with phosphorous in CS_2 (a two-phase system) in a well known work that forms the basis for what is now recognize as colloidal gold. The term colloid, which implies that the particles are dispersed in a medium, and do not separate on long standing, was coined shortly thereafter by Graham in 1861.[52]

The uses of silver, similarly, are dated as far back as several centuries. However, documenting of the scientific use of colloidal silver started in the late 1800s and was quite intense in the 1910/20 period;[53] the literature dating from 1910 is extensive with references giving the advantages for the use of colloidal silver for a wide variety of purposes.[53] Briefly, examples include the work of Henry Crook that showed silver along with mercury suspensions kill *B. Coli communis*.[53] Additionally, colloidal silver was used to kill *typhoid bacillus*, treat burn victims and as antibiotics.[53] When modern antibiotics were discovered in the late 1930s, clinical uses for silver as an antibiotic was discarded. However, with the rapid rise of antibiotic-resistant bacteria, the use of colloidal silver might very well be on the rebound, for several studies indicate that bacteria have a harder time becoming resistant to silver than to traditional antibiotics.[53]

The significance of silver and gold in history is evident by their use or their

exploration in alchemy, medicine, and modern science. But, the resurgence of interest in both is because of their attractive optical and electronic properties, related to quantum size effects and their promising applications in areas such as optics and optoelectronics.[54] Moreover, this renaissance is aimed at the development of advance nanostructured materials with uses as catalyst, photographic suspensions, nanostructural fabrication, and chemical/biological sensing.[55]

As for gold nanoshells, the surface plasmon peaks of these nanoshells are considerably red-shifted as compared to gold solid colloids having approximately the same dimensions. In addition, the surface plasmon resonance of gold nanoshells exhibits a much more sensitive response toward environmental changes, even when compared with solid colloids with a mean size much smaller than that of gold nanoshells.[56] Metal nanoshells are a new addition to the growing number of nanomaterials, such as quantum dots, nanorods and nanospheres.

1.3.2 Theoretical Background

Gold and silver particles with diameters on the nanometer scale exhibit very bright colors when viewed under normal light exposure. These bright colors have fascinated people for many centuries and are due to a striking phenomenon encountered in these nanoparticles, namely, the resonant excitation of a collective oscillation of the conduction band electrons in the particles, termed plasmon excitation. Plasmon modes exist in various metals, importantly in noble metals such as gold and silver. Under certain circumstances plasmons are excited by light, which leads to strong light scattering and absorption and an enhancement of the local electromagnetic field. The interest in plasmon modes dates back to the beginning of the 20th century by Zenneck[57] in 1907, also Mie[58] in

1908, and Sommerfeld[59] in 1909.

Although it was Faraday[50] who recognized that the red color of gold solution is due to metallic gold in colloidal form, Mie[58] was the first to provide a theoretical explanation of this phenomenon in 1908, by solving Maxwell's equation for the absorption and scattering of electromagnetic radiation by spherical particles. Mie presented a solution to Maxwell's equations[58,60,61] that describes the extinction spectra (extinction = scattering + absorption) of spherical particles of arbitrary size. Mie's theory has found wide applicability and has remained important because it is the only simple, exact solution to Maxwell's equations that is relevant to particles. Additionally, most of the standard colloidal preparations yield particles that are approximately spherical, and most of the optical methods for characterizing these nanoparticles spectra probe a large ensemble of these particles, which leads to results that can be modeled reasonably well using Mie's theory.

The discussion, below, presents a simple qualitative model used in understanding the properties of plasmons and is followed by a discussion of Mie's theory. In addition, other modern techniques presently in use to understand plasmons properties are mentioned.

1.3.2.1 Semi-Classical Model

Many properties of particle plasmons are qualitatively understood using this simple semi-classical model, illustrated in Figure 1.6. This model is reminiscent of an "optical antenna".[62] Given that the diameter of a nanoparticle is on the order of the penetration depth of electromagnetic waves in metals (ca. 30 nm for gold and silver), the excitation light is able to penetrate the particle. The oscillating electric field causes the

metallic nanoparticles conduction electrons to oscillate coherently. The field inside the particle shifts the conduction electrons collectively with respect to the fixed positive charge of the lattice ions. The electrons now build up a charge on the surface on one side of the particle. When the electron cloud is displaced relative to the lattice ions, a restoring force arises from the Coulomb attraction between electrons and the lattice ions that results in oscillation of the electron cloud relative to the nuclear framework.

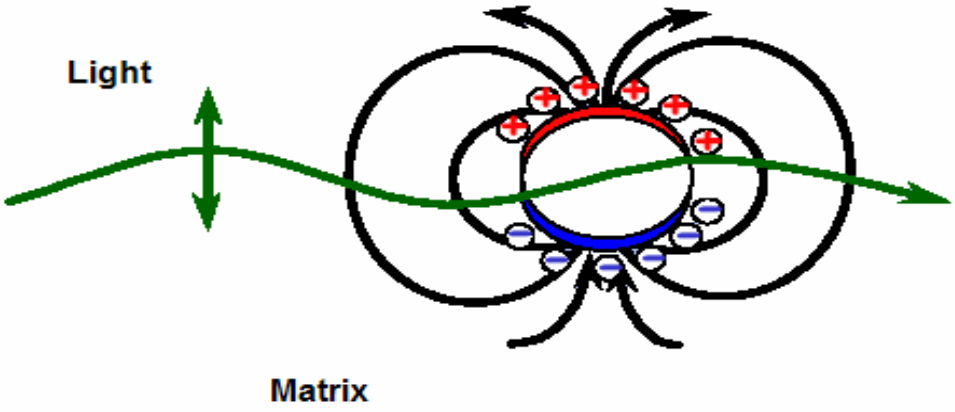

Figure 1.4: Schematic view of the excitation of a particle plasmon oscillation in a metal nanoparticle by an external light field. Reprinted with permission from reference 62.

The oscillation frequency is determined by four factors: the effective electron mass, the density of the electrons, and the shape and size of the charge distribution. If the frequency of the excitation light field is in resonance with the eigenfrequency of this collective oscillation, even a small exciting field leads to a strong oscillation. The collective oscillation of the electrons is called the dipole plasmon resonance of the particle, sometimes referred to as “dipole particle plasmon resonance” to differentiate from plasmon excitation that can occur in bulk metal or metal surfaces. Higher modes of plasmon excitation such as quadrupole mode are also possible where half of the electron

cloud moves parallel to the applied field and half moves antiparallel.[63]

Detailed understanding of the plasmon resonance in metal particles is further gained by classical electrodynamics. However, one severe limitation of this electro-dynamical treatment is that it depends on the knowledge of material parameters, particularly the complex dielectric function ε. To relate the dipole plasmon frequency of a metal nanoparticle to the dielectric constant, hence dipole approximation,[64] the interaction of light with a spherical particle that is much smaller than the wavelength of light is considered. Under these circumstances, the electric field of the light can be taken as a constant; therefore the interaction is governed by electrostatics rather than electrodynamics. This is often called the quasi-static approximation, as it uses the wavelength-dependent dielectric constant of the metal particle and of the surrounding medium in what is otherwise an electrostatic theory.

1.3.2.2 Mie Theory

The response of a metal sphere to an external electromagnetic field can be calculated by solving Maxwell's equations. For uncharged spherical particles, in a homogeneous medium, an analytical solution exists, i.e., an exact analytical electrodynamical treatment that is nowadays attributed to Mie.[62] Mie was not the first to derive a solution of this problem, but was the first to apply it to the problem of light scattering of metal spheres.[65] Briefly, here is the summary of the main results following the derivation by Bohren and Hufman. [61]

The spherical symmetry suggests the use of a multipole extension of the fields, here numbered by n. The Rayleigh-type plasmon resonance, used in the quasi-static approximation, corresponds to the dipole mode $n = 1$. In the Mie theory, taking into

account that the distance between particles is large enough to neglect any interaction between particles, and that the system contains particles of equal size, the scattering and extinction efficiencies are calculated by:

$$Q_{sca}^{(n)} = \frac{2}{x^2}(2n+1)\left(|a_n|^2 + |b_n|^2\right) \tag{1.21}$$

$$Q_{ext}^{(n)} = \frac{2}{x^2}(2n+1)\,\mathrm{Re}\left(a_n + b_n\right) \tag{1.22}$$

where $x = kr = \hbar\omega r\frac{N_{medium}}{\hbar c}$; k is the wave vector; r is the radius of the particle; N is the refractive index; Re refers to the real part of the referenced function; a_n, and b_n, are the Mie coefficients, which are given by:

$$a_n = \frac{m\psi_n(mx)\psi_n'(x) - \psi_n(x)\psi_n'(mx)}{m\psi_n(mx)\xi_n'(x) - \xi_n(x)\psi_n'(mx)} \tag{1.23}$$

$$b_n = \frac{\psi_n(mx)\psi_n'(x) - m\psi_n(x)\psi_n'(mx)}{\psi_n(mx)\xi_n'(x) - m\xi_n(x)\psi_n'(mx)} \tag{1.24}$$

In these functions, $m = \sqrt{\varepsilon_r} = \frac{N_{particle}}{N_{medium}}$ and ψn and ξn are Riccati-Bessel functions.[61] These equations allow the calculation of scattering cross-sections in a relatively straight forward manner using, for example, programs such as Mathematica™.

The optical spectra of metal nanoshells are considered to be plasmonic in origin; therefore, a generalized Mie scattering approach is usually employed to calculate the absorption and scattering cross sections of the metal nanoshells.[66,67] In other words, an extended Mie theory for a core particle covered by an arbitrary number of shells is used. Particles, having a dielectric function ε_{core}, covered by multi-shell layers were first studied by Aden and Kerker,[68] and Bhandari.[69]

The near-field properties of metallic nanoparticles can be calculated by a variety of methods. Early theoretical work focused on the solution of Maxwell's equations for a plane wave incident on a nanoparticle of highly symmetric geometry,[58,68] as in the case of the Mie theory and the Maxwell-Garnet theory.[58,34(a)] To further characterize these intriguing optical features, a number of theoretical approaches have been developed. These includes numerical methods such as the discrete dipole approximation (DDA),[63,70] finite difference time domain methods (FDTD),[71] the multiple multipole method,[72] and the modified long wavelength approximation;[63,70] DDA and FDTD are methods used for nanoscale objects of reduced symmetry.[73]

Finally, a new conceptual approach for understanding the plasmon response of metallic nanostructures, principally concentric nanoshells known as "plasmon hybridization" has been recently developed.[74] In this approach, using a rigorous isomorphism with molecular orbital theory, it was shown in a plasmon hybridization model that the plasmon resonances of complex shaped nanostructures arise due to the mixing and hybridization of fixed-frequency plasmon resonances of more elementary nanostructures. In brief, the approach presents an incomprehensible fluid model in which the electron gas in a nanoparticle is treated as an incompressible fluid. This model is used to calculate the plasmon frequencies of two simple systems, which are a solid sphere and a spherical cavity in the homogeneous electron gas. Applying the formalism to spherical nanoshells, the approach then shows how the nanoshell plasmons result from a hybridization of the solid sphere plasmons on the outer surface of the metallic shell and the cavity plasmons on the inner surface of the shell. The resulting plasmon resonances is viewed as hybridized elementary plasmons in a manner analogous to how molecular

orbitals are formed from atomic orbitals in electronic structure theory.

The plasmon hybridization model has been used to explain the properties of nanoshells, the tunable plasmonic nanoparticle consisting of a dielectric core and a metallic shell, whose plasmon resonance is a sensitive function of the inner and outer radius of the shell layer. For nanoshells, the tunable resonances arise from the interaction and mixing of two fixed-frequency plasmons, that of a sphere (the outer surface of the shell layer) and a cavity (the inner surface of the shell layer). The hybridization of the sphere and cavity plasmons gives rise to two new plasmon oscillation modes, referred to as "bonding" and "antibonding" plasmons in analogy with molecular orbital theory.[74(a)] The energies of these two eigenmodes are determined by the strength of the interaction between the sphere and cavity plasmons and that is controlled by the thickness of the shell layer. A thin shell results in strong plasmon mixing, while a thick shell effectively isolates the plasmons of the two surfaces. This approach to the calculation of plasmon energies is in quantitative agreement with the results obtained using classical Mie scattering theory.[74(b)] The hybridization principle provides a very simple conceptual approach for the rational design of nanostructures with desired plasmon energies.

1.3.3 Properties and Applications

Colloidal metal nanoparticles, which can exist as spherical, rods, wires, and platelets exhibit many unique chemical and physical properties. In particular, due to their especially small size (1-100 nm), metal nanoparticle possess properties (optical, catalytic, electrical, magnetic, etc.) that are greatly different from either the corresponding bulk materials or the individual atoms of which they are composed.[75] Additionally, they exhibit the surface-enhanced Raman property.[76]

The most unique property of these nanoparticles is the optical plasmon resonance associated with the collective oscillation of the conduction electrons confined in the nanoparticle. Furthermore, nanoparticles possess large surface-to-volume ratio, and consequently their properties are mostly governed by the surface states.

As regards nanoshells, they possess quite notable properties that differ dramatically from those of solid nanoparticles. Also, nanoshells can yield new and tunable optical properties that solid nanoparticles do not possess.[77] Recent research has focused on properties such as the tunable plasmon resonance,[77] sphere cavity resonance,[78] surface-enhanced Raman scattering,[79] enhanced thermal stability,[80] and infrared extinction properties.[81] Metal nanoparticles, i.e., both solid and nanoshells are examples of nanostructured materials with functional properties based on their size, shape and composition.

The growing interest and importance in metal nanoparticle research as stated above stem from the various unique applications[82] that nanoparticles have, such as contrast agents in electron microscopy as,[83] chemical and biological sensors,[84] electronics as single electron transistors and electrical connects,[85] catalysis (for instance CO oxidation on Au/TiO_2 composites),[86] dyes and conducting coatings,[87] and fundamental research. The increased understanding of how metallic nanostructures manipulate light will augment the number of applications for these nanostructures.

It is worth noting some historical applications of metallic nanoparticles. For instance, gold nanoparticles were use in the staining of church windows in the middle ages and in the Lycurgus cup (see Figure 1.5) manufactured during Roman rule and now at the British museum in London.

Figure 1.5: Lycurgus cup, 4th century AD (now at the British Museum, London). The colors originate from metal nanoparticles embedded in the glass: light transmitted through the glass appears red; light scattered near the surface appears greenish.

Strong research efforts are still underway to exploit new applications of metal Nanoparticles, which will continue to draw intense scientific and technological interest due to the burgeoning nanotechnology revolution.

1.3.4 Preparation of Metal Nanoparticles

Preparation of metallic colloidal particles, metal nanoparticles, dates back to the middle ages, however, the nature of these colloids remained unclear until Faraday realized that the gold colloids contained small metallic particles, which he called divided metals.[50] The term "nanoparticle" has become in vogue only in recent years. A nanoparticle has dimensions in the nanometer range, i.e. between 0.5 and 100 nm. The term colloid is more elusive, the particle size can range from nanometers to several hundreds of micrometers. Additionally, a colloid implies that the particles are dispersed in a medium and do not separate on long standing.

Nanoparticles can be synthesized utilizing a variety of methods. Different methods are used in order to optimize specific properties of the nanomaterials. These properties include, but are not limited to size (diameter, length, volume), size distribution, symmetry, surface properties, surface coating, purity, ease of manipulation, yield, and suitability for scaling up.

The methods used for the production of nanoparticles may be divided into four main groups as follows:

- Gas phase processes including flame and laser induced pyrolysis, laser ablation, high temperature evaporation and plasma synthesis.
- Vapor deposition synthesis.
- Colloidal, or liquid phase methods in which chemical reactions in solvents lead to the formation of colloids.
- Mechanical processes including grinding, milling and alloying

These four main groups of nanoparticle production processes have been used to produce many materials including metals, oxides, organics and pharmaceuticals products.

As regards the colloidal methods, i.e., the third group above, these methods represent well established “conventional” wet chemistry precipitation processes in which solutions of the different ions are mixed under controlled conditions of temperature and pressure to form insoluble precipitates. Colloidal methods provide a simple route to the synthesis of nanoparticles. Such approaches enable the relatively straightforward production of significant quantities of nanoparticle material at modest capital cost. As with other approaches, much of the recent emphasis has been on the development of more monodisperse particles with better defined shape.

The fourth group of methods, i.e., the mechanical attrition methods, in contrast to the prior three groups, where nanoparticles are built "bottom-up" from individual molecules, result in nanoparticles produced using a "top-down" approach, where larger particles are broken down to smaller ones.

The work presented in this dissertation exclusively dealt with the well established "conventional" wet chemistry precipitation processes; to be precise, nanosized Ag and Au particles and Au nanoshells in aqueous solution or organic solvent were produced by the reduction of relevant metal salts, sometimes in the presence of a suitable protecting agent, using wide selections of reducing agent.

2 Experimental Techniques

2.1 Introduction

From the great number of analyzing techniques that may be applied for characterizing the physical, chemical and optical properties of nanoparticles, molecular aggregates, and composite nanostructured materials, only those that were extensively used in the present work are briefly described in the following sub-sections. These are, absorption spectroscopy, steady-state fluorescence spectroscopy, dynamic light scattering (DLS) measurements, atomic force microscopy (AFM), and near-field scanning optical microscopy (NSOM) ─ collectively known as the scanning probe microscopes ─ and Raman spectroscopy. Absorption and steady-state fluorescence spectroscopy were used to study the optical properties of the prepared nanostructured materials. DLS, AFM and NSOM were used to investigate nanoparticle composite materials from the morphological and structural point of views; with AFM, the structural characteristics of specimens under investigation can be retrieved down to the atomic scale of resolution. Raman spectroscopy was used to further investigate the structural features of the prepared nanostructured materials.

In addition to the aforementioned, main techniques used in this work, a wide range of complementary techniques and methods were use to aid in the complete characterization of the prepared nanostructured materials. These additional techniques and methods are the following: transmission electron microscopy (TEM), scanning electron microscope (SEM), high pressure liquid chromatography (HPLC), sedimentation, spin coating, Rayleigh scattering, dark-field microscopy, and diffuse reflectance (DR) spectroscopy.

Moreover, computational studies, specifically density functional theory (DFT) calculations, were conducted in an effort to couple structural theory and spectroscopic methods to gain insight into molecular aggregate structures. Density functional theory (DFT) with functionals,[1] specifically, B3LYP, in which the exchange functional is of Becke's three parameter type, including gradient correction,[2] and the correlation correction involves the gradient-corrected functional of Lee, Yang and Parr,[3] was used The basis set of split valence type 6-31G(d,p) and 6-31+G(d,p),[4] as contained in the Gaussian 98 software package, was employed to calculate bond distances, bond angles, charge distributions and Raman vibrational frequencies.

Microcal's OriginPro 7.0 program was utilized for all the data analysis and background subtraction if needed.

2.2 Absorption Spectroscopy

Absorption spectroscopy, a widely used spectroscopic tool, provides the wavelength of a transition and the corresponding wavelength dependent molar extinction coefficient (ε_λ) of a chromophore that is under investigation. The absorption spectrum of a chromophore is sensitive to the environmental conditions. These environmental effects alter the relative energy of ground and excited states, and this alteration causes spectral shifts.

Absorption measurements were recorded on a double beam, ultraviolet-visible (UV-Vis) spectrophotometer (Perkin-Elmer Lambda 18).

At room temperature most molecules will be in their electronic and vibrational ground states. In ultraviolet and visible (UV-Vis) spectroscopy, a molecule will absorb light and undergoes a transition from the ground to an excited state. This occurs if, in the

interaction between the electromagnetic radiation and the molecule, the energy of a quantum of light is equal to the energy difference between the excited and ground states of the molecule. Thus, the following relation holds:

$$\Delta E = E_f - E_i = h\nu \tag{2.1}$$

E_f and E_i are the final and initial molecular energy levels in the molecule, h is the Planck constant, and ν is the frequency of the light absorbed.

Regardless of the type of transition, not all light of the correct energy is absorbed by a sample of molecules. Empirically, the fraction of light absorbed by a sample follows Beer's law. If I_o is the intensity of the light entering the sample and I is the intensity of the light emerging from the sample, then

$$\log\left(\frac{I_0}{I}\right) = \varepsilon \cdot C \cdot l \tag{2.2}$$

C and l are the concentration and the path length of the sample respectively; ε is the constant of proportionality, also known as the extinction coefficient. The quantity log (I_o/I) is known as the optical density (OD) or the absorbance (A). Both the absorbance and extinction coefficient depend on the wavelength of the light, *i.e.*

$$A_\lambda = \varepsilon_\lambda \cdot C \cdot l \tag{2.3}$$

The extinction coefficient, which characterizes the absorption process, is an empirical measure of the fraction of light absorbed by the molecule as a function of wavelength. By convention, the concentration C is measured in mole/liter and the path length l in centimeters. Since logarithms are unitless, the extinction coefficient has the dimension liter/(mole·cm). Concentrations were determined using eq. 2.3 and using the molar extinction coefficient ε at wavelength l. Mostly path length of 1.0 cm was used for

the measurements. All the absorption measurements were carried out at room temperature. Quartz cuvettes was often used, but in some instances where there was undesired coating of the quartz cuvette by the dyes, special UV-cutoff plastic cuvettes were used.

2.3 Steady State Fluorescence Spectroscopy

Fluorescence is the most sensitive molecular property that is used for studying the structure and dynamics of molecular systems. Any electronically excited molecule comes back to its ground state either by radiative mechanism or non-radiative mechanism. The chromophores following the radiative mechanism emit photons and the process is called fluorescence emission. The fluorescence photons have the information about energy (wavelength), time, polarization and intensity (number of photons) at a given wavelength. Each of the above parameter of the fluorescence photon gives information about the local environment surrounding the fluorophore under investigation. So, fluorescence intensity spectrum, polarization and their time dependence are important parameters that one can use for the characterization.[5]

The mechanisms by which electronically excited molecules come to ground state are given by the Jablonski diagram as shown in Figure 2.1. The absorption of a photon takes the molecule from ground state (singlet state, S_0) to either first excited state (singlet state S_1) or second excited state (S_2). Then the excited molecule relaxes to the lowest vibronic level of the first excited state through internal conversion (IC). Now it can relax from the singlet excited state to the ground state via three-mechanisms. First by emitting a photon (radiative process), second without emitting a photon (non-radiative mechanism) and third it goes to a triplet state (T_1) by intersystem crossing (ISC) which is

also a non-radiative process. The transition from triplet (T_1) to ground singlet state is forbidden and hence is a very slow process relative to florescence. Emission from T_1 is called phosphorescence, and generally is shifted to longer wavelengths relative to the fluorescence. Also the excited state S_1 can be deactivated by a quenching reaction in which a quencher Q quenches the excited state of the fluorophore S_1 through an excited state reaction.

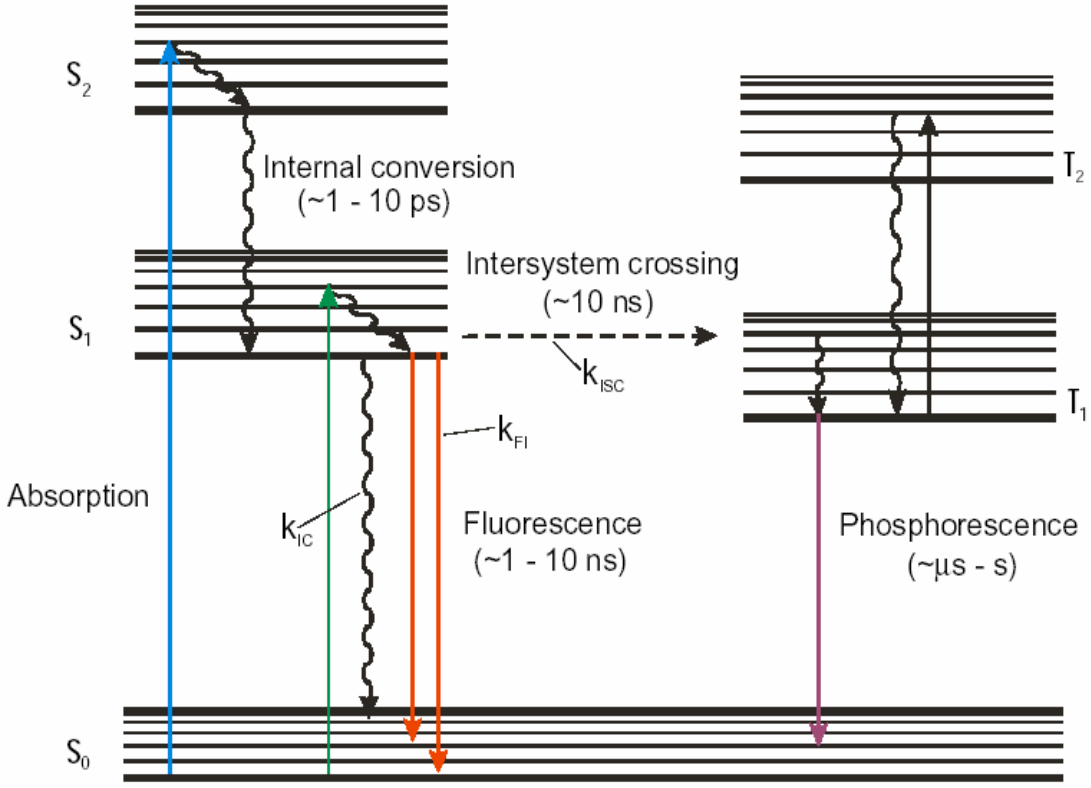

Figure 2.1: Energy term scheme (Jablonski-diagram) showing the energy levels and various processes in an electronically excited molecule with conjugated π-electron system (e.g., cyanine dyes). The non-radiative transitions are depicted by the wiggling line. The straight lines represent radiative transitions Typical lifetimes of each relaxation channel are given in brackets below. k_{Fl}, k_{ISC}, k_{IC} denote the rates of the fluorescence, intersystem crossing and internal conversion transitions, respectively.

Steady state fluorescence spectra were carried out on a SPEX Fluorolog-τ2

spectrofluorometer. The excitation source was a Xe-lamp. All the fluorescence spectra were corrected for the spectral sensitivity of the photomultiplier (Hamamatsu R928A). The band width used was between 1 nm and 5 nm. For solution sample measurements the right angle (RA) geometry was used and for all thin film studies front face (FF) geometry was chosen. In the right angle geometry (RA), the emitted light from the sample was collected at angle of 90° with the direction of the incident light whereas in the case of front face geometry (FF), the emitted light was collected at an angle of 22.5°. Appropriate filters were used before the emission monochromator to avoid the excitation light entering it. Emission spectrum was recorded by keeping the excitation wavelength fixed and varying the emission wavelength. Quartz cuvette was used for all measurements and all measurements were carried out at room temperature.

2.4 Dynamic Light Scattering (DLS)

There are various techniques aside from the scanning probe measurements available for particle size measurements such as Dynamic light scattering (DLS)[6,7] small angle X-ray scattering (SAXS),[8] small angle neutron scattering (SANS),[9] time resolved fluorescence anisotropy,[10] etc. DLS, of all the available techniques, is the standard technique to measure the particle size distribution (hydrodynamic radii ranging between 1 nm and 1 mm) in solution of macromolecules and molecular assemblies.

DLS experiments were performed with a PD2000DLS (Precision Detector), using nonlinear regularization without normalization and with a spherical normalization which both gave statistically similar results. The reported distributions are in number density. Experiments were done using a solution sample (~5 mL) in a glass capillary which was illuminated with a continuous laser light (826.8 nm, 55 mW). Intensity of the scattering

light from the solution was measured in perpendicular direction to that of the incident laser light by an Avalanche Photodiode (APD). The autocorrelation function of the fluctuations in the scattered light was determined as a function of delay time by an autocorrelator.

DLS is different from another light scattering technique called resonance light scattering (RLS) ─ an extremely sensitive and selective method for probing various electronically coupled chromophore arrays ─ in the way that it uses a non-absorbing wavelength by the particle under study. The function G(τ) describes the autocorrelation of the scattered light as a function of delay time, τ. If the particle undergoes simple Brownian motion the expected auto correlation function is as given in eq. 2.4.[7]

$$G(\tau) = 1 + \exp^{(-2D_T q^2 \tau)} \tag{2.4}$$

The wave vector $q = \left(4\pi \frac{ns}{\lambda}\right)\left(\sin\frac{\theta}{2}\right)$, depends on the scattering angle q, the refractive index ns of the solvent, and the wavelength λ of the incident radiation. The diffusion constant DT is given by the Stokes-Einstein relationship:[11]

$$D_T = \frac{k_B T}{6\pi\eta R_H} \tag{2.5}$$

where k_B is the Boltzmann constant, T is absolute temperature in Kelvin, η is the viscosity of the solvent and R_H is the hydrodynamic radius of the scattering particle.

2.5 Atomic Force Microscopy (AFM)

The atomic force microscope (AFM) is a member of a new class of microscopes known as the scanning probe microscopes (SPMs).[12] Unlike optical and electron microscopes which 'look' at the sample, the probe microscopes image the surface by 'feeling' the atoms on the surface.

In AFM, the probe is mounted on a 'soft' spring, and is brought into contact with a surface such that it experiences a very small interaction force, usually on the order of nanonewtons. The probe is then raster scanned across the surface, while maintaining a constant force between the tip and the sample. These deflections of the cantilever, which are caused by changes in surface stiffness or topography, allow the AFM to record topographic contours of a surface.

Atomic force microscopy, depicted in Figure 2.2, is able to offer local surface information at atomic resolution by sensing the force between a small sharp tip and a surface, which corresponds to the bending of the compliant cantilever the tip is attached to, and is translated into the laser signal change of a position sensitive photodiode. A tube scanner controlled by a feedback loop will move the tip to keep the force or height constant while scanning in X-Y direction. The negative feedback loop moves the tip up and down via a piezoelectric scanning tube (PZT) so as to maintain the interaction force to a pre-selected level.

A three-dimensional image can finally be constructed by recording the cantilever motion in Z direction as a function of the sample's X and Y position. AFM studies were carried out on a ThermoMicroscopes Explorer™ SPM (from Veeco Instruments, USA) equipped with microfabricated silicon nitride Cantilever (100 – 200 mm). The substrate, usually glass slides, holding the sample was glued to the magnetic disk on top of an XY manual translator. The AFM tip was scanned in either contact or non-contact mode using piezoelectric transducers while the sample was held stationary. The scanning was activated by applying voltages across the piezo translator which was controlled by software from an electronic control unit (ECU-Plus™).

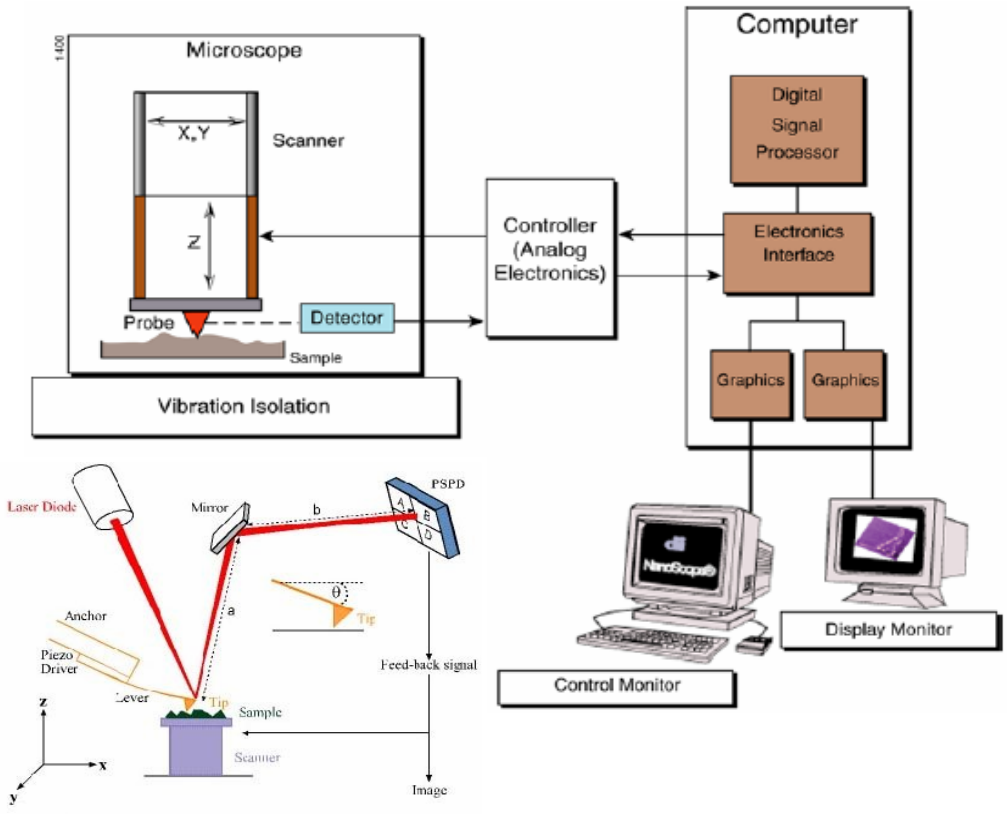

Figure 2.2: Schematic of the major components of the ThermoMicroscopes Explorer™ scanning probe microscope system (i.e., AFM) and its use.

Additional AFM studies, particularly in Chaper 4 (Figure 4.14-4.16), were carried out using a Digital Instrument Bioscope AFM scanner with a Nanoscope IIIa controller ((from Louis E. Brus' laboratory, Columbia University) operating in tapping mode at ambient conditions. The solution in these studies was spin-cast onto a polylysine-coated quartz cover slip.

2.6 Near-Field Scanning Optical Microscopy (NSOM)

Near-field Scanning Optical Microscopy (NSOM) also known SNOM is another member of the new class of microscopes known as the scanning probe microscopes (SPMs). While resolution in conventional far-field microscopy is limited by the well-

known diffraction limit to approximately the wavelength of light, scanning near-field microscopy (SNOM) circumvents this limit by scanning a local source of radiation across the sample surface. The resolution is then mainly limited by the source dimension and the sample to source distance, both of which have to be much smaller than the wavelength of visible light to improve resolution as compared to conventional light microscopy. The most commonly employed realization of this concept is to use light leaking out of a small aperture at the tip of a metal coated sharpened glass fiber as the local light source. This fiber tip is then brought very close to the sample surface. The tip to sample distance is usually kept constant by shear force feedback mechanism using a tuning fork, which allows simultaneous collection of topography and optical signals. Of course, many variations of this idea exist; see for example Paesler and Moyer.[13]

The use of tuning fork technology means there is no need for an additional feedback laser (used as an optical lever) as in other NSOM designs. NSOM offers the potential for spatially resolving the spectroscopic constituents of heterogeneous material systems on a sub-micron length scale, thereby shedding light on the relationship between spectroscopic properties and nanoscopic structures.

The small aperture at the end of the single-mode optical fiber illuminates only a very small portion of the sample, thus significantly reducing photo-bleaching and also providing a clear relationship between the topographic and optical structures of a sample. Conventional optical components and detectors are used to collect and measure the various properties of the near-field signal, such as intensity, wavelength, etc. A laser with chosen optical properties is used to pump light through the optical probe in order to generate the near-field signal.

NSOM measurements were carried out using a topometrix Aurora-2 system, shown in Figure 2.3. The Aurora-2, equipped with a non-optical, non-contact (~5-10 nm separation) sheer-force feedback mechanism and closed-loop piezo scanner scans the sample surface underneath the fiber optic probe aperture. Commercial chemically etched, metal coated SiO_2 fiber optic probes with a ~ 50 nm diameter aperture were used. A tunable argon ion laser was used to achieve excitation at 488 and 514 nm. The beam was coupled into the cleaved end of an approximately 0.5 m long single-mode optical fiber (Thorlabs FS-SN-3224) whose other end was tapered and coated with aluminum to form the near-field probe.[14] The sample on a coverslip was mounted beneath the NSOM probe on a piezo-electrically driven sample stage with *X*, *Y*, and *Z* motions. The sample-probe distance was maintained to within 7 ± 0.25 nm by a tuning fork shear-force mechanism.[15] The fluorescence excited by the NSOM probe was collected with a 0.6 numerical aperture objective, directed through mirrors and filters and imaged onto the active area of a PMT.

The fluorescence signal for transparent samples is collected while operating the instrument in transmission mode, whereas for opaque samples, fluorescence signal is collected using reflection NSOM mode.

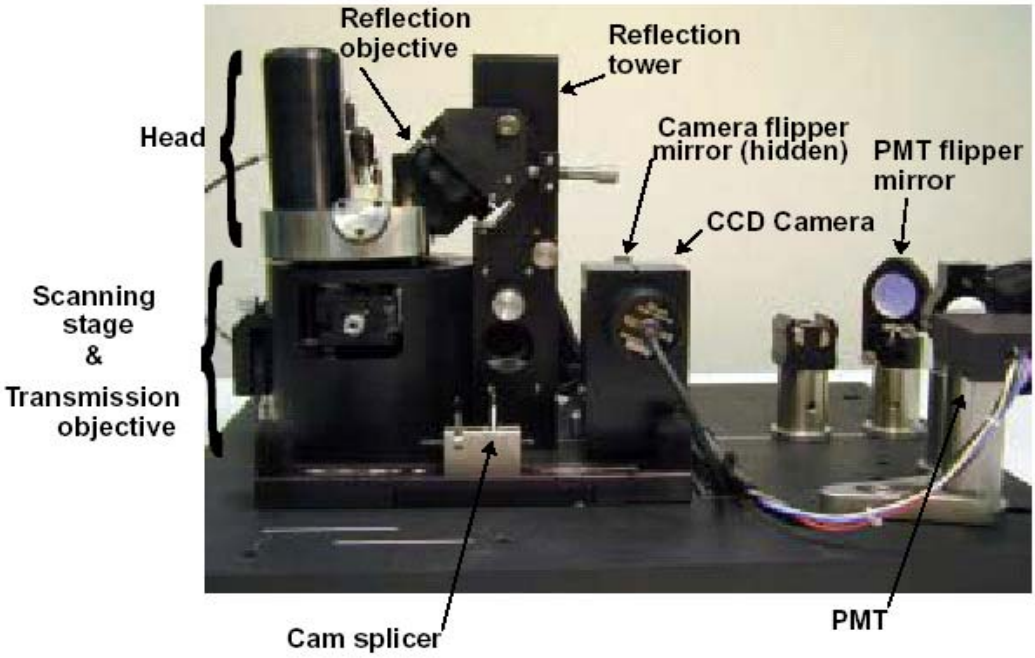

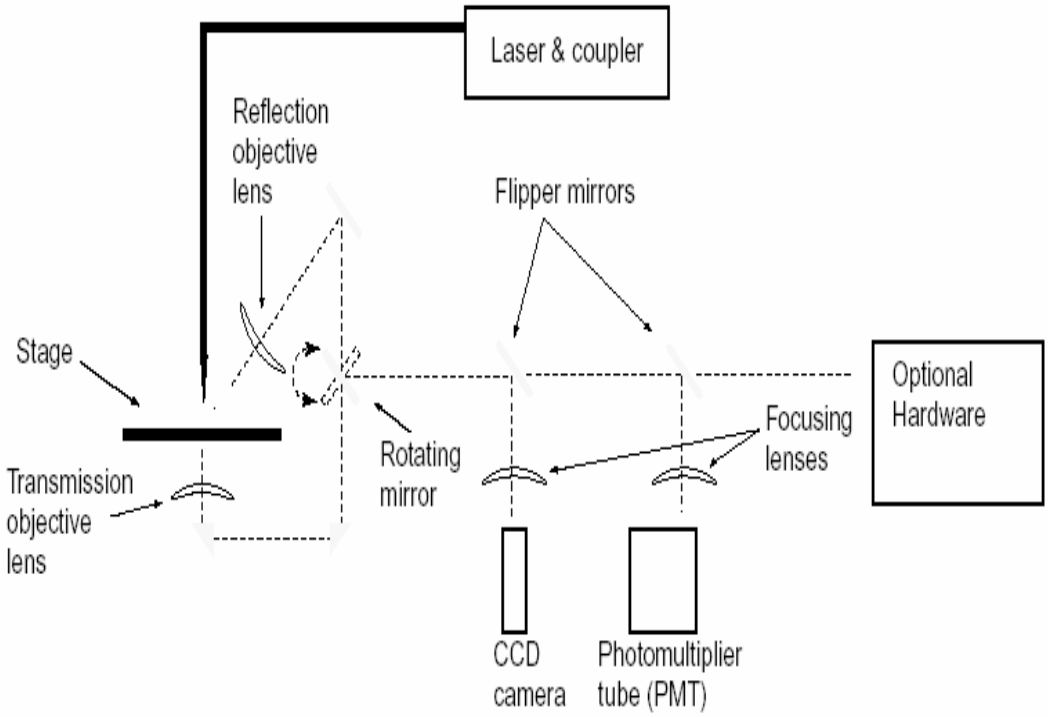

Figure 2.3: Schematic of the major components of the ThermoMicroscopes Aurora-2 near-field scanning optical microscope (NSOM).

2.7 Raman Spectroscopy

Raman spectroscopy, one of the spectroscopic methods based upon light scattering phenomena, with the advent of laser sources and better detection means, has been a prominent tool in the chemist tool bag for studies of the structure of individual molecules to the nature of coupling interactions between molecules and to other interfacial phenomena probing. Below, a brief overview of the Raman effect and the different enhancement mechanism that has made Raman spectroscopy more relevant in the modern laboratory by increasing its resolving power is presented.

2.7.1 The Raman Effect

The Raman effect was first predicted from theoretical considerations by A. Smeka in 1923.[16] But in 1928, the effect was observed by C. V. Raman[17] in India almost coincidentally with the observation by G. Landsberg[18] and L. Mandelstant[19] in the Soviet Union.

When light is scattered from a molecule most photons are elastically scattered. The scattered photons have the same energy (frequency) and, therefore, wavelength, as the incident photons. However, a small fraction of light (approximately 1 in 10^7 photons) is scattered at optical frequencies different from, and usually lower than, the frequency of the incident photons. The process leading to this inelastic scatter is termed the Raman effect. Raman scattering can occur with a change in vibrational, rotational or electronic energy of a molecule. Chemists are concerned primarily with the vibrational Raman effect, thus, the term Raman effect is used here to only mean vibrational Raman effect.

Moreover, when light is passed through a sample, some light will be absorbed and some will be scattered. This scattering process is a two-photon process, and, though

quantum-mechanically incorrect, can be seen as where an incident photon is momentarily absorbed to a "virtual state". A new photon is created and scattered from this virtual level. Then the final state can be either the ground state (Rayleigh scattering) or a vibrationally excited state (Stokes-Raman scattering). The scattering process can also originate from the vibrational excited state. In this case the process is known as anti-Stokes Raman scattering.

Light scattering can be described with a simple wave model. This is the classical approach, and it requires less understanding of mathematics and quantum-mechanics than the more correct sum-over-states picture or other quantum-mechanical models.

The electric field E of electromagnetic radiation can be described as a periodic function: $E = E_0\cos(2\pi\nu t)$, with ν being the frequency of the incident light. Electromagnetic radiation will, upon interaction with a molecule, induce an electrical dipole moment μ (according to $\mu = \alpha E$) where α, is the polarizability of the molecule, and it is a function of the separation between the atoms. This induced electrical dipole moment disappears when the molecule re-emits a photon.

The polarizability α is affected by molecular vibrations. These vibrations, which are also periodical functions,[20] are given in eq. 2.6.

$$r - r_{eq} = r_m \cos\left(2\pi\nu_{vib}\, t\right)$$
$$\alpha = \alpha_0 + \left(\frac{d\alpha}{dr}\right) r - r_{eq} \qquad (2.6)$$

$r\text{-}r_{eq}$ is the equilibrium distance difference, r_m is the maximal difference in the equilibrium distance and ν_{vib} is the vibrational frequency. Substituting the above two equations yields:

$$\alpha = \alpha_0 + \left(\frac{d\alpha}{dr}\right) r_m \cos\left(2\pi\nu_{vib} t\right)$$

$$m = \alpha_0 \left(E_0 \cos\left(2\pi\nu t\right)\right) + \left(\frac{d\alpha}{dr}\right) r_m \cos\left(2\pi\nu_{vib} t\right)\left(E_0 \cos\left(2\pi\nu t\right)\right) \quad (2.7)$$

Applying the relationship (cosx)(cosy) = [cos(x+y) + cos(x-y)]/2 to eq. 2.7 gives:

$$m = \alpha_0 \left(E_0 \cos\left(2\pi\nu t\right)\right) + \frac{E_0}{2} r_m \left(\frac{d\alpha}{dr}\right) \cos\left[2\pi\left(\nu - \nu_{vib}\right)t\right] + \frac{E_0}{2} r_m \left(\frac{d\alpha}{dr}\right) \cos\left[2\pi\left(\nu + \nu_{vib}\right)t\right] \quad (2.8)$$

Since the dipole radiates light at its oscillating frequency, the molecule will emit light at three frequencies, ν, ν - ν_{vib}, and ν + ν_{vib}, as shown in Figure 2.4.

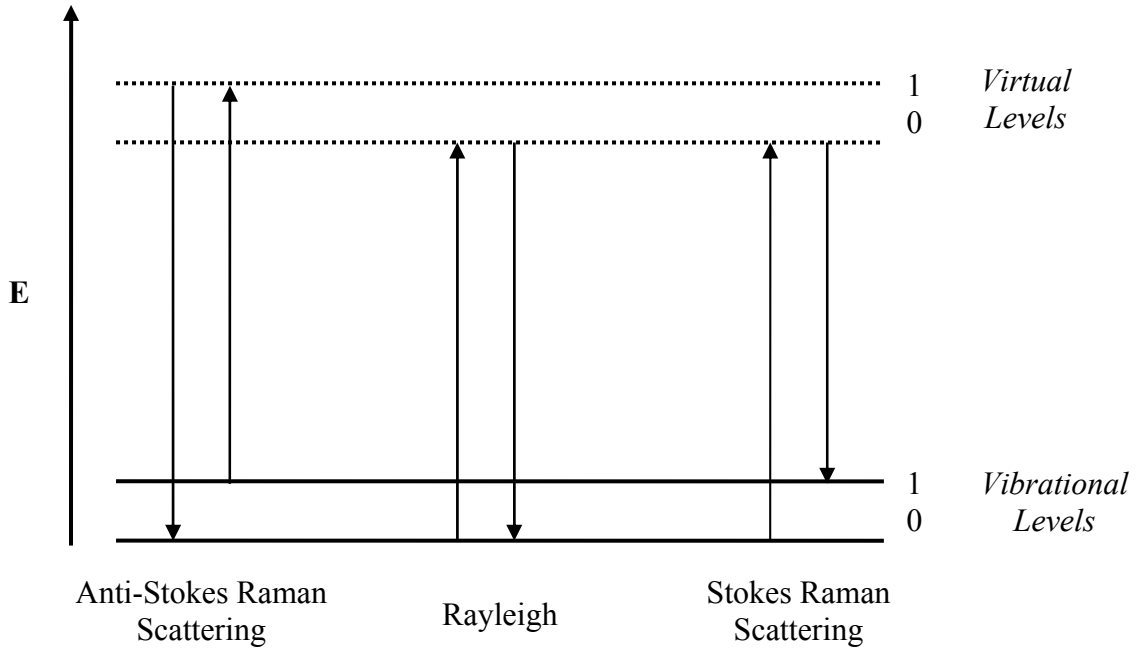

Figure 2.4: Energy level diagram for Rayleigh, Stokes Raman scattering and anti-Stokes Raman scattering.

Equation 2.8 describes the Rayleigh scattering in the first term, while the second

term is the Stokes Raman scattering and the third term representing the anti-Stokes Raman scattering. The ratio of Stokes to anti-Stokes intensities is governed by the temperature, with which it varies according to Boltzman's energy dependency.

The difference in energy between the incident photon and the Raman scattered photon is equal to the energy of a vibration of the scattering molecule. A plot of intensity of scattered light versus energy difference is a Raman spectrum.

The normal Raman effect is a "non-resonant" phenomena where no absorption of the photon is involved and the effect is not dominated by one of the transition moment as happens in the resonant methods. It is good for colorless substances which do not absorb in the visible region of the electromagnetic spectrum.

2.7.2 Resonance Raman Spectroscopy

Some thirty years after the discovery of the Raman effect, Shorygin,[21] in 1962, described the resonance Raman effect. In resonance Raman spectroscopy, the exciting light coincides with an electronic transition of a chromophoric group in the molecule of interest. A simple explanation for the resonance effect is that the transition probability is greater if the intermediate state (Mm) of the molecule resembles an existing state, i.e., the first electronically excited state of the chromophore. As a result, more molecules is excited, and the Raman signal increases with several orders of magnitude. The transition probability of the other scatterers in the molecule of interest remains unchanged, and the spectrum is dominated by the spectrum of the chromophore. The resonance effect can be understood more completely upon revision of the Albrecht theory (the sum-over-states picture). It has been shown that the scattering tensor can be calculated with[20]:

$$\left(\alpha_{\rho\sigma}\right)_{g,g'} = \frac{1}{h}\sum_{M,m}\left(\frac{\left\langle Gg\left|\mu_\rho\right|Mm\right\rangle\left\langle Mm\left|\mu_\sigma\right|Gg'\right\rangle}{\nu_{Gg,Mm}-\nu_0+i\Gamma_M}+\frac{\left\langle Mm\left|\mu_\rho\right|Gg'\right\rangle\left\langle Gg\left|\mu_\sigma\right|Mm\right\rangle}{\nu_{Gg,Mm}+\nu_0+i\Gamma_M}\right) \tag{2.9}$$

The value of the scattering tensor becomes very high when ν_0 is close to $\nu_{Gg,Ee}$ (the damping factor is already very small). When the excitation energy $h\nu_0$ is close to an electronic transition E, for this electronic state the denominator becomes very small so that further terms in the summation over M can be neglected and the equation for the scattering tensor is simplified to[33]:

$$\left(\alpha_{\rho\sigma}\right)_{g,g'} = \frac{1}{h}\sum_{e}\left(\frac{\left\langle Gg\left|\mu_\rho\right|Ee\right\rangle\left\langle Ee\left|\mu_\rho\right|Gg'\right\rangle}{\nu_{Gg,Ee}-\nu_0+i\Gamma_E}\right) \tag{2.10}$$

The vibrational and electronic coordinates can be separated and the electronic transition moment can be expanded (according to a Herzberg-Teller expansion) in a Taylor series with respect to the normal coordinates Q as[33]:

$$\left\langle G\left|\mu_\rho\right|E\right\rangle_Q = \left\langle G\left|\mu_\rho\right|E\right\rangle_{Q_0} + \sum_t\left(\delta\left\langle G\left|\mu_\rho\right|E\right\rangle/\delta Q_t\right)_{Q_0}Q_t + \cdots \tag{2.11}$$

Neglecting higher order terms, the above two equations (2.10 and 2.11) can be combined to yield two terms which are commonly referred to as the A-term and the B-term[33]:

$$A = \frac{1}{h}\mu_\rho^e\mu_\sigma^e\sum_e\frac{\langle g|e\rangle\langle e|g'\rangle}{\nu_{Gg,Ee}-\nu_0+i\Gamma_E}$$

$$B = \frac{1}{h}\sum_e\frac{1}{\nu_{Gg,Ee}-\nu_0+i\Gamma_E}\left[\sum_{Q_t}\left\{\begin{array}{l}\mu_\rho^e\left(\delta\mu_\sigma^e/\delta Q_t\right)\langle g|e\rangle\langle e|g'\rangle+\mu_\sigma^e\left(\delta\mu_\rho^e/\delta Q_t\right)\langle g|e\rangle\langle e|g'\rangle\\+\left(\delta\mu_\sigma^e/\delta Q_t\right)\left(\delta\mu_\rho^e/\delta Q_t\right)\langle g|e\rangle\langle e|g'\rangle\end{array}\right\}\right] \tag{2.12}$$

where μ_ρ^e and μ_σ^e are the electronic transition moments, and $\langle g|e\rangle$ and $\langle e|g'\rangle$ are the vibrational overlap integrals.

The A-term contains the Franck-Condon factor, which is defined as the amount of overlap between the ground and the (relaxed) excited state. The scattering tensor is the sum of both factors (i.e., $\left(\alpha_{\rho\sigma}\right)_{g,g'} = A + B$). Depending on the excitation wavelength and the properties of the molecule, either the A-term or the B-term can dominate. Excitation in strong electronic transitions usually favors the A-term because $\mu^e >> \delta\ \mu^e / \delta\ Q_t$. Only totally symmetric modes can be enhanced via the A-term since for non-totally symmetric modes the Franck-Condon products are zero. The B-term becomes dominant for excitation a weakly allowed or forbidden transitions.

Except for the selective enhancement of vibrations of certain symmetries, the resonance Raman spectrum differs from the Raman spectrum because of the presence of overtone or combination bands. Overtones and combination bands are almost absent in Raman spectra. In resonance Raman spectra, however, long, well-defined progressions of overtones corresponding to totally symmetric vibrations may be observed.

2.7.2.1 Surface-Enhanced Raman Scattering (SERS)

Surface-enhanced Raman scattering (SERS) is a spectroscopic technique used to obtain information on vibrations of molecules adsorbed at metal surfaces parallel to that which has been extensively employed for molecules in solids, liquids or gases using the normal resonance Raman spectroscopy. SERS has become a useful tool with considerable potential for studying molecules adsorbed on solid substrates.[22]

The effect was first obtained from molecules adsorbed on silver metal working electrodes of electrochemical cells by Fleischmann and colleagues.[23] His method has become a useful method for electrode/electrolyte interfacial studies. But, in their publication, Fleishmann et al.,[23] reported a normal Raman spectrum with good signal-to-noise

ratio which was explained by the increase of the surface area enough to have sufficient number of molecules in the beam. It was other workers who afterwards independently observed and reported the enhancement effect[24,25] as a new phenomenon. The intensity of the Raman spectrum of pyridine was enhanced by a factor of five to six orders of magnitude over what could be expected from the scattering cross section of the isolated molecule, i.e., normal Raman scattering. This anomalous intense Raman scattering observation gives birth to the name "surface-enhanced Raman scattering" (SERS).

The enhancement magnitude in SERS is relatively independent of the identity of the adsorbed molecule but not of the metal surface. There is sufficient evidence that the royal family of the periodic table, family IB, gives SERS to some extent, but silver exhibits the strongest enhanced scattering effect and has received more attention.[26] For both copper and gold, better results were obtained with laser excitation in the red end of the visible spectrum.[27]

The effect is not limited to electrochemical systems alone. It has been observed, for example, at a metal/gas interface,[28] at metal island film/liquid interfaces,[29] and at silver and gold metal sol or nanoshell/liquid interfaces[30] to name a few. The observation of SERS in a diversity of interfacial systems allows the study of some of the systems which are normally difficult to study with most spectroscopic techniques, thus leading to the understanding of such systems.

A number of theories have been advanced to explain the mechanism contributing to surface enhancement.[31] The widely accepted view is that both chemical and electrodynamic interactions play fundamental roles in the enhancement mechanism.[32] The electrodynamic theories attribute enhancement to the effect of roughness and

structures that support and enhance electrodynamic fields,[33] while the chemical effect is based on the presence of resonances between the exciting radiation and quantum states created by coupling between quantum states of the adsorbed species and the quantum states of the substrate.[32 (b),34]

2.7.2.2 Aggregation Enhanced Raman Scattering (AERS)

Working with cyanine dyes adsorbed on colloidal silver and silver electrodes,[30(a,b),35] Akins et al. have found that the enhancement properties exhibited by these systems differ substantially from those noted from other systems. The primary explanation, for this observation, proposed by Akins et al.[36] is associated with the rather unique properties exhibited by cyanine dyes aggregating on surfaces to form ordered macrostructures,[37] and the increased polarizability of such structures. The enhanced Raman scattering by cyanine dyes when the incident radiation is in resonance with the shifted aggregated absorption is attributed to a resonance-Raman scattering couple with the molecular exciton states of the aggregate which acts, possibly, in concert with the electromagnetic mechanism. The theory embodying this explanation is discussed in detail elsewhere.[38]

2.7.3 The Raman Setup

All measurements unless otherwise stated have been performed using the HR800, an integrated dispersive Raman microscope system with backscattering geometry. The microscope is coupled confocally to a 800 mm focal length spectrograph equipped with two switcheable gratings. Figure 2.5 shows the main parts of the instrument as they can be seen when the cover is taken off. The excitation wavelength is supplied by an internal HeNe 20 mW laser mounted on the back of the instrument.

The laser is totally reflected by the notch towards the sample under microscope

and the Raman scattering is totally transmitted through the notch filter towards the confocal hole and entrance slit of the spectrograph. The confocal hole, notch filter, and entrance slit of the spectrograph can be accessed in the higher part of the instrument (entrance optics).

Raman microscope setups provide the advantage that small volumes or spots can be examined. In the setup, a high stability BX 40 microscope was employed. The objectives used are either 10X (NA 0.25), 50X (NA 0.7) or 100X (NA 0.9). Focusing occurs manually, using transmitted white light for transparent samples or incident white light for opaque samples. A black and white camera is used for the observation of the sample.

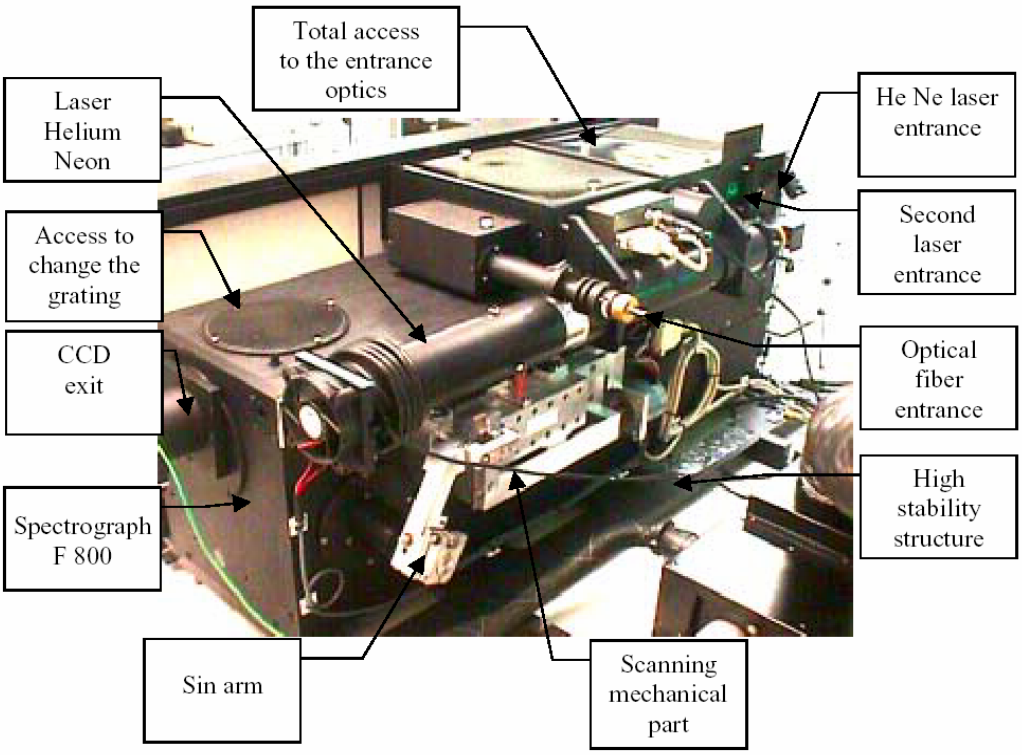

Figure 2.5: Schematic of the Raman microscope setup that was used.

For this setup, an air-cooled Andor standard 1024 X 256 pixels of 26 microns CCD-camera model DU420-OE-324 (Belfast, Nothern Ireland) was used. A Pentium computer with Labspec software and Rio card for TV image digitalization was used for spectral acquisition.

For Raman spectroscopy, sample preparation is not necessarily needed, provided that the compounds of interest are on the surface of the object that has to be analyzed. However, for solution spectra, a macro adapter with 40 mm objective under the microscope was used. Quartz or glass cuvette was use for all solution measurements.

3 Noble-Metal Nanoparticles: Synthesis, Assembly and Characterization

3.1 Introduction

Colloidal metal nanoparticles have been known for a long time and are now widely investigated as new materials with novel properties. Metal nanoparticles have been intensively studied in recent years because of their attractive optical and electronic properties, related with the quantum size effect, and their promising applications in areas such as optics, optoelectronics, catalysis, nanostructure fabrication, and chemical and biochemical sensing.[1] For these colloidal metal nanoparticles, the catalytic activity as well as their electrical, thermodynamic, chemical, and optical properties is dependent on their size and shape.[2] It is, therefore, very important to control the nanoparticles' morphology and size. Equally important is to attain particle dispersion with a narrow size distribution. However, specific control of shape and size is often difficult. Generally, this control is achieved by varying the nanoparticle synthesis method, reducing agent and stabilizer use, and pH of the reaction system. In spite of these controlling methods, the size of nanoparticles produce cannot exactly be controlled during synthesis; it is only possible to narrow the size distribution

Colloidal preparation of nanosized metal and their characterization has gained considerable interest in recent years, mostly, because of new synthetic methods and new and better characterization means. Both physical and chemical preparation methods have been reported in the literature, however, certain physical methods seem arduous when compared to chemical routes.[3] As a matter of fact, the majority of published reports concerning metal nanoparticles that focus on the chemical preparation and their characterization reveal that the shape, size, size distribution, and stability, as well as

chemical and physical properties, are dependent on the specific preparation methods, particularly on the reducing agents employed.[4] It has been recognized that the use of mild or weak reductants can result in small metal nanoparticles with a narrow size distribution. So far, a large variety of materials such as hydrazine, sodium borohydride, sodium citrate, sodium formate, hydrogen, carbon monoxide, potassium bitartrate, Tollen's reagent, ascorbic acid, ethylene glycol, formaldehyde, among others, have been used as reducing agents to prepare metal nanoparticles.[5] A common feature of the conventional chemical methods is that the metal seeding formation and growth are often fulfilled in the same liquid phase at slightly different times. In this instance, the metal nanoparticle that is being synthesized must be kept in liquid solution. To control particle sizes and morphology and to improve particle stability, stabilizers are often added to the solution during the course of particle synthesis. Surfactants and polymers, such as cyclodextrin,[6] cetyltrimethylammonium bromide (CTAB),[7] 3-mercaptopropionate acid (MPA),[8] polyvinyl-pyrrolidone (PVP),[5(e)] polyvinyl alcohol (PVA),[9] and citrate,[10] are examples of stabilizers used to hinder metal nanoparticle's tendency to agglomerate

The production of metal colloids by the reduction of their ions in solution involves two distinct stages: nucleation and growth.[11] The former requires relatively high activation energies associated with the high area-to-volume ratio of the embryo particles. The latter is usually characterized by lower potential energy barriers and is often diffusion controlled. The relative rates of these two processes determine the final size distribution of the colloid. An increase of the nucleation rate relative to the growth rate generally results in a higher concentration of finer dispersion.

The relative rates of nucleation and growth can be affected by many of the control

parameters of the system: the temperature,[12] the concentration of the reactants,[13] the potency of the reductant,[13] the pH,[13] the extent of mixing,[14] and the rate reactants added.[15] The rates can also be influence by other constituents of the system. For example, molecules may adsorb on the colloidal particles, at various stages of the entire process, and modify the rate of the reaction at that specific stage. Also, additives may form complexes with the reacting metal ions effectively reducing the concentration of the free ions, while opening new channels for reaction on the other.

Colloidal metal nanoparticles exhibit extremely exciting physicochemical and optoelectronic properties both on an individual scale[16] and collectively as two-dimensional arrangements.[17] The latter aspect has spurred research into the organization of nanoparticles into thin film on a substrate. Among the many techniques being used, one approach for the immobilization of colloidal particles onto substrates is based on the derivatization of the substrate surface with polymers having pendant functional groups with high affinity for Ag and Au (e.g., CN, SH, NH_2). For instance, alkoxysilanes followed by adsorption of the colloidal nanoparticles onto the self-assembled monolayers (SAM).[18] Covalent and noncovalent self-assembly of colloidal metal nanoparticles is fast becoming popular as a viable "bottom-up" route for the generation of mesoscale architecture and macroscopic surfaces.[19] The ability to tailor the size as well as the separation between the particles is a desirable element in modifying the electronic and optical properties of the nanoparticles as well as elements on the macroscopic surface.

In this chapter, the emphasis has been on the preparation of mono-disperse, stable, sized-controlled Ag and Au nanoparticles. Different published methods, sometimes with modifications, were used to prepare these nanoparticles. Also, Ag and Au nanoparticles

of different sizes were purchased from BBI International,[20] UK and used in comparison to the in-house synthesized nanoparticles in size dependent studies. The synthesized and purchased nanoparticles are used as substrates to adsorb cyanine dyes molecular aggregates. Efforts to prepare metal colloidal film to be used in a similar fashion as the nanoparticles are also reported. The preparation strategy involves assembly of colloidal Ag and Au particles into macroscopic two-dimensional arrays on polymer-derivatized substrates, e.g., glass. The produced nanoparticles were characterized for reproducibility and stability using sedimentation, atomic force microscopy (AFM), high pressure liquid chromatography (HPLC) and UV-Visible spectroscopy.

3.2 Experimental

3.2.1 Materials

All reagents were of analytical grade or the best grade commercially available unless otherwise mentioned. Triply distilled water was utilized for preparation of all aqueous solutions. The stabilizers, polyvinylpyrrolidone (PVP; molecular weight (MW) = 40,000; Acros), cetyltrimethylammonium bromide ($C_{16}H_{33}N(CH_3)_3Br$, 99%, denoted as CTAB hereinafter; Acros), sodium 3-mercaptopropionate (MPA-Na, i.e., 3-mercaptopropionic acid (Aldrich) neutralized with NaOH) were used as received. The following chemicals were obtained from Aldrich: hydrogen tetrachloroaurate ($HAuCl_4 \cdot 4H_2O$), potassium tetrachloroaurate ($KAuCl_4$), silver nitrate ($AgNO_3$, 99.99%), sodium borohydride ($NaBH_4$), trisodium citrate dehydrate ($Na_3C_2H_5NO_3 \cdot H_2O$), Ethylene glycol, spectrophotometric grade methanol (MeOH) and ethanol (EtOH), H_2O_2, concentrated H_2SO_4, HCl, and HNO_3, and used without treatment. (3-mercaptopropyl)-trimethoxysilane (MPTMS), and (3-aminopropyl)-trimethoxysilane (APTMS) were

obtained from Aldrich and used as derivatization reagent to anchor colloidal Ag and Au monolayer to a hydroxide-rich glass surface. Glass microscope slides were obtained from Fisher Scientific. All glassware used in the following preparations was thoroughly cleaned in aqua regia (3 parts HCl, 1 part HNO_3), rinsed in triply distilled H_2O, and oven-dried prior to use.

3.2.2 Preparation of Ag Nanoparticles

The following different Ag colloidal particles were prepared according to the following procedures:

I. Native nanoscale silver particles were prepared by reduction of $AgNO_3$ solution with $NaBH_4$ (borohydride-reduced, b. r.) or sodium citrate (citrate-reduced, c. r.) using modified published procedures.[5(f,g)] Briefly, in the b. r. synthesis, an aqueous solution of sodium borohydride (300 mL, 2×10^{-3} M) was placed in a round-bottom flask in an ice bath. An aqueous solution of silver nitrate was prepared (100 mL, 1×10^{-3} M) and ice-cooled prior to use. The silver nitrate solution was added dropwise to the sodium borohydride solution with vigorous stirring, over a period of 20 min, to aid monodispersity. The flask was then removed from the ice and stirring was continued for a further 45 min. The resulting silver sol was divided into two fractions; one was transferred to an amber bottle and kept for future use; the other was heated for approximately 1 h, then cooled and transferred to an amber bottle for future use. For the c. r., approximately 500 mL of distilled water was placed in a clean 1 L round-bottomed flask. This was heated to approximately 45 °C, at which point silver nitrate was added (90 mg). Heating was continued until the mixture was brought to boiling, then 10 mL of 3.4×10^{-2} M trisodium citrate was added dropwised. The mixture was kept at boiling for

about 1 h and stirred throughout. The resulting colloids were kept in an amber bottle until ready to be used.

II. Surfactant- and polymer-stabilized Ag nanoparticles were prepared according to the following methods.[21] In the first method, silver nanoparticles were synthesized in an aqueous solution by reducing $AgNO_3$ with $NaBH_4$ in the presence of PVP and sodium citrate. Briefly, 48 mL of water was deoxygenated by bubbling with nitrogen gas for 30 min before 0.5 mL aqueous solution of sodium citrate (30 mM) and 1 mL aqueous solution of silver nitrate (5 mM) were added. A 0.5 mL aliquot of freshly prepared sodium borohydride (50 mM) was rapidly added, and the solution immediately turned into a light yellow color. After 30 s 0.5 mL aqueous solution of polyvinylpyrrolidone (PVP, 14 mg/2 mL, Mw = 40, 000) was added. The solution changed to a darker yellow color after the reaction had proceeded for another 30 min.

In a second method, nanoscale silver particles were prepared by reduction of $AgNO_3$ solution with $NaBH_4$ in the presence of the surfactant CTAB. In a typical preparation, $NaBH_4$ concentration was 2×10^{-3} M, $AgNO_3$ and surfactant concentration were 1×10^{-3} M and the usual mole ratio of 3 to 1 to 2 was used.

III. In order to produce colloidal Ag particles in organic solvents, the polyol process according to Silvert et al. was used.[5(h)] In a typical synthesis, 5 g PVP was dissolved in 75 mL ethylene glycol at room temperature; to this solution 0.41 g of $AgNO_3$ was added. The suspension was then stirred at room temperature until complete dissolution of the silver nitrate was achieved. Then, the system was heated to 120 °C at a constant rate of about 1 °C/min and the reaction allowed to proceed for 1 h at this temperature. At the end of the reaction period, the colloidal dispersion was cooled in tap water until the

system reached room temperature. The silver colloid was then separated from the ethylene glycol by adding large amount of acetone followed by centrifugation. Then, the precipitate was redispersed in either methanol or ethanol and kept for use.

3.2.3 Preparation of Au Nanoparticles

The following two different Au nanoparticles preparations were used:

i. Colloidal gold particles were prepared by reaction of $KAuCl_4$ with sodium borohydride.[5(g)] Briefly, 25 mL of 2.5×10^{-3} M $KAuCl_4$ was added dropwise, with vigorous stirring, over a period of 20 min to 75 mL 1×10^{-3} M $NaBH_4$ solution in an ice bath. The resulting gold sol was divided into two portions: one was transferred to an amber bottle and kept for future use; the other was heated for approximately 1 h, then cooled and transferred to an amber bottle for future use.

ii. Another system was prepared in a manner quite similar to that reported in ref. 9. Aqueous tetrachloroauric (III) acid ($HAuCl_4 \bullet 4H_2O$, 5.8×10^{-3} M, 25 mL) was added to 250 mL water contained in a 500 mL round-bottom flask, and the solution was heated to boiling. A mixed solution, (25 mL) of MPA-Na and citrate ion (trisodium citrate dehydrate, 2.0 wt. %) was then added simultaneously. After the addition of reductant and stabilizer, the color of the solution turned from yellow to red or brown.

3.2.4 Preparation of Ag and Au Self-Assemblies(Films)

25 × 25 mm, ~0.17-0.25 mm thick glass slides were cleaned using detergent, rinse with deionized (DI) water and then sonicated in acetone and methanol for 2 min each. The slides where then placed in piranha solution (v/v, 7:3 H_2SO_4 : H_2O_2) for 1 h at 60 °C, rinsed using copious amount of DI water and dried under flowing dry nitrogen. The cleaned glass slides were then derivatized with alkoxysilanes by immersing them in vials

of (3-mercaptopropyl)-trimethoxysilane (MPTMS) or (3-aminopropyl)-trimethoxysilane (APTMS) diluted 1:4 with spectrophotometric grade methanol for 24 h. Afterward, the glass substrates were removed and rinsed profusely by sonicating them in methanol for 2 min. This process was repeated three times to remove any unbound monomer from the surface. At this point, the resulting silanized substrates were stored in MeOH until needed. Prior to derivatization with colloidal Ag and Au particles, the substrates were rinsed with H_2O; they were then submerged in vials with 50 mL of colloidal Ag or Au particles for varied times. A final DI water rinse and drying in air concluded the derivatization process.

3.3 UV-Visible Spectra of Ag and Au Nanoparticles

From the optical spectra of Ag and Au colloidal particles, one may obtain information about the particle concentration (absorbance), particle size (position of λ_{max}), and dispersity of particle size in solution (width of absorbance band). Figure 3.1 (A) shows the optical spectra of aqueous dispersions of Ag nanospheres synthesized using borohydride reduction that is surfactant- and/or polymer-free (1), hereinafter, named native Ag; CTAB-stabilized Ag (2); PVP-stabilized Ag (3); and using citrate reduction (4). Figure 3.1 (B) shows the diffuse reflectance spectrum of (a) dried Ag precipitates, and (b) the absorption spectrum of the redispersed precipitates in MeOH. The four colloidal Ag particle systems shown in Figure 3.1 (A) represent different nanoparticle environments for adsorption of cyanine dyes, and are discussed in the following chapter. The spectra shown in Figure 3.1 were acquired immediately after synthesis. To investigate the surface plasmon resonances of the differently prepared nanoparticles more systematically, the homogeneous linewidth (full width at half maximum, FWHM) and

peak position (λ_{max}) of the plasmon resonance band was extracted for each of the measured spectra.

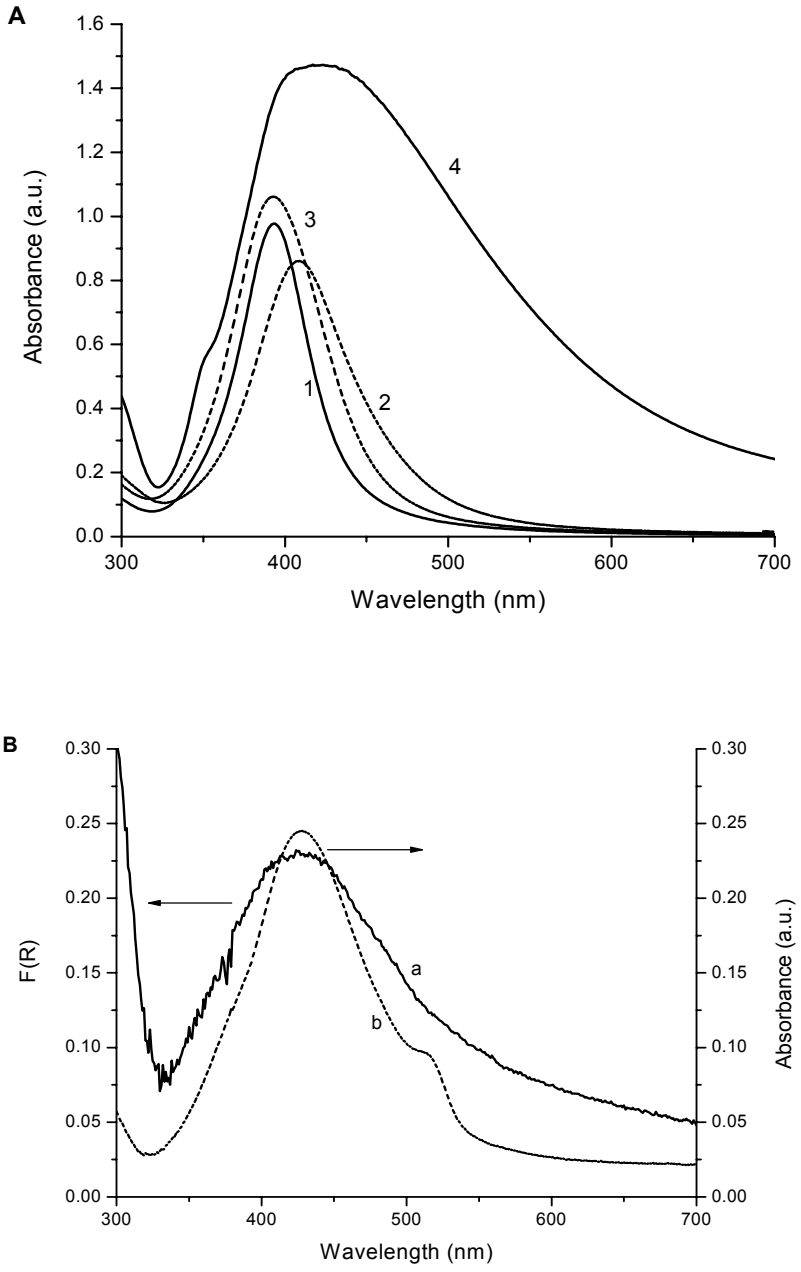

Figure 3.1: UV-Visible absorption spectra of aqueous dispersion of (A) Ag nanospheres synthesized using borohydride reduction: (1, surfactant-free), (2, CTAB-stabilized), (3, PVP-stabilized) and (4) citrate reduction. (B) Shows diffuse reflectance spectrum of (a) dried Ag precipitates and (b) redispersed precipitates absorption spectrum in MeOH.

The borohydride-reduced Ag nanospheres have symmetric and narrow peaks with different λ_{max} and full width at half maximum (FWHM). The data is given in Table 3.1. The citrate colloid, on the other hand, has an asymmetric peak with large tail that extends into the red. The more symmetrical and narrow Ag nanospheres suggest smaller average particle size and greater monodisperse size range for the preparation. The redox reaction for the preparation of nanoscale silver particles by reduction of $AgNO_3$ solution with $NaBH_4$ can be written as:

$$2\ AgNO_3 + 2\ NaBH_4 + 6\ H_2O \rightarrow\ 2\ Ag^0 + 2NaNO_3 + 2H_3BO_3 + 7\ H_2$$

Table 3.1: Summary of the data obtained from the UV-Visible spectra and pH obtained from the prepared silver nanoparticles.

Nanoparticle type	λ_{max} (nm)	FWHM (nm)	Abs. (a.u.)	pH
Native	394	45	2.28	9.70
Citrate	406	152	2.22	6.41
PVP-stabilized	393	59	2.20	7.49
CTAB-stabilized	409	64	1.90	9.17
Methanol-transferred	428	88	0.25	5.75

The mole ratios of $NaBH_4$ to $AgNO_3$ (R_{BAG}) used in all of the Ag colloids was usually between 2 and 4. A reduction in the ratio of sodium borohydride to silver nitrate concentration usually resulted in an increase in the extinction. This reduction occurred because the decrease ratio was achieved by increasing the silver nitrate concentration, which resulted in an increase in the number of particles in the colloid and consequently an increase in the UV-Visible extinction. The sodium borohydride to silver nitrate ratio also has an effect on the full width at half maximum (FWHM) of the absorption band. Specifically an increase in the ratio of sodium borohydride to silver nitrate concentration results in a decrease of the FWHM of the UV-Visible extinction peak. A decrease in the

FWHM in the extinction peak is indicative of a narrower particle size distribution.

Based on the UV-Visible spectra and the data summary in Table 3.1, the native and the PVP-stabilized Ag nanoparticles represent systems with smaller particle size and lower dispersity. The intention was to find noble metal nanoparticles of a specific size that are nearly monodisperse to serve as substrates for molecular aggregates, specifically, J-aggregates. The pH of the different preparations, an important parameter in promoting J-aggregation, is also given in Table 3.1. The native Ag nanospheres represented the most basic system. The system in Figure 3.1 (B) represents a nonaqueous environment for forming J-aggregates. Methanol was chosen as the solvent in this particular case, but any solvent of choice could have been chosen provided that the silver powders dissolved.

UV-Visible spectra of aqueous dispersion of Au nanoparticles, another metal colloidal system that was employed as substrates for coating with molecular aggregates, are presented in Figure 3.2. Gold nanoparticles have a surface plasmon at ca. 530 nm (FWHM = 58 nm) for the citrate-reduced MPA-stabilized nanoparticles (1) and ca. 540 nm (FWHM = 69 nm) for the borohydride-reduced Au nanoparticles (2). However, using the borohydride reduction, the surface plasmon resonance bands of the Au nanoparticles can range from ca. 520-550 nm, dependent on the ratio of reducing agent to salt used. The uniqueness of the MPA or thiol-stabilized system, and thus the reason it was utilized as a substrate, is that it produces Au nanoparticles surrounded by thiol with a pendant negative charge as shown in scheme 3.1. Cationic cyanine dyes are used to coat the nanoparticles in this system. The pH for (1) and (2) were 6.49 and 3.62, respectively.

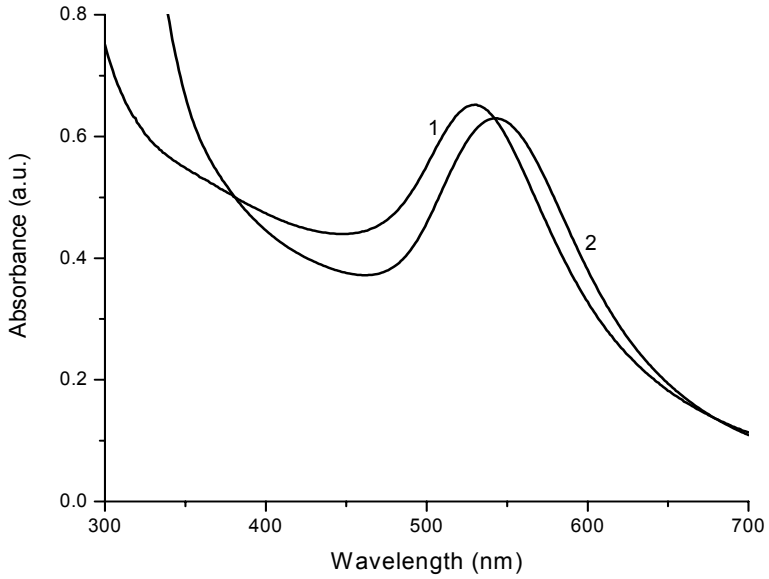

Figure 3.2: UV-Visible absorption spectra of aqueous dispersion of freshly prepared citrate-reduced 3-mercaptoproprionate-stabilized Au nanoparticles (1) and (2) borohydride-reduced Au nanoparticles.

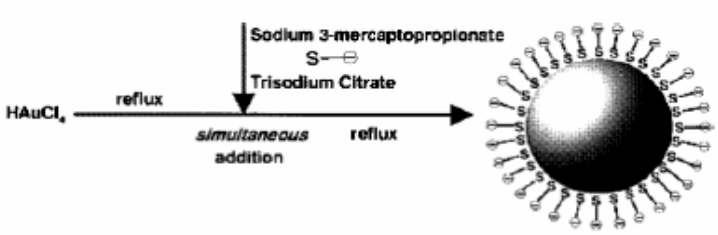

Scheme 3.1. Preparation of 3-mercaptopropionate-stabilized Au nanoparticles in water.[22]

In addition to the in-house synthesized nanoparticles, Ag and Au nanoparticles of different sizes were purchased from BBInternational (Cardiff, CF145DX, UK). The nanoparticles were formed using the citrate reduction method and sold as a suspension in H_2O. As specified by the manufacturer, they were no surfactant, protein, or polymer used to stabilize their nanoparticles. The pH was reported to be around 8, but measured to be about neutral. The particles according to the manufacturer were stable, once opened, for

about a month and thus were used within that period of time. The UV-Visible spectrum of each purchased Ag and Au nanoparticles were taken and presented in Figure 3.3. Table 3.2 presents the related data, including average diameter given by the manufacturer, measured λmax, the full width at half maximum (FWHM) and the absorbance.

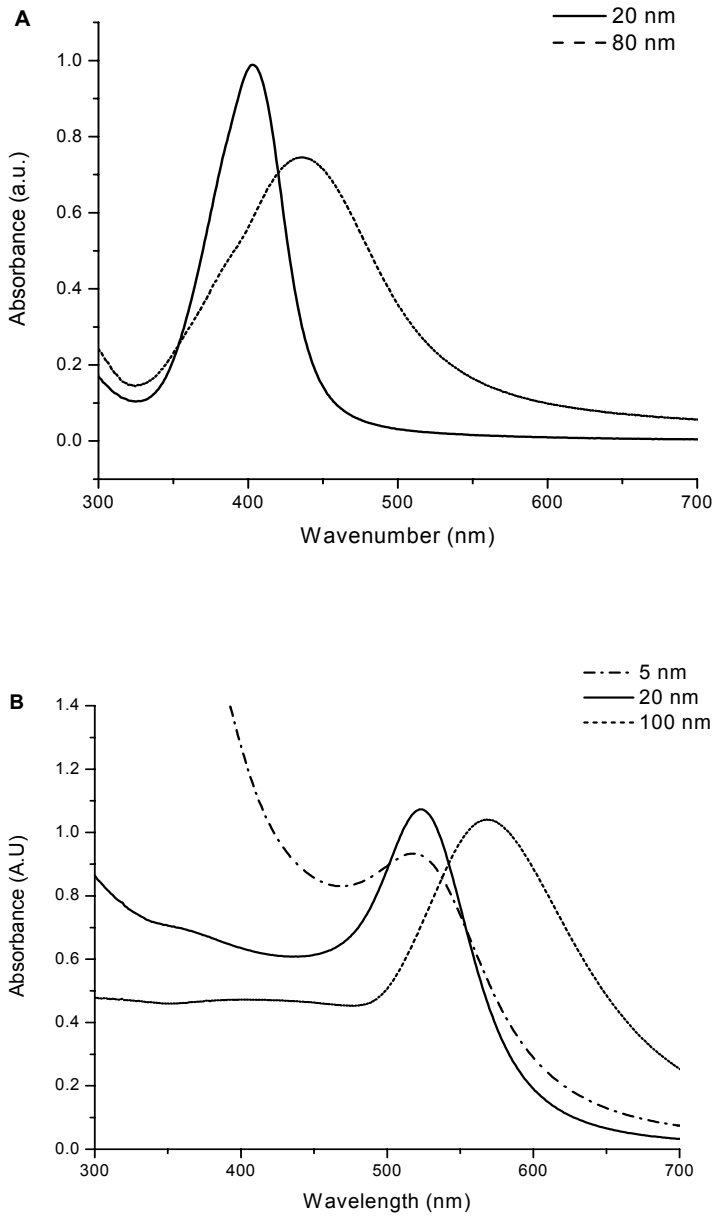

Figure 3.3: Absorption spectra of BBInternational purchased (A) Ag and (B) Au nanoparticles of different sizes.

Table 3.2: Summary of the data from the UV-Visible spectra obtained from the BBInternational purchased Ag and Au nanoparticles and the average diameter given.

Nanoparticle type	Mean diameter (nm)	λ_{max} (nm)	FWHM (nm)	Abs. (a.u.)
Ag	21.6	403	50	0.80
Ag	80	435	92	0.51
Au	5	525	61	0.17
Au	20	525	52	0.50
Au	106.5	568	86	0.55

Along with the purchased nanoparticles, stable dispersions of nearly spherical silver or gold nanoparticles of different sizes were prepared by reduction of dilute solutions of simple silver or gold salts using sodium borohydride or citrate as the reducing agent, and for some nanoparticles, stabilizers such as CTAB, PVP and MPA, were utilized. These metal nanoparticles have one or more peaks in the absorption spectrum in the visible range, depending on the particle size. As the nanoparticle sizes increased, for example as shown in Figure 3.3, a red-shift is observed in the absorption spectra. The color of the metal nanoparticles, yellow for Ag and deep red-purple for gold, reflects the surface plasmon band; an absorption band in the visible region around 400 nm for Ag and around 530 nm for Au. The surface plasmon band is due to the collective oscillations of the electron gas at the surface of the nanoparticles (5s and 6s electrons of the conduction band for Ag and Au nanoparticles, respectively) that is correlated with the electromagnetic field of the incoming light, i.e., the excitation of the coherent oscillation of the conduction band. The nature of the surface plasmon band has been clarified by Mie.[23] According to Mie theory, the total cross section composed of the surface plasmon absorption and scattering is given as a summation over all electric and magnetic oscillations. Mie's theory attributes the plasmon band of spherical particles to the dipole oscillations of the free electrons in the conduction band occupying the energy states

immediately above the Fermi energy level.[24] The surface plasmon band maximum and bandwidth are also influence by the particle shape, the dielectric constant of the medium, and the temperature. A stabilizer, treated like a ligand shell, alters the refractive index and cause a red or blue shift. The spectroscopic data obtained from these systems often deviate from the prediction of the Mie theory, which deals with naked nanoparticles.[24] However, agreement with the Mie theory can be obtained when the shift induced by the ligand shell is taken into account.

3.4 High-Pressure Liquid Chromatography (HPLC) Fractionation of Particles

High pressure liquid exclusion chromatography has been used to determine the size distribution of a colloidal metal,[25] to characterized semiconductor particles,[26] and has been applied in the study of luminescent silicon particles.[27] As part of the present study, an attempt was made to use HLPC in an analogous manner to characterize the in-house synthesized Ag nanoparticles in aqueous solution as well as redispersed in MeOH solution, principally, in an effort to identify the degree of dispersity for the two in-house synthesized Ag nanoparticles and also to attempt to separate different sizes by collection of the liquid fractions as a function of elution time. The chromatography apparatus used was an Agilent 1100 series with Agilent quad pump, type G1311 A, and an Agilent variable wavelength detector, type G1314 A. A set of two 5 μm columns (4.6 mm internal diameter) was used, the first was a Hypersil MOS from Supelco Inc. and the second was a Zorbax SB-CN from Agilent. The mobile phase was an aqueous solution of 1×10^{-9} M trisodium citrate or a 60:40 methanol-ethylene glycol mixture with 1.5×10^{-3} M sodium methylate. The sample volume was 20 μL.

Figure 3.4 (A) shows the chromatograms of the native Ag colloid in aqueous

solution. Figure 3.4 (B) shows that of the Ag colloid made using the polyol process and redispersed in methanol. The chromatograms in Figure 3.4 (A), based on the different peaks at different elution time suggest two particle size distributions, while the one in Figure 3.4 (B) suggest three. Hence, the Ag nanoparticles redispersed in methanol suggest greater size distribution compared to that of the native Ag nanoparticles in aqueous solution. This suggestion is confirmed by inspecting the full width at half maximum (FWHM) for the two differently prepared Ag colloids. The native Ag colloids in aqueous solution had a FWHM of 45 nm while the redispersed-MeOH system had one of 88 nm which suggest greater dispersion. In addition, the larger size for the redispersed Ag colloids suggested by bigger λ_{max} (408 nm) and greater dispersion may explain the appearance of the shoulder or bump (λ = 515 nm) in the absorption spectra of Figure 3.1 (B) which is indicative of colloidal clustering or coagulation.

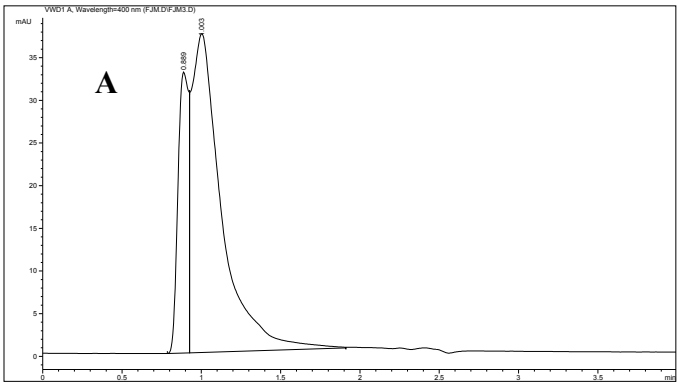

Figure 3.4 (A): HPLC chromatogram of borohydride-reduced Ag nanoparticles in aqueous solution.

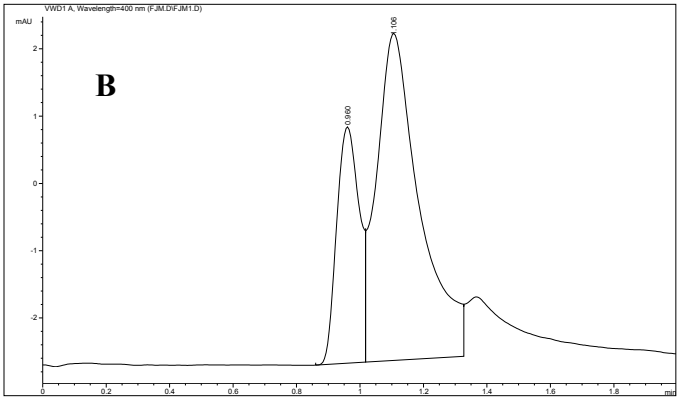

Figure 3.4 (B): HPLC chromatogram of the Ag nanoparticles redispersed in MeOH.

3.5 Stability of the Differently Prepared Nanoparticles

The in-house prepared silver nanoparticles were intended to be used over time. As a result, the stability of the differently prepared systems was of interest and thus was ascertained (over a period of time) following the absorption spectra. The UV-Visible spectrum of each Ag nanoparticles preparation was run immediately after synthesis, then after one month, and again three months after synthesis. In the case of the native Ag nanoparticles a spectrum was taken after 8 months and showed that the naked Ag nanoparticles were stable with little change. Figure 3.5 shows UV-Visible spectra of the differently prepared borohydride-reduced Ag colloids over time.

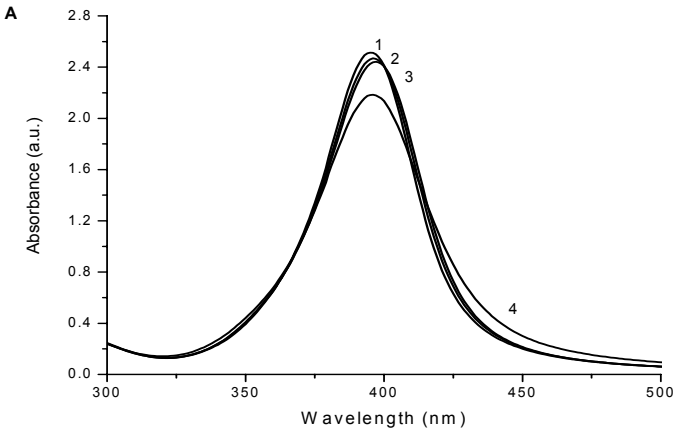

Figure 3.5 (A): Optical absorption spectra as a function of time for Ag colloidal solution prepared using borohydride reduction: surfactant-free. Aging is as follows (1) fresh, (2) one month, (3) three months, and (4) 8 months.

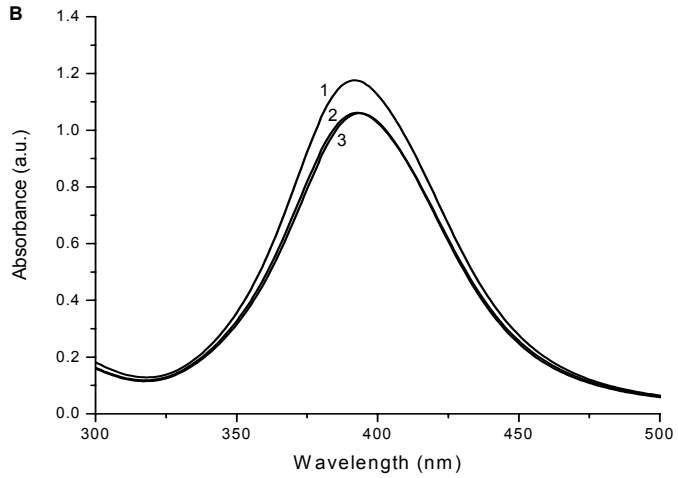

Figure 3.5 (B): Optical absorption spectra as a function of time for Ag colloidal solution prepared using borohydride reduction: PVP-stabilized. Aging is as follows (1) fresh, (2) one month, (3) three months.

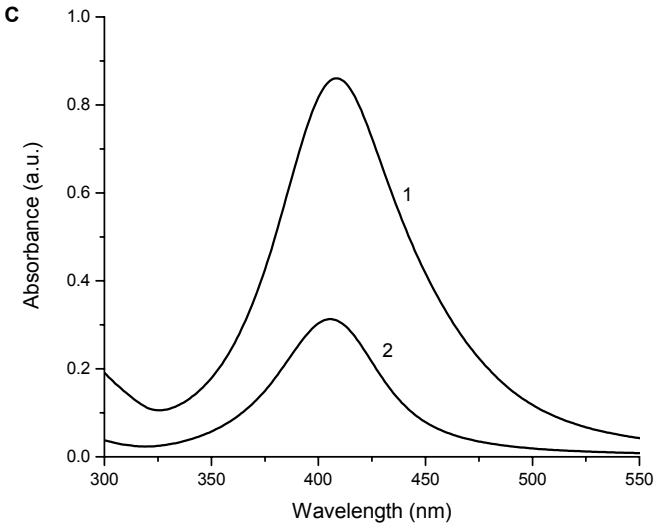

Figure 3.5 (C): Optical absorption spectra as a function of time for Ag colloidal solution prepared using borohydride reduction: CTAB-stabilized. Aging is as follows (1) fresh, (2) one month, (3) three months.

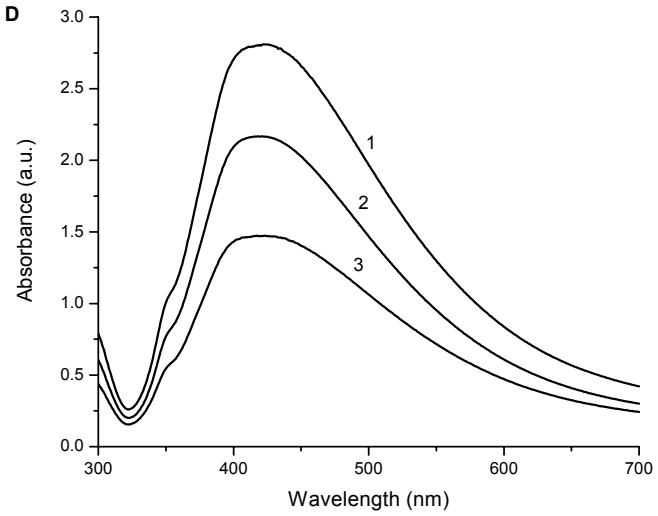

Figure 3.5 (D): Optical absorption spectra as a function of time for Ag colloidal solution prepared using borohydride reduction: citrate reduction. Aging is as follows (1) fresh, (2) one month, (3) three months.

For the native Ag nanoparticles in Figure 3.5 (A), the λ_{max} and [FWHM] of the different time periods were as follows, for (1), 392 nm [60 nm]; (2), 393 nm [61 nm]; (3), 394 nm [59 nm]; and for (4), 392 nm (59 nm). The data showed little variation in the position and FWHM of the surface plasmon band, indicating a stable system over the 8 months period; the absorbance decreased from 1.02 initially to 0.46 after 8 months is possibly due to precipitation. The PVP stabilized, Figure 3.5 (B), showed little peak

(width) variation as well; the data are as follows, for (1), 392 nm [52 nm]; (2), 393 nm [52 nm]; and (3), 394 nm [51 nm]. The decrease in the absorbance is possibly for the same reason stated for the native Ag. The CTAB-stabilized nanoparticle system in Figure 3.5 (C), for which measurements were conducted only for two months, precipitated faster than the other systems and consequently was the least stable. The citrate-reduced system in Figure 3.5 (D) showed some variations. The data are as follows, for (1), 411 nm [145 nm]; (2), 410 nm [138 nm]; and (3), 406 nm [143 nm]. The UV-Visible system used had a resolution of 2 nm; hence, anything greater than 2 nm as a shift is considered to be potentially due to the particle size increase. For the FWHM, the variations may be due to the arbitrary choice of baseline, thus it is assumed that anything more than 5 nm may be regarded as significant. Although the absorption spectra of the Au nanoparticles were not followed consistently, as was done for the Ag nanoparticles, the MPA-stabilized nanoparticles were stable for about a month and the borohydride-reduced Au for well over 2 months.

Considering that heating-up the borohydride-reduced Ag and Au nanoparticles will remove excess $NaBH_4$, i.e., keeping in mind that $AgNO_3$ is the limiting reagent, some portion of the prepared Ag and Au was heated up to about 60 °C for about 20 min in an attempt to further improve the stability of the surfactant- or polymer-free prepared nanoparticles. Figure 3.6 shows the absorption spectra of the Ag nanoparticles prepared. A comparison of the absorption spectrum for the fresh (unheated) and heated portion is presented in Figure 3.6 (A). Figure 3.6 (B) and (C) show the absorption spectra over a three months period for the fresh and heated portion, respectively.

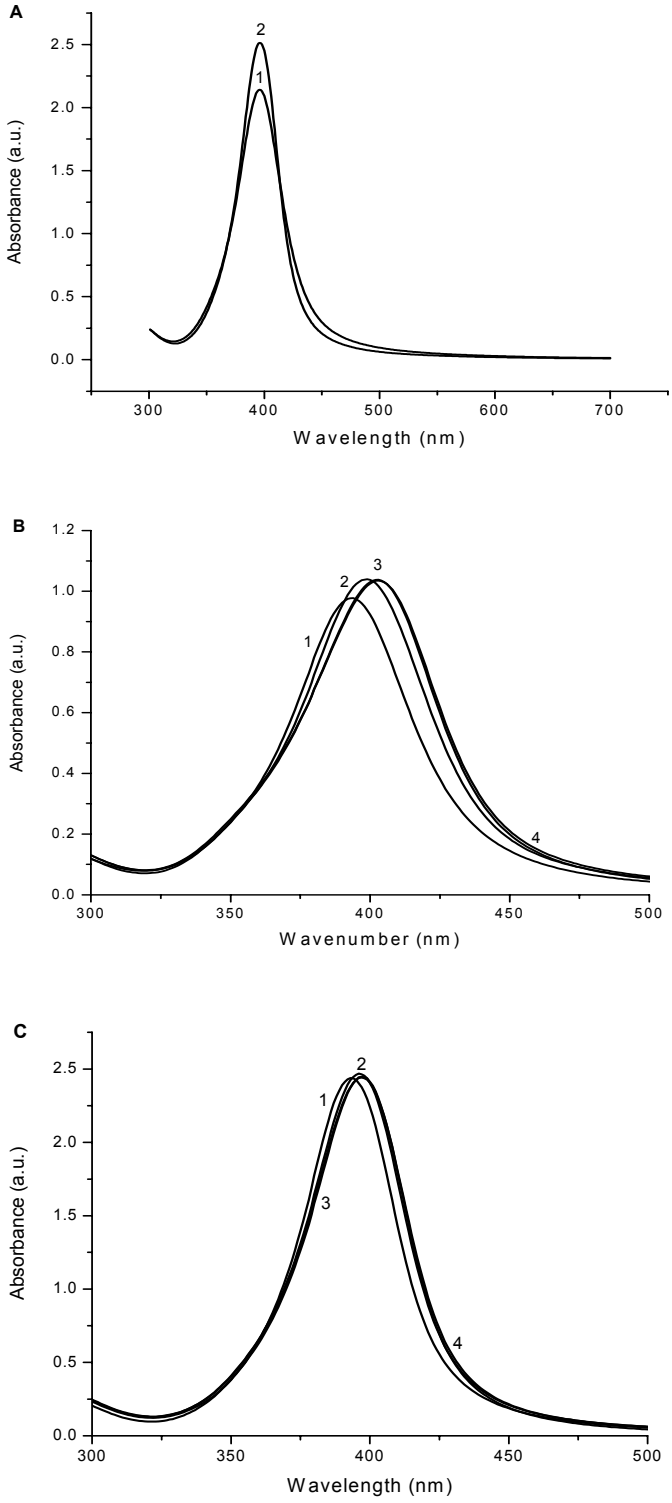

Figure 3.6: Absorption spectra of freshly prepared and heated Ag nanoparticles. (A) fresh (1) and heated (2). (B) Aging of freshly prepared Ag nanoparticles. (C) Aging of the heated Ag nanoparticles. Aging of the fresh and heated nanoparticles were as follows: (1) fresh, (2) one month, (3) two months, and (4) 3 months.

A similar course of action was followed for the prepared borohydride-reduced Au nanoparticles. A comparison of the absorption spectrum for the fresh and heated portion is presented in Figure 3.7 (A). Figure 3.7 (B) and (C) show the absorption spectra over the same three months time period. Table 3.3 summarizes the data retrieved from the optical spectra of the fresh colloids and that from the heated colloids. From the data in Table 3.3, one can gather that the Ag nanoparticles, fresh or heated, are more stable than the Au nanoparticles. This is due to the fact that there is less variation in the FWHM for the Ag when compared to the Au. In comparing the fresh and heated silver in Figure 3.6 (A), it can be seen that the surface plasmon band (λ_{max}) did not change and that the FWHM, which is 40 nm for (1) and 38 nm for (2), did not change neither. The same trend was observed for Au.

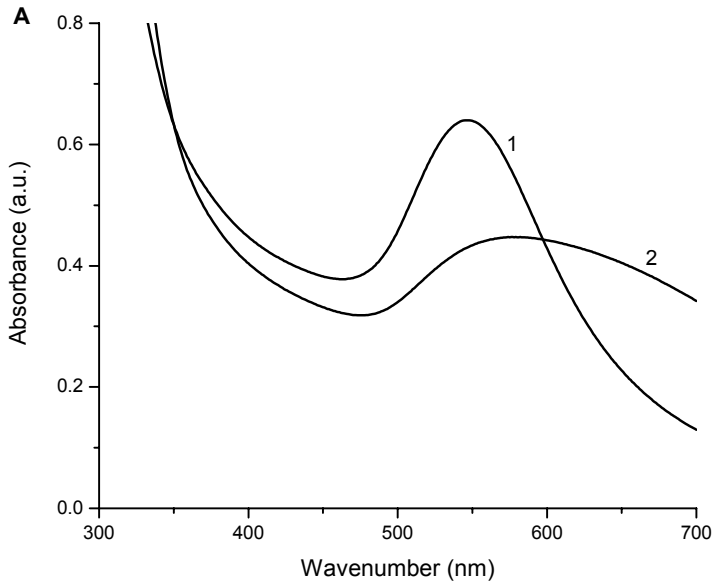

Figure 3.7: (A) Absorption spectra of (1) freshly prepared and (2) heated Au nanoparticles.

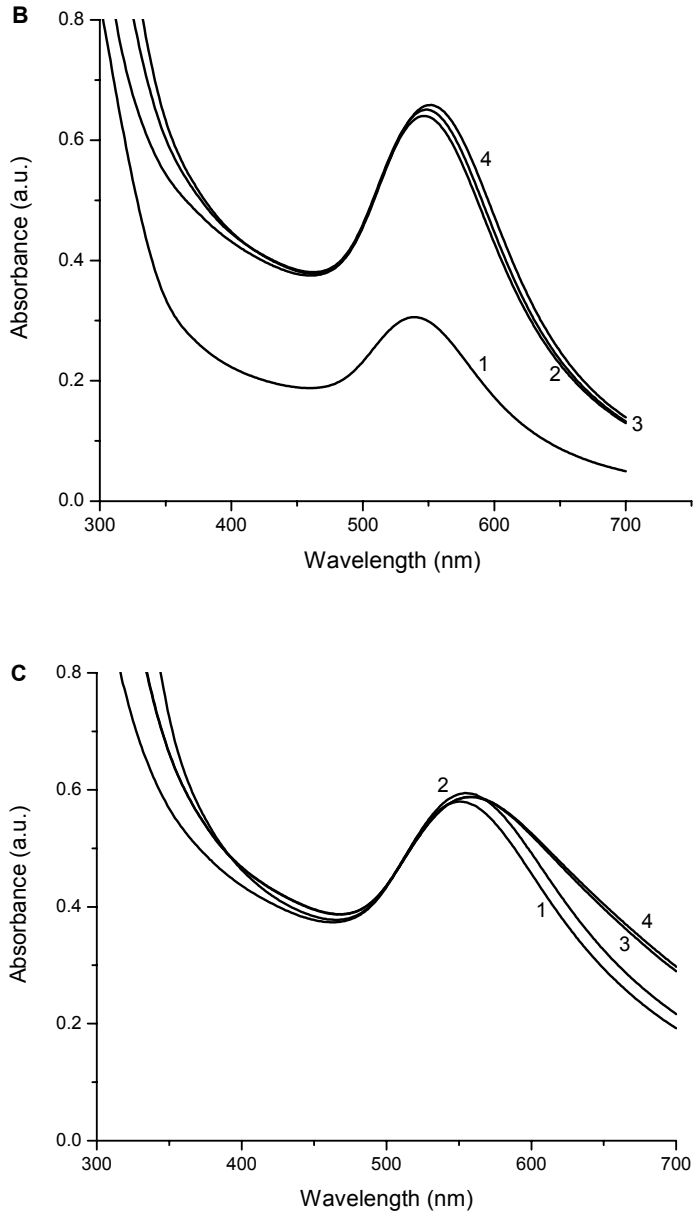

Figure 3.7: Absorption spectra as a function of time for (B) freshly prepared and (C) heated Au nanoparticles. Aging of the freshly prepared and heated nanoparticles were as follows: (1) fresh, (2) one month, (3) two months, and (4) 3 months.

Table 3.3: Summary of the data from the UV-Visible spectra obtained from the fresh and heated Ag and Au nanoparticles portions.

Nanoparticle type	λ_{max} (nm)	FWHM (nm)	Abs. (a.u.)
Fresh Ag 1	394	43	0.73
Fresh Ag 2	399	44	0.80
Fresh Ag 3	403	45	0.78
Fresh Ag 4	403	46	0.78
Heated Ag 1	393	35	2.06
Heated Ag 2	397	38	2.13
Heated Ag 3	397	37	2.03
Heated Ag 4	396	36	2.07
Fresh Au 1	542	66	0.11
Fresh Au 2	548	68	0.22
Fresh Au 3	550	76	0.25
Fresh Au 4	553	80	0.28
Heated Au 1	553	76	0.17
Heated Au 2	558	75	0.16
Heated Au 3	561	89	0.17
Heated Au 4	562	83	0.14

For the Au nanoparticles, heating caused coagulation or particle aggregation, i.e., clustering of particles. This particle aggregation is different from the molecular aggregation, which is J-aggregation that has been introduced before. Hence, for clarity and steering clear of unnecessary confusion, nanoparticle aggregation will be referred to as coagulation and aggregation will only be use to indicate molecular aggregation. The heated Au coagulation is evident in that the FWHM is 109 nm as compared to 67 nm for the freshly prepared Au. Also, the heated Au has greater size (λ_{max} = 582 nm) than the freshly prepared ((λ_{max} = 546 nm) Au nanoparticle. The natural consequence of heating is to cause the colloids to coagulate; however, only slight heating was applied for a short period of time. The heating effect was that it enhanced the stability of both Ag and Au nanoparticles as can be seen from the reduced variation of the FWHM for the heated portion when compared to the fresh portion. This effect, as suggested by the data, is more pronounce for the Au nanoparticles. As for the observed increase in absorbance upon

heating, it is rationalized by noting that the nanoparticle concentration is greater upon heating. The high baseline for the Au nanoparticles, shown in Figure 3.7, is due to the inherent turbidity in the Au system.

Sedimentation was used to test the stability of the nanoparticles prepared. Sedimentation provides a simple and inexpensive method that can effectively sort out coagulated and uncoagulated colloids, i.e., separating particle sizes that are increase by coagulation of smaller uncoagulated colloids. For the sedimentation study, a centrifuge or graduated cylinder was used to either centrifuge the prepared colloids or let the colloid stand for over a month in an aluminum foil wrapped cylinder. The prepared nanoparticles showed no sedimented fractions and hence little to no coagulation. Visible or quantifiable amount of precipitate would have been taken as evidence of sedimentation that is due to coagulation. There was not any precipitate from the prepared colloids both after 30 min centrifuge and upon letting the colloidal solutions stand in the graduated cylinder for over a month. The lack of precipitate is taken as evidence of colloidal stability. Moreover, as the centrifugate is decanted from the centrifuge tube and from any amount of precipitate that might have garnered, that centrifugate is expected to be uncoagulated and more size uniformed.

3.6 Confirmation of Particle Size and Morphology

Confirmation of the particle sizes and shapes of some of the in-house synthesized Ag and Au colloids was made using AFM analysis. Figure 3.8 shows AFM images for four (A-D) of the prepared Ag colloids. The images reveal that the colloids are almost all spherical, except for in Figure 3.8 (D) and of nearly homogeneous sizes. Also, that the polydispersity is to a low degree because there appears to be no visible binding of

particles of a particular size. Figure 3.8 (D) shows the AFM image for the Ag precipitate obtained from the polyol synthesis that was re-dispersed in MeOH. Large particle coagulation, evidenced by the large number of particles in close proximity to one another in Figure 3.8 (D) is believed to be due to drying effect, which may also exists for A to C, but is possibly accelerated in the MeOH system as compared to the aqueous solution used for A to C. The increase tendency of large particle to coagulate[28] can be argued as the reason for the coagulation seen in Figure 3.8 (D). The re-dispersed Ag colloid contains bigger size nanoparticles and therefore a greater fraction of the bigger particles is anticipated to be found in clusters. The difference in surface density for the different substrates seen in Figure 3.8 is due to unequal amount of drops used in preparing the substrates. Figure 3.9 shows the AFM image of the native Ag colloid and the corresponding line scan. From the line scan, the height is measured to range from 11 to 21 nm.

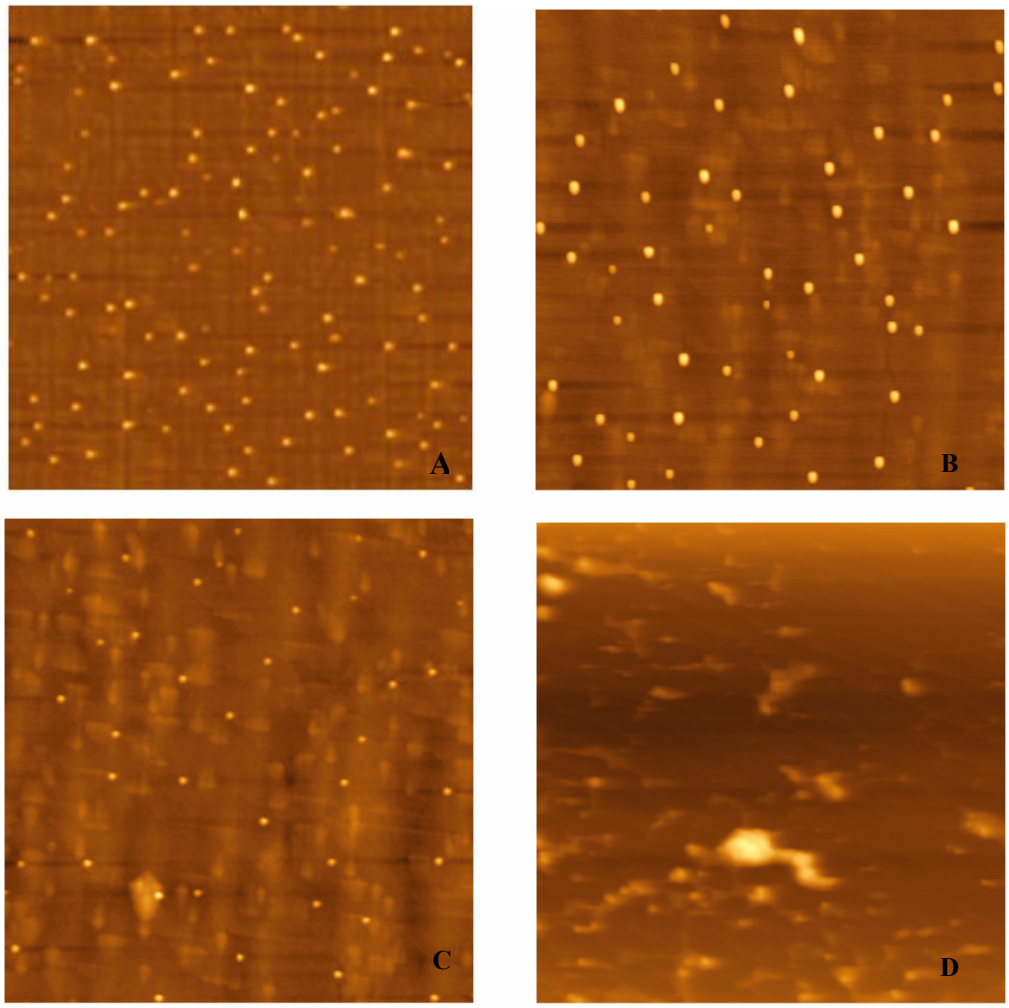

Figure 3.8: 5 μm × 5 μm AFM images acquired in ambient, contact mode condition of four silver nanoparticles (A-D) prepared in-house: A, native Ag nanoparticles; B, CTAB-stabilized Ag nanoparticles; C, PVP-stabilized Ag nanoparticles; and D, Ag nanoparticles re-dispersed in MeOH. To prepare these substrates, 10-20 drops of colloidal solution was spin-casted onto polylysine-coated glass slides. Z scale is 50 nm and 100 nm for A to C and D, respectively.

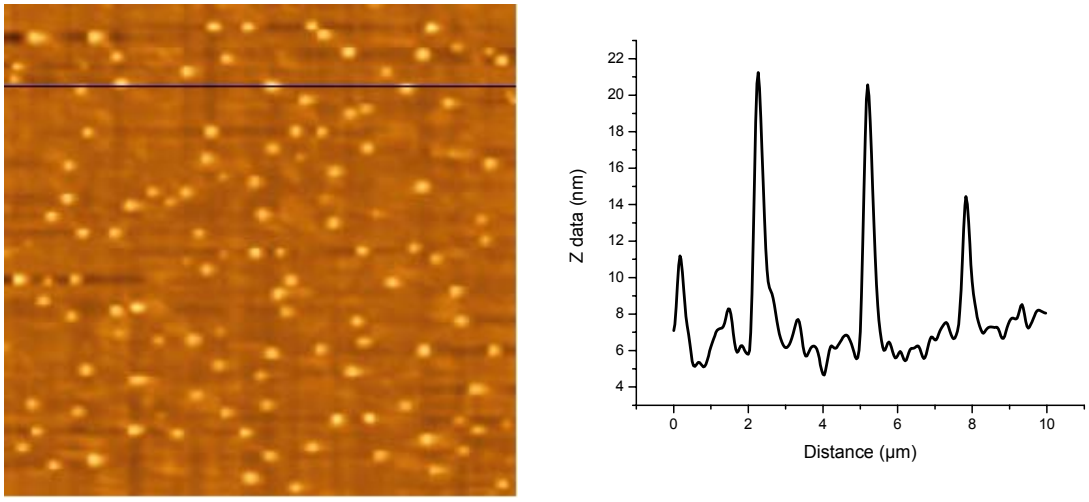

Figure 3.9: 5 μm × 5 μm AFM images acquired under ambient, contact mode condition and line scan of the native Ag nanoparticles. Z scale is 50 nm.

Figure 3.10 shows the 3D AFM images for the borohydride-reduced Au nanoparticles and the MPA-stabilized Au nanoparticles. The Au nanoparticles are spherical in shape having sizes of about 30-55 nm in the borohydride-reduced system and about 12-20 nm for the MPA-stabilized Au. Following the citrate reduce Ag, the borohydride-reduced Au had the highest degree of polydispersity among all the nanoparticle preparations. There is, however, no evidence of coagulation in both systems when centrifuged and upon standing over time in a graduated cylinder. The lower density in the MPA-stabilized nanoparticles in the bottom of Figure 3.10 is due to the lower amount of solution (3 drops) that was spin coated onto the substrates. As regards to the apparent roughness of that particular surface, the roughness was slightly higher than the other surfaces and that is probably due to over-cleaning, which resulted in more than usual etching for that particular glass slide. In the other AFM images, the need for very low clustering and narrow size variation was accomplished for most of the surface preparations.

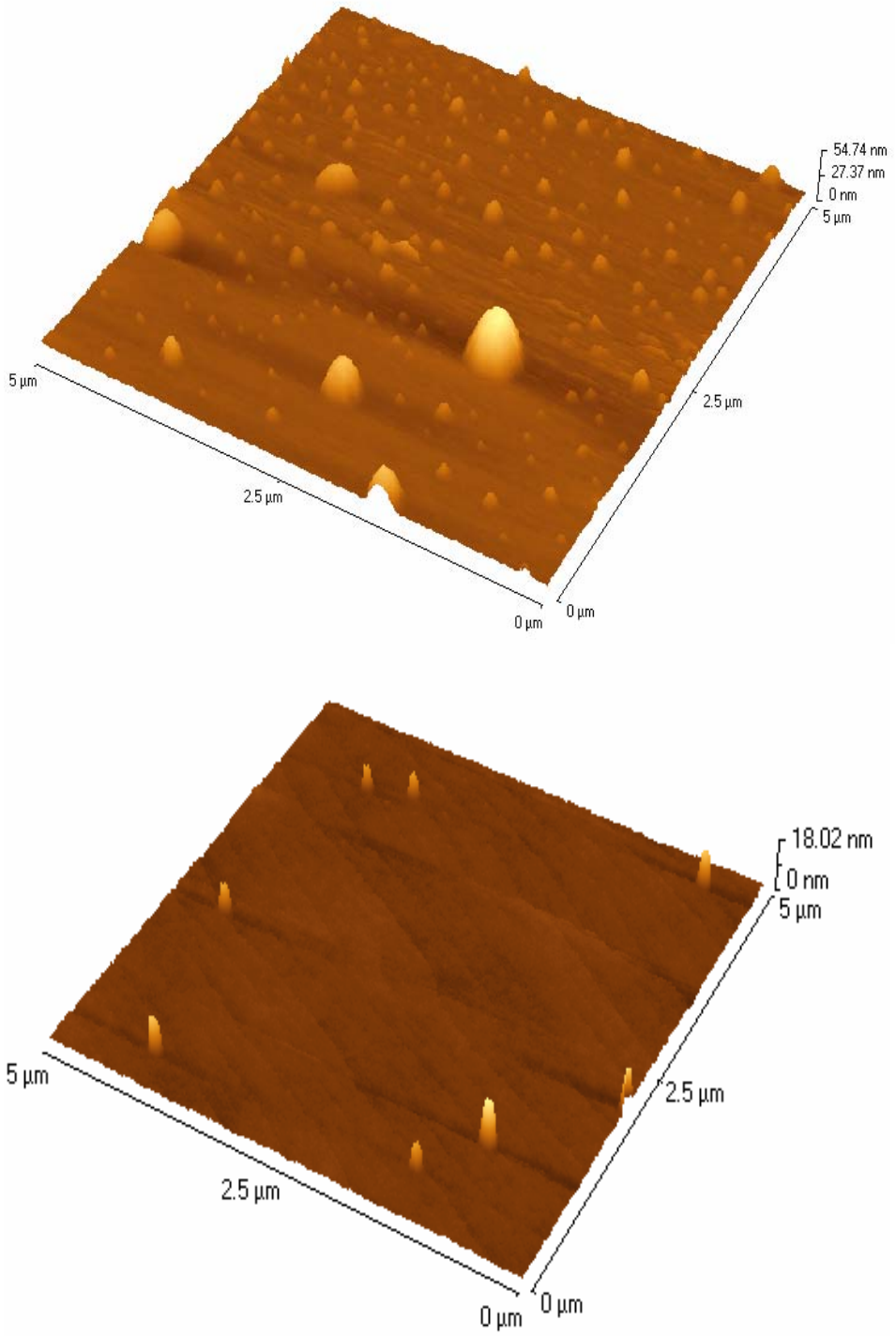

Figure 3.10: 5 µm × 5 µm 3D AFM images acquired under ambient, contact mode condition for the two in-house prepared gold nanoparticles: top, borohydride-reduced Ag nanoparticles; bottom, MPA-stabilized Au nanoparticles.

For the purchased nanoparticles, information about the mean diameter and coefficient of variation was provided, but they did not provide any morphological data. Thus, AFM analysis was performed on their samples prior to using the samples. Figure 3.11 shows the AFM image and accompanied line scan for the 5 nm Au nanoparticles.

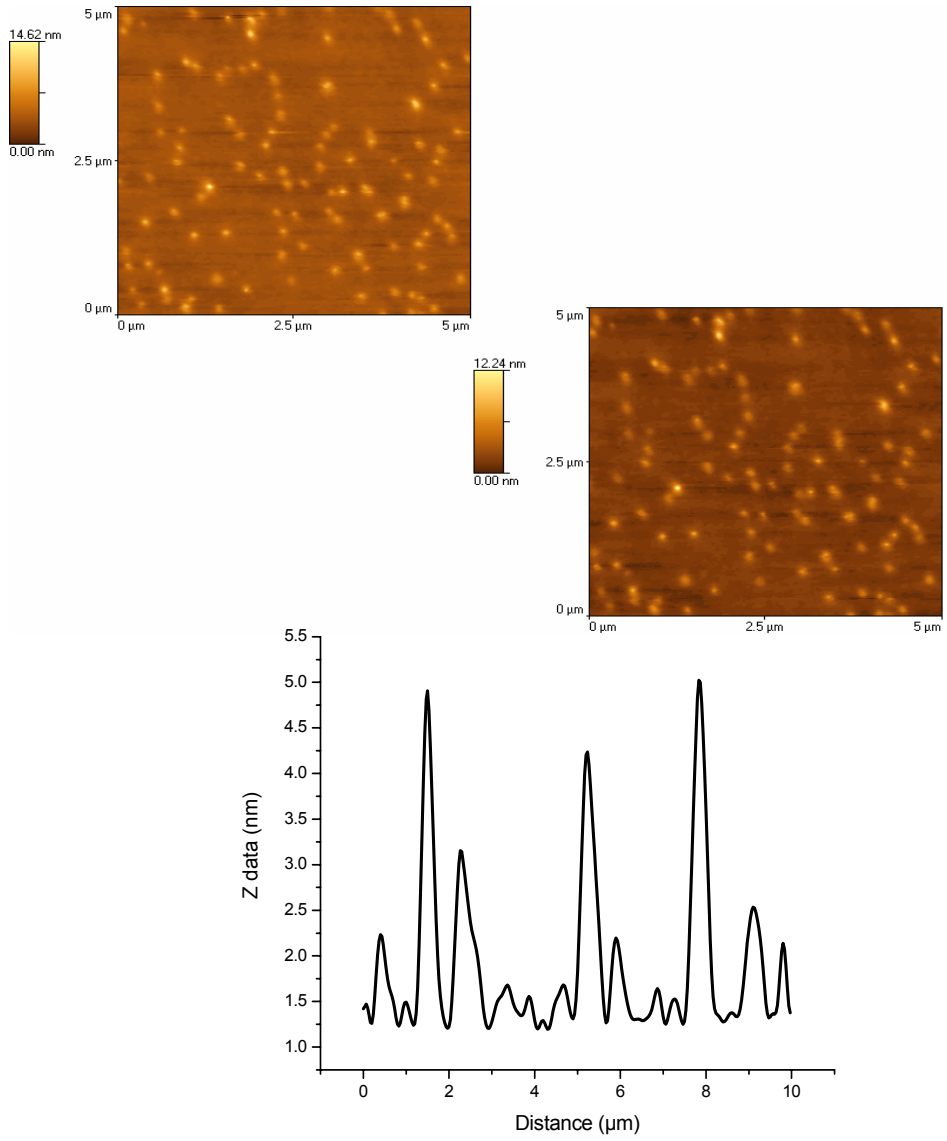

Figure 3.11: 5 µm × 5 µm AFM images acquired in ambient, contact mode condition of 5 nm BBInternational purchased gold nanoparticles and the accompanied line scan: top, forward scan; bottom, reverse scan. Z scale is 12 nm.

The AFM images in Figure 3.11 show the forward scan and the simultaneous reverse scan that was acquired. Recording the AFM tip scanning in both the forward and reverse directions provides complementary scans that ascertained that the morphology that is being revealed is real. Hence, since the two images reveal the same features, it confirms the images from the scan to be true images and not artifacts. For the purchase Au nanoparticles, BBInternational gave a mean diameter of 5 nm with a coefficient of variation of less than 15%. The AFM measurements confirmed that given diameter and coefficient of variation. The BBInternational nanoparticles were also used as a height standard for the ThermoMicroscope AFM apparatus used.

3.7 Characterization of the Immobilized Ag and Au nanoparticles

To immobilize the Ag and Au nanoparticles, the assembly strategy first reported by Natan et al.[18(b)] as a new approach to prepare surface enhance Raman spectroscopy (SERS) substrates that involves assembly of colloidal Ag and Au particles into macroscopic two-dimensional surfaces was adopted. In this approach (scheme 3.2), reactive hydroxyl/oxides groups are generated on a substrate surface. For glass substrates, such functional groups are already present in high concentration. A second step involves surface-initiated polymerization of bifunctional organosilanes such as $(RO)_3Si(CH_2)_3A$. The alkoxysilane forms covalent attachments to the surface via hydrolysis. The pendant functional group A, chosen for its high affinity toward noble metal surfaces, extend out into solution. In the final step, the organosilane-derivatized substrate is immersed into a solution of colloidal Ag or Au particles, where surface assembly spontaneously occurs.

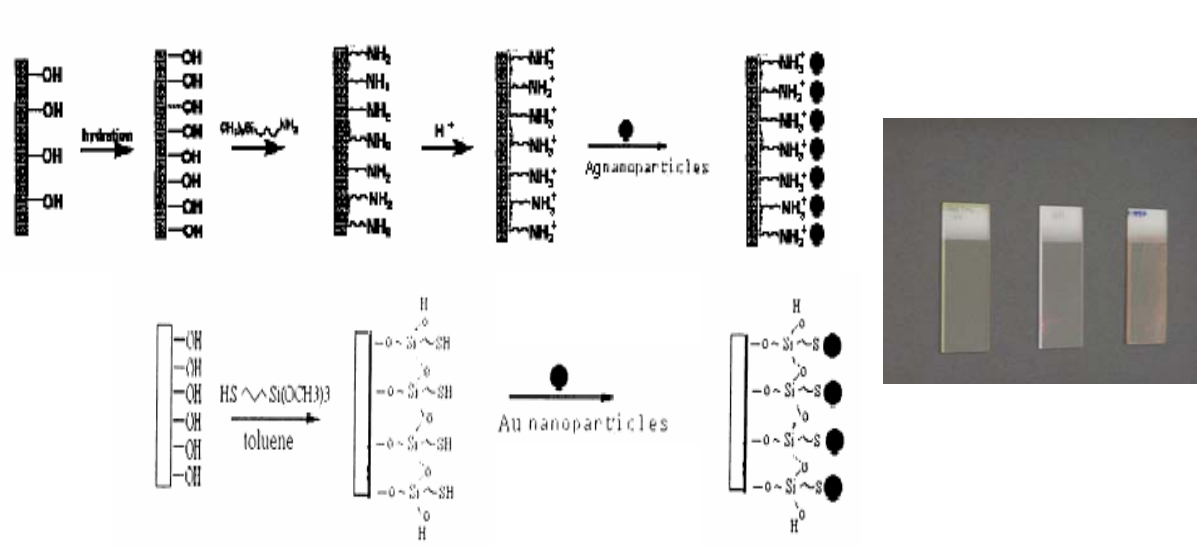

Scheme 3.2. Depiction of the basic strategy for preparation of macroscopic two-dimensional metal film by colloidal assembly and the final assembly on glass slides.

The high-extinction surface plasmon resonance of colloidal Ag and Au and the nature of the self-assembly allowed the opportunity to monitor the particle immobilization on the transparent glass substrates by UV-Visible spectroscopy. The evolution of Ag and Au colloid-based films on glass slides coated with polymerized APTMS and MPS immersed in a solution of colloids for varying lengths of time is shown in Figure 3.12. Binding of Ag to amine groups and Au nanoparticles to thiol groups is indicated by an absorbance feature at about 400 nm for Ag and at about 530 nm for Au, the location for Mie scattering of isolated small Ag and Au particles. As expected, the absorbance increases as the immersion time is increased indicating higher particle coverage on the surface. Increase immersion time also leads to broadening of the absorbance band (due to overlapping of the plasmon band) as established from the FWHM data.

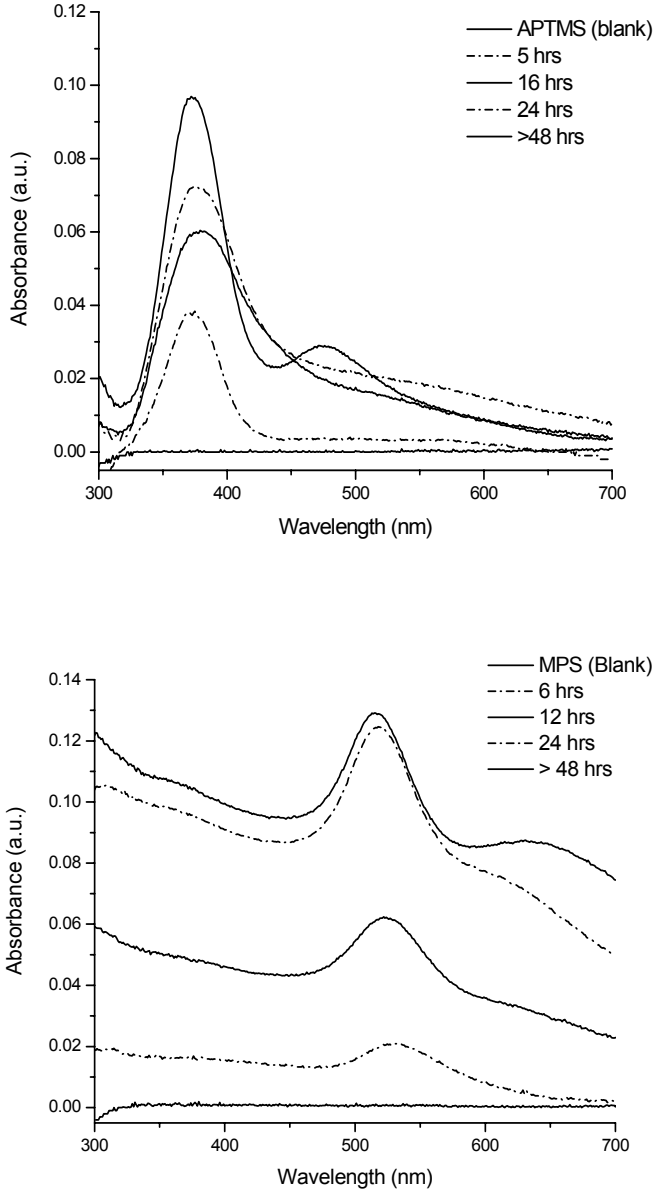

Figure 3.12: UV-Visible spectra as a function of time of Ag (top) and Au (bottom) nanoparticles immobilized onto organosilane functionalized glass slides.

As the particle coverage increases, interparticle spacing becomes small compared to the incident wavelength, and a new low energy feature corresponding to a collective particle surface plasmon oscillation grows at 477 nm for Ag and at 642 nm for Au. This

new red-shifted feature occurs when the interparticle repulsive forces are sufficiently screened causing irreversible particle clustering. The intensity and λ_{max} of this feature is scaled with the extent of clustering; with large chains exhibiting increased extinction and red-shifted peaks. This "cluster" band is also responsible for the enhanced SERS activity of collections of metal colloidal particles.[1(e)]

The rate and extent of surface formation can be altered using one of four factors. These four factors are immersion time, the choice of organosilane, the colloid concentration, and the presence or absence of an adsorbate, for example, stabilizing agent on the colloidal particle. The rate of surface formation is the same for the thiol and the amino pendant group. Control of the particle density, for example will in turn dictate the optical properties of the nanoscale surface.

The kinetic behavior of the adsorption of colloidal particles to a surface modified with organosilanes containing either thiol or amino-terminated groups for self assembling Ag and Au nanoparticles was reported by Natan and Park et al.[29] Natan showed that the surface coverage is roughly proportional to the square root of immersion time within 45 min, and that colloidal particle coverage is limited by repulsive interparticle interaction inhibiting additional particle immobilization on the Au particle. Natan observed that the absorbance of the colloidal metal films constructed by longer immersion was not significantly changed even for periods of 6 weeks. Park, on the other hand, observed an apparent plateau of the increase in absorbance at longer reaction time and this was consistently observed from immobilization reactions of Au colloids of various particle sizes. To elucidate the rate constant of the surface immobilization reaction of the colloidal particle, he used the well known Michaelis-Menten model to describe the

relationship of maximal absorbance at the absorption peak to immersion time. Park found that k_3/k_1 value were proportional to particle size, which implies that the rate of formation of the first monolayer of relatively small nanoparticles is faster than any multilayer formation. Contrary to smaller particles, for large colloid particles Park found that the rate of formation of the first layer is slower than the rate of the multilayer formation, suggesting large colloid particles aggregate more effectively.

AFM analysis was used principally to gain evidence concerning the morphology, particle coverage and interparticle spacing. Figure 3.13 shows representative AFM images acquired in ambient, contact mode condition for silver (top) and gold (bottom) nanoparticles immobilized onto organosilane functionalized glass slides. Two time periods for both the Ag and Au nanoparticles was examined. For Ag, the top left image is for 6 h and the right image is for 24 h. For Au, the bottom left image is for 5 h and the right one is for 24 h. Figure 3.14 shows the AFM image for Ag nanoparticles immerse for more than 48 h. In all the AFM images, it is evident that as the immersion time is increased the particle coverage is increased. There appears to be clustering at higher immersion time. For the Ag film observed for over 48 h, a condensed surface evolves, clearly demonstrating the increase coverage and lesser particle inter-spacing that resulted from increase immersion time. For the immobilized Ag and Au nanoparticles, it was not investigated whether or not it was a monolayer or multilayer on the surface. However, due to the intense rinsing post the immobilization, it is assumed that only the chemisorbed nanoparticles stayed on the surface and all the physisorbed nanoparticles was washed away. Thus, yielding a 2D surface that is assumed to be a monolayer or sub-monolayer in nature. Further examination of the AFM images verifies that the particles

are closely spaced and that there is no abundant clustering. In addition, the particle coverage is observed to be somewhat uniformed over the macroscopic area and the roughness, defined solely by the particle height, uniformed as well. The fractal clusters or strings observed are associated with particle coagulations.

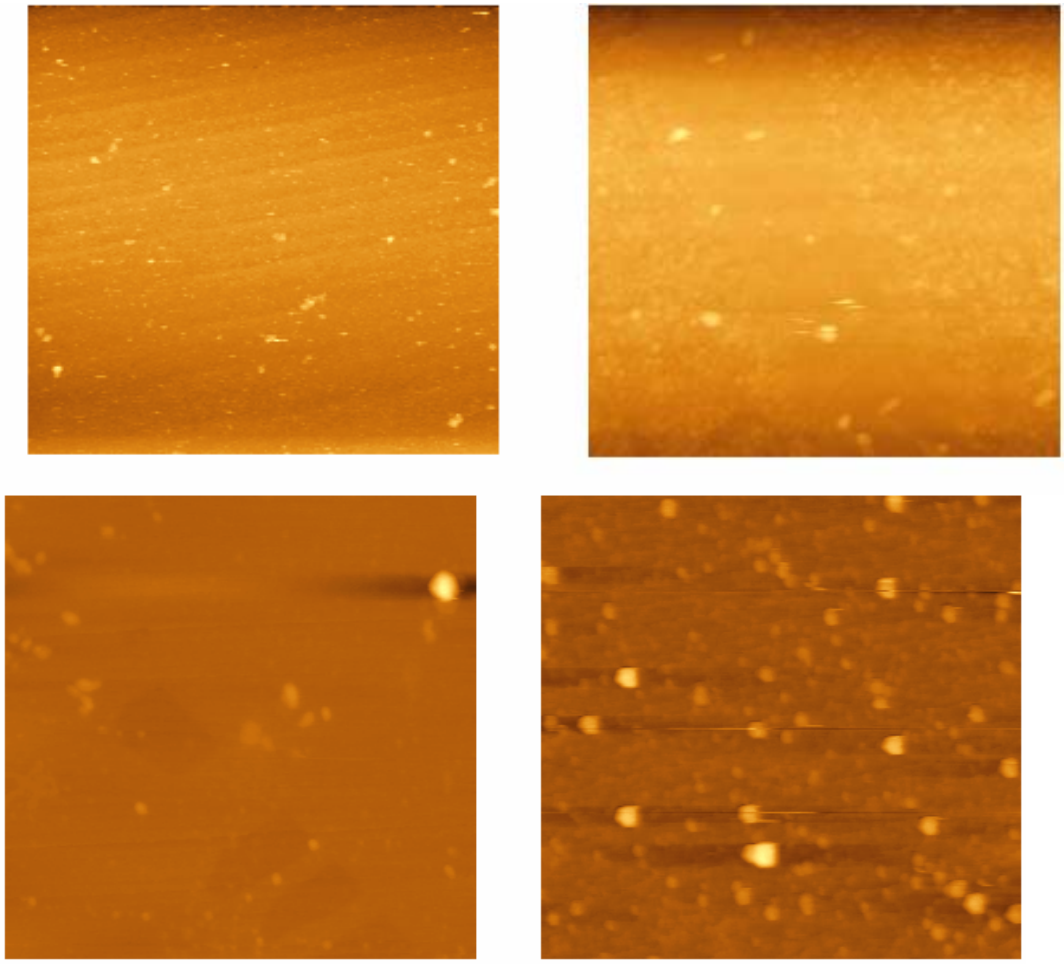

Figure 3.13: 5 μm × 5 μm representative AFM images acquired in ambient, contact mode condition of silver (top) and gold (bottom) nanoparticles immobilized onto organosilane functionalized glass slides. Top-left, 6 h; right, 24 h. Bottom-left, 5 h, right, 24 h. Z scale is 50 nm

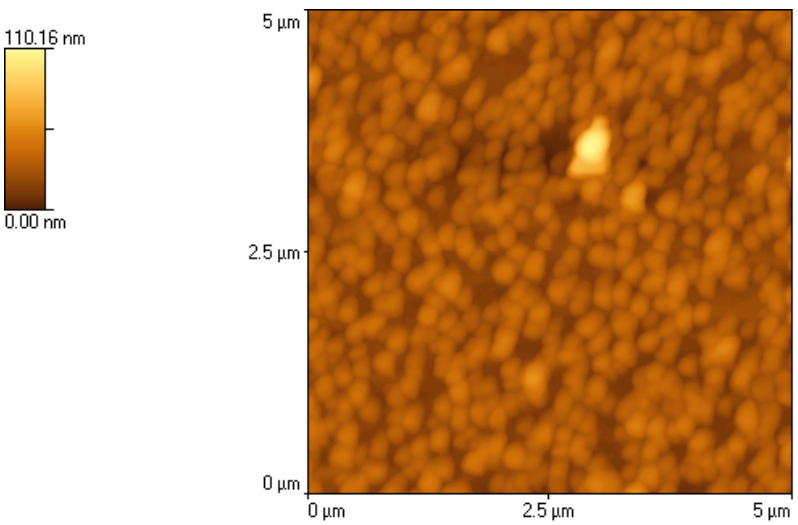

Figure 3.14: 5 µm × 5 µm AFM images acquired in ambient, contact mode condition for colloidal Ag particles immobilized onto organosilane functionalized glass slides for over 48 h. Z scale is 110 nm.

3.8 Conclusion

It has been demonstrated that well monodispersed Ag and Au colloids could be prepared using different techniques. The procedures are reproducible and the dispersions obtained are stable. Surfactants were used in some of the preparations but did not clearly improve the stability when compared to the native colloids. It is found that when the borohydride-reduced Ag and Au colloidal nanoparticles are slightly heated, it improved the stability of the nanoparticles. Ag and Au colloidal metal films were prepared by self-assembly onto organosilane-coated glass substrates. The assembly method consists of essentially immersing a glass substrate into three different solutions, the first for surface hydroxyl group formation, the second for organosilane polymer formation, and the third for colloid immobilization. The nanoparticles are strongly bound to the surface through the covalent bonds formed to the polymer functional groups, which are NH_2 and SH. UV-Visible spectroscopy is used to assess the particle coverage and spacing on the

optically transparent substrates. The solution-based assembly strategy makes substrate fabrication routine. Particle size, particle-polymer interactions, and the physical and chemical properties of the substrates can be manipulated to control the nanoscale structure produced.

4 J-Aggregation of Cyanine Dyes Anchored to Nanoparticles Dispersed in Solution and Immobilized on Surfaces

4.1 Introduction

Construction of ordered molecular assembly is a current topic from a wide range of scientific and practical viewpoints.[1] Principally, fabrication of well-organized molecular assemblies on solid surfaces, especially metal nanoparticles, is an interest shared by many research groups in different disciplines. Accordingly, the preparation of heterostructured hybrid materials consisting of noble metal nanoparticles and organic cyanine dyes constituents have been a primary goal of this dissertation and thus it is the subject of this chapter. The J-aggregate of cyanine dyes is one unique form of such organized molecular assemblies, characterized by an unusually sharp visible absorption and resonance fluorescence band (J-band) that are markedly red-shifted from the monomer band, a result of exciton delocalization over the molecular building blocks of the aggregates.[2] The sharp and well defined absorption bands of J-aggregates have been most successfully utilized for spectral sensitization in silver halide photoimaging systems.[3] There have also been much interest in the excitation energy transfer and the radiative decay kinetics in J-aggregates,[4] along with the related nonlinear optical properties that are potentially useful for optoelectronic molecular devices.[5,6]

J-aggregation of cyanine dyes, in practice and in a broad sense, can be observed in many different environments such as concentrated aqueous solutions,[7] polymer[8] and sol-gel matrices,[9] liposomal membranes,[10] Langmuir-Blodget (L-B) films,[11] colloidal solution,[12] crystalline states[13] and even trivial dye deposits on an arbitrary substrate. It is only in very limited conditions, however, that one can achieve complete and selective J-

aggregation that is free from any other forms of aggregates and residual monomers. A two dimensional (2D) controlled layered assembly, i.e., J-aggregates, supported either as a single monolayer or as a stacked multilayer on a nanoparticle substrate is potentially preferential to allow such complete and selective aggregation.

It is anticipated that dye-coated noble-metal nanoparticles will modulate and improve the composites optical properties due to the electromagnetic interaction between metal core and dye shell, particularly in the case of the absorption frequency of a dye molecule lying close to the surface plasmon of the metal particle.[14] In general, multicomponent nanostructured assemblies, consisting of metals and photoactive dyes, have numerous possible applications in developing efficient light energy conversion systems, optical devices, and sensors.[15]

In particular, immobilization of dye molecules onto noble-metal nanoparticles ─ an increasingly important class of nanonostructures ─ has captured recent interest in exploiting their optical properties for chemical and biological applications, including fluorescence quenching of small dye molecules on gold nanoparticles,[15,16] complementary oligonucleotides for single stranded DNA linked metal nanoparticles,[17] and dye-doped nanoparticles for medical diagnostics and labeling.[18] In addition, dye-capped metal nanoparticles have also garnered interest in various basic research areas, for example, water soluble monolayer-protected clusters (MPCs),[19,20] which are functionalized with tiopronin for fluorescence quenching of fluorescein and molecular interactions involving electron or energy transfer for fluorescence quenching as a result of the proximity of the dye molecules to the metal nanoparticle surface.[21]

Even when the formation of J-aggregates is well known for cyanine dyes, vide

supra, a number of other dyes,[22] and many promising applications of dye-nanoparticle combination arise. The detail understanding of the nanoparticle role, interparticle interactions, reactivities, and how such interactions are operative in the adsorption and assembly is somewhat limited. In recent studies,[23] cyanine dyes affixed onto nanoparticles of synthetic clay or silica have been shown to form J-aggregated assemblies in water, exhibiting absorption characteristics corresponding to small J-aggregate domains and fluorescence superquenching characteristics. Photoexitation of the surface plasmon in Ag nanoparticles coated with J-aggregates of a cyanine derivative was shown to lead to exciton dynamics different from J-aggregates monolayers on bulk metal surfaces due to a coherent coupling between the exciton of a J-aggregate and the electronic polarization of metal nanoparticles. The coherent coupling to the conduction band electrons leads to constructive interference and a long-lived exciton for Ag nanoparticles, whereas it interferes destructively with bound electron transition dipoles for Au nanoparticles.[24] The study of the absorption and emission spectral characteristics of the fluorescent dye, eosin, on gold nanoparticles revealed that smaller particles stimulate J-aggregation of eosin on the surface of metal particles, whereas larger particles could not induce any kind of aggregation.[25] On the other hand, the study of gold nanoparticles capped with fluorescein isothiocyanate[26] showed that the chemisorbed dyes do not induce any aggregation. Thus, there is further need to understand the interparticle interactions and reactivities by probing the changes in optical properties involving both dyes and nanoparticles.

In this chapter, results on investigations involving J-aggregation of cyanine dyes dispersed in Ag and Au nanoparticle solutions and immobilized onto glass substrates are

reported. The J-aggregates anchored onto these nanoparticles were characterized by UV-Visible, fluorescence, dynamic light scattering (DLS), atomic force microscopy (AFM) and near field scanning optical microscopy (NSOM).

The resulting cyanine dye-nanoparticle composite can potentially serve as model systems for the exploration of the aforementioned interaction and reactivities. Such a system then involves a combination of electrostatic and π-π interactions for the utilized cyanine dyes which are studied by probing the unique optical properties of J-aggregates from the dyes and the surface plasmon resonance from the nanoparticles. Measurements of the optical absorption and fluorescence properties of this dye-nanoparticle complex have provided a fundamental understanding of the role of the nanoparticles, the interparticle molecular interaction and reactivities, which will be of useful guidance for practical applications, for instance regarding dye-structured nanoprobes. Moreover, understanding the various intermolecular interactions such as π-π interactions in J-aggregates, in addition to electrostatic and hydrophobic interactions, will be important for controlling different functional nanostructures where J-aggregates are components.

4.2 Experimental

4.2.1 Materials

All cyanine dyes were purchased from the indicated suppliers and used as received. Iodide salts of 1,1'-diethyl-2,2'-cyanine (PIC) and 1,1'- 3,3'-tetraethyl-5,5',6,6'-tetrachlorobenzimidazolocarbocyanine (TTBC) were purchased from Nippon Kanko Shikiso Co., Japan, and Accurate Chemical and Scientific Company (Westbury New York), respectively. Sodium salt of 1,1'-diethyl-3,3'-bis(4-sulfobutyl)-5,5',6,6'-tetrachlorobenzimidazolocarbocyanine (TDBC) was obtained from Few Chemicals,

Germany. Lastly, chloride salt of 3,3'-diethyl-5,5-dichloro-9-benzothiacarbocyanine (DDPT) was purchased from the Japanese Research Institute for Photosensitizing dyes, Ltd.., Okamaya, Japan. Spectroscopic grade methanol, NaCl and KOH were obtained from Aldrich and triply distilled water was used when needed. The structure of the four cyanine dyes (1, 2, 3 and 4**)** investigated in this chapter are illustrated in Table 4.1. All the dyes, except for dye 1, were carbocyanine dyes with a trimethine bridge between the two heterocyclic rings, which are benzimidazoles for TTBC and TDBC and benzothiazoles for DDPT. The dyes are all symmetrical cyanines. PIC has two quinoline rings.

4.2.2 Preparation of Dye Coated Nanoparticles.

The methods for preparing different nanoparticles were described in chapter 3. The different nanoparticle solutions were used based on their propensity to promote J-aggregation. However, in the interest of assessing the interaction of the cyanine dyes with the bare nanoparticles, preference was given to the heated native Ag and Au nanoparticles, which were the nanoparticles prepared without stabilizers.

Dye-coated nanoparticles were prepared by adsorbing cyanine dye molecules on the surface of the metal nanoparticles. This was done by mixing a known concentration of the particular cyanine dye with 0.15 mM silver or gold colloidal solution at different volume ratios and then the final volume of all the solutions were made to be 3 mL. A typical ratio used was 0.5 mL dye and 2.5 mL colloidal nanoparticle. The aim was to have far less dye than colloid so that there is no free dye in solution. The mixture was subsequently allowed to stand for a few minutes and subjected to absorption and emission measurements.

For the dye-coated nanoparticles immobilized on glass substrates, the nanoparticle derivatized slides that were prepared in chapter 3, was bathe in a vial of the interested dye monomeric solution, which contained a pinch of KBr or KCl to promote adsorption, for 1 h. Afterwards, the slides were removed from the solution vials and allowed to dry prior to taking their spectra.

Table 4.1: Chemical structure of the four cyanine dyes studied.

Name	Chemical Structures
1. PIC **Cationic**	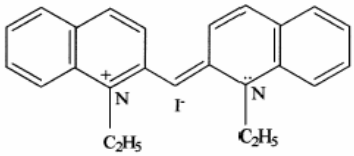 **1,1′-Diethyl-2,2′-cyanine**
2. TTBC **Cationic**	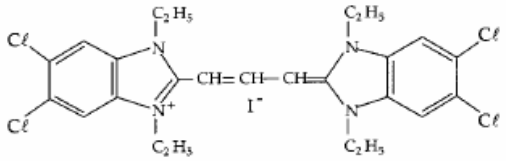 **1,1′,3,3′-tetraethyl-5,5′,6,6′-tetrachlorobenzimidazolocarbocyanine**
3. TDBC **Anionic**	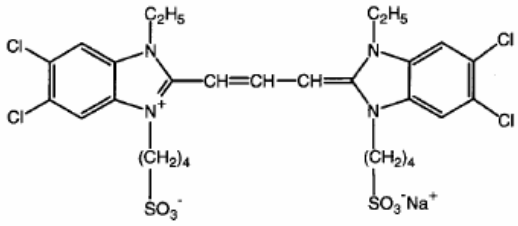 **1,1′-diethyl-3,3′-di(4-sulfobutyl)-5,5′,6,6′-tetrachlorobenzimidazolocarbocyanine**
4. DDPT **Cationic**	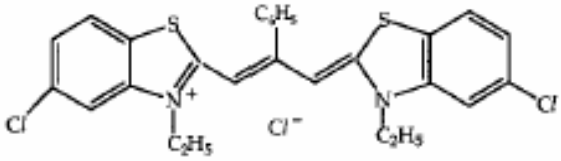 **3,3′-diethyl-5,5′-dichloro-9-benzothiacarbocyanine**

4.3 Steady-state Absorption and Fluorescence Spectroscopic Studies

Figure 4.1 shows the UV-Visible absorption spectra obtained for each of the cyanine dyes dissolved in methanol. The absorption bands of the monomeric solutions

have identical shapes, a result due to the fact that the considered dyes have nearly the same chromophores, which are the polymethine chain and the heterocyclic rings. The absorption spectrum of each cyanine dye exhibits a broad 0 ← 0 vibronic band at 523, 514, 519, and 566 nm for PIC, TTBC, TDBC, and DDPT, respectively, with a weak "shoulder" associated with the 1 ← 0 vibronic transition. The spectral pattern exhibited in Figure 4.1 does not change with increasing the concentration of each dye in methanol up to 10^{-3} M. The concentration of PIC and TDBC was lowered to allow for an absorbance below 1. The full width at half maximum (FWHM) for the monomer band was measured, and are 54 nm, 27 nm, 28 nm and 23 nm for PIC, TTBC, TDBC, and DDPT, respectively.

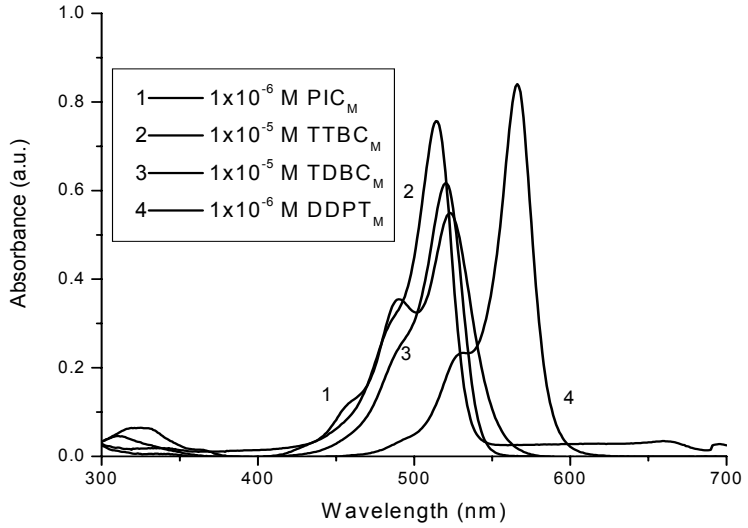

Figure 4.1: Absorption spectra of monomeric cyanine dyes in methanol.

However, upon addition of the monomeric dye solution to a Ag or Au nanoparticle solution, the emergence of an additional absorption band red shifted from the monomeric band appears. This band, termed the J-band, at times, grows at the expense of the monomer absorption band and its position is only weakly dependent on

the concentration. The results and observations for the different cyanine dyes studied in the presence of Ag or Au nanoparticles is presented below along with analysis of the different outcomes resulted from the different dye-nanoparticle systems.

4.3.1 1,1′-diethyl-2,2′-cyanine, iodide salt (PIC)

Figure 4.2 shows the absorption spectra of the solutions of Ag nanoparticle with the characteristic surface plasmon at about 400 nm and the previously discuss monomeric PIC in methanol. Figure 4.2 also shows the absorption spectra of Ag colloidal solutions containing PIC concentrations of 1×10^{-5} M (Figure 4.2- 3) and 5×10^{-5} M (Figure 4.2-4). The formation of the J-band (λ_{max} = 591 nm) using both concentrations is observed to bring about a decrease in the Ag plasmon absorption band. The Ag surface plasmon band FWHM was measured to be about 54 nm prior to adding PIC and did not change much upon adsorption of PIC onto the Ag surface. There is a 1 - 2 nm change observed, however because the instrument resolution is about 2 nm, it is not considered a shift because it is within the instrument margin of error. Another cautionary note is on the FWHM measurements; because of the arbitrary baseline selection, the accuracy of the measurements can not be certain.

Upon increasing the PIC concentration, as shown in Figure 4.2, an increase in the monomer absorption is observed. The increase is proportional to a decrease in the surface plasmon absorption. The J-band did not experience any significant change upon increasing the concentration. Also, it is to be noted that Figure 4.2 (3) and (4) show that there is an increase in the dye-nanoparticle hybrid baseline. This increase is due to the turbidity of the composite solution. Looking at the low energy side of the J-band, it appears to be narrowing as the concentration is increased. This narrowing is indicative of

enhance self-organization of the PIC molecules on the surface of the Ag nanoparticle as more PIC molecules is added.

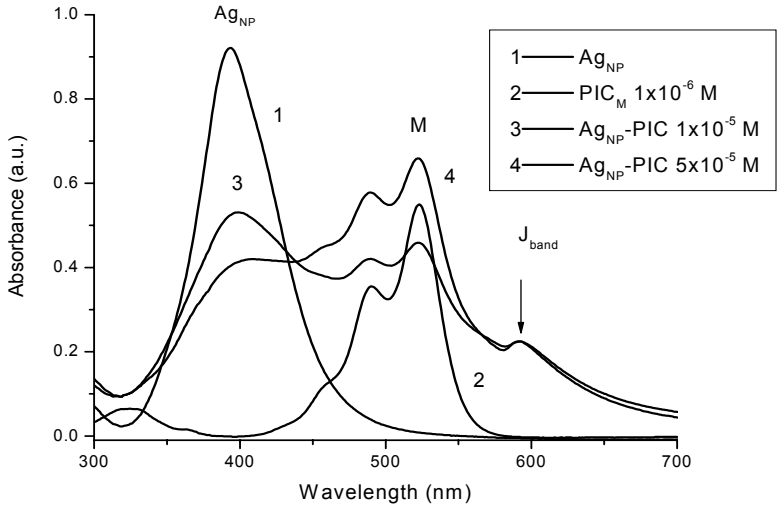

Figure 4.2: (1) Absorption spectra of Ag colloidal solution, (2) monomeric PIC in MeOH, (3) 1×10^{-5} M PIC and (4) 5×10^{-5} M PIC coated Ag nanoparticles.

4.3.2 1,1′,3,3′-tetraethyl-5,5′,6,6′-tetrachlorobenzimidazolocarbocyanine, iodide salt (TTBC)

Figure 4.3 (A) shows the absorption spectra of Ag colloidal solution, the monomeric TTBC in MeOH and TTBC added to the Ag nanoparticles. Figure 4.3 (B) shows the absorption spectra of the MPA- stabilized Au nanoparticles, monomeric TTBC in MeOH and TTBC coated Au nanoparticles. The Au nanoparticle, in this instance, is a surfactant stabilized Au nanoparticles and is different from the native Au nanoparticles (without surfactants) also studied in this dissertation. As shown in scheme 3.1, the MPA-stabilized Au yielded nanoparticles with pendant negative charges on the surface.

Analysis of Figure 4.3 (A) shows the 400 nm Ag nanoparticle surface plasmon band and the J-band formation. Similarly to what is observed for PIC, upon adding TTBC monomeric solution to the nanoparticle solution, the formation of the J-band (λ = 595

nm) for both concentrations used, which accompanied a decrease in the Ag plasmon absorption band was observed. Figure 4.3 (A) shows broadening of the Ag band and an increase in the monomer absorption that is proportional to a decrease in the surface plasmon band upon increasing the concentration. The J-band did not experience any significant change. But, it is interesting to observe an 8 nm blue shift in the monomer absorption, an indication of monomer molecules rearrangement and interaction with the nanoparticle, which was not observed in the PIC system. Figure 4.3 (B) depicts the TTBC coated MPA-stabilized Au system. The surface plasmon for the Au nanoparticle is observed at 526 nm. The J band in this system was measured at 593 nm. For the monomer band, a similar blue shift of 11 nm is observed when compared to the monomer band position in methanol. The greater monomer blue shift in Figure 4.3 (B), when compared to Figure 4.3 (A), is indicative of greater interaction between TTBC monomer molecules with the MPA-stabilized Au nanoparticles than with Ag nanoparticles. Also, the amount of J-aggregates form is greater in the Au system. This is possibly due to greater electrostatic interaction in the MPA-stabilized Au system. By using MPA, the surface charge on the Au nanoparticles is expected to be far greater than that on the Ag nanoparticles. It is also worth noting that Au is more electronegative than Ag.

The TTBC coated MPA-stabilized Au system was also interesting in the sense that it precipitated at a greater rate than noticed for the other nanoparticles. The aging effect for about an hour was investigated. Figure 4.4 shows the absorption spectra for time 0 (t_0), for the fresh solution, and after allowing the solution to stand for 20 min (t_{20}). There was no further change in the absorption spectrum up to the hour but completely precipitated out of solution when the absorption spectrum was retaken after 5 h. The J-

band for t_0 was measured at 593 nm and for t_{20} at 594 nm; the 1 nm difference is within the margin of error for the instrument. The FWHM for both time spectra are about 7 nm that is the same for the Ag nanoparticle system. In an effort to assess the lost in the J-aggregate band, the area under the curve for the aging systems was analyzed. The area under the curve decreased by a half for t_{20} pinpointing to the lost of aggregation in the solution via precipitation.

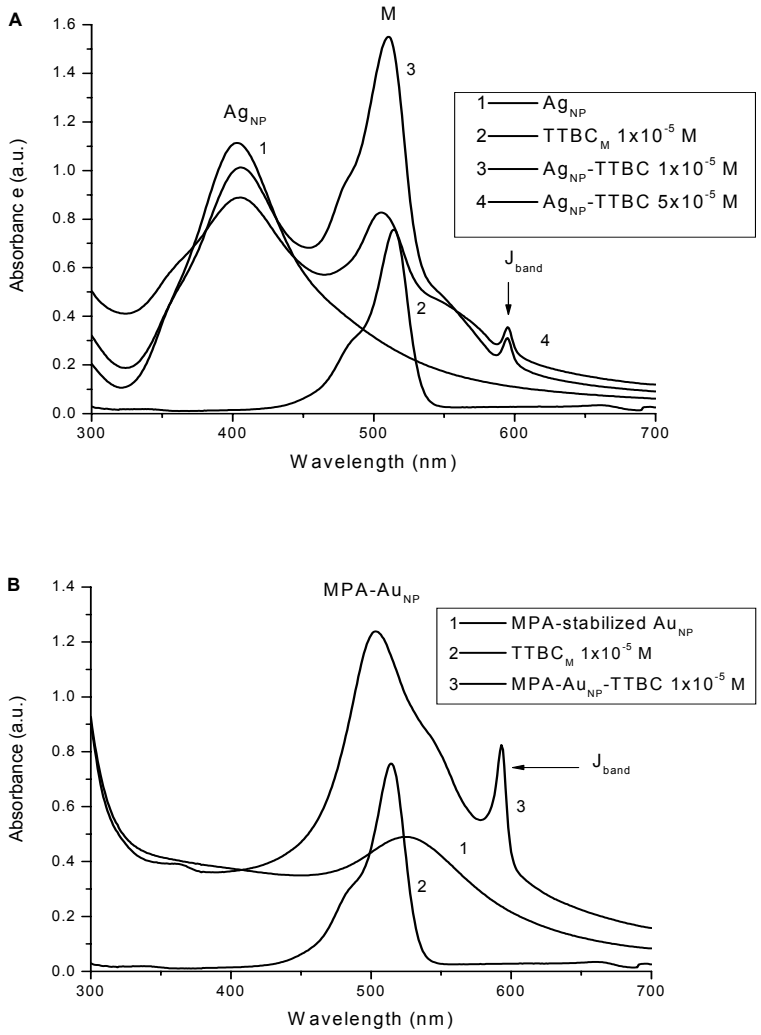

Figure 4.3: (A): (1) Absorption spectra of Ag, (2) monomeric TTBC in MeOH, (3) 1×10^{-5} M TTBC and (4) 5×10^{-5} M TTBC coated Ag nanoparticles. (B): (1) Absorption spectra of MPA stabilized Au, (2) monomeric TTBC in MeOH and (3) 1×10^{-5} M TTBC coated Au nanoparticles.

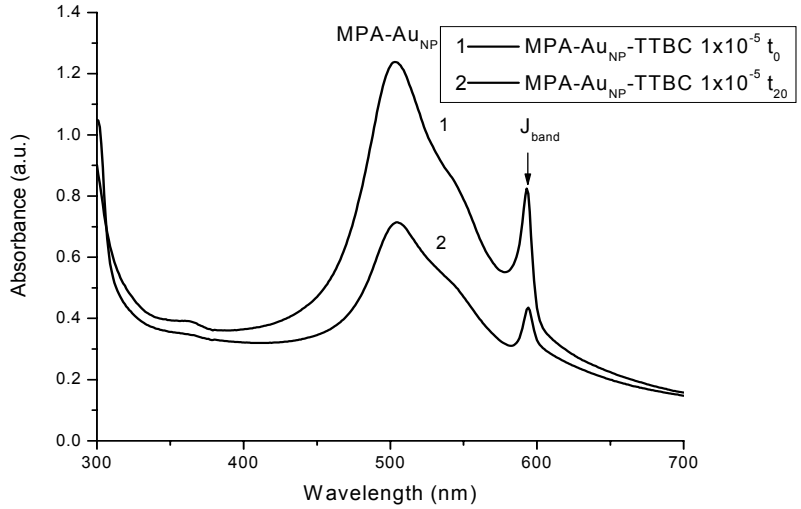

Figure 4.4: Evolution of absorption spectra with time for the TTBC-coated MPA stabilized Au: (1) taken fresh and (2) after 20 min.

It will have been interesting to be able to compare the MPA-Au to the native Au, but TTBC was not able to aggregate in the native Au environment. Both TTBC and PIC were not able to aggregate in the native Au environment due to protonation of the dye molecules in the acidic native Au (pH 3.92). PIC and TTBC have a pKa of about 4 and 7, respectively, and are prone to protonation.[9(b)] The pH of the MPA-stabilized Au was about 7.

Struganova and co workers[27] have reported that inorganic salts and bases complete the transformation of the absorption spectra of very diluted water solutions of TDBC from a monomer shape to a J-aggregate shape. They also reported on the influence of inorganic salts and bases on diluted and concentrated solutions of PIC.[28] So, the influence of NaCl and KOH on TTBC coated Ag nanoparticles was investigated. The Ag nanoparticle employed for the salt and base effect studies was the heated one. The heated Ag nanoparticle solution was found to be very stable when salt and base were added. The

non heated Ag nanoparticles precipitated out of solution upon adding salt and base to the solution.

Figure 4.5 shows the absorption spectra obtained from the salt and base effect study. Figure 4.5 (A) compares TTBC coated Ag with (2) and without (1) NaCl. Figure 4.5 (B) compares TTBC coated Ag with (2) and without (1) KOH. As the TTBC coated Ag nanoparticle is perturbed with either NaCl or KOH, a similar blue shift for the monomer bands (vide supra) and an increase in the J-aggregation formation along with accompanied shifts were observed relative to the system without salt or base. After adding NaCl, an 11 nm blue shift for the monomer band and a 2 nm red shift for the J band were observed. Also, the J-band FWHM went from 6 nm to 8 nm with the added NaCl. Now, when KOH was added a 9 nm blue shift was observed for the monomer band and a rather unusual 4 nm blue shift was observed for the J band; the FWHM for the J-band went from 6 nm to 13 nm with the added KOH. From this result, it is inferred that NaCl is possibly a better aggregation promoter. The 2 nm J-band shift observed with the NaCl is within the margin of error for the UV-Vis instrument.

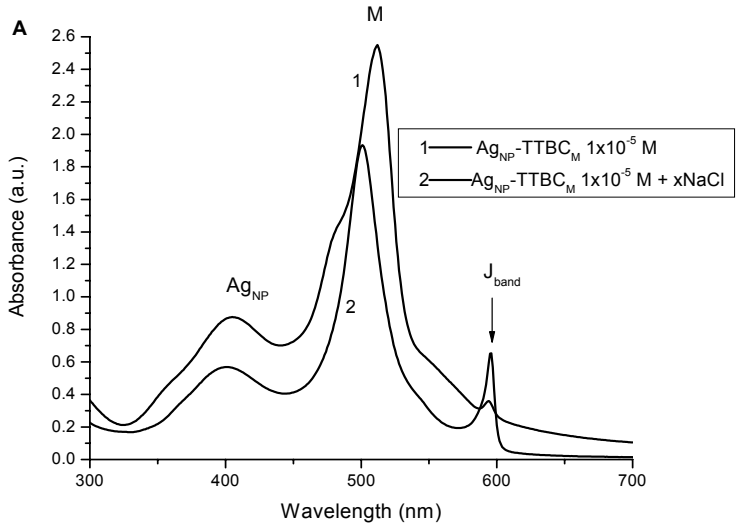

Figure 4.5 (A): (1) Absorption spectra of TTBC coated Ag and (2) TTBC coated Ag containing 10 μL (x) 1 mM NaCl.

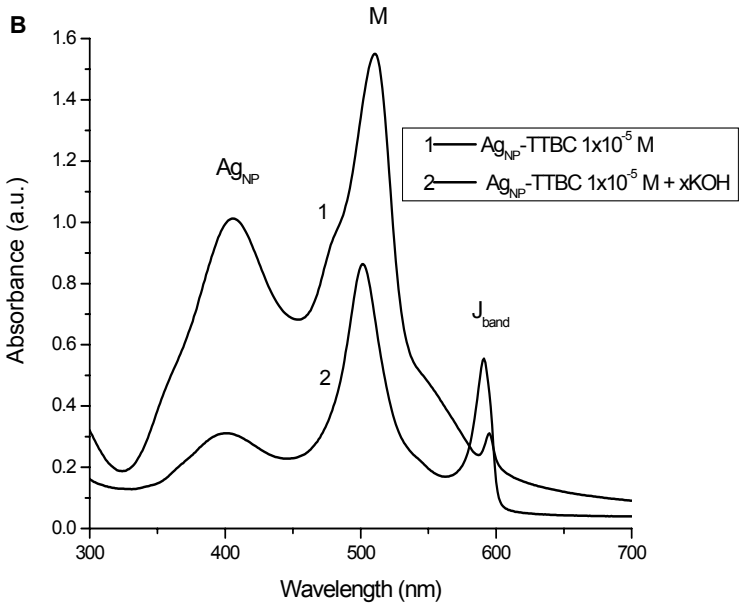

Figure 4.5 (B): (1) Absorption spectra of TTBC coated Ag and (2) TTBC coated Ag containing 4 drops (x) 1 mM KOH. The pH of the solution was 11.1.

In order to probe the increase in J-aggregation with added NaCl and KOH, the monomer to aggregate absorbance ratio (M/A), before and after salt and base addition, was analyzed. For NaCl, M/A = 6.89 before and 3.03 after, and for KOH, M/A = 5.13 before and 1.59 after. In both cases, an increase in J-aggregation upon adding salt or base is observed. However, adding KOH offered more aggregation than NaCl, but possibly a less stable aggregation judging from the J-band blue shift and the increase in its FWHM.

The influence of inorganic salt and base on J-aggregation formation is to facilitate the formation of stable aggregates. First, inorganic salts increase the effective dielectric constant of water. This leads to less repulsion between TTBC cations in the aqueous solution, facilitating their aggregation. Also, inorganic ions are expected to shift the ionic balance in the solutions and thus further promoting aggregation.

4.3.3 1,1′-diethyl-3,3′-di(4-sulfobutyl)-5,5′,6,6′-tetrachlorobenzimidazolocarbocyanine, sodium salt (TDBC)

TDBC like TTBC has a conjugated chain, a positively charged nitrogen atom at one end of the chain, and three other nitrogen atoms, each with a lone electron pair. However, unlike TTBC, TDBC contain sulfonyl substituents that enable it to be easily soluble in aqueous solution. In aqueous solution TDBC exists as $TDBC^-$ anions and Na^+ cations and is well known to form J-aggregation. The threshold concentration of TDBC required for the appearance of the J-band at room temperature in distilled water is 10^{-5} mol/L.[27] Here, TDBC because of its ease to aggregate is employed to probe the role of the nanoparticle on the TDBC aggregation and generally in the hybrid system.

Figure 4.6 (A) shows the absorption spectra 1×10^{-5} M (Figure 4.6- 1) and 5×10^{-5} M (Figure 4.6- 2) TDBC in Ag colloidal solution. The J-band (λ_{max} = 588 nm) formation with both concentrations was noticed and was accompanied to a decrease in the Ag plasmon absorption band. The full width at half maximum (FWHM) for the Ag surface plasmon band, about 60 nm, did not change much upon adsorption of the TDBC molecules onto the Ag nanoparticle surface. Figure 4.6 (B) shows the absorption spectra of the solutions of native Au nanoparticle with Au characteristic surface plasmon at about 528 nm (1), monomeric TDBC in methanol (2) and TDBC coated Au nanoparticles (3). Figure 4.7 shows the absorption spectra of aggregated TDBC in alkaline aqueous solution.

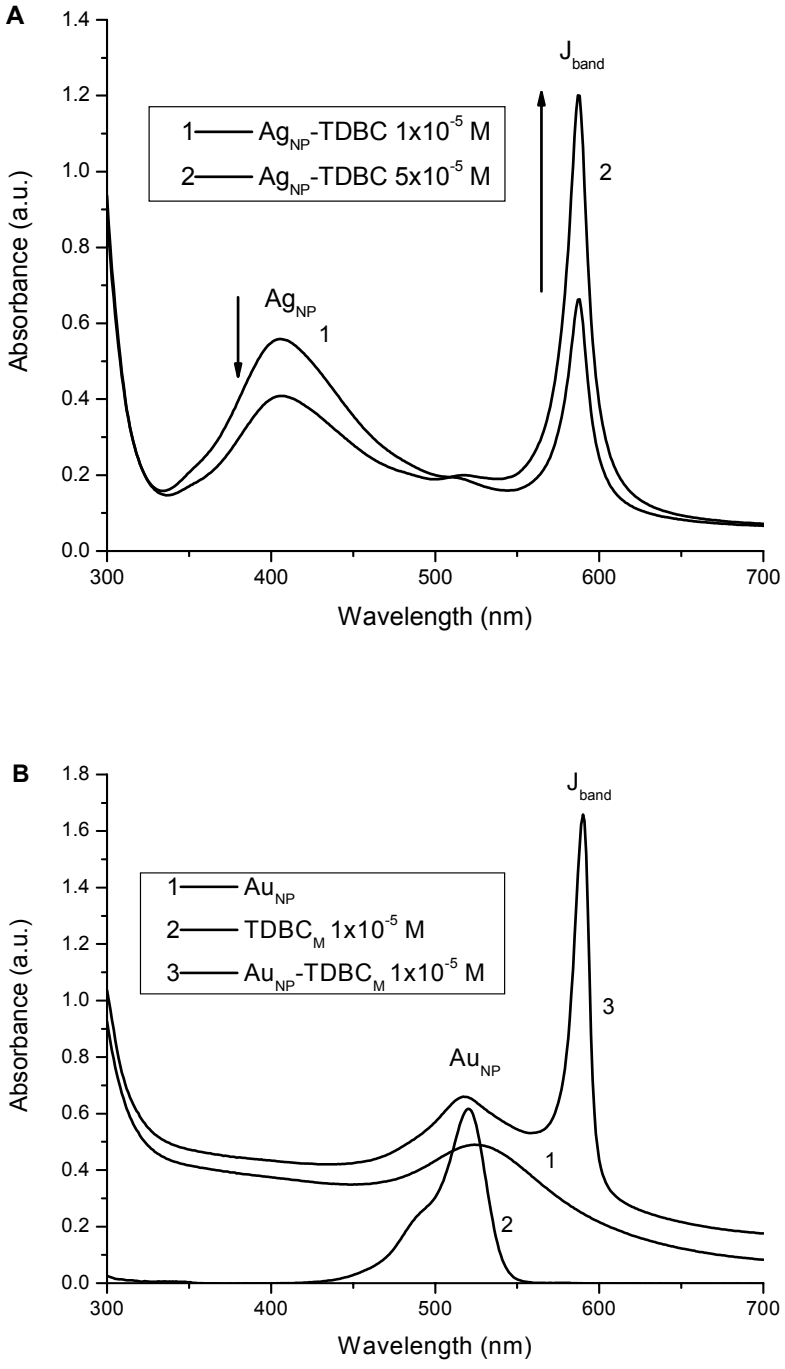

Figure 4.6: (A): (1) Absorption spectra of 1×10^{-5} M and (2) 5×10^{-5} M TDBC-coated Ag nanoparticles. (B): (1) Absorption spectra of Au nanoparticles, (2) monomeric TDBC in MeOH and (3) 1×10^{-5} M TDBC coated Au nanoparticles.

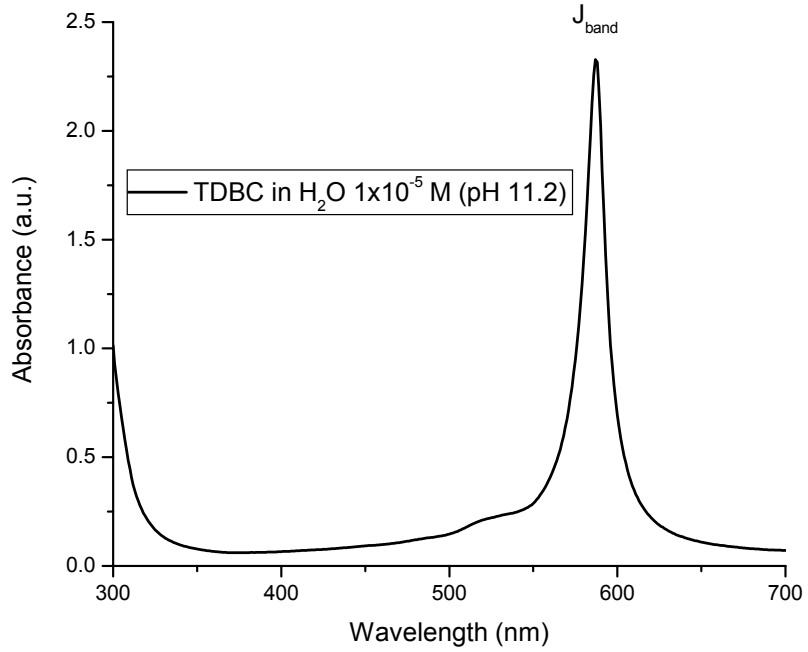

Figure 4.7: Absorption spectra of aggregated TDBC in alkaline aqueous solution.

When the surface plasmon band of the Ag and Au nanoparticles and excitonic band of TDBC is analyzed in Figure 4.6 and 4.7, using FWHM and shifts as an indicator, differences in the J-aggregate formation in the different nanoenvironments are recognized. For the TDBC coated Ag, as the concentration is increased, the J-band increased and the plasmon band decreased. The Ag surface plasmon band absorbance decrease is indicative of coverage. The J-band measured FWHM is 14 nm. In the TDBC-Au system the J-band appears at 590 nm, a 3 nm red shift from the TDBC-Ag J-band, the FWHM for the TDBC-Au J-band is 10 nm, a 4 nm shift from that of the TDBC-Ag. TDBC aggregate in the alkaline aqueous solution, like that in the Ag colloid, shows an exciton band at 587 nm and a FWHM of 14 nm. Consequently, it is conjectured that the dye molecules are more tightly pack on the Au then on the Ag. The electronegativity of

Au being bigger than Ag might be a factor. It is possible that the charged nanoparticles or other ions in solution serve in a similar fashion as salt and base in promoting aggregation, which is by reducing the repulsion between TDBC anion.

Figure 4.8 shows the absorption spectra of TDBC coated Ag nanoparticle of two different sizes purchase from BBInternational. The trend of increase in the monomer absorption band couple to plasmon band absorption decrease was observed but the J-aggregate band was not observed for the purchase nanoparticle solutions. This result may be due to pH, stabilizers or low concentration of colloidal particles associated with the purchased nanoparticles. Although the vendor stated that there was no stabilizer used in their system and the pH was measured to be about neutral, it is found extremely difficult to get TDBC at the studied concentration to aggregate using the purchased nanoparticles. TDBC was the only cyanine dye that was studied using different nanoparticle sizes in order to understand if there was any size effect. It is possible that TDBC may aggregate upon increasing the concentration of the dye in the nanoparticle solution. However, much higher concentration was not attempted. Another point worth noted is that even for the monomer absorption band, were big shifts have been observed in the in-house produced nanoparticles systems, there was no shift noticed. Thus, it is concluded that there is no interaction between TDBC and the purchased nanoparticles.

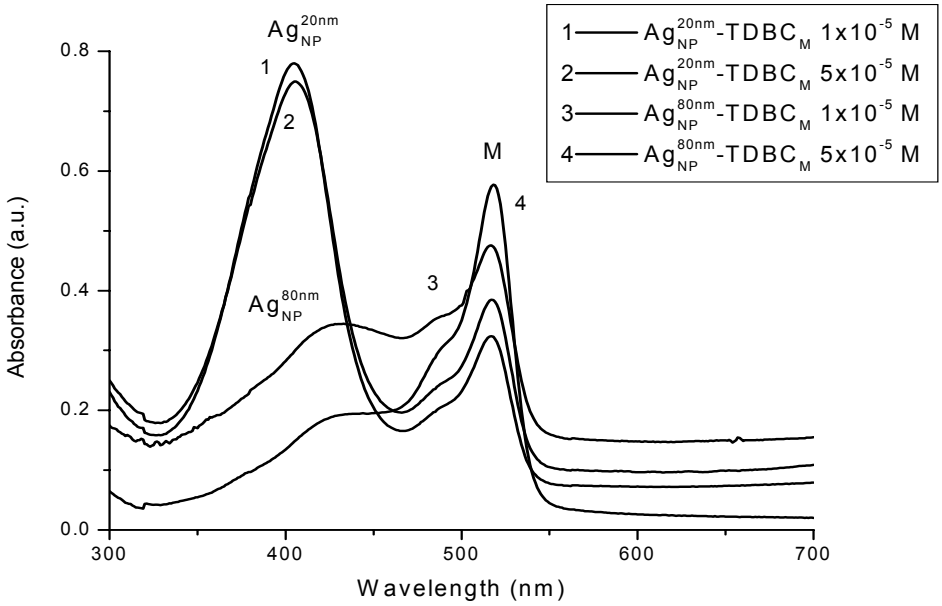

Figure 4.8: (1) Absorption spectra of 1 × 10^{-5} M, (2) 5 x 10^{-5} M TDBC coated 20 nm Ag; (3) 1x10^{-5} M, and (4) 5x10^{-5} M TDBC coated 80 nm Ag nanoparticles.

4.3.4 3,3′-diethyl-5,5′-dichloro-9-benzothiacarbocyanine, chloride salt (DDPT)

Figure 4.9 (A) shows the absorption spectra of DDPT monomer in methanol (3), DDPT coated Ag (1) and DDPT in an alkaline aqueous solution (2). Figure 4.9 (B) shows the time evolution of the DDPT coated Ag, fresh at (t_0) (1), 20 min later (2), then followed 60 min afterwards (3). The time study was undertaken in an effort to probe the role of the nanoparticle on the stability of the J-band. For comparison, the absorption spectra of DDPT in fresh alkaline aqueous (1) then 60 min later (2) were taken. In the Ag nanoparticle environment, the DDPT J-band appeared at 662 nm with a FWHM of 21 nm. In the alkaline solution, DDPT showed a J-band at 664 nm and a FWHM of 18 nm. The resulted red shift─ lower energy─ and smaller FWHM in the alkaline solution indicate that in the aqueous solution the DDPT is better organized or more tightly packed.

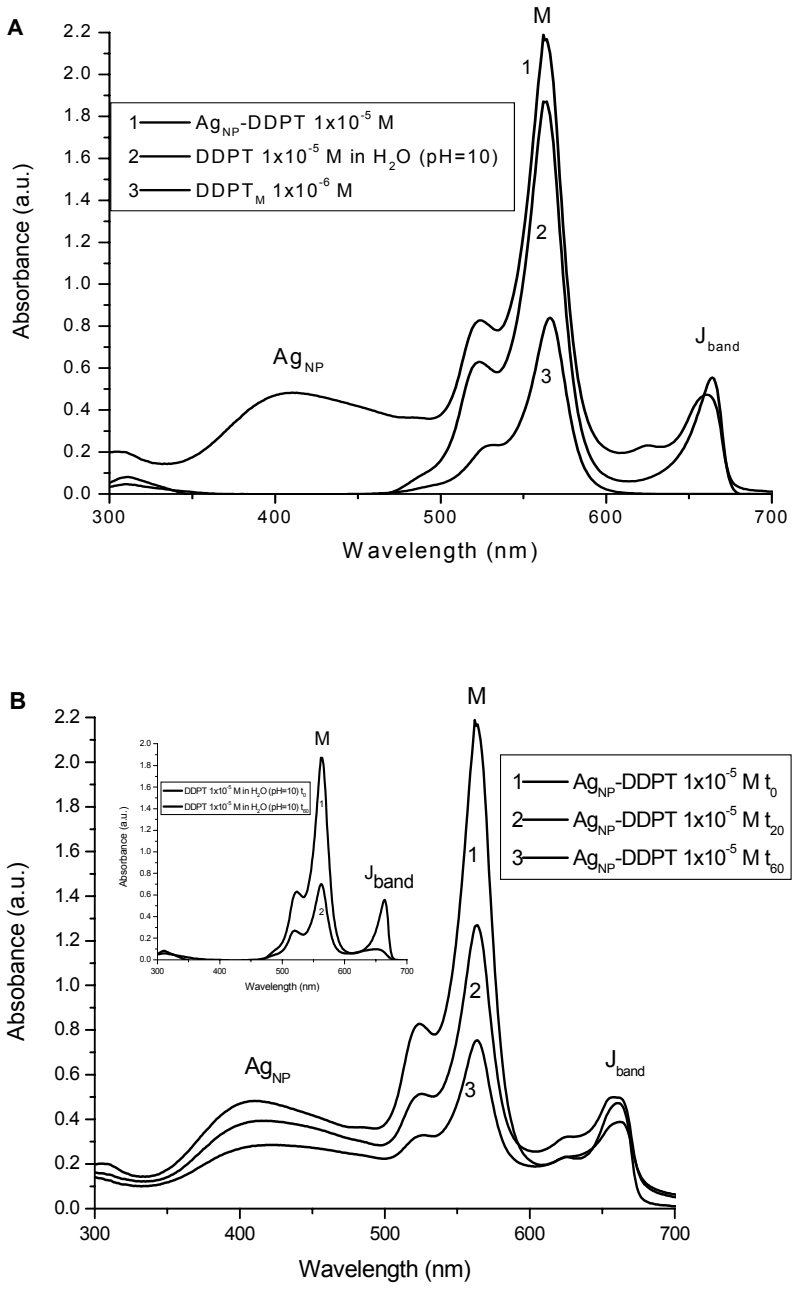

Figure 4.9: (A): Absorption spectra (1) 1×10^{-5} M DDPT-coated Ag nanoparticles, (2) 1×10^{-5} M DDPT in alkaline aqueous solution and (3) monomeric DDPT solution. (B): Evolution of absorption spectra with time, (1) 1×10^{-5} M TDBC-coated Ag at t_0, (2) at t_{20} and (3) at t_{60}. For comparison, the inset shows the absorption spectra in aqueous solution of (1) 1×10^{-5} M DDPT at t_0 and (2) at t_{10}.

The previously noted blue shift for the monomer band is again observed for these DDPT coated Ag nanoparticles. Better organization in the aqueous solution can be probably rationalized by the added hydrophylicity gained from the DDPT sulfur group, which enhanced DDPT dissolution in the solution. It is noteworthy, however, that in the Ag nanoparticle environment that after 60 min, the J-band was retained. Whereas, in the aqueous solution (shown in the inset for comparison), the DDPT J-band is nearly gone. In this instance, the Ag surface charge is possibly providing added stability. This stability may be due to reduce repulsion of DDPT cations in the solution brought about by the Ag nanoparticles.

Formation of the cyanine dyes J-aggregate in the different nanoparticles environment can also be confirmed using fluorescence spectra as shown in Figure 4.10. The emission spectra consist of a J-band at 596 nm, 669 nm and 589 nm for TTBC, DDPT and TDBC, respectively. The J-aggregate emission spectra for the three dyes, shown in Figure 4.10, have a few nanometer shifts from their respective absorption maxima. Small Stokes shifts are a characteristic of J-aggregates. The small stokes shifts are indicative of the excitonic nature of the excited state of the aggregate.[29]

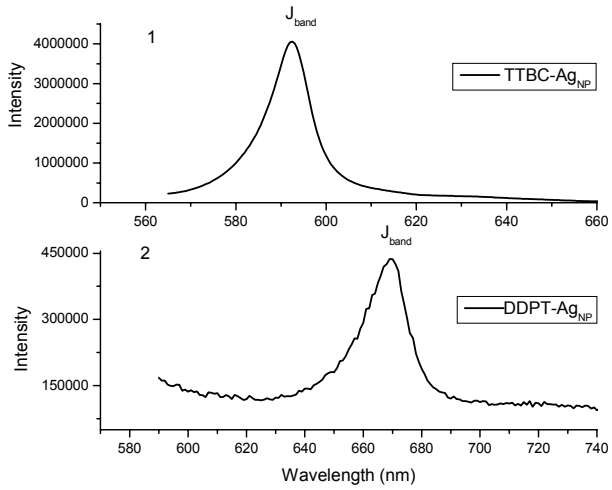

Figure 4.10 (1, 2): Fluorescence spectra (1) TTBC, (2) DDPT coated Ag nanoparticles. λ_{ex} = 530 nm and 550 nm for TTBC and for DDPT, respectively.

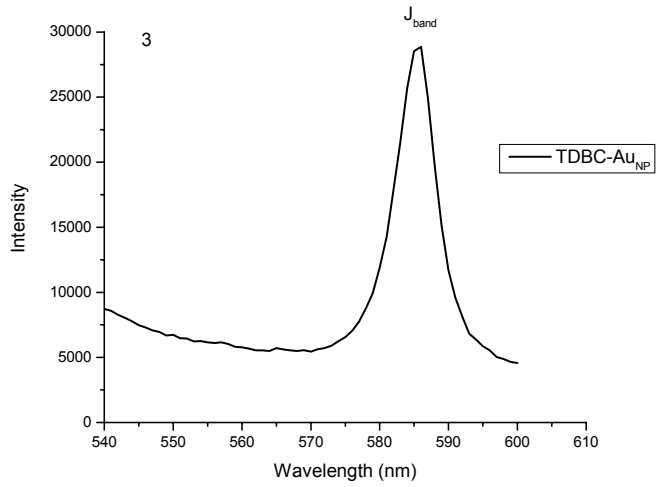

Figure 4.10 (3): Fluorescence spectra of TDBC coated Au nanoparticles. λ_{exc} = 530 nm for TDBC.

The reactivities of the nanoparticles with the four structurally different cyanine dyes may be assessed. As shown in Table 4.1, the structure of the four cyanine dyes differ in terms of the nature of their charge, the size of their conjugated moiety, the type of heterocyclic ring and the character of the substituents found in each. These structural variations are shown to exhibit differences in the optical absorption data, which in effect characterize the reactivities of the dyes with the nanoparticle. Table 4.2 summarizes the results of the studied cyanine dyes aggregation behavior in the different nanoparticles environments.

Table 4.2: Cyanine dyes aggregation behavior in different nanoparticle environments

Cyanine Dye	Nanoparticle	J-Aggregate	Notes
PIC	1. Native Ag 2. Polymer-stabilized Ag 3. Ag transferred in MeOH 4. Ag film 5. Native Au 6. MPA-stabilized Au	1. yes 2. yes 3. no 4. yes 5. no 6. did not try	The concentration of PIC was 5×10^{-5} M for the entire positive aggregate results.
TTBC	1. Native Ag 2. Polymer-stabilized Ag 3. Ag transferred in MeOH 4. Ag film 5. Native Au 6. MPA-stabilized Au	1. yes 2. did not try 3. no 4. yes 5. no 6. yes	The concentration of TTBC tried were 1×10^{-5} M and 1×10^{-4} M. Aggregate was found for the higher concentration if not for the lower one.
TDBC	1. Native Ag 2. Polymer-stabilized Ag 3. Ag transferred in MeOH 4. Ag film 5. Native Au 6. MPA-stabilized Au	1. yes 2. yes 3. no 4. yes 5. yes 6. did not try	The concentration of TDBC used was varied and are stated with the accompanying graphs in the text.
DDPT	1. Native Ag 2. Polymer-stabilized Ag 3. Ag transferred in MeOH 4. Ag film 5. Native Au 6. MPA-stabilized Au	1. yes 2. did not try 3. no 4. yes 5. no 6. did not try	The concentration of DDPT limited to 1×10^{-5} M in these studies and was not fully explored.

It is important to note that the observation of the peak-shaped J-aggregate band formed for the studied cyanine dyes is in fact consistent with previous experimental observations for silver nanoparticles with other cyanine dyes and theoretical modeling of the coupling between the surface plasmon of the metal core and the molecular exciton of the dye.[12(a),24(b)] A peak-shaped J-band develops when the J-band exciton absorption is located at slightly longer wavelength than the surface plasmon resonance absorption, which is indeed the case for the dye-nanoparticle system studied in this chapter. The red-shifted J-band for the dye-nanoparticle systems is initially very sharp, which is in agreement with the fact that red-shifted bands appears as an intense narrow absorption band due to motional narrowing.[30] However, the fact that at times, in some of the

nanoparticle systems, this band became relatively broad and weak suggests that the dye molecules could be oriented in a less than optimal fashion for J-aggregation in these particular environments. Lattice disorder is often considered as one of the possible reasons for this type of surface reorganization for adsorbed dyes.[31] More study will be needed to probe possible contributions to the J-band from intramolecular (dyes on the same nanoparticle) and intermolecular (dyes between two nanoparticles) J-aggregation. For example, strong dependence of the J-band intensity on the concentration of nanoparticles will be indicative of the formation of interparticle J-aggregation.

4.4 Raman Spectra of Cyanine Dye-Nanoparticle Solutions

In an attempt to further understand the binding event taking place between the cyanine dyes and the nanoparticles, off-resonance Raman spectroscopy was performed. The interest in these measurements were not for surface enhanced-Raman scattering (SERS) nor aggregated enhanced-Raman scattering (AERS) but simply to probe the Ag-N, Au-N, Ag-S or Au-S stretching vibration band which usually occurs in the low frequency region of 200-250 cm^{-1}.[32] Figure 4.11 shows the off-resonance Raman spectra of TDBC (A), TTBC (B) coated Ag nanoparticles and PIC (C) coated Au nanoparticles. The observed Raman bands for PIC have been thoroughly established in the literature.[33] TDBC and TTBC, on the other hand, have not been characterized to the same extent due to fluorescence issues. Not yet published work from Akins' group have performed Raman measurements on TDBC and have assigned the observed vibrational bands for the monomer and aggregated TDBC anion based on predicted vibrational modes of frequencies using DFT methods. Briefly, the three band marks with the asterisks are assigned as follows: the ~670 cm^{-1} band as mainly out of plane ring deformation, and out

of plane waging of the CH bonds on the trimethine bridge; the ~1200 cm^{-1} band as in plane skeletal deformation of the macrocycle moieties and stretching of the S-O bonds; the ~1608 cm^{-1} band as in plane bonding deformation of the rings and trimethine bridge. These same spectral assignments can be applied to the TTBC coated Ag spectrum.

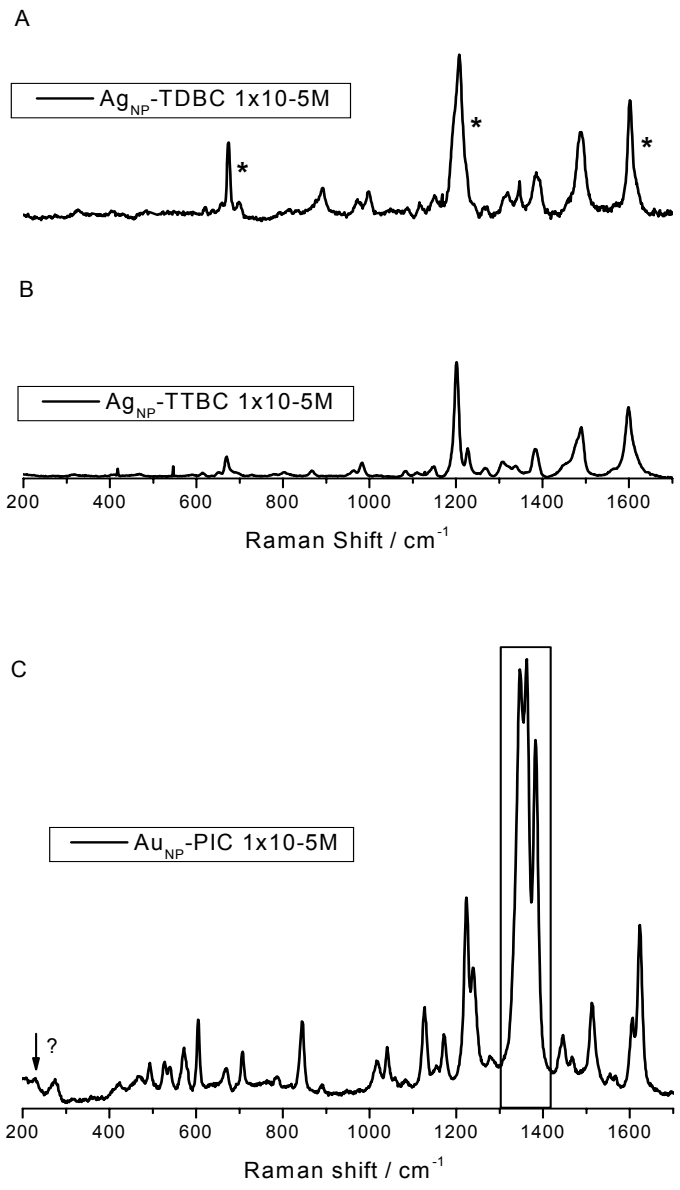

Figure 4.11: Raman Spectra (A) TDBC, (B) TTBC coated Ag nanoparticles, and (C) PIC coated Au nanoparticles. Samples were excited using 632.82 nm radiation; laser power 17 mW at the source, accumulation time 2 minutes, and spectral resolution 0.4 nm.

For TTBC and TDBC coated Ag, the respective off-resonance Raman spectrum, in Figure 4.11 (A) and (B), shows no Ag-N stretching vibration band in the low frequency region. For the PIC-Au system in Figure 4.11 (C), the well known triplet attributed to the symmetrical stretching of bridge carbons at the lower energy end, the quinoline distortion due to pyridyl deformation caused by certain carbons symmetrical stretching, and the quinoline distortion due to phenyl deformation cause by certain carbons asymmetric stretching on the higher energy end were observed.[33] In the PIC-Au spectrum (Figure 4.11 (C), there are two low frequency lying bands at 227 cm^{-1} and 275 cm^{-1}. According to Guo et. al.,[33(a)] these two bands though weak when off-resonance excitation is used and greatly enhanced when resonant excitation is used, hence the phenomenon of aggregation enhanced-Raman scattering (AERS), are due to out-of-plane motion distortion of the quinoline macrocycle. Moreover, according to Guo the bending of the phenyl ring with respect to the pyridyl ring is the predominant contribution for the 275-cm^{-1} Raman band, while the major contribution for the 225-cm^{-1} band is the mutual twisting of phenyl and pyridyl rings. Noting this explanation for the two bands questions the Au-S stretching vibration band possibility. Therefore, more studies are needed to clarify this point.

4.5 Dye Aggregates Formed on Self-Assembled Nanoparticles on Glass Slides

Figure 4.12 shows the absorption spectra of the four studied dyes on Ag colloidal film. The first observation is that except for PIC all the other three dyes aggregated with the monomer band completely vanishing. Another observation is that there were some shifts in the J-aggregate band in the film when compared to the J-band formed in solution. The results are as follows: PIC, in the film, had a J-band at 582 nm (a 9 nm blue shift from that in solution) and an equal FWHM of 13 nm; TTBC, in the film, had a J-

band at 588 nm (a 7 nm blue shift from that in solution) and a FWHM of 13 nm (an increase of 12 nm from the solution J-band FWHM); TDBC, in the film had a J-band at 588 nm as in solution and a FWHM of 16 nm (an increase of 2 nm from the solution J-band FWHM); finaly, in the film, DDPT had J-band at 665 nm (a 7 nm blue shift from that in soltuion) and an equal FWHM of 22 nm.

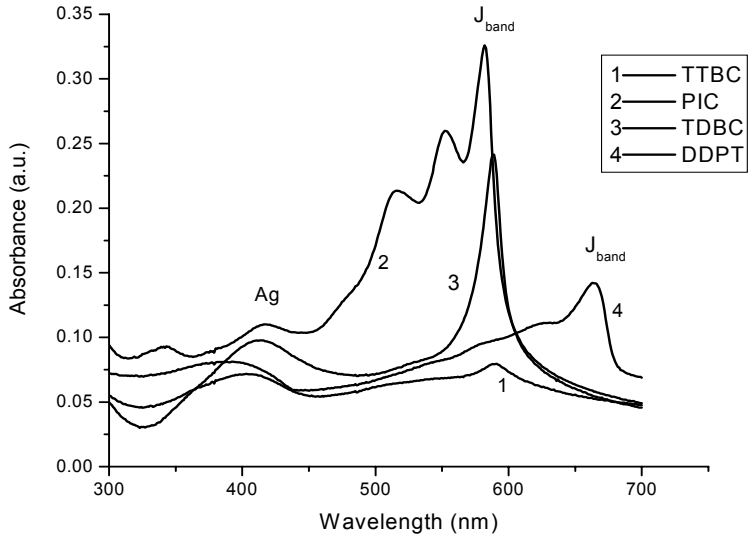

Figure 4.12: Absorption spectra (1) 1×10^{-6} M TTBC, (2) $1x10^{-5}$ M PIC, (3) 1×10^{-5} M TDBC and (4) 1×10^{-6} M DDPT self-assembled onto Ag nanoparticle film.

Figure 4.13 shows the normalized absorption spectra of PIC in methanolic solution and PIC coated Au nanoparticles immobilized onto a thiol derivatized glass slide and the fluorescence spectrum of the PIC coated Au nanoparticles. Figure 4.13 (A) is characteristic of PIC monomers; it shows the previously mentioned two maxima at about 490 nm and at 522 nm. These two bands are the dimer band, and monomer band, respectively. In Figure 4.13 (B), in addition to the two maxima in the methanolic solution, the J-aggregate band is detected. The inset in Figure 4.13 shows the surface plasmon absorption band (λ_{max}) for Au nanoparticles immobilized on the SH

functionalized substrate at ca. 525 nm. The gold nanoparticles prior to immobilization are relatively homogenous and composed of mainly spherical nanoparticles with an average diameter of 20 to 40 nm. The shoulder present in the inset is indicative of bigger sizes and clustering.

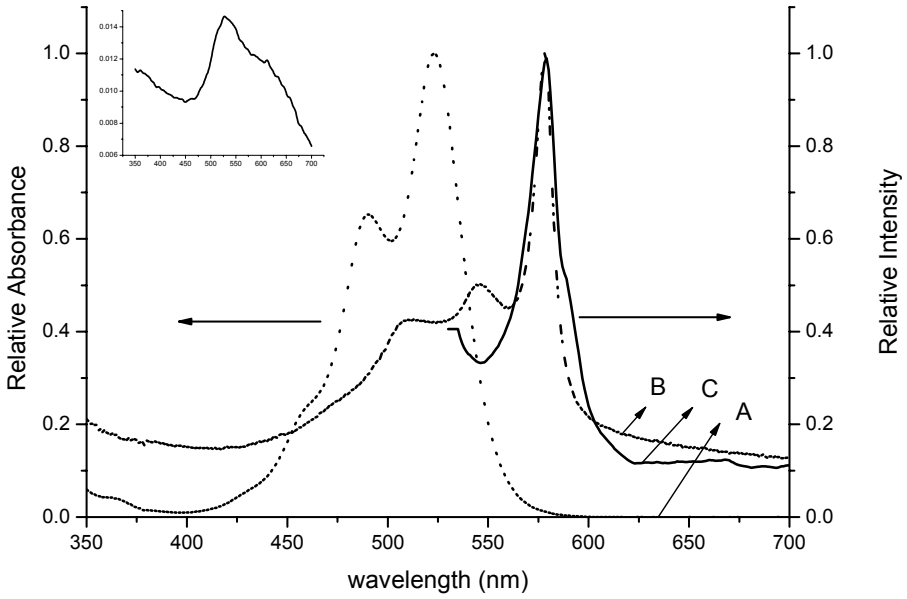

Figure 4.13. Absorption spectra (A) PIC methanolic solution, (B) 6 drops of 8×10^{-4} M PIC on Au-SH-substrate and (C) Fluorescence (λ_{exc} = 514 nm) of PIC on Au-SH substrate. Inset is the absorbance of the Au coated functionalized glass slide.

Analysis of the absorption and fluorescence spectra in Figure 4.13 demonstrates the aforementioned shifts associated with the monomer and the J band. Comparing the PIC bands in the Ag colloidal solution, the Ag film and Au film, a red shift associated with the dimer (488 nm in solution; 517 nm in Ag film, and 511 nm in Au film) and the monomer band (488 nm in solution; 523 nm in Ag film, and 545 nm in Au film) was observed. As for the J-band, a λ_{max} = 591, 582, and 578 nm, for Ag colloidal solution, Ag film and Au film, respectively was observed.

The results in figure 4.12 and 4.13 clearly indicate that all four dyes form J-aggregates in the film. The blue shifts associated with the film J-aggregates relative to solution J-aggregates are suggestive of smaller size aggregates in the film. The broadening in the J-band formed in solution relative to that in the film may be explained by inhomogeneous broadening. This example of J-aggregate coated nanoparticle immobilized onto a glass support, using the deposition methods describe in the experimental section, provides an approach to explore the fabrication of ordered structures, such as molecular aggregates in the solid state.

4.6 Atomic Force Microscopic (AFM), Dynamic Light Scattering (DLS) and Near-Field Scanning Optical Microscopic (NSOM) Studies

It is generally anticipated that the size of a J-aggregate domain should correlate with the wavelength of the absorption, the sharpness of the J-aggregate transition (as measured by $\Delta\nu_{1/2}$), and the Stokes shift between absorption and fluorescence.[2(a)] The J-aggregate physical size form on crystal surfaces such as silver bromide can be estimated from the ratios of bandwidths of the monomer and aggregate as well as other approaches.[23(a)] Typical values are in the range of 6-15 molecules for dyes structurally similar to TTBC.[34] Similar values may be assumed for TDBC. To probe the physical arrangements of the TDBC dye chromophores and size of the J-aggregate domain on the native Ag nanoparticles, atomic force microcopy and dynamic light scattering was employed.

Figure 4.14 shows the AFM image for the native Ag colloid and the accompanied line scans. The height, hence, size of the spherical Ag nanoparticles can be discerned from Figure 4.14 to be about 30 nm. Figure 4.15 shows TDBC solution spin-casted onto a cover slip. Analysis of the image height and lateral size, represented in the cartoon in the

bottom of Figure 4.15, reveals that individual J-aggregates have height measurements of about 12 nm ± 2 nm and lateral sizes in the range of 60 to 70 nm. The actual lateral size should be lower than the measured value due to the limiting radius of the curvature of the AFM cantilever tip. J-aggregate formation on the cover slip was confirmed using UV-Visible absorption spectroscopy by detecting the aforementioned characteristic J-band.

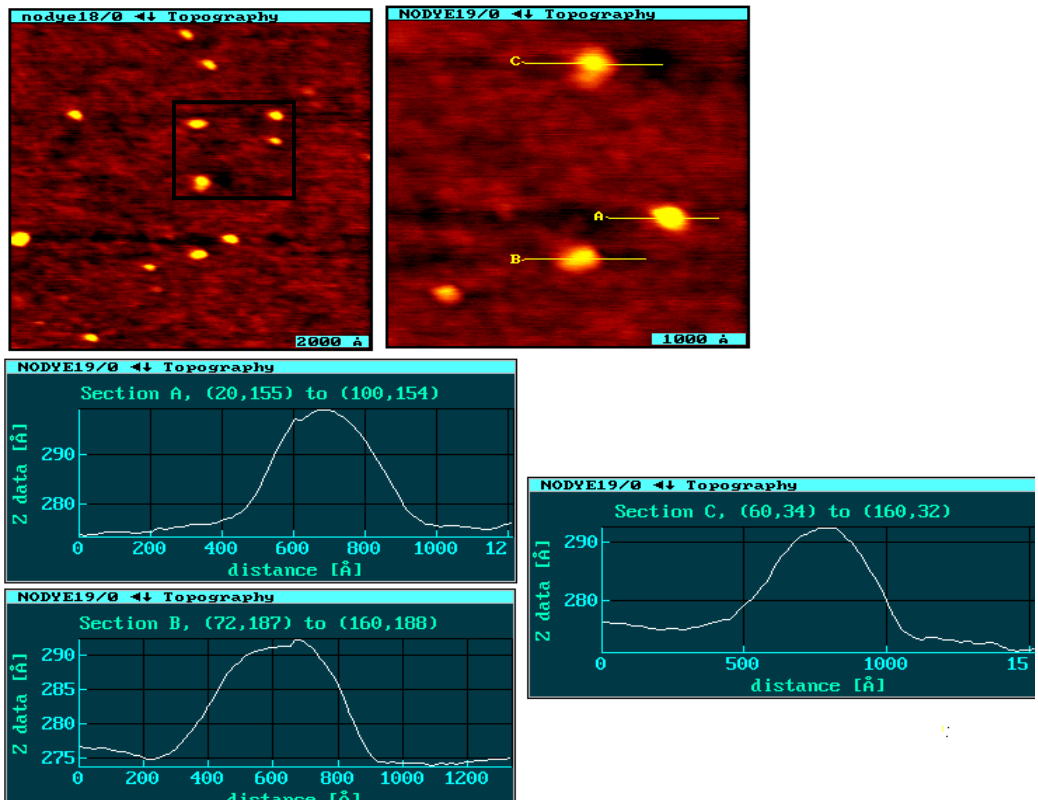

Figure 4.14: AFM image of Ag nanoparticles and corresponding line scans.

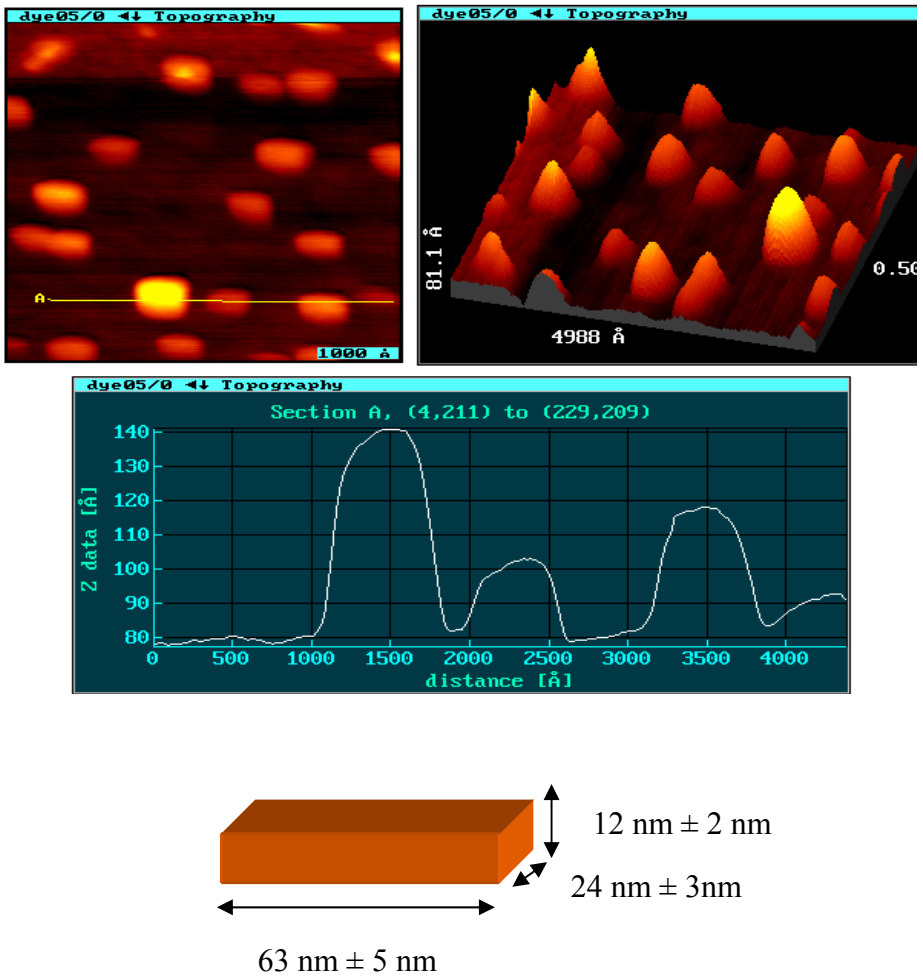

Figure 4.15: AFM image of TDBC and corresponding line scan. Underneath is a cartoon picture of a J-aggregate molecule and its dimensions measured from the AFM image.

The rectangular cartoon in Figure 4.15 is representative of a J-aggregate domain deposited on the cover slip. Because when we use a blank cover slip, the surface topography is flat and there is no absorption present, the lateral size and height measured from the AFM image in Figure 4.15 is attributed solely to the J-aggregate domain. The physical size of a J-aggregate domain, which is composed of many closely spaced molecules, maybe considered to be 63 × 24 nm in size and 12 nm thick for TDBC based on the AFM analysis.

Figure 4.16 shows TDBC coated Ag nanoparticles spin-casted onto a cover slip.. Analysis of the image from Figure 4.16 discloses an increase in the height of the TDBC coated Ag nanoparticles when compared to the bare Ag nanoparticles in Figure 4.14. The increased in height measured from Figure 4.16 (the enlarged image, line A) is between 50 to 70 nm.

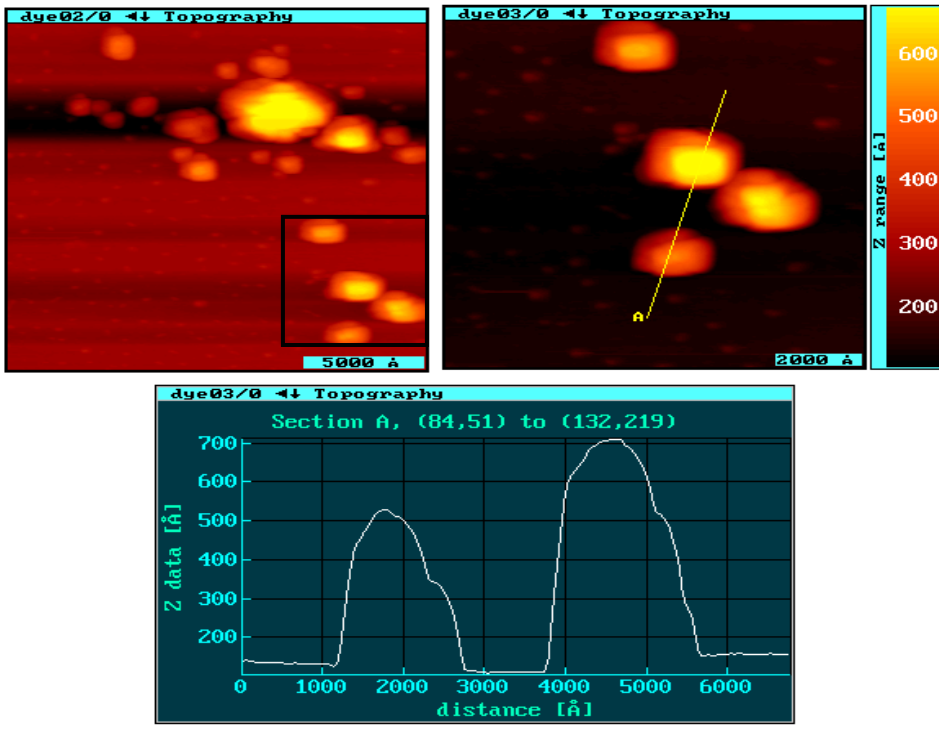

Figure 4.16: AFM images of TDBC coated Ag nanoparticles and corresponding line scan.

Now, taking into account the height of the bare Ag nanoparticle from Figure 4.14 and the height of the TDBC molecule spin coated onto the cover slip (Figure 4.15), a total height of nearly 50 nm is obtained, which correlates well with the height being measured for TDBC coated Ag shown in Figure 4.16. This result is indicative of the TDBC molecules depositing and adsorbing on the surface of the Ag nanoparticles. The coated

nanoparticle coagulation observed in Figure 4.16 is another evidence of interaction between the TDBC molecules and Ag nanoparticles upon the adsorption process.

In another experiment to probe the adsorption of TDBC on Ag nanoparticles, dynamic light scattering measurement was carried out. Figure 4.17 shows DLS measurements of Ag nanoparticles (A) having a diameter of about 40 nm and of TDBC coated Ag nanoparticles (B) with a diameter 47 nm. The DLS result shows a size difference of about 7 nm for the TDBC coated Ag relative to the bare Ag nanoparticles. Figure 4.17 (C) shows the AFM image and accompanying line scan (Figure 4.17 (D)) that was taken for the same TDBC concentration (1×10^{-6} M) in the DLS experiment but without the Ag nanoparticles The topographic cross section taken for height measurements shows three J-aggregate domains with height from 7 to 10 nm. Analogous to the AFM analysis argument presented above, this AFM analysis couples with the DLS measurement clearly demonstrate that TDBC J-aggregates form single domains with height from 7 to 12 nm. The lateral sizes were not measured for this AFM image. The TDBC concentration used in the DLS experiment is equal to that used in the AFM experiment, thus the same amount of molecules is assumed to be present in the single J-aggregate domain. More experiment will be needed for better height measurements and to look at more than one concentration. Nonetheless, the findings, which are nanoparticle height increases upon addition of dyes and clustering on occasion, clearly demonstrate that J-aggregates are formed and deposited on the nanoparticle surface.

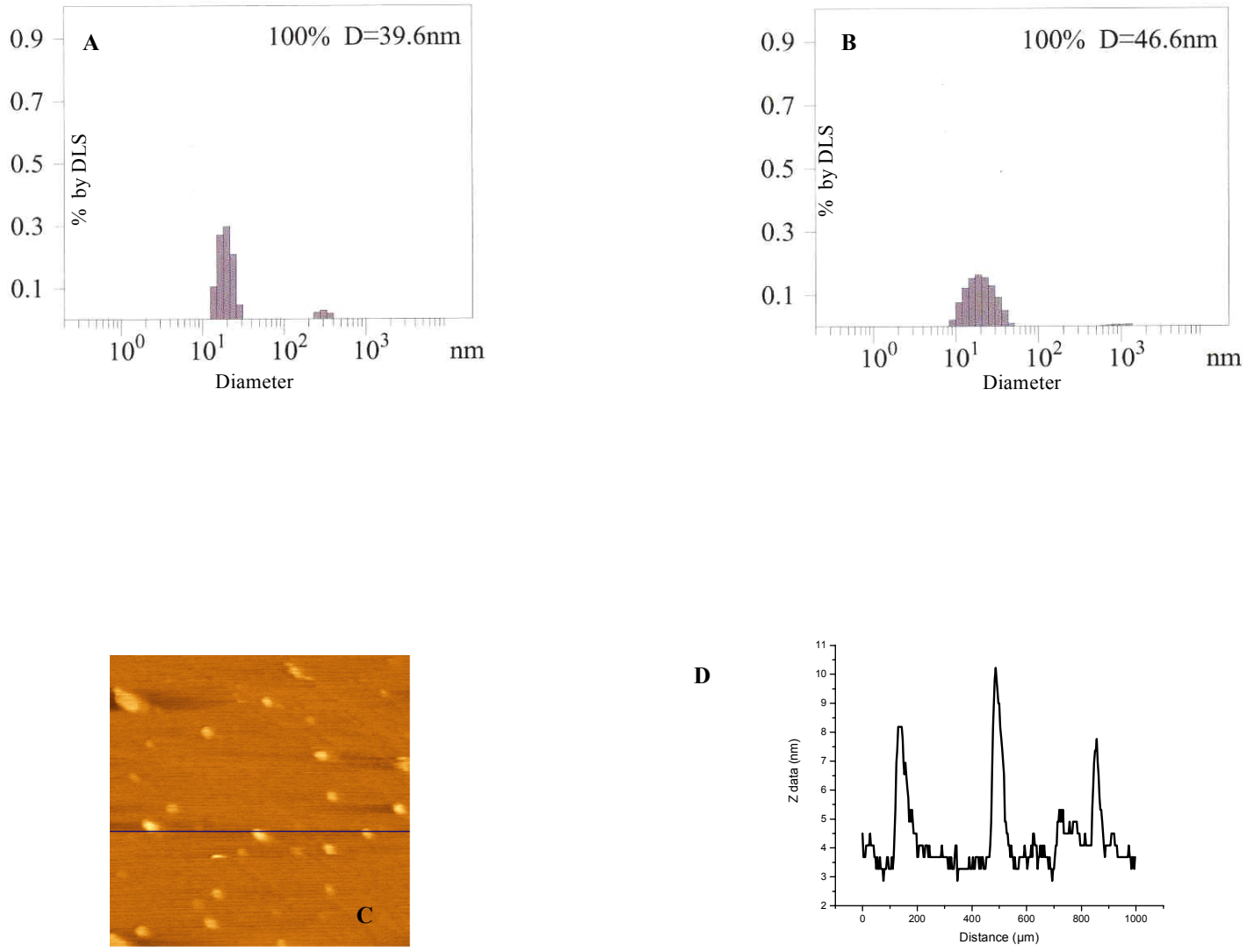

Figure 4.17. DLS characterization of (A) Ag nanoparticles and (B) TDBC coated Ag nanoparticles. (C) AFM image of TDBC spin-cast onto a silicon surface and (D) accompanying line scan.

As in the AFM experiment, the formation of J-aggregates was confirmed with UV-visible absorption for the solution used in the DLS experiment. Both AFM and DLS experiments confirmed the coating of the nanoparticles with TDBC molecules. Scheme 4.1 illustrates the possible π-π interactions between TDBC molecules. π-π interactions, an intermolecular interaction, is one of the driving forces along with electrostatic and

hydrophobic interactions believed to be responsible for J-aggregation. However, because of the usually anticipated negative surface charge for Ag nanoparticle and the anionic nature of the TDBC molecules it is not clear what electrostatic role is taking place or how much. But it is certain that the Ag nanoparticle is providing a surface for the formed J-aggregates to be deposited on.

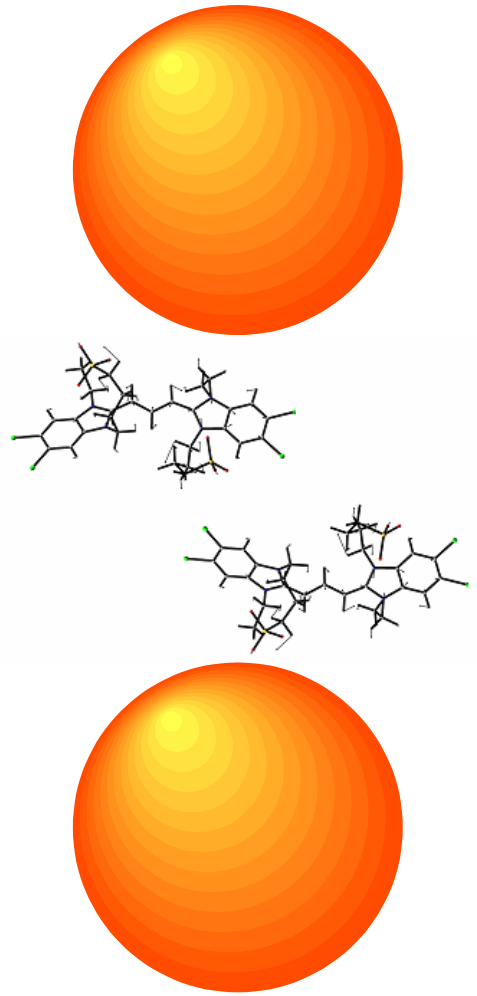

Scheme 4.1: Schematic illustration of the electrostatic and/or π-π interactions of the adsorbed TDBC on Ag nanoparticles.

AFM and NSOM studies of the morphology of pseudocyanine (PIC), so far the most investigated cyanine dye, was conducted on self-assembled Au nanoparticle onto

thiol (SH) functionalized glass substrate. Figure 4.18 (A) shows the AFM image of a relatively low density Au nanoparticle substrate. The surface plasmon band of the Au nanoparticles on the substrate is at about 527 nm (Figure 4.13, inset) and the nanoparticle sizes were measured to be between 20 and 40 nm from AFM line scans. In Figure 4.18 (C), the J-aggregate of PIC dyes on the Au-SH-substrate has a fiber-like morphology. On the other hand, on the SH-substrate without Au (Figure 4.18 (B)), the aggregate of PIC dyes unlike in the presence of Au disperse on the substrate as particles. PIC dye J aggregate particles on the SH-substrate are spherical with sizes of about ~80 nm high and 150-388 nm wide. The PIC dye molecules forming fiber-like J-aggregates in the presence of the Au nanoparticle, have height about 1.6-12 nm and width of about 50-80 nm. Further inspection of Figure 4.18 (C) suggests that PIC J-aggregates maybe growing among or between the Au nanoparticles.

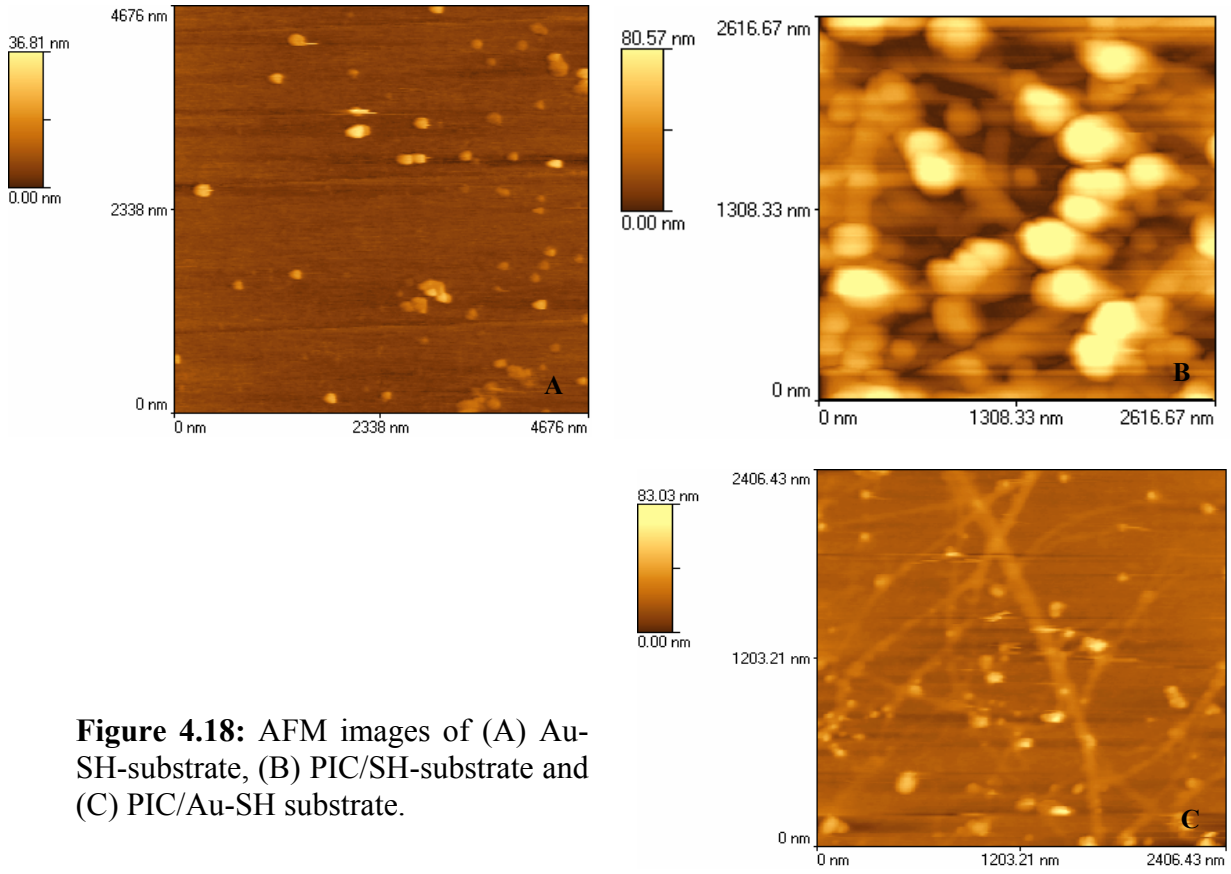

Figure 4.18: AFM images of (A) Au-SH-substrate, (B) PIC/SH-substrate and (C) PIC/Au-SH substrate.

Near-field scanning optical microscopy (NSOM), both shear force and fluorescence, was used as a complementary technique to probe the morphology of the PIC. As in the AFM images, the NSOM fluorescence shown in Figure 4.19 (A) and topography shown in Figure 4.19 (B) similarly illustrate the rod-like or fiber-like morphology of the PIC J-aggregate in the presence of Au nanoparticles. Analysis of the NSOM fluorescence and topography images shows that the PIC J-aggregate rod is about 290 nm high and 2.4 μm wide on the Au-SH substrate. AFM is considered to give more accurate measurements.

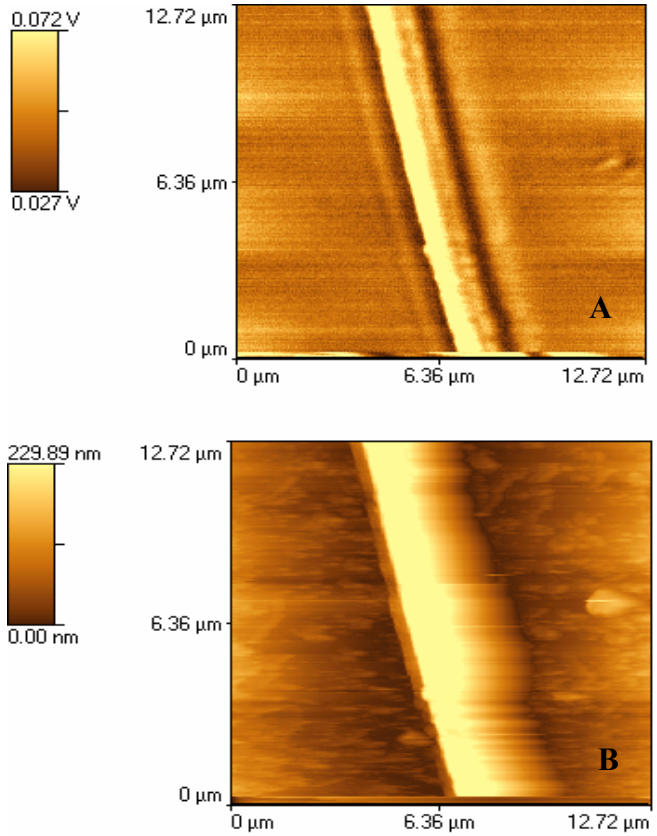

Figure 4.19: (A) NSOM fluorescence and (B) topography of PIC/Au-SH substrate.

The interpretation of the NSOM image contrast is not straightforward due to the complex nature of the interaction of the sample with the near-field excitation. The

fluorescence NSOM image is simply understood to be an estimate of the spatially resolved probe-induced fluorescence intensity from the PIC molecules. This intensity is proportional to the product of the local absorbance and quantum yield. The PIC fluorescence NSOM image is obtained for the fiber-like morphology, i.e., the J-aggregate and not for the accompanying Au nanoparticles on the surface. The presence of the NSOM florescence image, particularly matching the morphology for the fiber-like structure present in the shear force topography image may be further proof of PIC aggregation on the Au-nanoparticle.

A model for PIC J-aggregates formation on the self-assembled Au nanoparticle is illustrated in scheme 4.2. The gold nanoparticles is assume to be possibly acting as starting points for J-aggregate growth and helping direct the PIC J-aggregate fiber growth as they form macroaggregates.

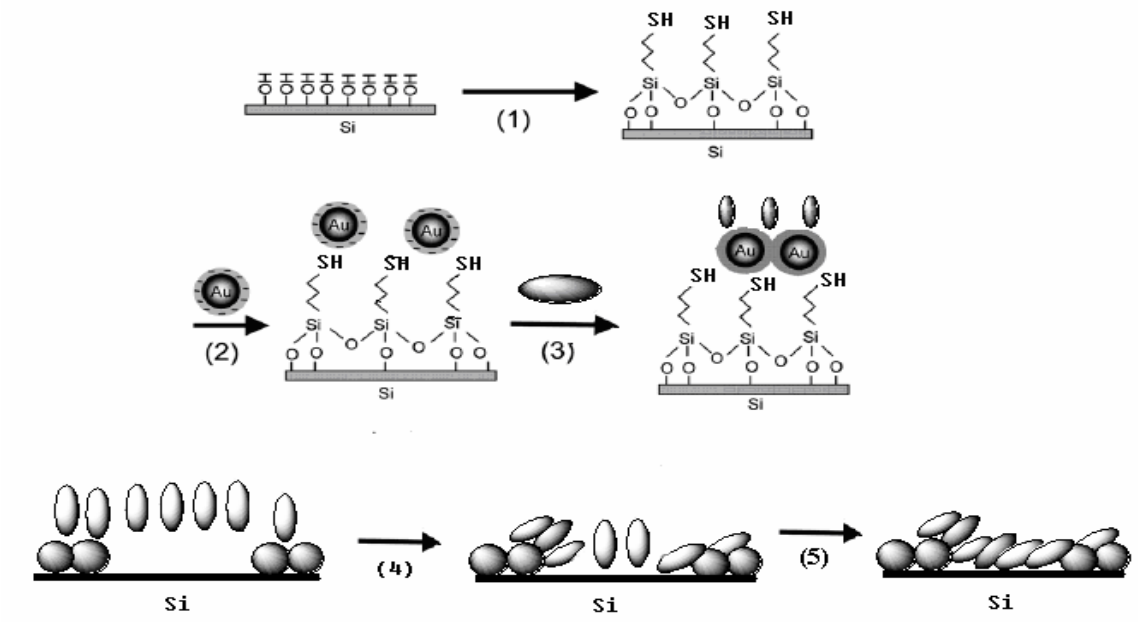

Scheme 4.2: Schematic illustration of PIC dyes forming rodlike J-aggregate.

4.7 Conclusion

The adsorption and aggregate formation of cyanine dyes on Ag and Au nanoparticles have been investigated for aqueous suspension and cast films. The J-aggregates of the four cyanine dyes studied using absorption and fluorescence spectroscopy were shown to be produced in the various nanoenvironments and showed the characteristic optical features: a sharp and narrow absorption and fluorescence band, the J-band. J-aggregate stabilization at the nanoscopic level is possible by depositing the monomer dye onto the nanoparticle surface as evidence in the DDPT aggregate in water compared to that formed on the Ag nanoparticles. Through Raman experiments, it was possible to ascertain whether or not there were covalent attachments from the cyanine dyes studied to the surface of the nanoparticles probed. Scanning probe microscopic studies further confirmed the deposition and adsorption of cyanine dye molecules onto the nanoparticle surfaces both in solution and in cast films. Inorganic salts and bases was shown to have influence on the absorption characteristic of TTBC J-aggregates in aqueous solution and adsorbed onto nanoparticle surfaces. Also, the addition of salts and base was shown to increase the amount of J-aggregate form. Models were constructed showing the possible arrangements of TDBC dye molecules on the surface of nanoparticles and the role of nanoparticles in orienting and directing the formation of PIC J-aggregate fibers on Au nanoparticle surfaces and embedded into films.

5 Density Functional Theory Applied to Structure and Vibrational Band Analysis of an Aggregated Cyanine Dye

5.1 Introduction

Density Functional Theory (DFT)[1] is a quantum mechanical method used in physics and chemistry to investigate the electronic structure of many-body systems, in particular molecules and in the condense phases. The main idea of DFT is to describe an interacting system of fermions via its density and not via its many-body wave function as done for other traditional methods in electronic structure theory, such as Hartree-Fock theory and its descendants. For N electrons in a solid, which obey the Pauli principle and repulse each other via the Coulomb potential, it means that the basic variable of the system depends only on three ─ the spatial coordinates x, y, and z, rather than 3 x N─ degrees of freedom. The density is only a function of three variables and thus is a simpler quantity to deal with both conceptually and practically.

Even though density functional theory has its conceptual roots in the Thomas-Fermi model from the 1920s,[1] it was not until the Hohenberg-Kohn (H-K)[2] theorems, that DFT gained a firm theoretical footing. The first of these demonstrates the existence of a one-to-one mapping between the ground state electron density and the ground state wavefunction of a many-particle system. Further, the second H-K theorem proves that the ground state density minimizes the total electronic energy of the system. In other words, the first Hohenberg-Kohn theorem asserts that the density of any system determines all ground-state properties of the system, that is, $E = E[n_0]$, where n_0 is the ground-state density of the system. Then, the second H-K theorem shows that there exists a variational principle for the above energy density functional E [n]. Namely, if n' is not the ground

state density of the above system, then E [n'] > E [n_0].

Some significant outcomes from DFT are as follows: (1) as mentioned above, the wavefunction Ψ of an N-electron system includes 3N variables, while the density, no matter how large the system is, has only three variables x, y, and z. Moving from E [Ψ] to E [n] in computational chemistry significantly reduces the computational effort needed to understand electronic properties of atoms, molecules, and solids, (2) Formulation along this line provides the possibility of the linear scaling algorithm currently in fashion, whose computational complexity goes essentially linear in N when N is very large, (3) it provides some chemically important concepts, such as electronegativity (chemical potential), hardness (softness), response function, etc.. These concepts can be conveniently used to explain chemical properties and the changing of molecules.[1]

DFT is among the most popular and versatile methods available in condensed matter physics and computational chemistry. Computational chemistry, as the term says, deals with computations that are used to either enhance the understanding of chemical processes or to obtain data that are difficult to acquire experimentally. While DFT in principle gives a good description of ground state properties, practical applications of DFT are based on approximations for the so-called exchange-correlation potential. The exchange-correlation potential describes the effects of the Pauli principle and the Coulomb potential beyond a pure electrostatic interaction of the electrons. However, possessing the exact exchange-correlation potential means that the many-body problem exactly has been solved, which is not feasible, for example in solids.

Although the theory and practical framework were already developed in the 1960's, only in the last fifteen years has this method really gained importance due to the

development of new and accurate exchange-correlation potentials.[1] Moreover, the increase in computing power contributed to the range of applicability of the method. Also, computational quantum chemistry has emerged in recent years as a viable tool for the elucidation of molecular structure, molecular properties and chemical reaction mechanism.

Research dealing with understanding the structure and optical properties of molecular aggregates that are formed through noncovalent, self-assembly of molecules has garnered significant attention because such information may provide models for investigating intermolecular interactions between molecules in other systems; the prospect of gaining insight concerning the optical and population dynamics for small grouping of molecules; and the utilization of molecular aggregate structures as the functional elements for device and chemical sensor applications. Some key studies in the literature concerning aggregated molecules as model systems have focused on charge-separation steps in photosynthesis,[3] spectral sensitization,[4] photoconduction,[5] optical probes in biological and synthetic membrane systems,[6] and nonlinear optical materials.[7]

Simplified, and widely used, structural models for aggregates that appear to identify the important interactions between monomers within the extended structure are the so-called J- and H-aggregate spatial alignments. These alignment structures, i.e., the J- and H-aggregates, are defined by the relative orientations of induced transition dipole moments of the constituent monomers, either "head-to-tail" or "head-to-head," respectively. The absorption spectra for J- and H-type aggregates are red- and blue-shifted, respectively, relative to that of the absorption band of the monomer, and the optical dynamics of such aggregates differ substantially from that of the monomer as

well. In this chapter, the structure of aggregated 3,3'-diethyl-5,5'-dichloro-9-benzothiacarbocyanine (hereinafter referred to as DDPT) is investigated. Experimental techniques utilized in this study include UV-Vis absorption, emission, and Raman spectral measurements. Also, density functional theory (DFT) at the B3LYP level using the 6-31G(d) basis set has been employed to calculate bond distances, bond angles, charge distributions and Raman vibrational frequencies, for isolated single molecules of DDPT. The present study is a continuation of efforts to couple structural theory and spectroscopic methods to gain insight into molecular aggregate structure, similar to that provided by an earlier quantum chemical investigation for pseudoisocyanine (PIC) that was reported by this laboratory.[8]

5.2 Experimental System and Computational Methods

Experimental Section: All spectroscopic measurements were conducted at room temperature. DDPT was purchased from the Japanese Research Institute for Photosensitizing Dyes, Ltd., Okayama, Japan, and used without further purification. Two stock solutions of DDPT were prepared: one with the chloride salt of DDPT dissolved in HPLC grade methanol as solvent to prepare a solution of concentration ca. 1×10^{-3} M.; the second consisting of the chloride salt dissolved in distilled water to form a solution of concentration ca. 2.5×10^{-4} M. A colloidal silver sol was also prepared according to the method of Creighton et al., with slight modification.[9]

The UV-Vis spectrum of DDPT in aqueous solvent is shown in Figure 5.1. Raman spectroscopic studies were conducted using a 1:1 volume ratio of the aqueous stock solution (ca. 2.5×10^{-4} M) and the silver colloid solution (ca. 1×10^{-4} M) placed in a 1 cm quartz cuvette. For nonresonant excited Raman spectra of DDPT in the

homogeneous methanol solution and the mixed aqueous colloidal systems, the 705 nm line (of a Coherent Innova 200 argon-ion laser pumped Ti:Sapphire Coherent 899 ring laser) and the 514.5 nm line (of the same argon-ion laser) were used, respectively. For resonant excitation of Raman spectrum of the colloidal system, the 488-nm line of the argon-ion laser was used to pump a Coherent 599 dye laser using DCM to provide 646 nm radiation. Incident radiation entered at right angle to the collected Raman scattered light, which was focused onto the entrance slit of a 0.6 m Spex 1877 Triplemate grating spectrometer, with the 1200 gr/mm grating selected, and then imaged onto a Spex Spectrum-1 liquid nitrogen cooled charge-couple-device (CCD) detector.

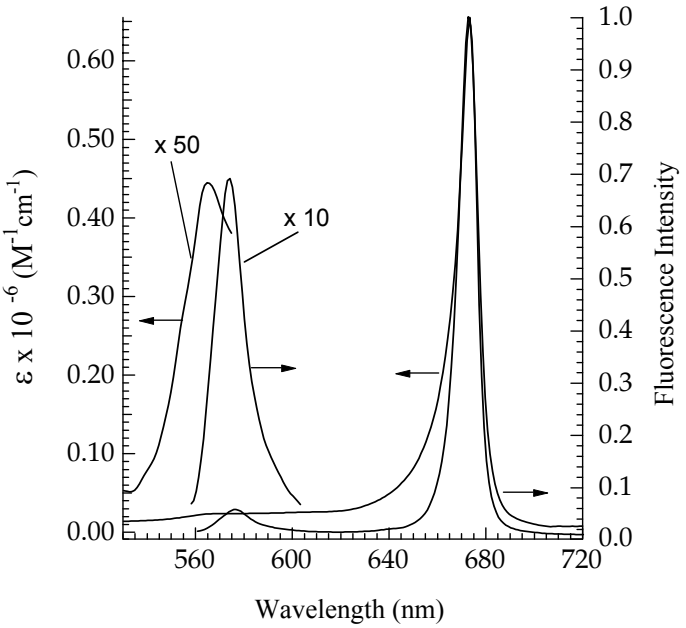

Figure 5-1: Absorption and fluorescence spectra of 10^{-5} M DDPT in water. Scale factors for enhancement of signals for weak bands are indicated as numbers tagged to bands. Spectra taken from earlier paper published by D. L. A. (Özçelik, S.; Akins, D. L. *J. Phys. Chem. B* **1999**, *103*, 8926.).

Calculations: The ground state geometry of the DDPT was optimized without symmetry restriction on the initial structure. Both structure optimization and vibrational analysis calculations were implemented by using DFT with functionals,[10] specifically, B3LYP, in which the exchange functional is of the Becke's three parameter type, including gradient correction,[11] and the correlation correction involves the gradient-

corrected functional of Lee, Yang and Parr.[12] The basis set of split valence type 6-31G(d),[13] as contained in the Gaussian 98 software package, was used.[14] The vibrational mode descriptions were made on the basis of calculated nuclear displacements and relative intensities associated with measured vibrational frequencies and intensities, combined with visual inspection of the animated normal modes, to assess which bond and angle motions dominate the mode dynamics attributed to a particular vibrational band for the molecule.

5.3 Results and Discussion

Structure: The structure and atomic labeling of the DDPT molecule are depicted in Figure 5.2. The DFT method at the B3LYP/6-31G(d) level indicates that, as mentioned, there are two possible low energy geometric structures (see Figures 5.3 A and 5.3 B) for the gas phase species. The most stable of these structures is not quite planar, the two planar benzothiazole moieties twisted by 14.4° with respect to one another; the ethyl groups point in the opposite direction to the phenyl group on the methine change; while the methyl groups of the ethyl substituents are positioned on opposite sides of the structural surface of the macrocycle (see Figure 5.3 A). Hereinafter, this structure is referred to as the trans-configuration. The second favorable structure is planar (see Figure 5.3 B) with the methyl groups lying on the same side of the surface of the macrocycle (i.e., the cis-conformer). In both cases, the methyl groups are approximately perpendicular to the structural surface of the macrocycle, and the phenyl rings on the respective methine bridges make angles of 83.4° and 89.7° for the trans- and cis-conformers, referenced to the structural surface of the macrocycle. Calculations indicate that the cis-configuration lies only 107 cm-1 above the energy of the trans-conformer,

and, therefore, both structures are likely populated at room temperature.

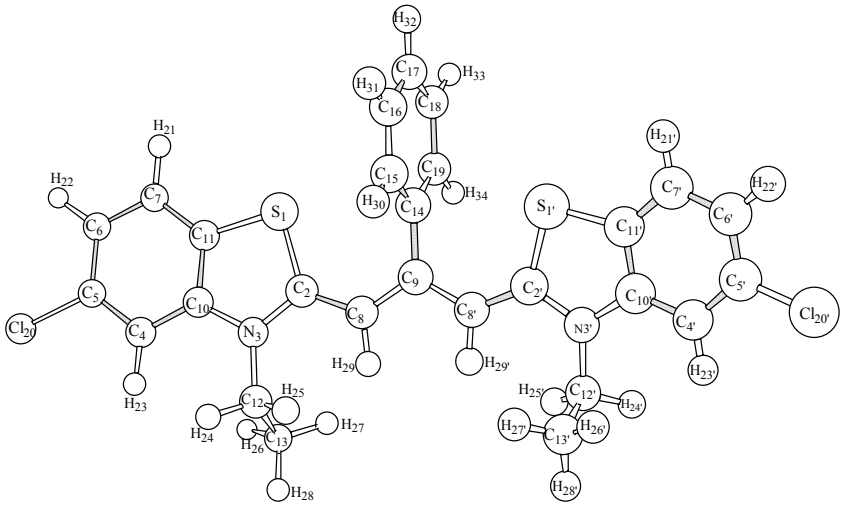

Figure 5.2: Structure and atomic labeling of the DDPT molecule.

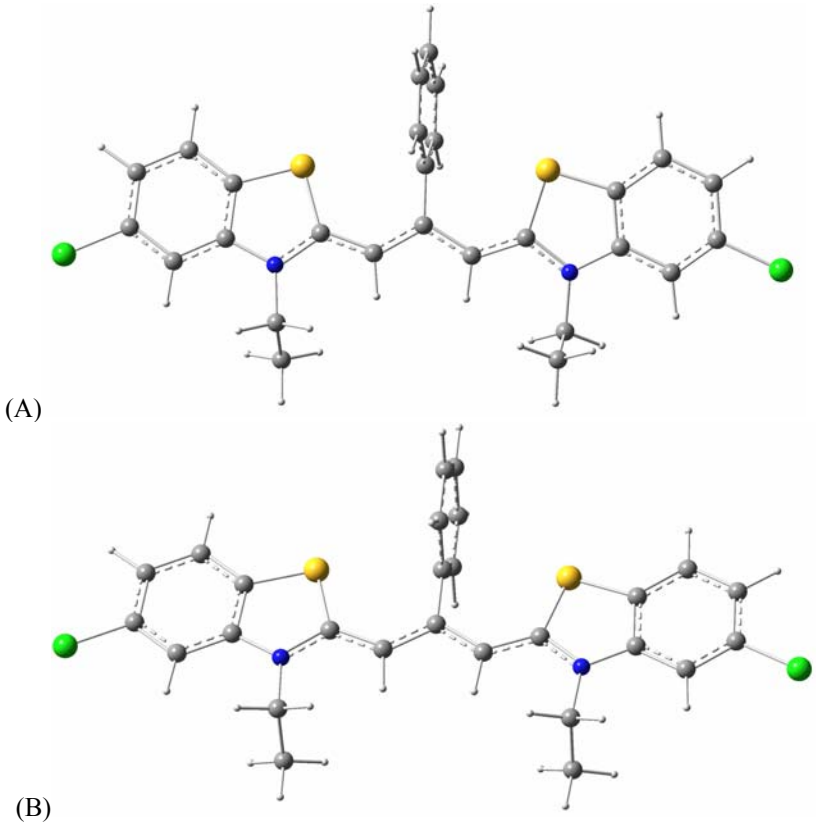

Figure 5.3: Low energy geometrical structures of DDPT calculated by the DFT method at the B3LYP/6-31G(d) level. (A) Trans-conformer; (B) cis-conformer.

The molecular structure of the DDPT is similar to that of the 3,3'-diethylthia-carbocyanine (DTCC), for which, in 1959, Wheatley studied the molecular structures of the solvated[15] and nonsolvated[16] DTCC-bromide crystals using X-ray single crystal methods. In those studies, it was determined that despite very close molecular dimensions of the cation, the molecular and crystal structures of the solvated and nonsolvated molecules were different. In particular, the nonsolvated cation was determined to be planar, with the methyl groups of the ethyl substituents lying on the same side of the cationic plane; the solvated form was found to deviate somewhat from being planar, with the two benzothiazole moieties twisted through an angle of 8^{o} with respect to one another, while the methyl groups of the ethyl substituents were determined to be on opposite sides of the cationic plane.

The nonplanarity of the solvated cation was not attributed to interaction with the ethanol solvate because there were no short contacts between the solvent and the atoms of the cationic plane that might account for the departure of the cation from planarity as a result of packing forces.[16] The experimentally determined molecular structures of the solvated and nonsolvated form of the DTCC cation are with those predicted for the two molecular structures of DDPT calculated using the DFT method reported herein.

Tables 5.1-5.3 provide predicted bond distances and angles for gas-phase DDPT as well as measured values of bonds and angles for the DTCC cation. For the latter, the bond length for the nonsolvated species is reported to a precision ca. 0.1 Å.[15] The predicted values of the bond lengths and angles of the DDPT cation are in good agreement with X-ray measurements for both of the solvated and nonsolvated forms of DTCC. (Note that in the tables, measured values for DTCC are provide in the format

(solvated/nonsolvated form)).

Table 5.1: DDPT bond lengths: calculated and experimental.

Bond	Trans-DDPT[(a)]	A[(b)]	Cis-DDPT[(a)]	B[(b)]
$S_1C_2/S_{1'}C_{2'}$	1.7610	1.79/178	1.7609	1.81/1.74
$S_1C_{11}/S_{1'}C_{11'}$	1.7582	1.73/1.77	1.7581	1.73/1.79
$C_2N_3/C_{2'}N_{3'}$	1.3705	1.43/1.38	1.3708	1.40/1.35
$N_3C_{10}/N_{3'}C_{10'}$	1.4006	1.41/1.41	1.4007	1.38/1.41
$N_3C_{12}/N_{3'}C_{12'}$	1.4748	1.48/1.49	1.4748	1.55/1.52
$C_4C_{10}/C_{4'}C_{10'}$	1.3982	1.39/1.41	1.3983	1.49/1.49
$C_5C_4/C_{5'}C_{4'}$	1.3936	1.40/1.42	1.3935	1.45/1.47
$C_5C_6/C_{5'}C_{6'}$	1.4014	1.41/1.41	1.4014	1.51/1.42
$C_6C_7/C_{6'}C_{7'}$	1.3923	1.39/1.39	1.3923	1.52/1.45
$C_7C_{11}/C_{7'}C_{11'}$	1.3934	1.39/1.38	1.3934	1.45/1.44
$C_{10}C_{11}/C_{10'}C_{11'}$	1.4015	1.41/1.42	1.4014	1.49/1.44
$C_2C_8/C_{2'}C_{8'}$	1.4019	1.41/1.45	1.4018	1.45/1.46
$C_8C_9/C_9C_{8'}$	1.4060	1.43/1.41	1.4060	1.45/1.46
$C_{12}C_{13}/C_{12'}C_{13'}$	1.5298	1.52/1.54	1.5297	1.54/1.54
C_9C_{14}	1.4947		1.4952	
$C_{17}C_{16}/C_{18}C_{17}$	1.3970		1.3971	
$C_{16}C_{15}/C_{19}C_{18}$	1.3946		1.3943	
$C_{14}C_{15}/C_{14}C_{19}$	1.4048		1.4046	
$C_5Cl_{20}/C_{5'}Cl_{20'}$	1.7469		1.7469	
$C_4H_{23}/C_{4'}H_{23'}$	1.0827		1.0827	
$C_6H_{22}/C_{6'}H_{22'}$	1.0839		1.0839	
$C_7H_{21}/C_{7'}H_{21'}$	1.0852		1.0852	
$C_8H_{29}/C_{8'}H_{29'}$	1.0846		1.0846	
$C_{12}H_{25}/C_{12'}H_{25'}$	1.0917		1.0917	
$C_{12}H_{24}/C_{12'}H_{24'}$	1.0923		1.0922	
$C_{13}H_{27}/C_{13'}H_{27'}$	1.0945		1.0945	
$C_{13}H_{26}/C_{13'}H_{26'}$	1.0942		1.0942	
$C_{13}H_{28}/C_{13'}H_{28'}$	1.0947		1.0947	
$C_{15}H_{30}/C_{19}H_{34}$	1.0865		1.0864	
$C_{16}H_{31}/C_{18}H_{32}$	1.0861		1.0861	
$C_{17}H_{32}$	1.0861		1.0861	

(a) The designations trans- and cis- refer to the relative positions of the methyl groups on the ethyl substituents. Trans- indicates that the methyl groups lie on opposite sides of the DDPT cation structural surface; cis- indicates that they lie on the same side. The bond lengths shown are calculated using B3LYP/6-31G(d).

(b) Measured bond lengths of the 3,3'-diethylthicarbocyanine cation for the methanol solvated form (A), see ref 19 and unsolvated form (B), see ref. 18. The uncertainty in the bond length for the unsolvated form is 0.1 Å.

Table 5.2: Bond angles of trans- and cis-DDPT.

Bond Angles	**Trans-DDPT[(a)]**	**Cis-DDPT[(a)]**	**Θ [(b)]**
C_6-C_5-C_4/$C_{6'}$-$C_{5'}$-$C_{4'}$	122.1	122.1	119/119
C_6-C_5-Cl_{20}/$C_{6'}$-$C_{5'}$-$Cl_{20'}$	119.2	119.2	
C_4-C_5-Cl_{20}/$C_{4'}$-$C_{5'}$-$Cl_{20'}$	118.7	118.7	
C_5-C_6-C_7/$C_{5'}$-$C_{6'}$-$C_{7'}$	119.8	119.8	124/118
C_5-C_6-H_{22}/C_5-C_6-$H_{22'}$	119.8	119.8	
C_6-C_7-C_{11}/$C_{6'}$-$C_{7'}$-$C_{11'}$	118.7	118.7	119/122
C_6-C_7-H_{21}/$C_{6'}$-$C_{7'}$-$H_{21'}$	120.3	120.3	
C_7-C_{11}-C_{10}/$C_{7'}$-$C_{11'}$-$C_{10'}$	121.1	121.1	114/119
C_{10}-C_{11}-S_1/$C_{10'}$-$C_{11'}$-$S_{1'}$	110.8	110.8	119/113
C_{11}-C_{10}-C_4/$C_{11'}$-$C_{10'}$-$C_{4'}$	120.6	120.6	129/120
C_{11}-C_{10}-N_3/$C_{11'}$-$C_{10'}$-$N_{3'}$	112.4	112.4	105/110
C_5-C_4-C_{10}/$C_{5'}$-$C_{4'}$-$C_{10'}$	117.6	117.6	114/121
C_5-C_4-H_{23}/$C_{5'}$-$C_{4'}$-$H_{23'}$	119.9	119.8	
C_{11}-S_1-C_2/$C_{11'}$-$S_{1'}$-$C_{2'}$	91.2	91.2	88/89
S_1-C_2-N_3/$S_{1'}$-$C_{2'}$-$N_{3'}$	110.6	110.6	109/111
S_1-C_2-C_8/$S_{1'}$-$C_{2'}$-$C_{8'}$	126.3	126.3	127/129
N_3-C_2-C_8/$N_{3'}$-$C_{2'}$-$C_{8'}$	123.1	123.1	122/120
C_{10}-N_3-C_{12}/$C_{10'}$-$N_{3'}$-$C_{12'}$	121.3	121.2	124/127
C_{10}-N_3-C_2/$C_{10'}$-$N_{3'}$-$C_{2'}$	115.0	115.0	117/116
C_{12}-N_3-C_2/$C_{12'}$-$N_{3'}$-$C_{2'}$	123.8	123.8	118/117
C_2-C_8-C_9/$C_{2'}$-$C_{8'}$-$C_{9'}$	129.3	129.4	115/118
N_3-C_{12}-C_{13}/$N_{3'}$-$C_{12'}$-$C_{13'}$	113.1	113.1	102/98
C_8-C_9-C_{14}/$C_{8'}$-C_9-C_{14}	121.0	121.0	
C_9-C_{14}-C_{15}/C_9-C_{14}-C_{19}	120.3	120.2	
C_8-C_9-$C_{8'}$	118.0	117.9	
C_{15}-C_{14}-C_{19}/C_{16}-C_{17}-C_{18}	119.4/120.0	119.4	
C_{14}-C_{15}-C_{16}/C_{14}-C_{19}-C_{18}	120.2	120.2	
C_{15}-C_{16}-C_{17}/C_{19}-C_{18}-C_{17}	120.1	120.1	
C_{14}-C_{15}-H_{30}/C_{14}-C_{19}-H_{34}	119.7	119.6	
C_{15}-C_{16}-H_{31}/C_{19}-C_{18}-H_{33}	119.7	119.7	
C_{16}-C_{17}-H_{32}/C_{18}-C_{17}-H_{32}	120.0	120.0	

(a) Same as (a) in Table 5.1.

(b) The bond angle (Θ) for the solvated form of 3,3'-diethylthiacarbocyanine; estimated using the GaussView package program from the orthogonal Cartesian coordinates provided in Ref. 19.

Table 5.3: Dihedral angles of trans- and cis-DDPT.

Dihedral Angles	Trans-DDPT[(a)]	Cis-DDPT[(a)]
C_4-C_5-C_6-C_7	0.2	0.2
C_4-C_5-C_6-H_{22}	180.0	180.0
Cl_{20}-C_5-C_6-C_7	-179.6	-179.6
C_6-C_7-C_{11}-C_{10}	-0.4	-0.3
C_6-C_7-C_{11}-S_1	179.7	179.5
C_7-C_{11}-C_{10}-C_4	0.7	0.7
C_7-C_{11}-C_{10}-N_3	-179.1	-179.1
S_1-C_{11}-C_{10}-C_4	-179.4	-179.2
S_1-C_{11}-C_{10}-N_3	0.8	1.0
C_{10}-C_{11}-S_1-C_2	0.3	0.1
C_{11}-S_1-C_2-C_8	177.2	178.3
C_{11}-C_{10}-N_3-C_{12}	178.4	178.5
C_2-N_3-C_{12}-C_{13}	-90.1	-89.4
N_3-C_2-C_8-H_{29}	5.3	3.8
N_3-C_2-C_8-C_9	-176.4	-176.3
C_2-C_8-C_9-C_{14}	3.6	0.1
C_8-C_9-C_{14}-C_{15}	83.4	89.7
C_8-C_9-$C_{8'}$-$C_{2'}$	-176.4	-179.4
C_9-C_{14}-C_{15}-C_{16}	179.8	180.0
C_9-C_{14}-C_{19}-C_{18}	179.8	-180.0
C_9-$C_{8'}$-$C_{2'}$-$N_{3'}$	-176.4	176.3
C_9-$C_{8'}$-$C_{2'}$-$S_{1'}$	5.1	-4.3
$C_{2'}$-$N_{3'}$-$C_{12'}$-$C_{13'}$	-90.1	89.4

(a) Same as (a) in Table 5.1.

The average C-C bond length of the trimethine bridge is found to be 1.4033 Å (1.424 Å/1.455 Å) and the 18 bonds of the phenyl groups average 1.3978 Å (1.397 Å/1.472 Å). The average value of the N-C bonds of the cation is 1.3705 Å (1.405 Å/1.375 Å) for the conjugated N_3-C_2-type bonds; 1.4006 Å (1.41 Å/1.395 Å) for N_3-C_{10}-type bonds; and 1.4748 Å (1.485 Å/1.535 Å) for the nonconjugated N_3-C_{12}-type bonds. These values are consistent with the well-known 1.34 Å for atomic N-C bonds and 1.47 Å for nonconjugated N-C bonds. Additionally, the C-C bonds of the ethyl groups average 1.5298 Å (1.53 Å/1.54 Å); the predicted C_{11}-S_1 and S_1-C_2 bonds are,

respectively, 1.7582 Å (1.75 Å/1.76 Å) and 1.7610 Å (1.785 Å/1.775 Å); and the C-Cl bonds average 1.7469 Å is in good agreement with the calculated value of 1.7394 Å[17] and experimental value of 1.737 Å[18] for the 1,1',3,3'-tetraethyl-5,5',6,6'-tetrachlorobenzimidazolo-carbocyanine (TTBC) cation.

The average values of the C-S-C and C-N-C bond angles of the thiazole moieties are calculated to be 91.2° (89.5°) and 115°(116°), respectively; the average Cl-C_5-C and Cl-$C_{5'}$-C angle is 119.2°, consistent with the calculated value of 117.67° and measured value of 116.1° for the TTBC cation; and the remaining phenyl angles average 119.6°(119.9°). As mentioned above and shown in Tables 5.1 and 5.2, the calculated bond distances and angles of the DDPT in the gas phase are to great accuracy consistent with the single crystal X-ray diffraction values for the DTCC[15,16] and TTBC[18] cations.

Information concerning the potential cause of the twist between the benzothiazole moieties is also provided by the structure calculation. The 14.4° distortion appears to be due to intramolecular steric interaction between H_{29} ($H_{29'}$) and the ethyl group at N_3 ($N_{3'}$) for the trans-conformation of the methyl groups of the ethyl substituents. As a result of this spatial proximity, the repulsive interaction between the ethyl groups and hydrogen on the bridge are in opposite directions for the trans-conformer and would explain the two benzothiazole moieties being twisted away from one another. For the cis-conformer, this repulsive interaction would be in the same direction, which would not result in a twist between the two chromophores. We calculate, additionally, that the average contacts between groups are: 2.530 Å for methylene–H on the trimethine bridge (i.e., $C_{12}\cdots H_{29}$); 7.084 Å for methylene···methylene (i.e., $C_{12}\cdots C_{12'}$); 7.180 Å for methyl···methyl (i.e., $C_{13}\cdots C_{13'}$); and 7.060 Å for methylene···methyl $C_{12}\cdots C_{13'}$ (and $C_{13}\cdots C_{12'}$). The dihedral

angles associated with N_3-C_2-C_8-C_9, C_2-C_8-C_9-$C_{8'}$, C_8-C_9-$C_{8'}$-$C_{2'}$, and C_9-$C_{8'}$-$C_{2'}$-$N_{3'}$ have the same value of -176.4°.

Charge Distribution: The calculated atomic charge distribution of the DDPT cation, using the B3LYP/6-31G(d) approach, is given in Table 5.4. For both conformers, our results indicate that the partial charge distribution of the DDPT cation is symmetrically distributed with respect to the y-axis, which passes through the C_9-phenyl bond. The charges among the atoms within the cation are found to be localized on the thiazole rings, with the sulphur and nitrogen atoms and their accompanying conjugated carbon atoms alternately charged negatively and positively. We find that the net charges on the nitrogen atoms are about twice that of their adjacent carbon atoms in the conjugated ring. Also, most of the partial charge among the atoms within the molecule is heavily localized on the C_{10}(0.1614), N_3(-0.3645) and S_1(0.5063) in the conjugated ring atoms and C_{13}(-0.6954) in side chain on the N atom. The remaining carbon atoms, including within the trimethine bridge, but not including the methyl carbon, have a relatively small and negative net charge. The chloride atoms have a small amount of net positive charge relative to their adjacent carbon atoms. Also, in the trimethine bridge, charge distribution alternates as follows: C_8(-0.3482), C_9(0.0672) and $C_{8'}$(-0.3482); in the phenyl ring on the bridge the localized charges are small and negative (<-0.2, see Table 5.4). The charge distribution, in general, is not symmetric with respect to the x-axis, leading to the y-component of the dipole moment alone differing from zero: μ_x= -0.0004, μ_y= -1.7209 and μ_z= 0.0004 Debye; where the x-axis is along the long molecular axis, the y-axis along the C_9-phenyl ring on the trimethine bridge, and the z-axis is perpendicular to the (x,y)-plane.

Table 5.4: Calculated atomic charges and dipole moments of the DDPT cation at the B3LYP/6-31G(d) level.

Thiacarbo-cyanine	Trans-DDPT[(a)]	Cis-DDPT[(a)]
S_1, $S_{1'}$	0.3455	0.3460
C_2, $C_{2'}$	0.1395	0.1397
N_3, $N_{3'}$	-0.5193	-0.5200
C_4, $C_{4'}$	-0.1511	-0.1512
C_5, $C_{5'}$	-0.0900	-0.0900
C_6, $C_{6'}$	-0.1094	-0.1094
C_7, $C_{7'}$	-0.1768	-0.1769
C_8, $C_{8'}$	-0.2697	-0.2688
C_{10}, $C_{10'}$	0.3719	0.3719
C_{11}, $C_{11'}$	-0.1693	-0.1695
C_{12}, $C_{12'}$	-0.1801	-0.1799
C_{13}, $C_{13'}$	-0.4556	-0.4553
Cl_{20}, Cl_{20}'	0.0332	0.0332
H_{21}, $H_{21'}$	0.1775	0.1775
H_{22}, $H_{22'}$	0.1857	0.1857
H_{23}, $H_{23'}$	0.1793	0.1794
H_{24}, $H_{24'}$	0.1929	0.1928
H_{25}, $H_{25'}$	0.1859	0.1854
H_{26}, $H_{26'}$	0.1822	0.1821
H_{27}, $H_{27'}$	0.1704	0.1709
H_{28}, $H_{28'}$	0.1826	0.1824
H_{29}, $H_{29'}$	0.1503	0.1497

Phenyl Group	Trans-DDPT[(a)]	Cis-DDPT[(a)]
C_9	0.1782	0.1779
C_{14}	-0.0836	-0.0844
C_{15}	-0.1315	-0.1292
C_{16}	-0.1266	-0.1265
C_{17}	-0.1231	-0.1233
C_{18}	-0.1266	-0.1264
C_{19}	-0.1315	-0.1337
H_{30}	0.1548	0.1547
H_{31}	0.1612	0.1614
H_{32}	0.1620	0.1619
H_{33}	0.1612	0.1611
H_{34}	0.1548	0.1553
H_{33}	0.1612	0.1611
H_{34}	0.1548	0.1553

μ_x	-0.0004	-0.0001
μ_y	-1.7209	-1.7317
μ_z	0.0004	-0.2077
μ_{tot}	1.7209	1.7441

(a) Relates to the same information as in Tables 5.1-5.3. For calculated dipole moments, the molecular coordinates are defined as: x-direction along the long molecular axis; y-direction along the axis passing through the C_9-phenyl bond; and, the z-direction perpendicular to the x-y plane.

The predicted charge distribution of the cation suggests a structural picture for the aggregate in which the DDPT cations within the aggregate are aligned such that the benzothiazole moieties of adjacent cations have a center of inversion relationship between them.

Vibrational Mode Assignments: The observed vibrational bands in the Raman spectrum of the DDPT cation in methanol were assigned based on the density functional prediction at the B3LYP/6-31G(d) level for the gas phase species. The calculated vibrational frequencies coincided with those observed in the Raman spectrum of DDPT using a linear factor of 0.973. We used the calculated frequencies in conjunction with the calculated intensity distribution to attribute observed vibrational frequencies and intensities to specific intramolecular motions of DDPT. These latter assessments were facilitated by analysis of the calculated nuclear displacements combined with animation of their vibrations, to identify specific motions as the dominant movements within the molecule. This is not a truly rigorous approach but should provide adequate insight. The assignments of the vibrational mode are provided in Table 5.5, while Figure 5.4 provides nuclear displacement for several selected vibrational modes. For this figure, since the vibrational motions of DDPT are spatially symmetrical with respect to the phenyl ring on the trimethine bridge, we display nuclear displacements using only half of the DDPT cation.

Table 5.5: Vibrational Raman band assigned to motions associated with normal vibrational modes of DDPT.

$\Delta\bar{\nu}^{calc.}_{unscaled}$	$\Delta\bar{\nu}^{calc.}_{scaled}$	**Intensity ($Å^4$/amu)**	$\Delta\bar{\nu}^{meas.}$ **monomer**†	$\Delta\bar{\nu}^{meas.}$ **aggregate**‡	**Assignment***
134.5	130.9	0.8		161	τ_{op}(Q)/w_{op}(Brd)
198.0	192.7	2.5		161	τ_{op}(Q)/w_{op}(Brd)/ρ(ethyl, C_2H_5)
224.1	218.0	2.7		212	w_{op}(bridge Ph.)/ρ(methyl, CH_3)
252.7	245.9	5.1		250	w_{op}(Brd)/δ_{op}(Q)/ρ(ethyl)
283.0	275.4	4.6		274	δ_{op}(Q)/w_{op}(Brd)/ρ(ethyl)
375.1	364.9	25.4		365	R_{ip}(half-Ph)/ρ(ethyl).
445.6	433.6	7.1		440	δ_{op}(bridge Ph.)/w(Brd)/ρ(methylene, CH_2)
483.0	469.9	10.6	471	471	R_{ip}(Q)/ρ(CH_2)/weak w(Brd)
613.4	596.9	65.9	598	598	τ_{op}(Q)/ρ(CH_2)/w_{op}(CH)$_{Brd}$
739.5	719.6	13.7	714	714	δ_{ip}(Q)/w(CH_2)
879.7	856.0	87.8	870	870	ρ(ethyl)/τ_{ip}(Q)/β(CH)$_{Brd}$.
1151.3	1120.3	726.7	1125	1125	δ_{ip}(half–bridge Ph.)/ν($C_8C_9C_{8'}$, Brd)/ρ(ethyl)/β(CH)$_{Ph\ at\ Brd}$
1174.7	1143.0	2072.5	1150	1150	δ_{ip}(bridge Ph.)/ν(Brd.)/ρ(ethyl)/weak δ_{ip}(Ph)/δ_{as}(Py)
1267.5	1233.3	3197.6	1237	1237	ρ(ethyl)/w(C_nH, n=4 and 7)/β(Brd)/weak δ_{ip}(Q)
1296.7	1261.7	501.6	1260	1260	β(CH)$_{Ph+Brd}$/τ(CH_2)/weak δ_{ip}(Q)
1402.0	1364.2	1057.7	1332	1332	w_{op}(CH_2)/β(CH)$_{Brd}$/weak δ_{ip}(Q)
1451.5	1412.3	249.7	1416	1416	β(Brd)/weak δ_{ip}(half-bridge Ph.)/β(CH)$_{Ph-Brd}$/weak ρ(methyl)
1474.6	1434.8	3450.0	1441	1441	$\delta_{ip,as}$(Q)/β(CH)$_{Ph}$/τ(methylene)
1509.0	1468.3	827.0	1471	1471	δ_{ip}(Ph)/weak δ_{ip}(Py)/β(CH)$_{Ph}$
1539.6	1498.1	3023.8	1504	1504	ν_{as}($C_8C_9C_{8'}$, Brd)/ρ(ethyl)/β(CH)$_{Brd}$
1600.9	1557.7	3305.3	1553	1553	ν_{as}(NC_2C_8)/β(Brd)/β(CH)$_{Brd}$/ρ(CH, in CH_2)
1622.4	1578.6	2353.0	1579	1579	δ_{ip}(Ph)/δ_{ip}(Py, half-ring)/β(CH)$_{Ph}$
1638.8	1594.5	149.6	1607	1607	δ_{ip}(Ph)

The scaling factor used is 0.975.

† Off-resonance Raman of the monomeric species was acquired using 705 nm excitation.

‡ Resonance Raman of the aggregate was acquired using 646 nm excitation.

* The identifications of specific motions of DDPT are represented by the following: deformation (δ); rotation (R); stretching (ν); rocking (ρ); wagging (w); twisting (τ); bending (β)--in-plane (ip) and out-of-plane (op); conjugated phenyl moieties (Ph); thiazole moieties (Py); benzothiazole macrocycle (conjugated phenyl plus thiazole moieties) (Q); trimethine bridge (Brd); asymmetric stretch (as).

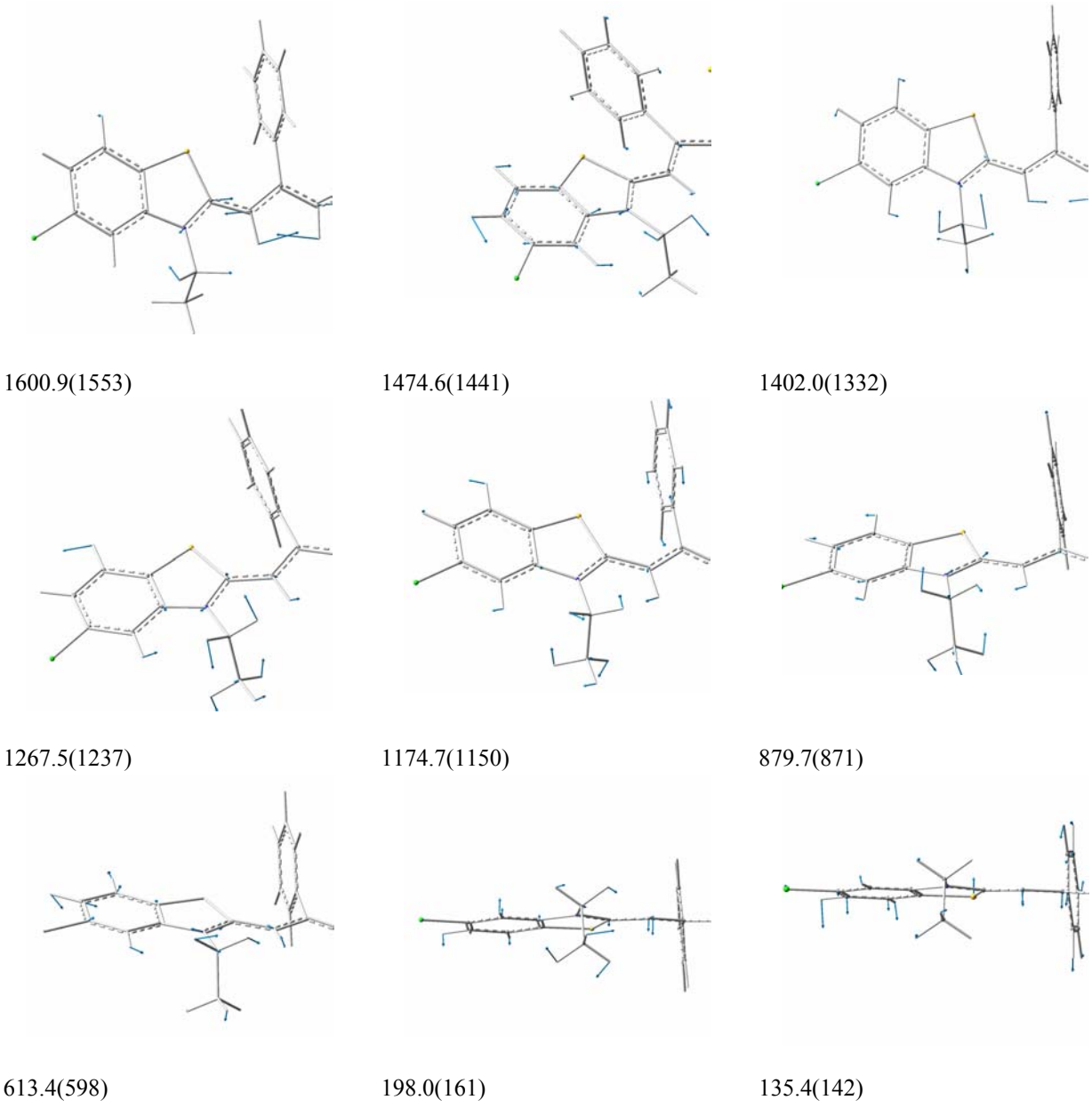

Figure 5.4: Calculated relative normal mode displacements for DDPT, as determined using B3LYP/6-31G(d) theory. Only the motion of half of the cation is provided since the other half undergoes the same movements.

The nonresonance Raman spectrum of monomeric DDPT exhibits many vibrational bands in the range 300-1700 cm^{-1}, as shown in Figure 5.5 A. The more intense Raman bands are found at 597, 1150, 1237, 1332, and 1442 cm^{-1}; medium intensity Raman features occur at 871, 1416, 1471, 1553 and 1579 cm^{-1}; and many relatively weak

peaks are dispersed throughout the spectrum. The calculations coupled with the animated motions suggest that the observed Raman vibrational modes of monomeric DDPT are due to symmetric and asymmetric skeletal deformations of the benzothiazole ring, combined with distortions of the trimethine bridge, as well as with rocking and wagging of the CH bonds in the phenyl central group.

Observed Vibrational Bands of Aggregated DDPT: There are several Raman bands of the DDPT cation whose decompositions into principal motions may provide high-resolution insight into intermolecular alignments of monomers within the aggregate structure. A method to make these special bands stand out from other bands, is to compare Raman spectra for DDPT existing as the isolated monomer versus intercalated within the aggregate. Further insight is gained by observing changes in Raman spectra of aggregated DDPT under both nonresonant and resonant excitation conditions. For nonresonant excitation, earlier studies from this laboratory have been interpreted as indicating that the Raman spectrum should emphasize the constricted environmental (or site) influence on vibrations, while the use of resonant excitation should identify bands whose motions have major components in the aggregate formation direction that should favor coupling between the motion of the exciton and charge oscillations associated with the vibrations.

Figure 5.5 shows Raman spectra of monomeric and aggregated DDPT with excitation at nonresonant wavelengths (Figures 5.5 A and 5.5 B, respectively). Comparison of the spectral patterns in these cases indicates that no significant shifts in spectral positions occur for any bands. However, significant differences in relative intensities are observed for many bands. For example, Figure 5.5 B when compared to

Figure 5.5 A indicates changes in the higher frequency region (associated with in-plane or very little motions of the macrocycle). The bands at 1332 and 1441 cm^{-1}, as indicated in Table 5.5, involve in-plane deformation (δ) of the macrocycle as well as component motions involving the methyl group within the ethyl attached to the benzothiazole moiety or phenyl group motions. Thus, it appears that vibrations involving the benzothiazole are enhanced when the molecule is part of the aggregate, even when nonresonant excitation is used. This is to be expected since π–π* interactions between aromatic chromophores are expected to play dominant roles in holding the aggregate together. And the motions of the aromatic groups, even when in-plane, are expected to be amplified through induced electronic distribution changes in adjacent aromatic chromophores, leading to increased polarizability of the aggregate structure, and enhanced Raman scattering.

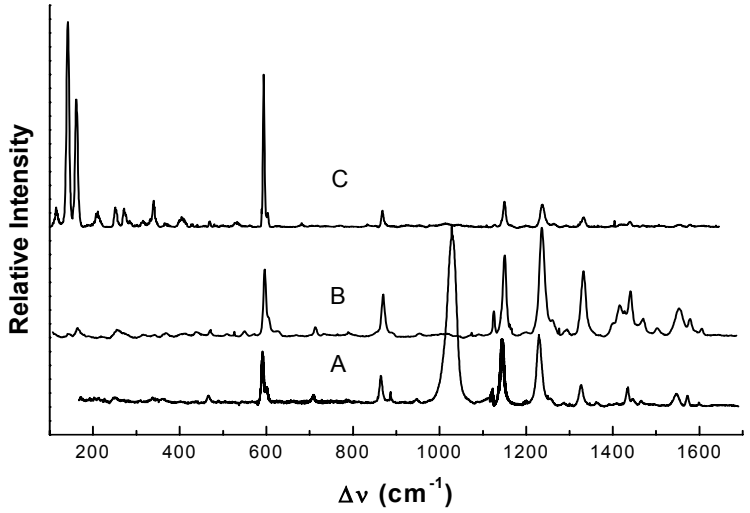

Figure 5.5: Raman spectra of monomeric and aggregated DDPT. (A) Nonresonant excitation of the monomer in MeOH solution using 705 nm radiation; laser power 300 mW at source, and accumulation time 12 minutes. (B) Nonresonant excitation of aggregate adsorbed onto aqueous Ag sol particles excited using 514.5 nm radiation; laser power 25 m, and accumulation time 2 minutes. (C) Resonance Raman spectrum of same system as (B) excited using 646 nm radiation; laser power 12 mW, and accumulation time of 6 s. (A), (B) and (C) have spectral resolution of 0.4 nm.

With resonant excitation (see Figure 5.5 C), three bands are found to be significantly affected. One of these bands, the isolated band at ca. 598 cm^{-1}, is found to involve twisting of the macrocycle (i.e., $\tau_{op}(Q)$) as well as rocking of the ethyl CH_2 (i.e., $\rho(CH_2)$), and out-of-plane wagging (i.e., $w_{op}(CH)_{Brd}$) of the CH in the methane bridge (see Table 5.5). The other two bands that are dramatically enhanced with resonance excitation are those at 142 and 161 cm^{-1}. The Raman band at 142 cm^{-1} is assigned to out-of-plane twisting of the benzothiazole moieties (i.e., $\tau_{op}(Q)$) accompanied by out-of-plane wagging of the bridge. The Raman feature at 161 cm^{-1} is attributed to out-of-plane twisting of the benzothiazole moieties (i.e., $\tau_{op}(Q)$), combined with out-of-plane wagging of the trimethine bridge (i.e., $w_{op}(Brd)$), and rocking of ethyl group (i.e., $\rho(ethyl)$). As mentioned earlier, the motion that dominates in both is the out-of-plane distortion of the macrocycle. This determination is consonant with the expectation that resonant excitation should identify bands whose motions have major components in the aggregate formation direction. Phenomena quite similar to those described above have been addressed in several earlier papers from this laboratory that have focused on so-called aggregation-enhanced scattering (AERS) theory,[19] which utilizes Herzberg-Teller intensity borrowing as developed by Albrecht.[20] In these publications, Akins has shown that the enhancement of Raman bands for aggregated molecules is mainly attributable to the existence of molecular exciton states and the concomitant enhanced polarizability of the aggregate structure. The Raman intensity, which is proportional to the square of the polarizability (α), can be decomposed into three terms, as follows: $\alpha_{ij}^{gv',\, gv''} = A + B + C$, where i and j represent polarization directions, g indicates the ground electronic state, and v' and v" refer to upper and lower vibrational states. The *C* term, as has been shown earlier,[19(c)]

is expected to be less important than the *A* or *B* terms. In summary, the AERS formulation attributes bands that show substantial intensity enhancement upon use of resonance excitation as due to nonvanishing matrix elements involving excited-state lattice phonon modes of the aggregate, resulting from the intermolecular potential function, and intramolecular modes (i.e., *A*-term bands). Also, Raman bands that are present when either nonresonant or resonant excitation is used are *B*-term bands, and are likely fundamentals, since with nonresonant excitation, these same modes, as a result of closure over excited-state modes, must be fundamentals in the harmonic oscillator approximation.[21]

The structure of the aggregate: The arrangement of DDPT monomers within the aggregate can be inferred from the charge distribution and Raman bands that are enhanced when the aggregate is formed. The monomer's arrangement is reasonably envision as having the methyl group of the ethyl substituent assuming a minimal interaction with the phenyl ring on the trimethine bridge. Such an arrangement can occur when the DDPT monomers assume a staircase, shifted deck-of-cards alignment, allowing for minimum repulsive interaction. This model is also supported by the predicted charge distribution within the single molecule, where the charge is mostly localized on the thiazole moiety. The permanent dipoles would be aligned in parallel in this picture, but the transition dipole, calculated using the Gaussian 98 software, is found to have components, referenced to the center of each monomer, that leads to the x-component of the transition dipole moment alone differing substantially from zero: μ_x= 4.7181, μ_y= 0.0000 and μ_z= 0.0328 Debye; where the x-axis is along the long molecular axis, the y-axis along the C_9-phenyl ring on the trimethine bridge, and the z-axis is perpendicular to

the (x,y)-plane. The alignment of transition dipole, as a result, would be head-to-tail, corresponding to the alignment that defines the so-called J-aggregate structure.

5.4 Conclusion

We have coupled theoretical methods with Raman scattering experiments that enable us to give some insight into aggregation of the DDPT cation. The DFT method at the B3LYP/6-31G(d) level, indicates that there are two favorable ground state-molecular structures for the DDPT cation, as determined by the relative positions of the methyl groups of the ethyl substituents relative to the surface defined by the macrocycle chromophore. One of these conformers has a trans- arrangement of the methyl groups, resulting in the groups protruding in opposite directions from the surface, while the other conformer, i.e., the cis-conformer, has the methyl groups on the same side of the macrocycle's surface. The cis-conformer is found to be planar, while the trans-conformer is twisted, with an angle of 14.4° between two benzothiazole moieties. Additionally, the angle between the benzothiazole moieties and phenyl group at the trimethine bridge is 83.4° for the trans-conformer and 89.7° for the cis-conformer. The lowest equilibrium ground state energy of the cis-conformer is found to lie 107 cm^{-1} above the trans-conformer.

The arrangement of monomers within the aggregate appears to be described by the traditional spread card deck model that gives rise to essentially parallel permanent dipole moments and a head-to-tail alignment of transition dipole, leading to the so-called J-aggregate structural picture.

6 Preparation of J-aggregates Coated Metal Nanoshells

6.1 Introduction

Metal nanoshells are a novel, fascinating type of composite spherical nanoparticle consisting of a dielectric core covered by a thin metallic shell, hence, termed "nanoshells." This configuration of a dielectric core covered with a thin metallic shell leads to quite remarkable properties for the nanoshell that differ dramatically from solid gold nanoparticles, like colloidal gold, a typical metallic nanoparticle. Nanoshells possess highly favorable optical and chemical properties for imaging and other unique applications in many areas such as nonlinear optics, catalysis, and SERS.[1,2] Further applications include environmental,[3] chemical,[3] and biological sensing.[4] Au nanoshells, in particular, are qualified for use in some of these various applications because of the well established functionalization chemistry of gold surfaces.[5]

As pointed out in previous chapters, the intense optical absorption of metal nanoparticles is derived from the collective electronic, or plasmon, resonance of the bulk metal, as modified by boundary conditions imposed by the nanoparticle geometry. In other words, the collective electronic resonance frequency in metal nanoparticles is dependent not only on the type of metal, but also on its shape. For instance, the plasmon resonance frequency of a metallic nanoparticle often repeated by $\omega = 3^{-1/2}\ \omega_{p,}$ where ω_p is the plasmon frequency of the bulk metal. For a thin film, however, the plasmon frequency often is given as $\omega = 2^{-1/2}\ \omega_p$, scaled relative to the bulk surface plasmon.[6] This scaling behavior suggests that modifying the shape of the metal nanostructure from the typical solid sphere would allow the modification of its optical response, and perhaps enable manipulation of that response though systematic modifications of the nanoparticle

structure.

A nanoscale geometry that has proved particularly easy for fabrication and structural manipulation of its optical response is that of a spherical dielectric core surrounded by a thin, uniform, metallic shell. The plasmon resonance of this structure, termed metal nanoshell, is determined by the relative core and shell size. The original properties of metal nanoshells were predicted by Aden and Kerker in 1951;[7] further theoretical considerations were detailed by Neeves and Birboim in 1989.[8] From the early theoretical work analyzing the surface plasmon response of metal nanoparticles, which focused on solving Maxwell's equations for a plane wave incident on a nanoparticle of high symmetry,[8,9] to subsequent theoretical advances in the development of computational techniques for the calculation of the electromagnetic response,[10] recently, a new conceptual approach for understanding the plasmon response of metallic nanostructures, known as "plasmon hybridization," has been developed.[10(b)] This plasmon hybridization model has been used to further explain the optical properties of nanoshells.

Several techniques have been developed for the fabrication of metal nanoshells on both the nanometer and micrometer scales. These techniques include chemical reduction,[11] electrostatic attraction,[12] self-assembly,[13] and the combination of self-assembly and seeding.[14,2(a)] Furthermore, an aggregation-based method[15] for the fabrication of nanoshells with tunable thickness and surface roughness and gold nanoshells having hollow interiors and thin wall synthesis method have also been developed.[3]

In the present studies, Au nanoshells have been synthesized using two methods: first, a one- step chemical method, involving the chemical reduction of $HAuCl_4$ to Au in

the presence of an aged Na_2S solution[5] and second, a procedure that involved the template-engaged replacement reaction between silver nanoparticles and an aqueous $HAuCl_4$ solution.[3] The first method yielded nanoshell with a solid core whereas the second method yielded nanoshell with a void space, hence, a hollow nanostructure. The resulting gold nanoshell was used to induce formation of J-aggregates of 3,3'-diethyl-5,5'-dichloro-9-benzothiacarbocyanine (DDPT). Examination of the literature shows that no attempts have been made before to prepare nanoshells, specifically, gold nanoshells coated with cyanine dyes J-aggregates. However, prior studies on several aggregated cyanine dyes in heterogeneous systems have been reported. For example, aggregation of cyanine dyes on electrode surfaces[16] as well as on the surfaces of different colloidal particles[17] has been reported and has provided evidence of aggregate formation on these particular surfaces. In this chapter, experimental results that demonstrate the formation of J-aggregates on the surface of the Au nanoshells are presented. UV-Visible spectroscopy, transmission electron microscopy (TEM), and atomic force microscopy (AFM) are used as spectroscopic and microscopic tools to characterize the gold nanoshell. Moreover, J-aggregate-coated Au nanoshells have been characterized using UV-Visible spectroscopic parameters such as the position and width of the absorption band, fluorescence and Raman spectroscopy.

The Au nanoshell system presents a new environment, an acidic environment, different from the usual basic media that generally are used for cyanine dyes J-aggregation formation. Metal nanoparticle-dye composites, taking advantage of the inherent optical properties of the nanoparticle and cyanine dyes, in particular the J-aggregates optical properties, are very promising for designing materials with novel

optical and photochemical properties. Such nanoshell-dye hybrid system may possibly permits the development of high sensitivity labels by allowing for large chromophore density on the nanoshell surface. Lastly, nanocomposites consisting of J-aggregate coated gold nanoshells may be used as photoresponsive nanomaterials in the design of novel photon-based devices based on their absorption and fluorescence properties.

6.2 Experimental

6.2.1 Materials

All reagents were purchased from the indicated suppliers and used as received. The following chemicals were obtained from Aldrich: Chloroauric acid ($HAuCl_4 \bullet 3H_2O$), sodium sulfide (Na_2S), sodium citrate, silver nitrate, anhydrous ethylene glycol, (HPLC)-grade methanol, ethanol, H_2O_2, H_2SO_4, (3-aminopropyl)trimethoxysilane (APTMS) and poly (vinyl pyrrolidone) (PVP, $M_W \approx 55\ 00$). Chloride salt of 3,3'-diethyl-5,5'-dichloro-9-benzothiacarbocyanine was purchased from the Japanese Research Institute for Photo-sensitizing dyes, Ltd. Water was triply distilled.

6.2.2 Preparation of Gold Nanoshells

Gold nanoshells with a gold sulfide core, i.e., solid core, and a gold shell (Au_2S/Au nanoshells) were prepared in water following the synthesis described by Zhou et al.,[18] using a two-step reaction of Na_2S with $HAuCl_4$. Typically, a sample is made by addition of 10 mL of 1 mM Na_2S to 10 mL of 2 mM $HAuCl_4$, which is then followed five minutes afterward by a second addition of 5 mL of 1 mM Na_2S. The Na_2S solution was aged for 24-48 h prior to use. Upon sulfide addition, the yellow $HAuCl_4$ solution turned golden brown; then after approximately 20 min the solution turned purple and as time

progressed, the solution retained its purple color. The reaction for the reduction process leading to the growth of the Au_2S/Au nanoshell is as follows:[19]

$$2AuCl_4^- + 3HS^- \rightleftharpoons 2Au + 3S + 3H^+ + 8Cl^-$$

Au and S are then available for subsequent nucleation and growth. The Na_2S solution was used one or two days after it was made in order to increase the HS^- activity. Solid Au, Au_2S and Au/Au_2S nanoshell are formed simultaneously under these reaction conditions. The pH of the reaction was 2.86 at the beginning and ended at 2.52 by the end of the reaction.

Gold nanoshell with a central void space, in other words a hollow core, was prepared using the method of Xia et al.[3] Briefly, silver nanoparticles were first prepared using the polyol process. The gold nanoshells were then prepared via a template-engaged replacement reaction between the silver nanoparticles and an aqueous $HAuCl_4$ solution. In a typical replacement reaction, a 250 μL aliquot of Ag nanoparticles was diluted with 5 mL of water and then refluxed at boiling temperature for 10 min. Then, an aliquot of 1 mM $HAuCl_4$ aqueous solution was added dropwised to the refluxing dispersion and the mixture would be continuously refluxed until its color had become stable. The resulting nanoshells, recovered via centrifugation, according to Xia et al. have a core consisting of the dielectric medium in which they were prepared, i.e, water. Three different nanoshell samples with different absorption peaks, resulting from varied shell thickness, were synthesized using the electroless deposition process of Xia and co-workers.

6.2.3 Preparation of DDPT/Au Nanoshells Composites

DDPT J-aggregate-coated nanoshells were prepared by adsorbing DDPT dye molecules on the surface of the nanoshells. This was done by mixing 0.2 mL of 1.0 mM

DDPT in methanol and 5 mL of the solid core Au nanoshell solution for a final DDPT concentration of 4×10^{-4} M. For the hollow core system, an approximately 1×10^{-5} M DDPT aqueous solution was prepared by dilution with water from a stock solution of 1×10^{-4} M DDPT solution in methanol. Then, in a series of measurements, mixtures containing 2.50 mL DDPT, *x* μL Au nanoshell and distilled water for a final volume of 3.50 mL were prepared. The final volume was to ensure that the DDPT concentration was held constant (to approximately 7×10^{-6} M) in all the experiments.

6.2.4 Nanoshell Films

For AFM measurements, the putative Au nanoshells were deposited onto an APTMS functionalized glass substrate. As in the previously described deposition, glass slides were first cleaned for 15 min in a piranha cleaning solution (H_2O_2:H_2SO_4 1:3, V/V) at 60 °C, rinsed plentifully with water, and submerged in a vial of APTMS diluted 1:4 with HPLC grade methanol for 24 h. The slides were rinsed with methanol upon removal from the APTMS solution. These APTMS-coated glass slides were then immersed in an aqueous suspension of gold nanoshells for 24 h. Finally, the Au coated slides were taken out, rinsed with water and air-dried. AFM image of the coated slide was then recorded.

6.3 Results and Discussion

Figure 6.1 (A) displays the UV-Visible absorption spectra obtained following the nanoshell reaction as it proceeded over time. There are two peaks in each spectrum due to the simultaneous formation of solid Au nanoparticles and Au-coated Au_2S nanoparticles, in other words gold nanoshells. The absorption peak which remains at about 535 nm throughout the reaction has been attributed to the surface-plasmon resonance of the solid gold nanoparticles similar to the readily prepared gold sol in chapter 4 and in the

literature.[20] The second peak, a modified surface plasmon resonance absorption of the coated particle, is attributed to the Au-coated Au_2S nanoparticles as originally determined by Zhou et al.[18] As the reaction proceeds, this second peak initially move to longer wavelengths (red-shifted), and with time to shorter wavelengths (blue-shifted). Also, as the reaction progresses, the Au nanoshell absorption peak intensity increases and its full width at half maximum (FWHM) narrows.

It is worth mentioning that the formation of gold nanoshells on Au_2S via reduction of $HAuCl_4$ by Na_2S, the method used here, first reported by Zhou et al.[18] and recently used by Raschke et al. [5] is disputed by Zhang and co-workers.[21] Using TEM data, Zhang and colleagues reported to observe particles of different morphology. In addition to TEM, they used electron energy loss spectroscopy (EELS) and X-ray Absorption Fine Structure (XFAS) measurements to support their claim. The EELS data, according to Zhang, suggest that the $HAuCl_4$-Na_2S reaction produced Au aggregates. Also, their XFAS data taken at the AuL_3 edge is reported to show no evidence of distinct sulfur coordination shell, hence an unambiguous presence of metallic gold, while showing no sign of crystalline Au_2S. From these results, Zhang and co-workers proposed that the reduction of $HAuCl_4$ by Na_2S produced primarily "aggregates", not to be confused with J-aggregates, which are taken to be responsible for the observed near-IR plasmon resonance band in the UV-Visible spectrum. Raschke and Zhou, on the other hand, have attributed this near-IR plasmon band to the nanoshell formation. This dispute of aggregates vs. shell presents a problem that needs additional probing; however, resolving this problem or contribution to the dispute was not within the scope of the work presented in this chapter and therefore will not be fully addressed. The Au_2S/Au system

will continue to be referred to as Au nanoshells.

Figure 6.1 (B) shows the peak position of the absorption spectra of the metal core and gold nanoshells plotted as a function of time. The results demonstrate that the core peak remains steady while the nanoshell peak blue-shifted until stabilized at about 730 nm, which agrees with published Au nanoshells surface plasmon band.[5,18,19] The initial red-shift observed by Halas et al. was also observed, but is not evident from Figure 6.1 (B).

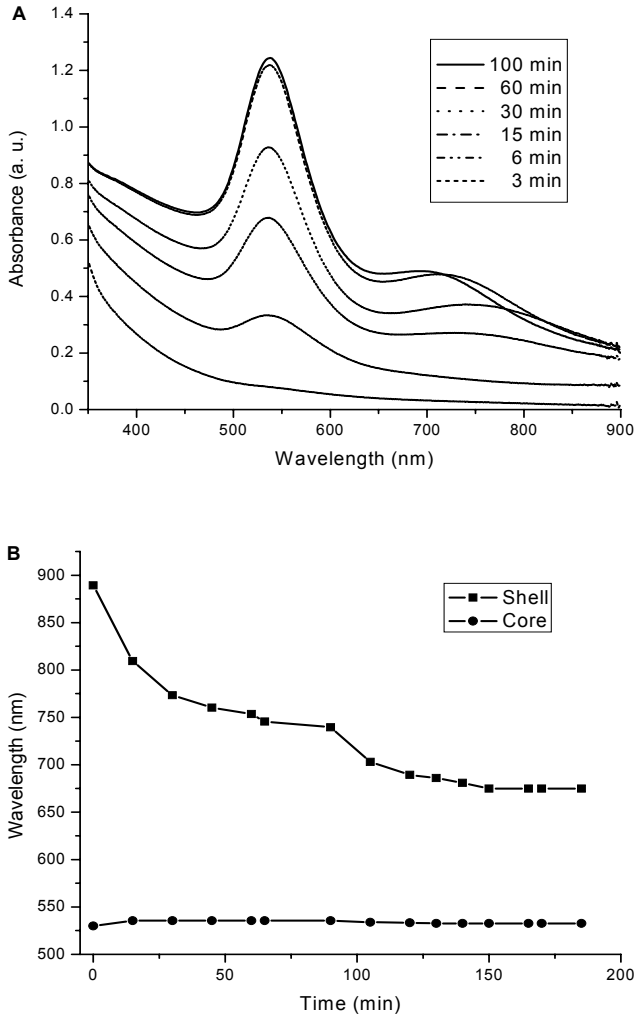

Figure 6.1: UV-Visible absorption spectra of Au nanoshells in aqueous solution: (A) The time evolution of the absorption spectra as the nanoshell growth proceeds on the Au_2S-core. (B) Variation in core and shell growth with time.

Figure 6.2 and Figure 6.3 show the image of a typical Au_2S/Au nanoshell taken by transmission electron microscopy (TEM) and atomic force microscopy (AFM), respectively. The TEM image shows small spherical particles coexisting with larger particles; this image and others do show clustering which supports Zhang's assertion of "Au aggregates" as oppose to Au nanoshells. The contact mode AFM image along with accompanying line scan in Figure 6.3 show representative Au nanoshells with an average size of about 45 nm that is in agreement with some of the reported sizes in the literature.[19] AFM, like TEM, shows similar clustering. Although both TEM and AFM images shown do not show different morphologies as reported by Zhang et al., one may possibly support a case for Au aggregates as opposed to Au nanoshell simply based on the clustering of the particles in the presented images. However, unlike what Zhang et al. have stated, the time evolution of the spectrum was reproduced several times. Also, because drying effect on the prepared slides or grid may be the cause of the clustering witnessed on the presented TEM and AFM images, the possibility of nanoshell formation as opposed to Au aggregates is also viable.

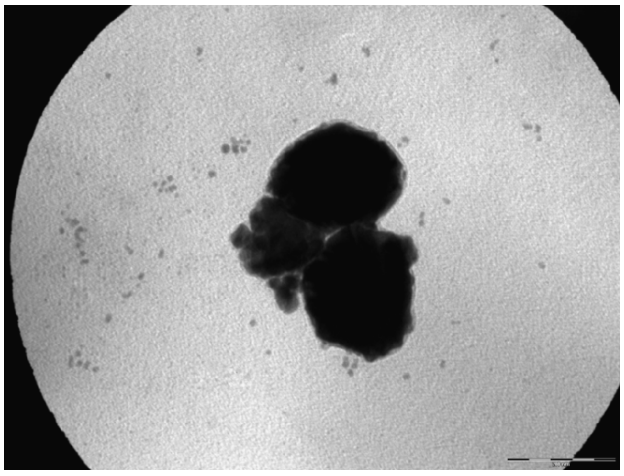

Figure 6.2: TEM image of Au/Au_2S nanoshell. The image was taken using a Zeiss EM 902 at 80 kV; the sample for TEM was prepared by placing a small drop of solution on a copper grid and allowing the solvent to evaporate at room temperature.

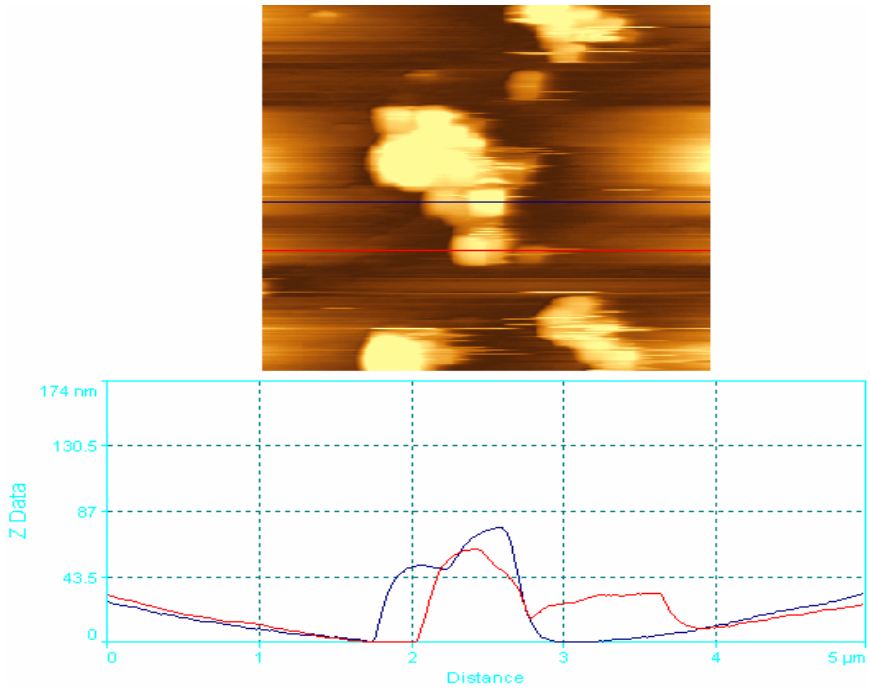

Figure 6.3: Contact mode AFM topography and corresponding line scans of Au/Au_2S nanoshell.

The aggregate vs. nanoshell dispute was further addressed in a comment on[22] and reply to comment on[23] exchange between the involve authors. Raschke and coworkers stood by their claims. Additional input is definitely needed for a consensus on this matter. Because of this dispute, a nanoshell system that did not have the gold nanoshells vs. gold aggregates ambiguity was prepared following the method of Xia et al. This method produced gold nanoshells with a void space, in other words a "hollow core", as opposed to the solid core of the first method.

Figure 6.4 shows the UV-Visible absorption spectra of the three differently prepared "hollow core" gold nanoshells. The different nanoshells, with varied wall thickness, exhibit surface plasmon bands at 611 nm (A), 685 nm (B) and 723 nm (C). These plasmon band values are taken to represent different nanoshell sizes, with (A) being the smallest and (C) being the biggest, as suggested by the red-shift in the UV-

Visible absorption spectra.

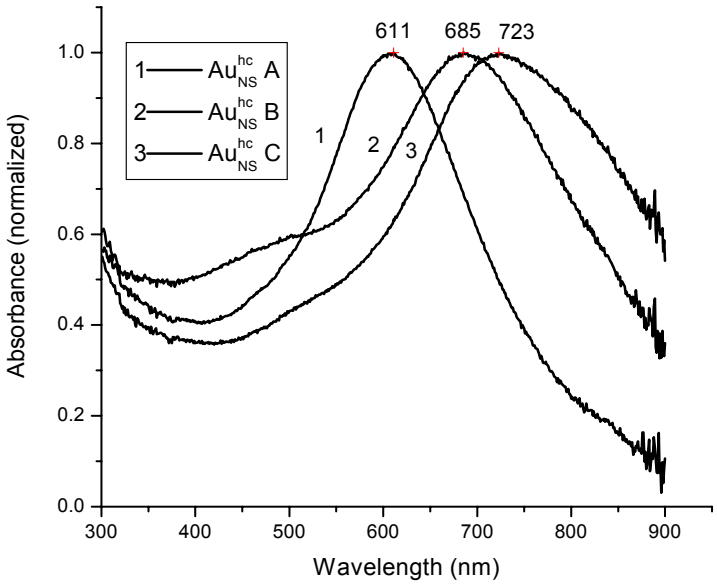

Figure 6.4: UV-Visible absorption spectra of Au nanoshells in aqueous solution.

It is noteworthy that the spectra, shown in Figure 6.4, do not show any evidence of the Ag nanoparticle surface plasmon resonance band which occurs at around 400 nm, indicating total consumption of the silver in the replacement reaction. There is also no significant feature at about 530 nm, the surface plasmon resonance peak for solid gold nanoparticles, indicating that solid gold was not formed during the reaction. The pH of the synthesized samples was 7.54 for (A), 4.70 for (B) and 4.91 for (C). The solid core (Au_2S/Au nanoshell) and some of the hollow core nanoshells (B and C) provided an acidic environment to probe DDPT J-aggregates formation.

Figure 6.5 shows a representative AFM image of sample (B) immobilized on glass slide treated with aminopropyltrimethoxysilane (APTMS). The results indicate well-defined and well-dispersed particles, for the most part (a few clusters are observed), with an average particle size of 26 ± 7 nm.

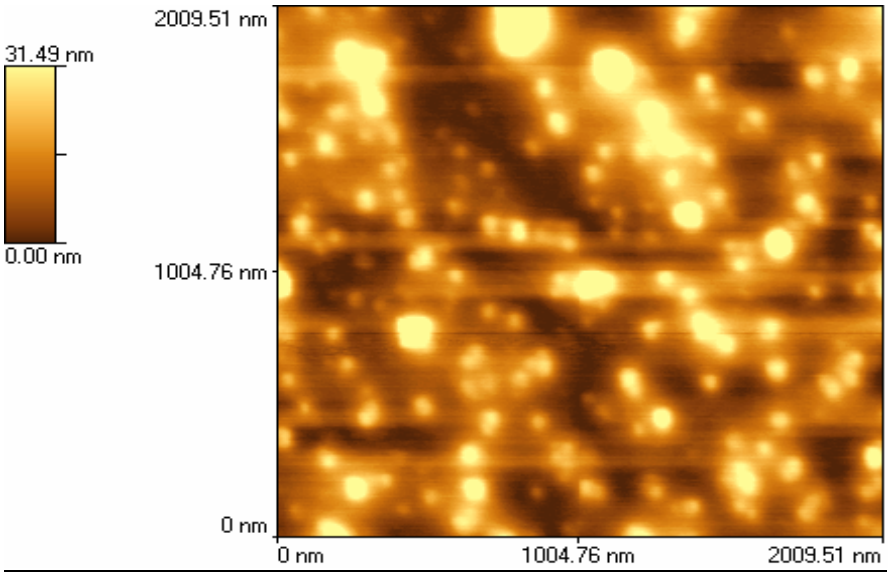

Figure 6.5: Representative AFM image of hollow core-Au nanoshells immobilized on APTMS derivatized glass slide.

Formation of DDPT J-aggregates onto the solid core nanoshell was confirmed by UV-Visible absorption spectrum as shown in Figure 6.6 (2). Figure 6.6 (1) and (3) shows the absorption spectrum of the native Au_2S/Au nanoshell and the DDPT monomer in methanol, respectively. DDPT monomer absorption spectrum has two main peaks at ca. 566 nm and 529 nm, attributable to the 0←0 and 1←0 vibronic transition, respectively. For the Au_2S/Au nanoshells absorption spectrum, the absorption peak at about 535 nm is due to the surface-plasmon-resonance of gold nanoparticles and the higher wavelength second peak at about 700 nm is attributed to the Au_2S/Au nanoshells. Now, cognizant of the aggregate vs. nanoshell dispute, this system is chosen to be referred to as Au_2S core-Au nanoshell (Au_2S/Au nanoshell), which is not confirmable.

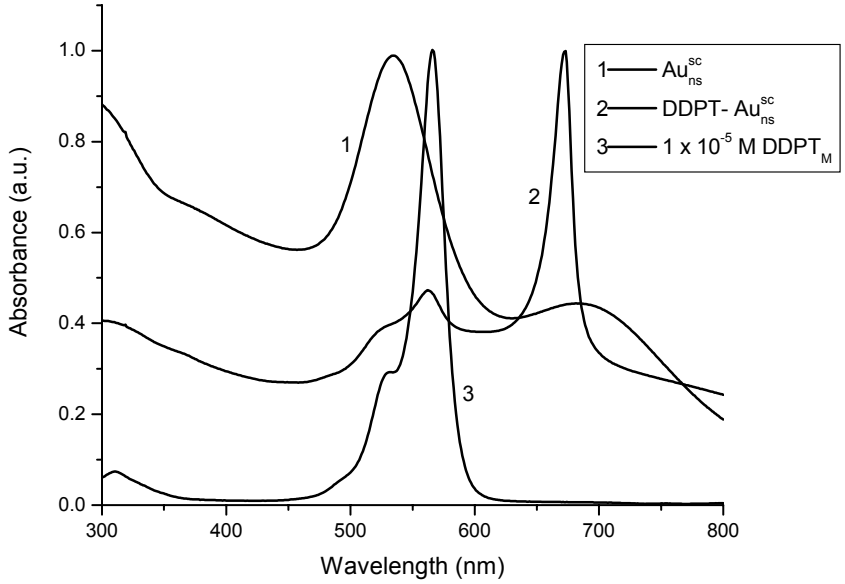

Figure 6.6: UV-Visible absorption spectra of (1) native Au_2S/Au nanoshell, (2) DDPT coated Au_2S/Au nanoshell and (3) DDPT monomer in methanol.

The absorption spectrum of DDPT adsorbed onto Au_2S/Au nanoshells, shown in Figure 6.6 (2), has an intense absorption band at ca. 673 nm and a much weaker band at 562 nm. The band at 673 nm is attributable to the J-aggregate, whereas the band at 562 nm, corresponding to a separation of 111 nm from the 562 nm band, unlikely to be due to a vibronic absorption band of the aggregate, is attributed to absorption by the monomer. The red-shift of the J-aggregate is due to the delocalization of the electronic excitation cause by dipole-dipole interactions between DDPT molecules. The narrow full width at half maximum, about 18 nm, at room temperature is an indication of a well ordered structure on the nanoshells surface. Gold nanoshells provided a surface for the nucleation and growth of DDPT molecules J-aggregates. The increase in baseline observed in the absorption spectra in Figure 6.6 (1 and 2) is due to inherent cloudiness of the nanoshell solution and additional cloudiness upon addition of DDPT to coat the nanoshells.

The hollow core nanoshells were also used for the formation of DDPT J-aggregates. Using the different size nanoshells prepared, size effect was again being probed as in chapter 4. Figure 6.7 shows UV-Visible absorption spectra of DDPT solution (2.50 mL) to which 1000 μL (A) and 200 μL (B and C) hollow core nanoshells were added followed by addition of water for a total volume of 3.5 mL for a final DDPT concentration of 7×10^{-6} M. Like on the solid core nanoshells surface, formation of DDPT J-aggregates onto the hollow core nanoshells was confirmed by the narrow red-shifted lower energy band with respect to the monomer band. The J-bands for DDPT coated hollow nanoshell A, B, and C, as shown in Figure 6.7 (A), (B) and (C), appear at 661 nm, 663 nm and 664 nm, respectively. The full width at half maximum (FWHM) for the J-bands was 40 nm for A, 34 nm for B, and 33 nm for C. Comparing the J-band position and FWHM obtained for DDPT coated onto solid-core with that of DDPT coated hollow core nanoshells, it is evident that there is a blue shift in the J-band from 673 nm [in the Au_2S/Au nanoshell, Figure 6.6 (2)], to 661 nm for hollow core nanoshell A, 663 nm for hollow core nanoshell B and 664 nm for hollow core nanoshell C. Also, the FWHM in the hollow core nanoshell solution is larger than that in the solid core nanoshell solution.

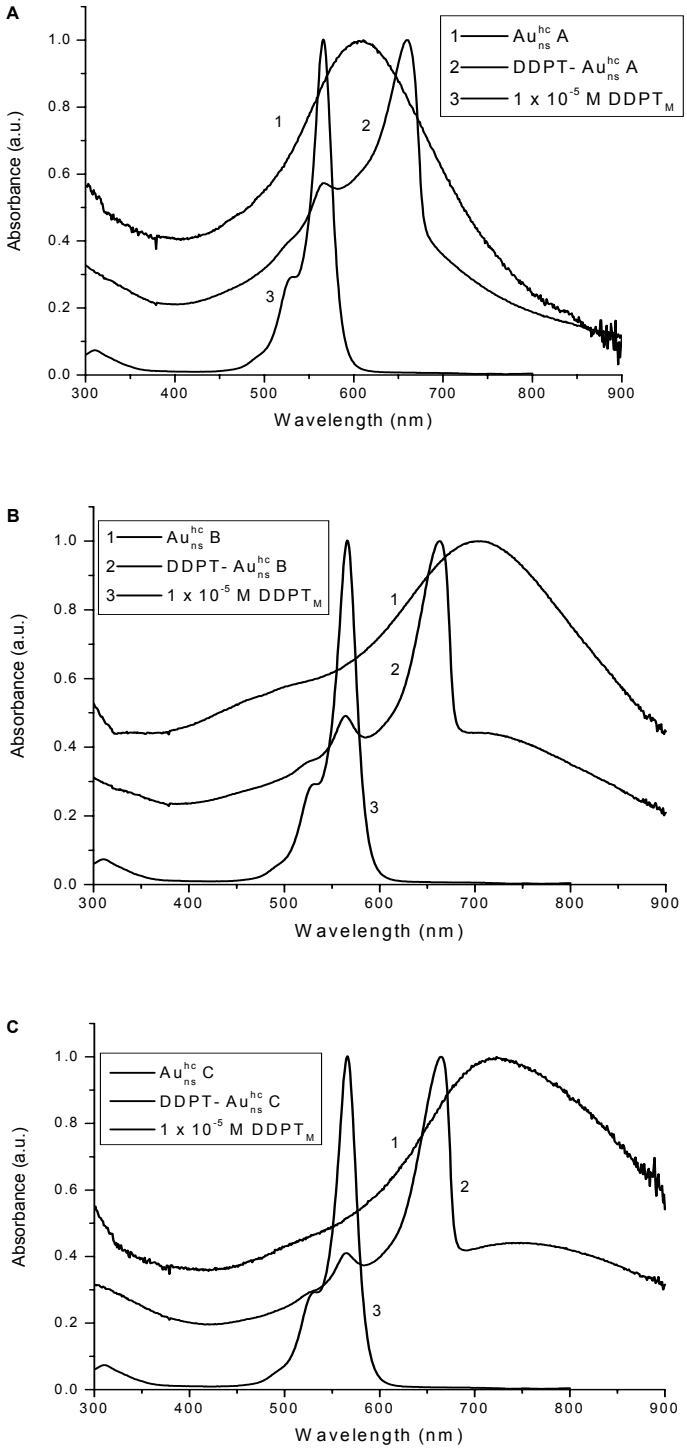

Figure 6.7: UV-Visible absorption spectra of 2.5 mL DDPT solution to which 1000 µL (A) and 200 µL (B and C) hollow core nanoshells were added for a total volume of 3.5 mL and DDPT final concentration of 7×10^{-6} M. 1, 2, and 3 in A to C represents the different nanoshell prepared (A, B, and C), DDPT coated nanoshells and DDPT monomeric solution, respectively.

J-aggregates coated Ag, Au, Au/Ag colloidal nanoparticles have been prepared previously,[17(a),20,24] but this is for the first time, to my knowledge, that this different nanoparticle system, i.e., Au nanoshells have been used as surface to induce J-aggregation. The results presented in this chapter for the J-aggregate coated nanoshells, to some extent, does not agree with the absorption peak and dip, or hole, reasoning presented by Kometani et al.[20] and Sato et al..[24(e)] This reasoning is that an absorption peak develops when the J-band peak (λ_{ex}) is located at a slightly longer wavelength than the surface plasmon peak (λ_{sp}) and that when λ_{ex} is located at a slightly shorter wavelength than λ_{sp}, a dip or hole is observed. The two nanoshell systems provide a good test case for this concept. In the solid core system, the Au_2S/Au nanoshell (λ_{sp} = 535 nm) is at shorter wavelength than the exciton band (λ_{ex} = 673 nm), whereas in the hollow core nanoshell system (nanoshell C), the λ_{sp} at about 700 nm, it is at longer wavelength than the exciton band (λ_{ex} = 673 nm). Thus, the J-aggregate peak observed in Figure 6.6 (2) is expected according to the concept above; i.e., a peak is expected since λ_{ex} is located at a slightly longer wavelength than $\lambda_{sp.}$ However, for the hollow core nanoshell, a dip was expected since the λ_{ex} is located at a slightly lower wavelength λ_{sp} = 673 nm. But, as can been seen in Figure 6.7 (B, 2) and (C, 2), the expected dip or hole was not observed.

Figures 6.6 (2), 6.7 (A, 2), 6.7 (B, 2) and 6.7 (C, 2) were all analyzed for indication of interactions between the nanoshells plasmon band and the exciton band. Although the solid core interacts with the monomer, the lack of interaction between the nanoshell peak and the exciton peak from Figure 6.6 (2), judging from the lack of peak shift, shoulder formation or peak broadening, may be suggestive that the nanoshell peak is not independent of the Au peak. Hence, supporting the Au aggregate position.

Adsorption studies like this may therefore be one possible way of probing the Au aggregates versus nanoshell question. This may be done by probing possible differentiation in the interactions of the two plasmon bands (core and shell) with the exciton band; assuming they are different species, different interactions may occur.

In the hollow core nanoshells, interactions with the monomer band, as in the solid core system, was clearly visible through the broadening of the high energy monomer shoulder (1←0 vibronic transition) and dampening of the monomer band (0←0 vibronic transition) itself. The interaction of the nanoshell peak with the exciton peak, unlike in the solid core nanoshell system, can be seen in Figure 6.7 (B, 2) and (C, 2). At the red tail of the two spectra, dampening in the nanoshell plasmon band is observed suggesting coverage of the nanoshells with J-aggregates. While J-aggregate formation is observed in both nanoshell systems, the results in Figure 6.6 and 6.7 suggest that better organized aggregates is obtained in the solid core system as confirmed by the lower energy and narrower aggregate exciton band.

Moreover, for the hollow core nanoshells, aging of the J-aggregates deposited onto the nanoshells was further probed using UV-Visible and fluorescence spectroscopy. The samples, which upon addition of nanoshells to DDPT solution resulted in immediate formation of J-aggregates, were allowed to stand for one week after which they were visually re-examined and UV-Visible and fluorescence spectra were recorded. The samples that showed evidence of precipitation were re-dispersed using sonication then their UV-Visible and fluorescence spectra were remeasured. Figure 6.8 depicts representative spectra of DDPT coated Au nanoshells (sample B) freshly prepared (1), after standing for 1 week (2) and upon redispersing (3). After standing for 1 week, the

sample showed evidence of precipitation and consequently the UV-Visible spectra of the supernatant showed a decrease in the ratio of aggregate to monomer as compared with the freshly prepared solutions.

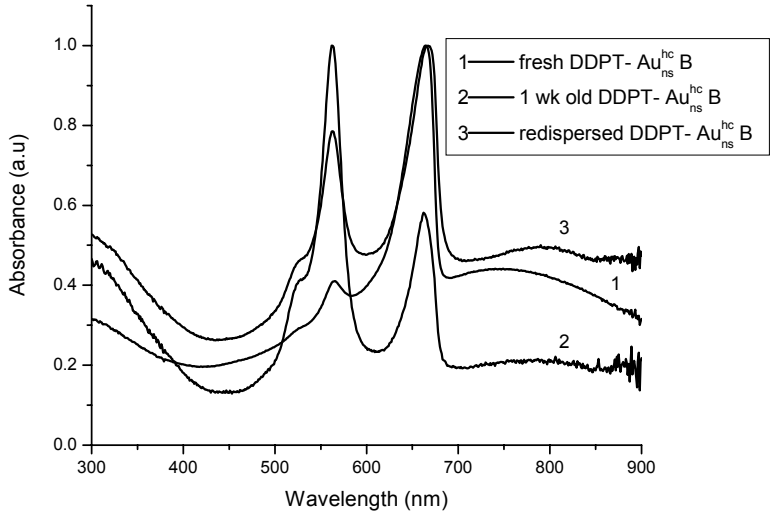

Figure 6.8: UV-Vis absorption spectra of DDPT coated Au nanoshells (sample B) (1) freshly prepared, (2) after standing for 1 week and (3) upon redispersing.

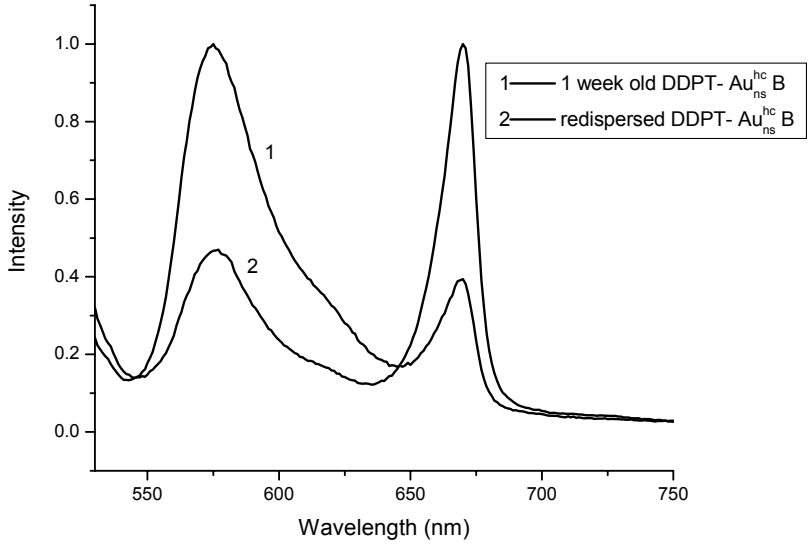

Figure 6.9: Fluorescence spectra of DDPT coated Au nanoshells (sample B) (1) after standing for 1 week and (2) upon redispersing.

Upon redispersing the precipitate in the aqueous solution through sonication in ice, the ratio of aggregate to monomer increased, reverting to nearly the same ratios observed in the freshly prepared solutions. Fluorescence spectra shown in Figure 6.9 demonstrate the emission band associated with J-aggregate formation and show that the ratio of aggregate to monomer fluorescence intensity mirrored that observed in the UV-Visible spectra when the precipitate, from the standing solution, is redispersed. Data from the other nanoshells, samples A and C, show similar behavior.

Additionally, the ease of DDPT aggregate formation in the hollow core nanoshell environment and in the aqueous solution was compared. DDPT aggregate formation onto the hollow core nanoshell surface, as depicted in Figure 6.8, was clear and intense. Figure 6.10 ─ the UV-Visible spectra of DDPT in aqueous solution that is freshly prepared (1) and after standing for 1 week (2) ─ on the other hand, indicates that the DDPT exists mainly in monomeric form in this environment.

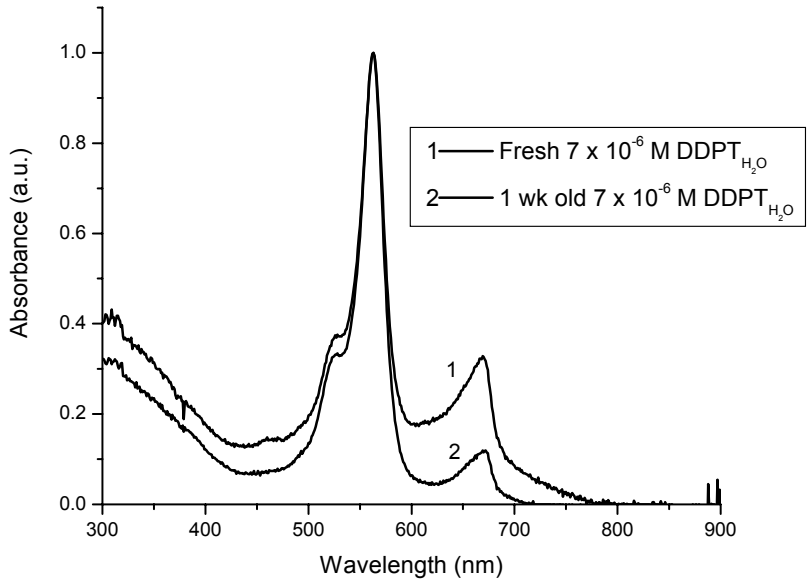

Figure 6.10: UV-Vis absorption spectra of 7×10^{-6} M DDPT in aqueous solution (1) freshly prepared and (2) after standing for 1 week.

To probe this difference further, the ratio of monomer to aggregate (M/A) and the J-band position in the two environments were examined. For the aqueous solution, the relative absorbance (M/A) = 3.05 for the freshly prepared sample and on standing for 1 week, M/A = 8.39, suggesting further decrease in the amount of J-aggregates. There was no visible precipitation for DDPT in the aqueous solution. As for the nanoshell solution, M/A = 0.41 for the freshly prepared sample. Upon standing for 1 week, which yielded precipitates, M/A = 1.72 and following sonication, M/A = 0.78. These results indicate that the aggregates are preferentially formed on the nanoshells rather than in solution. This is evident in the fact that at the concentration used, the pure nanoshells in water do not agglomerate and precipitate. Also, when the coated nanoshells precipitate, the UV-Visible spectrum of the supernatant measured reveals much higher monomer concentrations in the solution (M/A ratio is now 1.72 compared with 0.41 in freshly prepared solution). Then, when sonicated to redisperse the precipitate, the M/A decreased to 0.78. These observations imply that the aggregates are potentially formed on the surface of the nanoshells. The added weight of the aggregates causes the nanoshells to settle out of solution, but upon sonication most of the aggregates are recovered as demonstrated by the decrease in the ratio of monomer to aggregate.

The interaction between the aggregate and the nanoshell is expected to be non-specific, i.e., non-covalent in nature. Instead it is likely to be a purely electrostatic attraction between the negatively charged surface of the nanoshell and the cationic dye aggregate. However, in the case of the anionic aggregate formation in chapter 4, the solvent or solution favorable condition to induce J-aggregation is the main driving force.

Although the peak and dip characterization mentioned above can not fully be

apply for the nanoshell systems, a blue-shift of the exciton peak from the position in aqueous solution compared to that in the nanoshell solution was however observed in all cases where the nanoshell surface plasmon is at a lower energy (higher wavelength) than the J-aggregate exciton band. In the case where the nanoshell surface plasmon was at higher energy, the exciton peak was slightly red-shifted. The shifts suggest a perturbation of the aggregate system by the nanoshell, hence interactions. The observed shifts may be due to changes in the molecular axis of the aggregate caused by geometric considerations in packing onto the nanoshell surface. Also, it could be expected that the negative nanoshell surface to facilitate aggregation by reducing the repulsion between the similarly charged dye cations.

As in chapter 4, in an attempt to assess the binding process between DDPT and the Au nanoshell, off-resonance Raman spectroscopy was carried out. Figure 6.11 shows the Raman spectrum of aggregated DDPT under nonresonant excitation condition. Chapter 5 dealt with the Raman spectra of DDPT in monomeric and aggregated form, under both nonresonant and resonant excitation in the presence of Ag nanoparticles. In chapter 5, extensive assignments were provided from the experimentally measured Raman spectra with aid from calculated Raman vibrational frequencies using density functional theory at the B3LYP level and using 6-31G(d) basis set. Figure 6.11 displays similar bands in the higher frequency region associated with in plane or very little motion of the macrocycle. Specifically, the bands at 1329 cm^{-1} and 1416 cm^{-1}, as in chapter 5, involve in plane deformation of the macrocycle, as well as component motions that involve the methyl group within the ethyl attached to the benzothiazol moiety or phenyl group motions. In comparison to the DDPT Raman spectra on Ag nanoparticles in

chapter 5, the Au nanoshell, appears to have enhanced the bands in the low frequency region. This result suggests that the nanoshell constricted environment (or site) may have further influence the Raman vibrations. The two low lying bands at 217 cm^{-1} and 245 cm^{-1} seen in Figure 6.11 are not expected to be from Au-S nor from Au-N stretching vibration. Instead, the former is due to out of plane wagging of the bridge phenyl and rocking of the methyl group in the DDPT molecule. The latter, is a result of out of plane wagging of the trimethine bridge, out of plane deformation of the benzothiolole macrocycle and rocking of the ethyl group. These two bands correspond to the 212 cm^{-1} and 250 cm^{-1} vibrations in the Ag nanoparticle system discussed in chapter 5. The shift in the wavenumbers suggest a somewhat different interaction with the nanoshell when compare to the Ag nanoparticle.

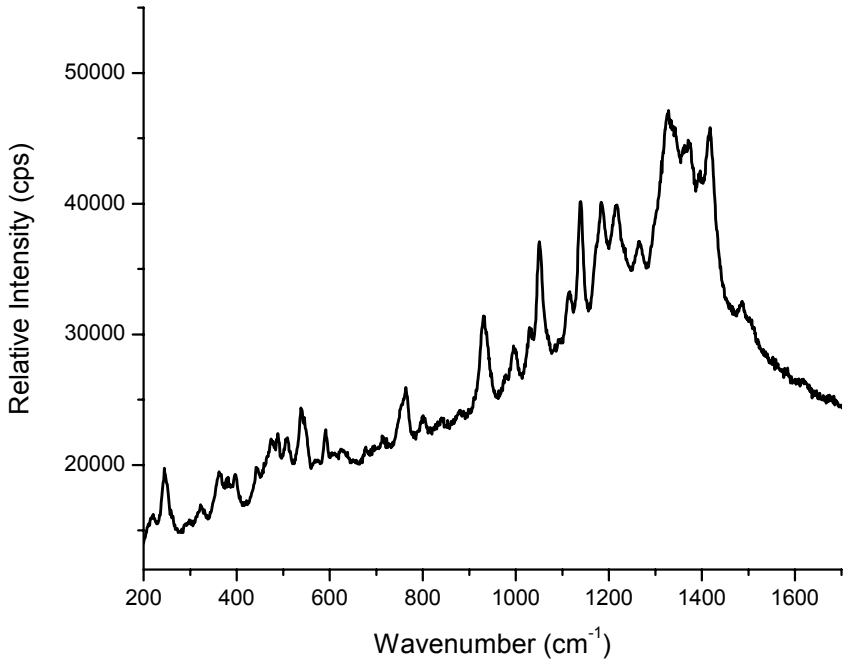

Figure 6.11: Raman spectrum of J-aggregated DDPT-coated nanoshells using 632.82 nm radiation; laser power 17 mW at source, accumulation time 2 minutes, and spectral resolution 0.4 nm.

Conclusion

The preparation of J-aggregated DDPT coated gold nanoshells has been reported. Two gold nanoshell systems were utilized, which are a solid core and a hollow core nanoshell, as substrates. The absorption peak, at ~ 673 nm in the solid core system and 664 nm in the hollow core system, affords direct evidence for the formation of DDPT J-aggregates. Experimental techniques utilized to characterize the systems include UV-Visible absorption and fluorescence spectroscopy, Raman spectroscopy, TEM and AFM measurements. The results indicate that better organized aggregates are formed on the solid core nanoshells. When DDPT aggregate formation in an aqueous solution and a nanoshell environment is compared, the results indicate that the aggregates are preferentially formed on the nanoshells rather than in the aqueous solution. Considering possible applications of J-aggregate-coated metal nanoparticles for electronic or optical devices, the fabrication J-aggregated coated nanoparticles and their characterization is very important. Taking into account that gold nanoshells possess quite remarkable optical properties that differ dramatically from those of solid gold nanoparticles makes them interesting surfaces to use for forming J-aggregates. Coupling of J-aggregate properties to either of these two different optical properties will provide some very interesting fundamental studies. The work presented in this chapter gives some interesting results and provides an excellent starting point for further work on these systems.

7 Summary and Future Directions

7.1 Summary

The research efforts presented in this dissertation concentrated on the investigation of cyanine dyes J-aggregate formation on silver and gold colloids and nanoshells and the resulting nanocomposite characterization. J-aggregates are a particular case of well-organized molecular self-assemblies, characterized by an unusually sharp absorption and resonance fluorescence that are markedly red-shifted from the monomer band. The appearance of the J-band was explained by formation of an excitonic state through the electronic coupling of tightly packed dye molecules in the aggregates. Cyanine dye aggregation is governed by a combination of electrostatic and π-π interactions. Moreover, the driving force for self-association in aqueous solution for such molecules is the enthalpically driven attractive interaction between the π-systems, leading to the formation of stack molecules, as oppose to the entropy-driven hydrophobic effect that control the aggregation of amphiphiles into micelles.

The first aim of this work was to synthesize stable, reproducible, monodisperse nanometric noble-metal spheres and nanoshells. Accordingly, well monodispersed Ag and Au nanoparticles were prepared using modified published methods. The preparation procedures yielded reproducible and stable Ag and Au nanoparticles from a few weeks to well over a year. Also, two different gold nanoshells, which are another type of nanoparticle, were prepared from modified published methods. One nanoshell had a solid core and the other had a hollow core. Ag and Au colloidal particles prepared had sizes of about 20 nm and 30 nm, respectively, as measured using AFM height and DLS measurements. The nanoshells were measured to be about 40 nm using TEM and AFM

measurements.

The second aim of the work presented was to fabricate J-aggregates coated nanoparticles and nanoshells. UV-Visible spectra were employed to show the effective aggregation of the cyanine dyes on the nanoparticles. The appearance of the J-band, characterized by the sharp absorption that is markedly red shifted from the monomer band, in the different nanoparticle systems, confirms the formation of J-aggregates adsorbed onto the nanoparticles prepared. Four structurally similar cyanine dyes (PIC, TTBC, TDBC and DDPT) were investigated for their J-aggregate formation onto the prepared nanoparticle surface. In the colloidal Ag and Au systems, evidence of the J-band was observed at 591 nm, 593 nm, 588 nm and 664 nm for PIC, TTBC, TDBC and DDPT, respectively. In the nanoshell systems, the absorption peak, at ~ 673 nm in the solid core system and 664 nm in the hollow core system, affords direct evidence for the formation of DDPT J-aggregates. Effects such as concentration of the cyanine dyes solution, size of the nanoparticle and added salt and base were investigated. These effects were assessed using shifts, either in the J-band or monomer band, which occurred in the dye-nanoparticle systems. Additionally, the full width at half maximum (FWHM) was taken as a measure of how well the cyanine molecules self-organized onto the nanoparticle surfaces.

Raman spectroscopy was employed to probe any binding event taking place between the cyanine dyes and the nanoparticles. This was done by looking for Ag-N, Au-N, Ag-S or Au-S stretching vibration band that may result from the interaction of the heteroatom (e.g., N, S) in the cyanine ring and the nanoparticle used. The absences of these stretching vibrations suggest that the interaction in the nanohybrid, form between

the dye and the nanoparticle, is electrostatic in nature and not covalent. Moreover, Raman spectral measurements with the aid of density functional theory were employed to gain insight into the molecular aggregate structure. Lastly, atomic force microscopy (AFM), near-field scanning optical microscopy (NSOM) and dynamic light scattering (DLS) studies were undertaken to estimate the J-aggregate size domain on the nanoparticle and to probe the physical arrangements of the dye chromophores on the nanoparticles.

The third aim of this work was focused on developing or implementing nanofabrication strategies to orient and pattern these nanostructures onto two-dimensional substrates. Using organosilane coupling agents, Ag and Au nanoparticles were self-assembled onto glass substrates. The nanoparticle treated glass substrates were subsequently treated with the cyanine dyes in methanolic solution. Orientation and patterning was not effective using this method. However, like in the solution work, the J-aggregation in the film was evident by observing the J-band formation. It is noteworthy that in the colloidal film, it is found that except for PIC, all the other dyes aggregated with the monomer band completely vanishing from the UV-Visible spectrum. Also, there were some shifts in the J band from the film relative to that coated on the Ag nanoparticles in solution. For instance, in the film, PIC had an absorption band at 582 nm (a 9 nm blue shift from that in solution) and an equal FWHM of 13 nm. In the film, TTBC had an absorption band at 588 nm (a 7 nm blue shift from that in solution) and a FWHM of 13 nm (an increase of 12 nm from the solution FWHM). As in the solution studies, the FWHM was taken as a measure of how well the cyanine molecules self-organized in the film. The blue shift and increase in the FWHM in the film suggest better

organization of the cyanine dye molecules on the nanoparticle surfaces in solution as compared to that in the film.

In summary, data gathered from the research efforts in this dissertation allows several conclusions to be made. First, J-aggregates are formed from monomers of PIC, TTBC, TDBC and DDPT in the presence of colloidal Ag and Au nanoparticles. The dyes' aggregation is strongly facilitated by the interplay of the dye-nanoparticle electrostatic interaction and by the aqueous nanoparticle solution environment. Inorganic salts and bases added to the solution have very important influences on the absorption spectral characteristics of the nanoparticle solutions. Second, the position of the J-band maximum does not depend on the number of dye molecules and is not affected by varying the size of the nanoparticles. Third, aggregation in the presence of the prepared nanoparticles occurs at concentrations below the critical aggregation concentration needed for other environmental condition that is without nanoparticles.

7.2 Future Directions

The future perspective of dye-nanoparticle hybrid systems is bright and fascinating. For instance, efforts to improve the performance of immunoassays and immunosensors by incorporating different kind of nanostructures have gained considerable momentum over the last decade. The focus is on artificial, particulate marker systems, both organic and inorganic. Preparation of supramolecular assembly consisting of self-assembled layer of chromophores on a metal nanoparticle core, which allows for packing of a large quantity of chromophores, may prove to be very efficient. J-aggregate-nanoparticle hybrid system is one example of such a system. The resulting nanomaterials can potentially act as ultra-bright fluorescent "nanobeacons" with effective

two-photon cross-section, large quantum efficiency and decrease sensitivity to photo-bleaching. There is a need for fluorescent labels with large two-photon cross-section and high quantum efficiency to enable detection at single label level in biological imaging.

There is much to be done with respect to a deeper understanding of the evolution of the optical properties of J-aggregates while in the process of growth and when couple to noble metal nanoparticles. Coherent exciton coupling to the conduction band of electrons have been reported to lead to constructive interference and a long live exciton or to destructive interference and a short exciton lifetime. Hence, coherent polarization coupling in heterostructured nanomaterials may strongly impact the functionality of nanoelectronic and nanoptical materials.

References for Chapter 1

1. Whitesides, G. M.; Mathias, J. P.; Seto, C. T. *Science* **1991**, *254*, 1312.

2. Koti, A. S. R. *Fluorescence Spectroscopy and Dynamics of Organic Molecules in Complex Systems*; Ph.D. Thesis, Tata Institute of Fundamental Research of Mumbai, 2002.

3. Alivisatos, A. P.; Barbara, P. F.; Castleman, A. W.; Chang, J.; Dixon, D. A.; Klein, M. L.; McLendon, G. L.; Miller, J. S.; Ratner, M. A.; Rossky, P. J.; Stupp, S. I.; Thompson, M. E. *Adv. Mater.* **1998**, *10*, 1297.

4. Wright, J. D. *Molecular Crystals*; Cambridge University Press: Cambridge 1995.

5. Feynman, R. P. *Miniaturization*; H. D. Gilbert, Ed.; Reinhold: New York 1961.

6. Bhattacharyya, K. *Organic Molecular Photochemistry*; Ramamurthy, V.; Schanze, K. S., Eds.; Marcel Dekker: New York 1999.

7. Scheibe, G. *Angew. Chem.* **1936**, *49*, 563.

8. Jelly, E. E. *Nature* **1936**, *138*, 1009.

9. Scheibe, G. *Z. Elektrochem*. **1941**, *47*, 73.

10. Waggoner, A. *J. Membrane Biol*. **1976**, *27*, 317.

11. Sasaki, F.; Kobayashi, S. *Appl. Phys. Lett.* **1993**, *63*, 2887.

12. Wang, Y. *Chem. Phys. Lett.* **1986**, *126*, 209.

13. Fleischer, E. B.; Palmer, J. M.; Srivastava, T. S.; Chatterjee, A. *J. Am. Chem. Soc.* **1971**, *88*, 3162.

14. Kobayashi, T., Ed.; *J-Aggregates*; World Scientific: Singapore 1996.

15. Zollinger, H. *Color chemistry: Syntheses, Properties and Applications of Organic Dyes and Pigments*, 2nd ed.; VCH: Weinheim 1991.

16. Lanzafame, J. M.; Muenter, A. A.; Brumbaugh, D. V. *Chem. Phys.***1996**, 210, 79.

17. Guo, C.; Aydin, M.; Zhu, H.-R. ; Akins, D. L. *J. Phys. Chem. B* **2002**, 1006, 5447.

18. Castleman Jr., A. W.; Wei, S. *Annu. Rev. Phys. Chem.* **1994**, *25*, 1401.

19. Owen, D. J.; VanDerveer, D.; Schuster, G. B. *J. Am. Chem. Soc.* **1998**, 120, 1705.

20. Tanaka, J.; Masashi, T.; Hayakawa, M. *Bull. Chem. Soc. Jpn.* **1980**, 53, 3109.

21. Brooker, L. G. S.; White, F. L.; Sprague, R. H.; Dent, S. G. J.; VanZandt, G. *Chem. Rev.* 1947, 41, 325.

22. Henrichs, P. M.; Gross, S.; *J. Am. Chem. Soc.* **1976**, 98, 7169.

23. West, W.; Pearce, S.; Grum, F. *J. Phys. Chem.* **1967**, 71, 1316.

24. Sturmer, D. M.; Heseltine, D. W. *The Theory of the Photographic Process,* 4th. ed., Chap. 8; James, T. H., Ed.; MacMillan: New York, 1977.

25. (a) Zweck, J.; Penzkofer, A. *Chem. Phys.* **2001**, *269*, 399. (b) Yao, H.; Kagoshima, Y.; Kitamura, S.; Isohashi, T.; Ozawa, Y.; Kimura, K. *Langmuir* **2003**, *19*, 8882. (c) Pawlik, A.; Ouart, A.; Kirstein, S.; Abraham, H. W.; Daehne, S. *Eur. J. Org. Chem.* **2003**, 3065. (d) Kato, N.; Prime, J.; Katagari, K.; Caruso, F. *Langmuir* **2004**, *20,* 5718.

26. (a) Gandini, S. C. M.; Yushmanov, V. E.; Borissevitch, I. E.; Tabak, M. *Langmuir* **1999**, *15*, 6233. (b) von Berlepsch, H.; Bottcher, C.; Ouart, A.; Regenbrecht, M.; Akari, S.; Keiderling, U.; Schnablegger, H.;Dahne, S.; Kirstein, S. *Langmuir* **2000**, *16*, 5908. (c) Tatikolov, A. S.; Costa, S. M. B. *Chem. Phys. Lett.* **2001**, *346*, 233. (d) Kato, N.; Mikami, Y.; Serata, T.; Uesu, Y. *Trans. Mater. Res. Soc. Jpn* **2002**, *27* 341.

27. (a) Vacha, M.; Takei, S.; Hashizume, K.; Sakakibara, Y.; Tani, T. *Chem. Phys. Lett.* **2000**, *331*, 387. (b) Vacha, M.; Furuki, M.; Pu, L. S.; Hashizume, K.; Tani, T. *J. Phys. Chem. B* **2001**, *105*, 12226.

28. Zhou, H. S.; Watanabe, T.; Mito, A.; Honma, I.; Asai, K.; Ishigure, K.; Furuki, M. *Mater. Sci. Eng., B* **2002**, *95*, 180.

29. De Rossi, U.; Daehne, S.; Reisfeld, R. *Chem. Phys. Lett.* **1996**, *251*, 259.

30. (a) Kometani, N.; Nakajima, H.; Asami, K.; Yonezawa, Y.; Kajimoto, O. *J. Phys. Chem. B* **2000**, *104*, 9630. (b) Nakajima, H.; Kometani, N.; Asami, K.; Yonezawa, Y. *J. Photochem. Photobiol., A* **2001**, *143*, 161.

31. Matsumoto, S.; Kobayashi, T.; Aoyama, T.; Wada, T. *Chem. Commun.* **2003**, 1910.

32. von Berlepsch, H.; Moller, S.; Dahne, L. *J. Phys. Chem. B* **2001**, *105*, 5689.

33. Herz, A. H. *Adv. Colloid. Interface Sci.* **1977**, 8, 237.

34. (a) Kometani, N.; Tsubonishi, M.; Fujita, T.; Asami, K.; Yonezawa, Y. *Langmuir* **2001**, *17*, 578. (b) Hranisavljevic, J.; Dimitrijevic, N. M.; Wurtz, G. A.; Wiederrecht,

G. P. *J. Am. Chem. Soc.* **2002**, *124*, 4536. (c) Yaglioglu, G.; Dorsinville, R.; Ozcelik, S. *J. Appl. Phys.* **2003**, *94*, 3143.

35. Kaufer, H.; Sheibe, G. *Z. Electrochem.* **1955**, 59, 584.

36. Sheppard, S. E.; Geddes, A. L. *J. Am. Chem. Soc.* **1944**, 66, 2003.

37. Levschin, V. L.; Baranova, E. G.; *J. Chem. Phys.* **1958**, 55, 869.

38. (a) McRae, E. G.; Kasha, M. *J. Chem. Phys.* **1958**, 28, 721. (b) Kasha, M.; Rawis, H. R.; El-Bayoumi, M. A. *Pure Appl. Chem.* **1965**, 11, 371. (c) Kasha, M. *Physical Processes in Radiation Biology*; Academic Press: New York, 1964. (d) Levinson, G. S.; Simpson, W. T.; Curtius, W. *J. Am. Chem. Soc.* **1957**, 79, 4314.

39. Frank, J.; Teller, E. *J. Chem. Phys.* **1938**, *6*, 861.

40. Struganova, I. A.; Lim, H.; Morgan, S. A. *J. Phys. Chem. B* **2002,** *106,* 11047.

41. Egorov, V. V. *Chem. Phys. Lett.* **2001**, *336*, 284.

42. Ozcelik, S. *Spectroscopic and Dynamic Properties of Molecules Adsorbed on Surfaces*; Ph.D. Dissertation, City University of New York, 1996.

43. (a) Osuka, A.; Maruyama, K. *J. Am. Chem. Soc.* **1988**, *110*, 4454. (b) Hunter, C. A.; Sanders, J. K. M.; Stone, A. J. *Chem. Phys.* **1989**, *133*, 395. (c) Kuhn, H.; Kuhn, C.; In *J-Aggregates*; T. Kobayashi, Ed.; World Scientific: Singapore 1996.

44. Aguilera, O. V.; Neckers, D. C.; *Acc. Chem. Res.* **1989**, *22*, 171.

45. (a) Das, S.; Thanulingam, T. L.; Thomas, K. G.; Kamat, P. V.; George, M. V. *J. Phys. Chem.* **1993**, 97, 13620. (b) Hotchandani, S.; Das, S.; Thomas, K. G.; George, M. V.; Kamat, P. V. *Res. Chem. Intermed.* **1994**, *20*, 927.

46. Hessemann, J. *J. Am. Chem. Soc.* **1980**, *102*, 2176.

47. Mees, C.E.K.; James, T.H. *The Theory of the Photographic Process*, 3rd ed.; MacMillan: New York, 1966.

48. Harrison, W. J.; Mateer, D. L.; Tiddy, G. J. T. *J. Phys. Chem.* **1996**, 100, 2310.

49. Higgins, D. A.; Reid, P. J.; Barbara, P. F. *J. Phys. Chem.* **1996**, 100, 1174.

50. Faraday, M. *Philos. Trans. R. Soc. London* **1857**, 197, 145.

51. Daniel, M.-C.; Astruc, D. *Chem. Rev.* 2004, 104, 293.

52. Graham, T. *Philos. Trans. R. Soc.* **1861**, 151, 183.

53. Gibbs, R. J. *Silver Colloid, Do they work?* Newark, Delaware 1999.

54. (a) Linden, S.; Kuhl, J.; Giessen, H. *Phys. Rev. Lett.* **2001**, 86, 4688. (b) Link, S. El-Sayed, M. A. *J. Phys. Chem. B* **1999**, 103,8410. (c)Merkin, C. A.; Letsinger, R. L.; Mucic, R. C.; Storhoff, J. J. *Nature*, **1996**.

55. Freeman, R. G.; Grabar, K. C.; Allison, K. J.; Bright, R. M.; Davis, J. A.; Guthrie, A. P.; Hommer, M. B.; Jackson, M. A.; Smith, P. C.; Walter, D. G.; Natan, M. J. *Science* **1995**, *267*, 1629. (b) Lin, S.; Liu, S.; Lin, C.; Chen, C. *Anal. Chem*. **2002**, *74*, 330. (c) Sastry, M.; Lala, N.; Patil, V.; Chavan, S. P.; Chittiboyina, A. G. *Langmuir* **1998**, *14*, 4138.

56. Sun, Y.; Xia, Y. *Anal. Chem.* 2002, 74, 5297.

57. Zenneck, J. *Annalen der Physik (4th series)*, **1907**, 23, 846.

58. Mie, G. *Ann. Phys.* **1908**, 25, 377.

59. Sommerfeld, A. *Annalen der Physik (4th series)*, **1909**, 28, 44.

60. Kerker, M. *The Scattering of Light and Other Electromagnetic Radiation*; Academic: New York, 1969.

61. Bohren, C. F.; Huffman, D. R. *Absorption and Scattering of Light by Small Particles*; Wiley Interscience: New York, 1983.

62. Sonnichsen, C. *Plasmons in metal nanostructures*; Ph.D. Dissertation, Ludwig-Maximilians University of Munich, 2001.

63. Kelly, K. L.; Coronado, E.; Zhao L. L.; Schatz, G. C. *J. Phys. Chem. B* **2003**,107, 668.

64. Kreibig, U.; Vollmer, M. *Optical Properties of Metal Clusters*; Springer: Berlin, 1995.

65. Logan, N. A. *Proc. IEEE.* **1965**, 53, 773.

66. Raschke, G.; Brogl, S.; Susha, A. S.; Rogach, A. L.; Klar, T. A.; Feldmann, J.; Fieres, B.; Petkiv, N.; Bein, T.; Nichtl, A.; Kurzinger, K. *Nano Lett.* **2004**, *4*, 1853.

67. (a) Zhou, H. S.; Honma, I.; Komiyama, H.; Haus, J. W. *Phys. Rev. B* **1994**, 50, 12052. (b) Hao, E.; Li, S.; Bailey R. C.; Zou S.; Schatz, G. C.; Hupp, J. T. *J. Phys. Chem. B* **2004**,108, 1224.

68. Aden, A. L.; Kerker, M. *J. Appl. Phys.* **1951**, *22*, 1242.

69. Bhandari, R. *Appl. Opt.* **1985**, 24, 1960.

70. Yang, W. H.; Schatz, G. C.; Duyne, R. P. V. *J. Phys. Chem.* **1995**, *99*, 869.

71. Bian, R. X.; Dunn, R. C.; Xie, X. S.; Leung, P. T. *Phys. Re*v. *Lett.* **1995**, *75*, 4772.

72. Moreno, E.; Erni, D.; Hafner, C.; Vahldieck, R. *J. Opt. Soc. A* **2002**, *19*, 101.

73. Jackson, J. B.; N. J. Halas *PNAS* **2004**, 101, 17930.

74. (a) Radloff, C.; Halas, N. J. *Nano Lett.* **2004**, 4, 1323. (b) Prodan, E.; Nordlander, P. *J. Chem. Phys.* **2004**, 120, 5444.

75. (a) Alivisatos, A. P. *Science* **1996**, 271, 933. (b) Lin, J.; Zhou, W.; O'Connor C. *J. Mater. Lett.* **2001**,49, 282.

76. (a) Emory, S. R.; Nie, S. *J. Phys. Chem. B* **1998**, 102, 493. (b) Michaels, A. M.; Jiang, J.; Brus, L. *J. Phys. Chem. B* **2000,** *104,* 11965.

77. Averitt, R. D.; Wescott, S. L.; Halas, N. J. *Opt. Soc. Am.* **1998**, 16, 1824.

78. Diao, J. J.; Chen, G. D. *J. Phys. D: Appl. Phys.* **2001**, 34, L79.

79. Oldenburg, S. J.; Westcott, S. L.; Averitt, R. D.; Halas, N. J. J. *Chem. Phys.* **1999**, 111, 4729.

80. Radloff, C.; Halas, N. J. *Appl. Phys. Lett.* **2001**, 79, 674.

81. Oldenburg, S. J.; Jackson, J. B.; Westcott, S. L.; Halas, N. J. *Appl. Phys. Lett.* **1999**, 75, 2897.

82. (a) Henglein, A. *Chem. Rev.* **1989**, 89, 1861. (b) Schmid, G. *Chem. Rev.* **1992**, 92, 1709. (c) Templeton, A. C.; Wuelfing, W. P.; Murray, R. W. *Acc. Chem. Res.* **2000**, 33, 27.

83. Hayat, M. A. *Colloidal gold: principles, methods, and applications*; Academic Press: San Diego, 1989; 3rd vol.

84. (a) Wuelfing, W. P.; Murray, R. W. *J. Phys. Chem. B* **2002**, 106, 3139. (b) Kim, Y. J.; Johnson, R. C.; Hupp, J. T. *Nano Lett.* **2001**, 1, 165. (c) Mirkin, C. A. *Inorg. Chem.* **2000**, 39, 2258-2272.

85. Sato, T.; Ahmed, H.; Brown, D.; Johnson, B. F. G. *J. Appl. Phys.* **1997**, 82, 696.

86. Pietron, J. J.; Stroud, R. M.; Rolison, D. R. *Nano Lett.* **2002**, *2*, 545.

87. (a) Musick, M. D.; Keating, C. D.; Lyon, L. A.; Botsko, S. L.; Pena, D. J.; Holliway, W. D.; McEvoy, T. M.; Richardson, J. N.; Natan, M. J. *Chem. Mater*. **2000**, 12, 2869. (b) Wuelfing, W. P.; Zamborini, F. P.; Templeton, A. C.; Wen, X. G.; Yoon, H.; Murray, R. W. *Chem. Mater.* **2001**, 13, 87-95.

References for Chapter 2

1. Bartolotti, L. J.; Flurchick, K. M. In *Reviews in Computational Chemistry*; Lipkowitz, K. B.; Boyd, D. B., Eds.; VCH Publishers Inc.: New York, 1996; Vol. 7, Chapter 4.

2. Becke, A. D. *Phys. Rev. A* **1988**, 38, 3098.

3. Lee, C.; Yang, W.; Parr, R. G. *Phys. Rev. B* **1993**, 37, 785.

4. Gordon, M. S. *Chem. Phys. Lett.* **1980**, 76, 163.

5. Lakowicz, J. R. *Principles of Fluorescence Spectroscopy*; Plenum Press: New York 1999.

6. Berne, B. J.; Pecora, R. *Dynamic Light Scattering;* Wiley & Sons, New York, 1976.

7. Brown W., Ed.; *Dynamics Light Scattering*; Clanrendon Press: Oxford 1993.

8. Glatter, O.; Kratky O., Eds.; *Small Angle X-ray Scattering*; Academic Press: London 1982.

9. Feigin, L. A.; Svergun, D. I. In *Structure Analysis by Small Angle X-ray and Neutron Scattering*; Taylor G. W. Ed.; Plenum Press, New York 1987.

10. Lakowicz, J. R., Ed.; *Topics in Fluorescence Spectroscopy: Principles*; Plenum Press, New York 1991; Vol. 2.

11. Atkins, P. W. *Physical Chemistry*, 5th ed.; Oxford University Press: London 1995.

12. (a) Binnig, G.; Rohrer, H.; Gerber, C.; Weibel, E. *Phys. Rev. Lett.* **1982**, *49*, 57. (b) Binnig, G; Quate, C. F.; Gerber, C. *Phys. Rev. Lett.* **1986**, *56*, 930.

13. Paesler, M.; Moyer, P. J *Near-Field Optics: Theory, Instrumentation, and Applications*. John Wiley & Sons, Inc.: New York . 1996.

14. Betzig, E.; Trautman, J. K.; Harris, T. D. *Science* **1991**, *251*, 1468.

15. Ruiter, A. J. T. *Appl. Phys. Lett.* **1997**, *71*, 28.

16. Smekal, A. *Naturwissenschaften* **1923**, 11, 873.

17. Raman C. V. *Nature* **1928** 121 619.

18. Landsberg, G. S. *Naturwissenschaften* **1928**, 16, 557.

19. Mandelstam, L. *Compt. Rend.* **1928**, 187,109.

20. Wang Y.; van Wart, H.E. *Methods in Enzymology* **1993**, 226, 319.

21. Shorygin, P. P. *Pure Appl. Chem.* **1962**, 4, 87.

22. Furtak, T. E.; Chang, R., Eds.; *Surface Enhanced Raman Spectroscopy*; Elsevier: Amsterdam, 1982.

23. Fleischman, M.; Hendra, P. J.; Mc Quillan, A. J. *Chem. Phys. Lett.* **1974**, 26, 163.

24. Jeanmarie, D. L.; van Duyne, R. P. *J. Electroanal. Chem.* **1977**, 84, 1.

25. Albretch, M. G.; Creighton, J. A. *J. Am. Chem. Soc.* **1977**, 99, 5215.

26. (a) Creighton, J. A.; Albretch, M. G.; Hester, R. E.; Matthew, J. A. D. *Chem. Phys. Lett.* **1978**, 55, 55. (b) Gu B.; Akins, D. L. *Chem. Phys. Lett.* **1985**, 113, 558. (c) Lombardi, J. R.; Birke, R. L.; Lu, T.; Xu J. *J. Chem. Phys.* **1986**, 84, 4174.

27. (a) Allen, C. S.; Schatz, G. C.; van Duyne, R. P. *Chem. Phys. Lett.* **1980**, 75, 201. (b) Temperini, M. L. A.; Chagas, H. C.; Sala, O. Chem. Phys. Lett. **1981**, 79, 75.

28. Otto, A. *Surf. Sci.* **1978**, 75, 1392.

29. Birman, J. L.; Cummins, H. Z.; Rebane, K. K., Eds.; *Light Scattering in Solids*; Plenum Press: New York, 1979; p. 479.

30. (a) Akins, D. L. Colloid *Interf. Sci.* **1982**, 90, 373. (b) Li, X.; Gu, B.; Akins, D. L. *Chem. Phys. Lett.* **1984**, 105, 263. (c) Lu, L.; Zhang, H., Sun, G.; Xi, S.; Wang, H.; Li, X.; Wang X.; Zhao B. *Langmuir* **2003**, 19, 9490. (d) Jackson, J. B.; Westcott, S. L.; Hirsh, L. R.; West, J. L.; Halas, N. J. *App. Phys. Lett.* **2003**, 82, 257.

31. (a) Gersten, J. L.; Birke, R. L.; Lombardi, J. R. *Phys. Rev. Lett.* **1979**, 43, 147. (b) Moskovits, M. *J. Chem. Phys.* **1982**, 77, 4408. (c) Schatz, G. C. *Acc. Chem. Res.* **1984**, 17, 370.

32. (a) Barz, F.; Gordon II, J. G.; Philpott, M. R.; Weaver, M. J. *Chem. Phys. Lett.* **1982**, 91,291. (b) Otto, A.; Billman, J.; Eickmans, J.; Erturks, U.; Pettenkofer, C. *Sur. Sci.* **1984**, 138, 319.

33. Chang, R. K.; Furtak, T. E. *Surface Enhanced Scattering*; Plenum Press: New York, 1982.

34. (a) Adrian, F. J. *J. Chem. Phys.* **1982**, 77, 5302. (b) Weitz, A. A.; Garoff, S.; Gersten, J. I., Nitzan, A. *J. Chem. Phys.* **1983**, 78, 5324.

35. Akins, D. L.; Akpabli, C. K.; Li, X. *J. Phys. Chem.* **1989**, 93, 1977.

36. Akins, D. L. *J. Phys. Chem.* **1986**, 90, 1530.

37. Hertz A. H. *Adv. Colloid Interf. Sci.* **1977**, 8, 237.

38. Akpabli, C. K., *Laser Raman Scattering By Sensitizing Dyes Adsorbed on Substrates*; Ph.D. Dissertation, City University of New York 1988.

References for Chapter 3

1. (a) Linden, S.; Kuhl, J.; Giessen, H. *Phys. Re*V. *Lett*. **2001**, *86*, 4688. (b) Link, S.; EI-Sayed, M. A. *J. Phys. Chem. B* **1999**, *103*, 8410. (c) Mirkin, C. A.; Letsinger, R. L.; Mucic, R. C.; Storhoff, J. J. *Nature* **1996**, *382*, 607. (d) Lin, S.; Liu, S.; Lin, C.; Chen, C. *Anal. Chem*. **2002**, *74*, 330. (e) Freeman, R. G.; Garbar, K. C.; Allison, K. J.; Bright, R. M.; Davis, J. A.; Guthrie, A. P.; Hommer, M. B.; Jackson, M. A.; Smith, P. C.; Walter, D. G.; Natan, M. J. *Science* **1995**, *267*, 1629. (f) Sastry, M.; Lala, N.; Patil, V.; Chavan, S. P.; Chittiboyina, A. G. *Langmuir* **1998**, *14*, 4138.

2. Leff, D. V.; Ohara, P. C.; Heath, J. R.; Gelbart, W. M. *J. Phys. Chem. B.* **1995**, 99, 7036.

3. Qi, Z.-m.; Zhou, H.; Matsuda, N.; Honma, I.; Shimada, K.; Takatsu, A.; Kato, K. *J. Phys. Chem. B.;* **2004**; *108*; 7006.

4. (a) Jana, N. R.; Gearheart, L.; Murphy, C. J. *J. Phys. Chem. B* **2001**, *105*, 4065. (b) Tan, Y.; Dai, X.; Li, Y.; and Zhu, D. *J. Mater. Chem.* **2003**, *13*, 1069. (c) Otsuka, H.; Akiyama, Y.; Nagasaki, Y.; Kataoka, K. *J. Am. Chem. Soc.* **2001**, *123*, 8226. (d) Brust, M.; Walker, M.; Bethell, D.; Schiffrin, D. J.; Whyman, R. *Chem. Commun*. **1994**, 801. (e) Mandal, T. K.; Fleming, M. S.; Walt, D. R. *Nano Lett.* **2002**, *2*, 3.

5. (a) Turkevich, J.; Stevenson, P. C.; Hillier, J. *Discuss. Faraday Soc*. **1951**, *11*, 55. (b)Turkevich, J.; Kim, G, *Science* **1970**, *169*, 873. (c) Jana, N. R.; Gearheart, L.; Murphy, C. J. *J. Phys. Chem. B* **2001**, *105*, 4065. (d) Tan, Y.; Dai, X.; Li, Y.; and Zhu, D. *J. Mater. Chem.* **2003**, *13*, 1069. (e) Zhang Z., Zhao B., Hu, L. *J Solid State Chem.* **1996**, 121, 105. (f) Meisel D.; Lee, P.C. *J. Phys. Chem.* **1982**, 86, 3391. (g) Creighton, J. A.; Blatchford, G.; Albretch, G. *J. Chem. Soc. Faraday Trans.* **1979**, 75, 790. (h) Silver P. Y.; Herrera-Urbana, R.; Duchauchelle, N.; Vijayakrishman, V. *J. Mater. Chem.* **1996**, 6, 573.

6. Komiyama, M.; Hirai, H. *Bull. Chem. Soc. Jpn.* **1983**, 56, 2833.

7. Sun, Y.; Mayers, B.; Herricks, T.; Xia, Y. *Nano Lett.* **2003**, 3, 955.

8. Yonezawa, T.; Sutoh, M.; Kunitake, T. *Chem. Lett.* **1997**, 7, 619.

9. Hoogsteen, W.; Fokkink, L. G. J. *J. Coll. Int. Sci.* **1995**, 175 12.

10. Henglein, A.; Giersig, M. *J. Phys. Chem. B.* **1999**, 103, 9533.

11. Heicklen, J. *Colloid Formation and Growth*; Academic Press: New York, 1976.

12. Sanchez-Cortes, S.; Carciaramos, J. V.; Morcillo, G.; Tinti, J. *Colloid Interface Sci.* **1995**, 175, 358.

13. Zhai, X.; Efrima, S. *J. Phys. Chem.*, **1996**, 100, 1779.

14. Shirtcliffe, N.; Nickel, U.; Schneider S. *J. Colloid Interface Sci.* **1999**, 211, 122.

15. Munro, C. H.; Smith, W. E.; Garner, M.; Clarkson J.; White, P. C. *Langmuir* **1995**, 100, 7293.

16. (a) Klein, D. L.; Roth, R.; Lim, A. K. L.; Alivisatos, A. P.; McEuen, P. L. *Nature* **1997**, *389*, 699. (b) Ingram, R. S.; Hostetler, M. J.; Murray, R. W.; Schaff, T. G.; Khoury, J.; Whetten, R. L.; Bigioni, T. P.; Guthrie, D. K.; First, P. N. *J. Am. Chem. Soc.* **1997**, *119*, 9279.

17. Collier, C. P.; Saykally, R. J.; Shiang, J. J.; Henrichs, S. E.; Heath, J. R. *Science* **1997** *277*, 1978.

18. (a) Colvin, V. L.; Goldstein, A. N.; Alivisatos, A. P. *J. Am. Chem. Soc*. **1992**, *114*, 5221. (b) Grabar, K. C.; Freeman, R. G.; Hommer, M. B.; Natan, M. J. *Anal. Chem*. **1995**, *67*, 735.

19. Patil, V.; Mayya, K. S.; Sastry, M. *Langmuir* **1999**, 15, 6587.

20. BBInternational website (www.bb-international.com)

21. Pal, T.; Sau, T. K.; Jana, N. R. *Langmuir* **1997**, 13, 1481.

22. Yonezawa, T.; Kunitake, T. *Colloids Surfaces A: Physicochem. Eng. Aspects* **1999**, 149, 193.

23. Mie, G. *Ann. Physik* **1908**, 25,377.

24. Daniel, M.-C.; Astruc, D. *Chem. Rev.* **2004**, 104, 293.

25. Siebrands, T.; Giersig, M.; Mulvvaney, P.; Fisher, Ch.-H. *Langmuir*, **1993**, 9, 2297.

26. Heiglein, A. *J. Phys. Chem.* **1993**, 97, 5457.

27. Littau, K. A.; Szajowski, P. J.; Muller, A. J. ; Kortan, A. R. ; Brus, L. E. *J. Phys. Chem.* **1993**, 97, 1224.

28. Fres, G. *Kolloid-Z. Z. Polym.* **1972**, 250, 736.

29. Park, S.-H.; Im, J.-J.; Im J.-W.; Chun, B.-H.; Kim, J.-H. *Microchemical J.* **1999**, 63, 71.

References for Chapter 4

1. *Photochemistry in Organized & Constrained Media*; Ramamurthy, V., Ed.; VCH Publishers: New York, 1991.

2. (a) Jelley, E. E. *Nature* **1936**, 138, 1009. (b) Scheibe, G. *Angew. Chem.* **1936**, 49, 563. (c) Kobayashi, T., Ed. J-Aggregates; World Scientific Publishing Co.: Singapore, 1996. (d) Higgins, D. A.; Reid, P. J.; Barbara, P. F. *J. Phys. Chem.* **1996**, *100*, 1174.

3. West, W.; Gilman, P. B. *The theory of the photographic Process*, 4th ed.; James, T. H. Ed.; Macmillan: New York, 1977; Chapter 10.

4. Kawasaki, M.; Sato, T.; Yoshimoto, T. *Langmuir* **2000**, 16, 5409.

5. Spano, F. C.; Mukamel, S. *Phys. Rev. A.* **1989**, 40, 5783.

6. Wang, Y. J. *Opt. Soc. Am.* **1991**, B8, 981.

7. Jelly, E. E. *Nature* **1936**, *138*, 1009. (b) Scheibe, G. *Z. Angew. Chem*. **1936**, *49*, 563.

8. (a) Misawa, K.; Ono, H.; Minoshima, K.; Kobayashi, T. *Appl. Phys. Lett*. **1993**, *63*, 577. (b) Kunisawa, T.; Sato, T.; Yonezawa, Y. *Mol. Cryst. Liq. Cryst*. **1997**, *294*, 169. (c) Vacha, M.; Furuki, M.; Pu, L. S.; Hashizume, K.; Tani, T. *J. Phys. Chem. B* **2001**, *105*, 12226.

9. (a) Zhou, H. S.; Watanabe, T.; Mito, A.; Honma, I.; Asai, K.; Ishigure, K.; Furuki, M. *Mater. Sci. Eng., B* **2002**, *95*, 180. (b) De Rossi, U.; Daehne, S.; Reisfeld, R. *Chem. Phys. Lett.* **1996**, *251*, 259.

10. Sato, T.; Kurahashi, M.; Yonezawa, Y. *Langmuir* **1993**, *9*, 3395.

11. (a) Gil, A.; Aristegui, I.; Suarez, A.; Sandez, I.; Mobius, D. *Langmuir* **2002**, *18*, 8527. (b) Gil, A; Mobius, D.; Sandez, I.; Suarez, A. *Langmuir* **2003**, *19*, 6430. (c) Tian, C.; Zoriniants, G.; Gronheid, R.; Van der Auweraer, M.; De Schryver, F. C. *Langmuir* **2003**, *19*, 9831.

12. (a) Kometani, N.; Tsubonishi, M.; Fujita, T.; Asami, K.; Yonezawa, Y. *Langmuir* **2001**, *17*, 578. (b) Hranisavljevic, J.; Dimitrijevic, N. M.; Wurtz, G. A.; Wiederrecht, G. P. *J. Am. Chem. Soc.* **2002**, *124*, 4536. (c) Yaglioglu, G.; Dorsinville, R.; Ozcelik, S. *J. Appl. Phys.* **2003**, *94*, 3143.

13. von Berlepsch, H.; Moller, S.; Dahne, L. *J. Phys. Chem. B* **2001**, *105*, 5689.

14. Kometani, N.; Tsubonishi, M.; Fujita, T.; Asami, K.; Yonezawa, Y. *Langmuir* **2001**, *17*, 578.

15. Ghosh, S. K.; Pal, A.; Nath S.; Kundu, S.; Panigrahi, S; Pal, T.; *Chem. Phys. Lett.* **2005**, 412, 5.

16. Huang, T.; Murray, R. W. *Langmuir* **2002**, *18*, 7077.

17. (a) Li, H.; Rothberg, L. J. *J. Am. Chem. Soc*. **2004**, *126*, 10958. (b) Li, H.; Rothberg, L. J. *Anal. Chem*. **2004**, *76*, 5414.

18. Lian, W.; Litherland, S. A.; Badrane, H.; Tan, W.; Wu, D.; Baker, H. V.; Gulig, P. A.; Lim, D. V.; Jin, S. *Anal. Biochem.* **2004**, *334*, 135.

19. (a) Thomas, K. G.; Kamat, P. V. *Acc. Chem. Res.* **2003**, *36*, 888. (b) Chandrasekharan, N.; Kamat, P. V.; Hu, J.; Jones, G., II. *J. Phys. Chem. B* **2000**, *104*, 11103. (c) Barazzouk, S.; Kamat, P. V.; Hotchandani, S. *J. Phys. Chem. B* **2005**, *109*, 716.

20. (a) Gu, T.; Whitesell, J. K.; Fox, M. A. *Chem. Mater*. **2003**, *15*, 1358. (b) Hranisavljevic, J.; Dimitrijevic, N. M.; Wurtz, G. A.; Wiederrecht, G. P. *J. Am. Chem. Soc.* **2002**, *124*, 4536. (c) Dulkeith, E.; Ringler, M.; Klar, T. A.; Feldmann, J.; Munoz Javier, A.; Parak, W. J. *Nano Lett*. **2005**, *5*, 585.

21. Thomas, K. G.; Kamat, P. V. *Acc. Chem. Res.* **2003**, *36*, 888.

22. (a) Guo, C.; Ren, B.; Akins, D. L. *J. Phys. Chem. B.***1998**,102, 8751. (b) Kubat, P.; Lang, K.; Janda, P.; Azenbacher, P., Jr. *Langmuir*, **2005**, 21, 9714.

23. (a) Lu, L. D.; Jones, R. M.; McBranch, D.; Whitten, D. *Langmuir* **2002**, *18*, 7706. (b) Jones, R. M.; Lu, L. D.; Helgeson, R.; Bergstedt, T. S.; McBranch, D. W.; Whitten, D. G. *Proc. Natl. Acad. Sci. U.S.A.* **2001**, *98*, 14769.

24. (a) Kometani, N.; Tsubonishi, M.; Fujita, T.; Asami, K.; Yonezawa, Y. *Langmuir* **2001**, *17*, 578. (b) Wiederrecht, G. P.; Wurtz, G. A.; Hranisavljevic, J. *Nano Lett*. **2004**, *4*, 2121.

25. Ghosh, S. K.; Pal, A.; Nath, S.; Kundu, S.; Panigrahi, S.; Pal, T. *Chem. Phys. Lett.* **2005**, *412*, 5.

26. (a) Makarova, O. V.; Ostafin, A. E.; Miyoshi, H.; Norris, J. R.; Miesel, D. *J. Phys. Chem. B* **1999**, *103*, 9080. (b) Templeton, A. C.; Wuelfing, W. P.; Murray, R. W. *Acc. Chem. Res*. **2000**, *33*, 27.

27. Struganova, I. A.; Lim, H; Morgan, S.A. *J. Phys. Chem. B* **2002**, *106*, 11047.

28. Struganova, I. A.; Hazell, M.; Gaitor, J.; McNally-Carr, D.; Zivanovic, S. *J. Phys. Chem. A* **2003**, *107*, 2650.

29. Place, I.; Perlstein, J.; Penner, T. L.; Whitten, D. G. *Langmuir* **2000**, 16, 9042.

30. An, B.-K.; Kwon, S. K.; Jung, S. D.; Park S. Y. *J. Am. Chem. Soc*. **2002**, 124, 14410.

31. Knapp, E. W. *Chem. Phys.* **1984**, 85, 73.

32. (a) Cardini, G.; Muniz-Miranda, M.; Schettino, V. *J. Phys. Chem. B* **2004**, 108,17007. (b) Pergolese, B.; Muniz-Miranda, M.; Bigoto, A. *J. Phys. Chem. B* **2004,** 108, 5698. (c) Jang N. K. *Bull. Korean Chem. Soc*. **2002**, 23, 1790.

33. (a) Guo, C.; Aydin, M.; Zhu, H.-R.; Akins, D. L. *J. Phys. Chem. B* **2002,** *106,* 5447. (b) Pan D.; Phillips, D. L. *Chem. Phys. Lett.* **1997**, 275, 227. (c) Kneipp, K. *J. Mol. Struct.* **1987**, 156,331.

34. (a) Lanzafame, J. M.; Muenter, A. A.; Brumbaugh, D. V. *Chem. Phys.* **1996**, 210,79. (b) McRae, E. G.; Kasha, M. *J. Chem. Phys.* **1958**, 28, 721. (c) Chowdhury, A.; Wachsmann-Hogiu, S.; Bangal, P. R.; Raheem, I.; Peteanu, L.A. *J. Phys. Chem. B* **2001**, 105, 12.

References for Chapter 5

1. (a) Jensen F. *Introduction to Computational Chemistry*, John Wiley & Sons: New York 1998. (b) Dreizler, R.; Gross, E. *Density Functional Theory*, Plenum Press: New York, 1995. (c) Koch, W.; Hotlthausen, M. C. *A Chemist Guide to Density Functional Theory*, 2nd ed. Wiley-VCH: Weiheim, 2002. (d) Parr, R. G.; Yang, W. *Density-Functional Theory of Atoms and Molecules* Oxford University Press: New York, 1989.

2. Hohenberg, P.; Kohn, W. *Phys. Rev.* **1964**, 136, B864.

3. (a) Pearlstein, R. M. *In Photosynthesis*; Amesz, J., Ed.; pp 299-317; Elsevier: Amsterdam, 1987. (b) Warshel, A.; Parson, W. W. *J. Am. Chem. Soc.* **1987**, 109, 6143. (c) Creighton, S.; Hwang, J. -K.; Warshel, A.; Parson, W. W.; Norris, *J. Biochemistry* **1988**, 27, 774. (d) Michel-Beyerle, M. E.; Plato, M.; Deisenhofer, J.; Michel, H.; Bixon, M.; Jorter, L. *Biochem. Biophys. Acta* **1988**, 932, 52.

4. Gilman, P. B. Photo. *Sci. Eng.* **1974**, *18*, 418.

5. Borsenberger, P. M.; Chowdry, A.; Hoesterey, D. C.; Mey, W. *J. Appl. Phys.* **1978**, 44, 5555.

6. Waggoner, A. J. *Membrane Biol.* **1976**, 27, 317.

7. (a) Krieg, M.; Bilitz, J. M.; Srichai, M.B.; Reymond, R. W. *Biochim. Biophys. Acta.* **1994**, *149*, 1199. (b) Smiley, S.; Reers, M.; Mottola-Hartshorn, C.; Lin, M.; Chen, A.; Smith, T. W.; Steele Jr., G. D.; Chen, L. B. *Proc. Natl. Acad. Sci. USA* **1991**, *88*, 3671. (c) Wang, Y. *J. Opt. Soc. Am. B* **1991**, *8*, 981.

8. Guo, Chu; Aydin, Metin; Zhu, Han-Ru; Akins, Daniel L. *J. Phys. Chem. B* **2002**, *106*, 5447.

9. Creighton, J. A.; Blatchford, C. G.; Albrecht, M. G. *J. Chem. Soc., Faraday Trans. 2* **1979**, 75, 790.

10. Bartolotti, L. J.; Flurchick. In *Review in Computational Chemistry*; Lipkowitz, K. B.; Boyd, D. B., Eds.; Vol. 7, Chapter 4; VCH Publishers Inc.: New York, 1996.

11. Becke, A. D. *Phys. Rev. A* **1988**, *38*, 3098.

12. Lee, C.; Yang, W.; Parr, R. G. *Phys. Rev. B* **1993**, *37*, 785.

13. Gordon, M. S. *Chem. Phys. Lett.* **1980**, *76*, 163.

14. Gaussian 98, revision A.7; Gaussian, Inc.: Pittsburg, PA, **1998**.

15. Wheatley, P. J. *J. Chem. Soc.* **1959**, 4096.

16. Wheatley, P. J. *J. Chem. Soc.* **1959**, 3245.

17. Aydin, Metin; Mercier, Philippe; Stevens, Nathan; Akins, Daniel "*Density Functional and Raman scattering Study for Structure and Vibrational Mode Analysis of TTBC and Its Aggregate*," in preparation.

18. Smith, Douglas L.; Luss, Henry R. *Acta Cryst. B* **1972**, *28*, 2793.

19. (a) Akins, D. L. *J. Phys. Chem.* **1986**, *90*, 1530. (b) Akins, D. L.; Macklin, J. W. *J. Phys. Chem.* **1989**, *93*, 5999. (c) Akins, D. L.; Akpabli, C.; Li, X. *J. Phys. Chem.* **1989**, *93*, 1977.

20. Albrecht, A. C. *J. Chem. Phys.* **1961**, *34*, 1476.

21. El-Azhary, A. A.; Suter, H. U.; Kubelka, J. *J. Phys. Chem*. *A* **1998**, *102*, 620.

References for Chapter 6

1. (a) Twardowski, M.; Nuzzo, R. G. *Langmuir* **2002**, *18*, 5529. (b) Hills, C. W.; Nasher, M. S.; Frenkel, A. I.; Shapley, J. R.; Nuzzo, R. G. *Langmuir* **1999**, *15*, 690.

2. (a) Lal, S.; Westcott, S. L.; Taylor, R. N.; Jackson, J. B.; Nordlander, P.; Halas, N. J. *J. Phys. Chem. B* **2002**, *106*, 5609. Chen, C. W.; Serizawa, T.; Akashi, M. *Chem. Mater.* **1999**, *11*, 1381

3. Sun, Y.; Xia, Y. *Anal. Chem.* **2002**, *74*, 5297.

4. Hirsch, L. R.; Jackson, J. B.; Lee, A.; Halas, N. J.; West, J. L. *Anal. Chem.* **2003**, *75*, 2377.

5. Raschke, G.; Brogl, S.; Susha, A. S.; Rogach, A. L.; Klar, T. A.; Feldmann, J.; Fieres, B.; Petkov, N.; Bein, T.; Nichtl, A.; Kurzinger, K. *Nano Lett.* **2004**, *4*, 1853.

6. Halas, N. *The Optical Properties of Nanoshells*; Optics & Photonic News, 2002.

7. Aden, A. L.; Kerker, M. *J. Appl. Phys. A* **1951**, 22, 1242.

8. Neeves, A. E.; Birnboim, M. H. *J. Opt. Soc. Am. B* **1989**, 6, 787.

9. Mie, G. *Ann. Phys.* **1908**, 25, 377.

10. (a) Kelly, K. L.; Eduardo, C.; Zhao, L. L.; Schatz, G. C. *J. Phys. Chem. B* **2003**, 107, 668. (b) Radloff, C.; Halas, N. J. *Nano Lett.* **2004**, 4, 1323.

11. Kobayashi, Y.; Salgueirino-Maceira, V.; Liz-Marzan, L.M. *Chem. Mater.* **2001**, 13, 1630.

12. Dong, A. G.; Wang, Y. J.; Tang, Y.; Ren, N.; Yang W. L.; Gao, Z. *Chem. Commun*. **2002**, 350.

13. Dokoutchaev, A.; James, J. T.; Koene, S. C.; Pathak, S.; Prakash, G. K. S.; Thompson, M. E. *Chem. Mater.* **1999**, 13, 238.

14. a) Twardowski, M.; Nuzzo, R. G. *Langmuir* **2002**, *18*, 5529. (b) Hills, C. W.; Nasher, M. S.; Frenkel, A. I.; Shapley, J. R.; Nuzzo, R. G. *Langmuir* **1999**, *15*, 690.

15. Lu, L.; Zhang, H.; Sun, G.; Xi, S.; Wang, H. *Langmuir*, **2003**, 19, 9490.

16. (a) Akins, D. L. *J. Phys. Chem.* **1986**, *90*, 1530. (b) Akins, D. L.; Zhuang, Y. H.; Zhu, H.-R.; Li, J. Q. *J. Phys. Chem.* **1993**, *98*, 1068. (c) Akins, D. L. In *J-Aggregate*; Kobayashi, T., Ed.; World Scientific: Singapore, 1996; pp 67-94.

17. (a) Akins, D. L. *J. Colloid Interface Sci.* **1982**, *90*, 373. (b) Ozcelik, S.; Akins, D. L. *Appl. Phys. Lett.* **1997**, *71*, 1. (c) Ozcelik, S.; Akins, D. L. *Appl. Phys. Lett.* **1998**, *73*, 1949.

18. Zhou, H. S.; Honma, I.; Komiyama, H.; Haus, J. W. *Phys. Rev. B* **1994**, 50, 12052.

19. Averitt, R. D.; Sarkar, D.; Halas, N. J. *Phys. Rev. Lett.* **1997**, 78, 4217.

20. Kometani, N.; Tsubonishi, M.; Fujita, T.; Asami, K.; Yonezawa, Y. *Langmuir* **2001**, *17*, 578.

21. Norman, T. J.; Grant, C. D.; Magana, D.; Zhang, J. Z.; Liu, J; Cao, D.; Bridges, F.; Van Buuren A. V. *J. Phys. Chem. B* **2002**, 106, 7005.

22. Zhang, J. Z.; Schwartzberg, A. M.; Norman Jr., T.; Grant, C. D.; Liu, J. Bridges, F.; Van Buuren, T. *Nano Lett.* **2005**, 5, 809.

23. Raschke, G.; Brogl, S.; Susha, A. S.; Rogach, A. L.; Klar, T. A.; Feldmann, J.; Fieres, B.; Petkov, N.; Bein, T.; Nichtl, A.; Kurzinger, K. *Nano Lett.* **2005**, *5*, 811.

24. (a) Hranisavljevic, J.; Dimitrijevic, N. M.; Wurtz, G. A.; Wiederrecht, G. P. *J. Am. Chem. Soc.* **2002**, *124*, 4536. (b) Wiederrecht, G. P; Wurtz, G. A.; Hranisavljevic, J. *Nano Lett.* **2004**, 4, 2121. (c) Yaglioglu, G.; Dorsinville, R.; Ozcelik, S. *J. Appl. Phys.* **2003**, *94*, 3143. (d) Thomas, K. G.; Kamat, P. V. *Acc. Chem. Res.* **2003,** 36, 888. (e) Sato T.; Tsugawa, F.; Tomita, T.; Kawasaki, M. *Chem. Lett.* **2001**, 30, 402.